IFS DOCUMENTATION CY28r1
(Operational implementation 9 March 2004)

IV: PHYSICAL PROCESSES

Table of contents

Part IV: PHYSICAL PROCESSES

CHAPTER 1 Overview

Table of contents

1.1 INTRODUCTION

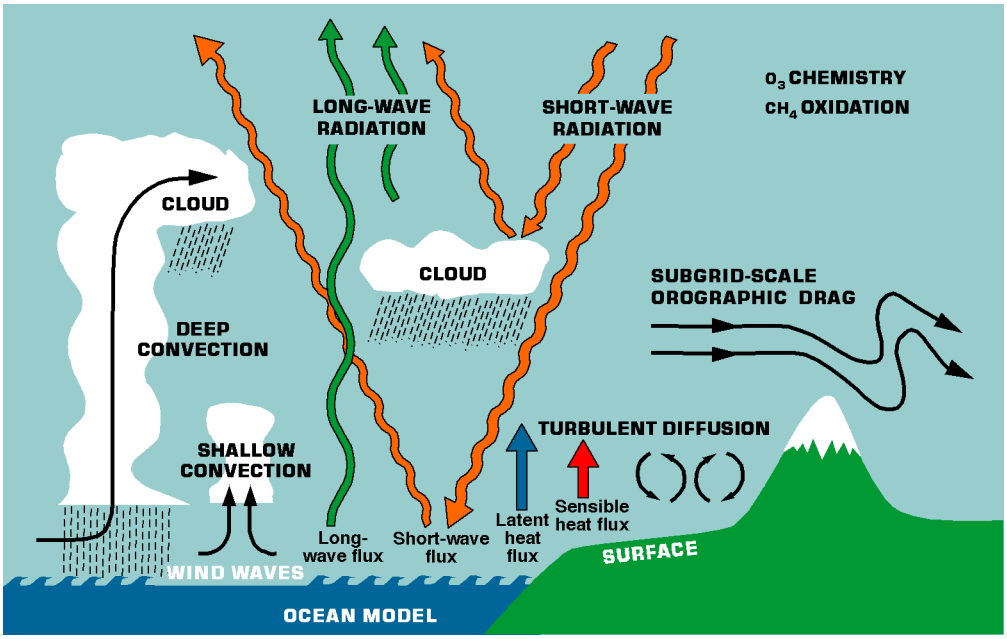

Figure 1.1 Schematic diagram of the different physical processes represented in the IFS model.

The physical processes associated with radiative transfer, turbulent mixing, subgrid-scale orographic drag, moist convection, clouds and surface/soil processes have a strong impact on the large scale flow of the atmosphere. However, these mechanisms are often active at scales smaller than the horizontal grid size. Parametrization schemes are then necessary in order to properly describe the impact of these subgrid-scale mechanisms on the large scale flow of the atmosphere. In other words the ensemble effect of the subgrid-scale processes has to be formulated in terms of the resolved grid-scale variables. Furthermore, forecast weather parameters, such as two-metre temperature, precipitation and cloud cover, are computed by the physical parametrization part of the model.

This part (Part IV 'Physical processes') of the IFS documentation describes only the physical parametrization package. After all the explicit dynamical computations per time-step are performed, the physics parametrization package is called by the IFS. The physics computations are performed only in the vertical. The input information for the physics consists of the values of the mean prognostic variables (wind components, temperature, specific humidity, liquid/ice water content and cloud fraction), the provisional dynamical tendencies for the same variables

and various surface fields, both fixed and variable.

The time integration of the physics is based on the following:

1) it has to be compatible with the adiabatic part of the IFS;

2) the tendencies from the different physical processes are computed in separate routines;

3) as a general approach, the value of a prognostic variable is updated with the tendency from one process and the next process starts from this updated value, in what is usually referred to as the 'method of fractional steps' (details are different for different processes);

4) explicit schemes are used whenever possible, but if there are numerical stability problems the scheme is made as implicit as necessary.

The radiation scheme is described in Chapter 2 'Radiation' and is the first process to be called in the physics. To save time in the rather expensive radiation computations, the full radiation part of the scheme is currently called every 3 hours. This is when the computation of the shortwave transmissivities and the longwave fluxes is performed, using the values of temperature, specific humidity, liquid/ice water content and cloud fraction at time-step $t - \Delta t$, and a climatology for aerosols, CO_2 and O_3. The computation of the fluxes is not necessarily done at every grid-point but is only performed at sampled points, using a sampling algorithm that is latitude dependent. The results are then interpolated back to the original grid using a cubic interpolation algorithm. The shortwave fluxes are updated every time-step using synchronous values of the zenith angle. The radiation scheme takes into account cloud- radiation interactions in detail by using the values of cloud fraction and liquid/ice water content, at every level, from the prognostic cloud scheme. The radiation scheme produces tendencies of temperature.

The turbulent diffusion scheme is called just after radiation (Chapter 3 'Turbulent diffusion and interactions with the surface'). The surface fluxes are computed using Monin–Obukhov similarity theory. The computation of the upper-air turbulent fluxes is based on the K-diffusivity concept. Depending on the atmospheric stability different formulations for determining the K-coefficients are used: a K-profile closure for the unstable boundary layer and a Ri-number dependent closure for the stable boundary layer. Because of numerical stability problems the integration of the diffusion equation is performed in an implicit manner. In fact, it uses a so-called 'more than implicit' method, in which the 'implicitness factor' α (which takes the value 0 in a fully explicit scheme and 1 in a fully implicit one) is set to 1.5. During the integration it uses the values of the prognostic variables at $t - \Delta t$ to compute the K-coefficients but uses the tendencies updated by the dynamics and radiation on the right hand side of the discretized diffusion equation. The turbulent diffusion scheme also predicts the skin temperature and the apparent surface humidity. The turbulent diffusion scheme produces tendencies of temperature, specific humidity and wind components. It does not compute fluxes or tendencies of the cloud variables (liquid/ice water content and cloud fraction).

The subgrid-scale orographic drag scheme is called after the turbulent diffusion and is described in Chapter 4 'Subgrid-scale orographic drag' . The subgrid-scale orographic drag parametrization represents the low- level blocking effects of subgrid-scale orography and the transports due to subgrid-scale gravity waves that are excited when stably stratified flow interacts with the orography. Numerically the scheme is similar to the turbulent diffusion and also requires an implicit treatment. In this case the 'implicitness factor' α is set to 1. The subgrid-scale orographic drag scheme produces tendencies of the wind components and temperature.

The moist convection scheme is described in Chapter 5 'Convection' . The scheme is based on the mass-flux approach and is divided in deep, mid-level and shallow convection. For deep convection the convective mass-flux is determined by assuming Convective Available Potential Energy (CAPE) is adjusted towards zero over a specified time-scale. For mid-level convection the cloud base mass-flux is directly related to the large scale vertical velocity. The intensity of shallow convection is estimated by assuming an equilibrium of moist static energy in the sub-cloud layer. The convection scheme provides tendencies of temperature, specific humidity and wind components.

In Chapter 6 'Clouds and large-scale precipitation' the prognostic cloud scheme is described. It solves two prognostic equations for liquid/ice water content and cloud fraction. The cloud scheme represents the cloud formation by cumulus convection, the formation of boundary layer and stratiform clouds. The scheme also takes into account several important cloud processes like cloud-top entrainment, precipitation of water and ice and evaporation of precipitation. In the numerical integration of the equations the terms depending linearly on the values of liquid/ice water and cloud fraction are integrated analytically. The cloud scheme produces tendencies of all the prognostic variables.

The soil/surface scheme is described in Chapter 7 'Surface parametrization' . The scheme includes prognostic equations for temperature and moisture in four soil layers and snow mass. The soil equations use an implicit time integration scheme. An interception layer collects water from precipitation and dew fall. The evaporative fluxes consider separately the fractional contributions from snow cover, wet and dry vegetation and bare soil.

Chapter 8 'Methane oxidation' describes a simple parametrization of the upper-stratospheric moisture source due to methane oxidation. A parametrization representing photolysis of vapour in the mesosphere is also included.

Chapter 9 'Ozone chemistry parametrization' gives a brief description of the ozone parametrization and Chapter 10 'Climatological data' describes the distributions of climatological fields.

1.2 OVERVIEW OF THE CODE

CALLPAR, the routine that controls the physical parametrization package, is called by CPGLAG that controls the grid-point calculations. CALLPAR calls the routines from the physics, the exception being the main radiation routine RADINT. RADINT controls the computation of the shortwave transmissivities and the longwave fluxes. RADINT is called via an interface routine RADDRV called by SCAN2MDM that is the multi-tasking interface to the computations in grid-point space (distributed memory version). RADINT is called outside CALLPAR because of the need to make the radiation space interpolation compatible with the distributed memory version of the IFS.

In CALLPAR the physics routines are called in the following order:

RADSRF:	Computes radiative properties of the surface.
CLDPP:	Computes cloud parameters required for the post processing (e.g. total cloud cover)..
RADHEATN: face	Computes the temperature tendencies and the downward radiation fluxes at the surwith updated (every time-step) values for the zenith angle.
VDFMAIN:	Controls the computation of the vertical exchange of u , v , T and q by turbulence.
GWDRAG:	Controls the computation of the tendencies for u , v and T due to the parametrization of subgrid-scale orographic drag.
CUCALLN:	Interface to call CUMASTRN that controls the computation of the tendencies for u , v , T and q due to the parametrization of moist convective processes.
CLOUDSC:	Controls the computation of tendencies for u , v , T , q , a and l due to the parametrization of the cloud processes.
SRFMAIN:	Controls the soil/surface scheme.
METHOX:	Computes tendencies for q due to methane oxidation and water vapour photolysis.

Part IV: PHYSICAL PROCESSES

CHAPTER 2 Radiation

Table of contents

2.1 RADIATIVE HEATING

The radiative heating rate is computed as the divergence of net radiation fluxes $\mathcal{F}$:

$$\left(\frac{\partial T}{\partial t}\right)_{\text{rad}} = -\frac{g}{c_p}\frac{\partial \mathcal{F}}{\partial p} \quad , \tag{2.1}$$

where c_p is the specific heat at constant pressure of moist air

$$c_p = c_{p_{\text{dry}}}\{1 + (c_{p_{\text{vap}}} - c_{p_{\text{dry}}})q / c_{p_{\text{dry}}}\} \quad ,$$

and $c_{p_{\text{dry}}}$ and $c_{p_{\text{vap}}}$ are the specific heats at constant pressure of dry air and water vapour, respectively. Sections 2.2 and 2.3 describe the computation of the longwave and shortwave radiative fluxes respectively. The solution of the radiative transfer equation to obtain the fluxes is unfortunately very expensive, and we cannot afford to do it more than every 3 hours at every fourth grid point. The interpolation scheme used for obtaining the radiative fluxes at every grid point and every time step for the relevant instantaneous temperature profile and solar zenith angle is described in Section 2.4.

A description of the inputs, in particular the climatologically defined quantities of radiative importance is given in Section 2.5. Finally, an alphabetical list of the subroutines of the radiation scheme is given in Section 2.6.

2.2 LONGWAVE RADIATION

Since cycle 22r3, two longwave radiation schemes are available in the ECMWF model, the pre-cycle 22r3 by Morcrette (1991), and the current longwave radiation transfer scheme, the Rapid Radiation Transfer Model (RRTM).

The rate of atmospheric cooling by emission-absorption of longwave radiation is

$$\frac{\partial T}{\partial t} = \frac{g}{c_p}\frac{\partial \mathcal{F}_{\text{LW}}}{\partial p} \tag{2.2}$$

where F_{LW} is the net longwave radiation flux (the subscript 'LW' is omitted in the remainder of this section).

Assuming a non-scattering atmosphere in local thermodynamic equilibrium, $\mathcal{F}$ is given by

$$\mathcal{F} = \int_{-1}^{1} \mu \, d\mu \left[\int_{0}^{\infty} d\nu \left\{ \mathcal{L}_\nu(p_{\text{surf}}, \mu) t_\nu(p_{\text{surf}}, p, \mu) + \int_{p' = p_{\text{surf}}}^{0} \mathcal{L}_\nu(p', \mu) \, dt_\nu \right\} \right] \tag{2.3}$$

where $\mathcal{L}_\nu(p, \mu)$ is the monochromatic radiance at wavenumber ν at level p, propagating in a direction θ (the angle that this direction makes with the vertical), where $\mu = \cos\theta$ and $t_\nu(p, p'; r)$ is the monochromatic transmission through a layer whose limits are at p and p' seen under the same angle θ, with $r = \sec\theta$. The subscript 'surf' refers to the earth's surface.

Subsections 2.2.1 to 2.2.4 describe the pre-cycle 22r3 scheme, and Subsection 2.2.5 describes the RRTM scheme in cycle 22r3.

2.2.1 The pre-cycle 22r3 scheme

After separating the upward and downward components (indicated by superscripts + and –, respectively), and integrating by parts, we obtain the radiation transfer equation as it is actually estimated in the longwave part of the

radiation code

$$\mathcal{F}_\nu^{+}(p) = [B_\nu(T_{\text{surf}}) - B_\nu(T_{0+})]t_\nu(p_{\text{surf}}, p; r) + B_\nu(T(p)) + \int_{p'=p_{\text{surf}}}^{p} t_\nu(p, p'; r)\mathrm{d}B_\nu$$

$$\mathcal{F}_\nu^{-}(p) = [B_\nu(T_\infty) - B_\nu(T_{\text{top}})]t_\nu(p, 0; r) + B_\nu(T(p)) + \int_{p'=p}^{0} t_\nu(p', p; r)\mathrm{d}B_\nu \qquad (2.4)$$

where, taking benefit of the isotropic nature of the longwave radiation, the radiance $\mathcal{L}_\nu$ of (2.3) has been replaced by the Planck function $B_\nu(T)$ in units of flux, W m^{-2} (here, and elsewhere, B_ν is assumed to always includes the π factor). T_{surf} is the surface temperature, T_{0+} that of the air just above the surface, $T(p)$ is the temperature at pressure-level p, T_{top} that at the top of the atmospheric model. The transmission t_ν is evaluated as the radiance transmission in a direction θ to the vertical such that $r = \sec\theta$ is the diffusivity factor (*Elsasser,* 1942). Such an approximation for the integration over the angle is usual in radiative transfer calculations, and tests on the validity of this approximation have been presented by *Rodgers and Walshaw* (1966) and *Liu and Schmetz* (1988) among others. The use of the diffusivity factor gives cooling rates within 2% of those obtained with a 4-point Gaussian quadrature.

2.2.2 Vertical integration

The integrals in (2.4) are evaluated numerically, after discretization over the vertical grid, considering the atmosphere as a pile of homogeneous layers. As the cooling rate is strongly dependent on local conditions of temperature and pressure, and energy is mainly exchanged with the layers adjacent to the level where fluxes are calculated, the contribution of the distant layers is simply computed using a trapezoidal rule integration, but the contribution of the adjacent layers is evaluated with a 2-point Gaussian quadrature, thus at the i th level,

$$\int_{p'=p_{\text{surf}}}^{p_i} t_\nu(p, p'; r)\mathrm{d}B_\nu =$$

$$\sum_{l=2}^{i-2} \mathrm{d}B_\nu(l) w_l t_\nu(p_i, p_l; r) + \frac{1}{2}\sum_{j=1}^{i-2} \mathrm{d}B_\nu(j)[t_\nu(p_i, p_j; r) + t_\nu(p_i, p_{j-1}; r)] \qquad (2.5)$$

where p_l is the pressure corresponding to the Gaussian root and w_l is the Gaussian weight. $\mathrm{d}B_\nu(j)$ and $\mathrm{d}B_\nu(l)$ are the Planck function gradients calculated between two interfaces, and between mid-layer and interface, respectively.

2.2.3 Spectral integration

The integration over wavenumber ν is performed using a band emissivity method, as first discussed by *Rodgers* (1967). The longwave spectrum is divided into six spectral regions.

1) 0 – 350 cm^{-1} & 1450 – 1880 cm^{-1}
2) 500 – 800 cm^{-1}
3) 800 – 970 cm^{-1} & 1110 – 1250 cm^{-1}
4) 970 – 1110 cm^{-1}

5) $350 - 500\ \mathrm{cm}^{-1}$

6) $1250 - 1450\ \mathrm{cm}^{-1}$ & $1880 - 2820\ \mathrm{cm}^{-1}$

corresponding to the centres of the rotation and vibration-rotation bands of H_2O, the 15 μm band of CO_2, the atmospheric window, the 9.6 μm band of O_3, the 25 μm "window" region, and the wings of the vibration-rotation band of H_2O, respectively. Over these spectral regions, band fluxes are evaluated with the help of band transmissivities precalculated from the narrow-band model of *Morcrette and Fouquart* (1985) - See Appendix of *Morcrette et al.* (1986) for details.corresponding to the centres of the rotation and vibration-rotation bands of H_2O, the 15 band of CO_2, the atmospheric window, the 9.6 band of O_3, the 25 "window" region, and the wings of the vibration-rotation band of H_2O, respectively. Over these spectral regions, band fluxes are evaluated with the help of band transmissivities precalculated from the narrow-band model of *Morcrette and Fouquart* (1985) - See Appendix of *Morcrette et al*. (1986) for details.

Integration of (2.4) over wavenumber ν within the kth spectral region gives the upward and downward fluxes as

$$\mathcal{F}_k^{+}(p) = \{B_k(T_{\mathrm{surf}}) - B_k(T_{0+})\}t_{B_k}\{r\mathcal{U}(p_{\mathrm{surf}}, p), T_{\mathcal{U}}(p_{\mathrm{surf}}, p)\} + B_k(T_p) + \int_{p'=p_{\mathrm{surf}}}^{p} t_{\mathrm{dB}_k}\{r\mathcal{U}(p, p'), T_{\mathcal{U}}(p, p')\}\mathrm{d}B_k \tag{2.6}$$

$$\mathcal{F}_k^{-}(p) = \{B_k(T_0) - B_k(T_\infty)\}t_{B_k}\{r\mathcal{U}(p, 0), T_{\mathcal{U}}(p, 0)\} - B_k(T_p) - \int_{p'=p}^{0} t_{\mathrm{dB}_k}\{r\mathcal{U}(p', p), T_{\mathcal{U}}(p', p)\}\mathrm{d}B_k \tag{2.7}$$

The formulation accounts for the different temperature dependencies involved in atmospheric flux calculations, namely that on T_p, the temperature at the level where fluxes are calculated, and that on $T_{\mathcal{U}}$, the temperature that governs the transmission through the temperature dependence of the intensity and half-widths of the lines absorbing in the concerned spectral region. The band transmissivities are non-isothermal accounting for the temperature dependence that arises from the wavenumber integration of the product of the monochromatic absorption and the Planck function. Two normalized band transmissivities are used for each absorber in a given spectral region: the first one for calculating the first right-hand-side. term in (2.4), involving the boundaries; it corresponds to the weighted average of the transmission function by the Planck function

$$t_B(\overline{\mathcal{U}p}, T_p, T_{\mathcal{U}}) = \frac{\int_{\nu_1}^{\nu_2} B_\nu(T_p)t_\nu(\overline{\mathcal{U}p}, T_{\mathcal{U}})\mathrm{d}\nu}{\int_{\nu_1}^{\nu_2} B_\nu(T_p)\mathrm{d}\nu} \tag{2.8}$$

the second one for calculating the integral term in (2.4) is the weighted average of the transmission function by the derivative of the Planck function

$$t_{dB}(\overline{up}, T_p, T_u) = \frac{\int_{\nu_1}^{\nu_2} \{dB(T_p)/dT\} t_\nu(\overline{up}, T_u) d\nu}{\int_{\nu_1}^{\nu_2} \{dB(T_p)/dT\} d\nu} \tag{2.9}$$

where $\overline{up}$ is the pressure weighted amount of absorber.

The effect on absorption of the Doppler broadening of the lines (important only for pressure lower than 10 hPa) is included simply using the pressure correction method of *Fels* (1979). A finite line width (assumed to represent the Doppler half-width of the line) is retained under low pressure conditions where the pure Lorentz line width (proportional to pressure) would normally become negligible (*Giorgetta and Morcrette,* 1995).

In the scheme, the actual dependence on T_p is carried out explicitly in the Planck functions integrated over the spectral regions. Although normalized relative to $B(T_p)$ or $dB(T_p)/dT$, the transmissivities still depend on T_u, both through Wien's displacement of the maximum of the Planck function with temperature and through the temperature dependence of the absorption coefficients. For computational efficiency, the transmissivities have been developed into Pade approximants

$$t(\overline{up}, T_u) = \frac{\sum_{i=0}^{2} c_i u_{\text{eff}}^{i/2}}{\sum_{j=0}^{2} d_j u_{\text{eff}}^{j/2}} \tag{2.10}$$

where $u_{\text{eff}} = r(\overline{up})\Psi(T_u, \overline{up})$ is an effective amount of absorber which incorporates the diffusivity factor r, the weighting of the absorber amount by pressure $\overline{up}$, and the temperature dependence of the absorption coefficients. The function $\Psi(T_u, \overline{up})$ takes the form

$$\Psi(T_u, \overline{up}) = \exp[a(\overline{up})(T_u - 250) + b(\overline{up})(T_u - 250)^2] \tag{2.11}$$

The temperature dependence due to Wien's law is incorporated although there is no explicit variation of the coefficients c_i and d_j with temperature. These coefficients have been computed for temperatures between 187.5 and 312.5 K with a 12.5 K step, and transmissivities corresponding to the reference temperature the closest to the pressure weighted temperature T_u are actually used in the scheme.

2.2.4 The incorporation of the effects of clouds

The incorporation of the effects of clouds on the longwave fluxes follows the treatment discussed by *Washington and Williamson* (1977). Whatever the state of the cloudiness of the atmosphere, the scheme starts by calculating the fluxes corresponding to a clear-sky atmosphere and stores the terms of the energy exchange between the different levels (the integrals in (2.4)) Let $\mathcal{F}_0^+(i)$ and $\mathcal{F}_0^-(i)$ be the upward and downward clear-sky fluxes. For any cloud layer actually present in the atmosphere, the scheme then evaluates the fluxes assuming a unique overcast cloud of emissivity unity. Let $\mathcal{F}_n^+(i)$ and $\mathcal{F}_n^-(i)$ the upward and downward fluxes when such a cloud is present in the nth layer of the atmosphere. Downward fluxes above the cloud, and upward fluxes below the cloud, are assumed to be given by the clear-sky values

$$\mathcal{F}_n^+(i) = \mathcal{F}_0^+(i) \text{ for } i \le n$$
$$\mathcal{F}_n^-(i) = \mathcal{F}_0^-(i) \text{ for } i > n \tag{2.12}$$

Upward fluxes above the cloud ($\mathcal{F}_n^+(k)$ for $k \ge n+1$) and downward fluxes below it ($\mathcal{F}_n^-(k)$ for $k > n$) can be expressed with expressions similar to (2.5) provided the boundary terms are now replaced by terms corresponding to possible temperature discontinuities between the cloud and the surrounding air

$$\mathcal{F}_n^+(k) = \{\mathcal{F}_{\text{cld}}^+ - B(n+1)\}t(p_k, p_{n+1}; r) + B(k) + \int_{p'=p_{n-1}}^{p_k} t(p_k, p'; r)\mathrm{d}B$$
$$\mathcal{F}_n^-(k) = \{\mathcal{F}_{\text{cld}}^- - B(n)\}t(p_k, p_n; r) + B(k) + \int_{p'=p_n}^{p_k} t(p_k, p'; r)\mathrm{d}B \tag{2.13}$$

where $B(i)$ is now the total Planck function (integrated over the whole longwave spectrum) at level i , and $\mathcal{F}_{\text{cld}}^+$ and $\mathcal{F}_{\text{cld}}^-$ are the longwave fluxes at the upper and lower boundaries of the cloud. Terms under the integrals correspond to exchange of energy between layers in clear-sky atmosphere and have already been computed in the first step of the calculations. This step is repeated for all cloudy layers. The fluxes for the actual atmosphere (with semi-transparent, fractional and/or multi-layered clouds) are derived from a linear combination of the fluxes calculated in previous steps with some cloud overlap assumption in the case of clouds present in several layers. Let N be the index of the layer containing the highest cloud, $\mathcal{C}_{\text{cld}}(i))$ the fractional cloud cover in layer i , with $\mathcal{C}_{\text{cld}}(0) = 1$ for the upward flux at the surface, and with $\mathcal{C}_{\text{cld}}(N+1) = 1$ and $\mathcal{F}_{N+1}^- = \mathcal{F}_0^-$ to have the right boundary condition for downward fluxes above the highest cloud.

Whereas the maximum and random overlap assumptions are also available in the code (*Morcrette and Fouquart*, 1986), the maximum-random overlap assumption is operationally used in the ECMWF model, and the cloudy upward $\mathcal{F}^+$ and downward $\mathcal{F}^-$ fluxes are obtained as

$$\mathcal{F}^+(i) = \mathcal{F}_0^+(i) \qquad \text{for } i = 1$$
$$\mathcal{F}^-(i) = \mathcal{C}_{\text{cld}}(i-1)\mathcal{F}^+_{i-1}(i) + \sum_{n=0}^{i-2} \mathcal{C}_{\text{cld}}(n)\mathcal{F}_n^+(i) \prod_{l=n+1}^{i-1} \{1 - \mathcal{C}_{\text{cld}}(l)\} \quad \text{for } 2 \le i \le N+1$$
$$\mathcal{F}^+(i) = \mathcal{C}_{\text{cld}}(N)\mathcal{F}_N^+(i) + \sum_{n=0}^{N-1} \mathcal{C}_{\text{cld}}(n)\mathcal{F}_n^+(i) \prod_{l=n+1}^{N} \{1 - \mathcal{C}_{\text{cld}}(l)\} \qquad \text{for } i \ge N+2 \tag{2.14}$$

In case of semi-transparent clouds, the fractional cloudiness entering the calculations is an effective cloud cover equal to the product of the emissivity due to the condensed water and the gases in the layer by the horizontal coverage of the cloud layer, with the emissivity, ε_{cld} , related to the condensed water amount by

$$\varepsilon_{\text{cld}} = 1 - \exp(-k_{\text{abs}} u_{\text{LWP}}) \tag{2.15}$$

where k_{abs} is the condensed water mass absorption coefficient (in $m^2 kg^{-1}$) following *Smith and Shi* (1992).

2.2.5 The Rapid Radiation Transfer Model (RRTM)

As stated in *Mlawer et al.* (1997), the objective in the development of RRTM has been to obtain an accuracy in the calculation of fluxes and heating rates consistent with the best line-by-line models. It utilizes the correlated-k methode and shows its filiation to the Atmospheric and Environmental Research, Inc. (AER) line-by-line model (LBLRTM, Clough et al., 1989, 1992, *Clough and Iacono*, 1995) through its use of absorption coefficients for the relevant k-distributions derived from LBLRTM. Therefore the k-coefficients in RRTM include the effect of the CKD2.2 water vapour continuum (*Clough et al.*, 1989).

The main point in the correlated-k method (*Lacis and Oinas*, 1991; *Fu and Liou*, 1992) is the mapping of the absorption coefficient $k(\nu)$ from the spectral space (where it varies irregularly with wavenumber ν) to the g-space (where $g(k)$ is the probability distribution function, i.e. the fraction of the absorption coefficients in the set smaller than k). The effect of trhis reordering is a rearrangement of the sequence of terms in the integral over wavenumber in the radiative transfer equation (RTE), which makes it equivalent to what would be done for monochromatic radiation.

In the ECMWF model, no provision is presently taken for scattering in the longwave. Therefore, in order to get the downward radiance, the integration over the vertical dimension is simply done starting from the top of the atmosphere, going downward layer by layer. At the surface, the boundary condition (in terms of spectral emissivity, and potential reflection of downward radiance) is computed, then, in order to get the upward radiance, the integration over the vertical dimension is repeated, this from the surface upward.

The spectrally averaged radiance (between ν_1 and ν_2) emerging from an atmospheric layer is

$$\overline{R} = \frac{1}{(\nu_1 - \nu_2)} \int_{\nu_2}^{\nu_1} d\nu \left\{ R_0(\nu) + \int_{t_\nu}^{1} [B(\nu, T(t'_\nu)) - R_0(\nu)]\, dt' \right\} \tag{2.16}$$

where R_0 is the incoming radiance to the layer, $B(\nu, T)$ is the Planck function at wavenumber ν and temperature T, t_ν is the transmittance for the layer optical path, and t'_ν is the transmittance at a point along the optical path in the layer. Under the mapping $\nu \rightarrow g$, this becomes

$$\overline{R} = \int_0^1 dg \left\{ B_{\text{eff}}(g, T_g) + [R_0(g) - B_{\text{eff}}(g, T_g)] \exp\left[-k(g, P, T) \frac{\rho \Delta z}{\cos\phi} \right] \right\} \tag{2.17}$$

where $B_{\text{eff}}(g, T)$ is an effective Planck function for the layer that varies with the layer's transmittance such as to ensure continuity of flux across layer boundaries for opaque conditions. The dependence of the transmittance is now written in terms of the absorption coefficient $k(g, P, T)$ at layer pressure P and temperature T, the absorber density ρ, the vertical thickness of the layer Δz, and the angle ϕ of the optical path.

For a given spectral interval, the domain of the variable g is partitioned into subintervals (see Table 2.6, number of g-points), each corresponding to a limited range of $k(g)$ values and for which a characteristicvalue κ_j of the absorption coefficient is chosen. These κ_j are then used to compute the outgoing radiance

$$\overline{R} = \sum_j W_j \left[B_{\text{eff}_j} + (R_{0j} - B_{\text{eff}_j}) \exp\left(-\kappa_j \frac{\rho \Delta z}{\cos\phi} \right) \right] \tag{2.18}$$

where W_j is the size of the sub-intervals ($\sum W_j = 1$).

The accuracy of these absorption coefficients has been established by numerous and continuing high-resolution validations of LBLRTM with spectroscopic measurements, in particular those from the Atmospheric Radiation Measurement program (ARM). Compared to the original RRTM (*Mlawer et al.*, 1997), the version used at ECMWF has been slightly modified to account for cloud optical properties and surface emissivity defined for each of the 16 bands over which spectral fluxes are computed. For efficiency reason, the original number of g-points ($256 = 16 \times 16$) has been reduced to 140 (see Table 2.6). Other changes are the use of a diffusivity approximation (instead of the three-angle integration over the zenith angle used in the original scheme) to derive upward and downward fluxes from the radiances, and the modification of the original cloud random overlapping assumption to include (to the same degree of approximation as used in the operational SW scheme) a maximum-random overlapping of cloud layers. Given the monochromatic form of the RTE, the vertical integration is simply carried out one layer at a time from the top-of-the-atmosphere to the surface to get the downward fluxes. The downward fluxes at the surface are then used with the spectral surface emissivities and the surface temperature to get the upward longwave fluxes in each of the 140 subintervals. Then the upward fluxes are obtained in a similar fashion from the surface to the ToA.

For the relevant spectral intervals of the RRTM schemes, ice cloud optical properties are derived from *Ebert and Curry* (1992), and water cloud optical properties from *Fouquart* (1987). Whereas in the operational scheme the cloud emissivity used to compute the effective cloud cover is defined over the whole LW spectrum from spectrally averaged mass absorption coefficients and the relevant cloud water and/or ice paths (following *Smith and Shi*, 1992), in RRTM, the cloud optical thickness is defined as a function of spectrally varying mass absorption coefficients and relevant cloud water and ice paths, and is used within the true cloudy fraction of the layer. Alternate sets of cloud optical properties are also available for RRTM, based on *Savijarvi and Raisanen* (1997) for liquid water clouds, and *Fu et al.* (1998) for ice clouds.

2.3 SHORTWAVE RADIATION

The rate of atmospheric heating by absorption and scattering of shortwave radiation is

$$\frac{\partial T}{\partial t} = \frac{g}{c_p}\frac{\partial \mathcal{F}_{\mathrm{SW}}}{\partial p} \tag{2.19}$$

where $\mathcal{F}_{\mathrm{SW}}$ is the net total shortwave flux (the subscript SW will be omitted in the remainder of this section).

$$\mathcal{F}(\delta) = \int_0^{\infty} d\nu \left[\int_0^{2\pi} d\phi \left\{ \int_{-1}^{+1} \mu \mathcal{L}_\nu(\delta, \mu, \phi) d\mu \right\} \right] \tag{2.20}$$

is the diffuse radiance at wavenumber ν, in a direction given by the azimuth angle, ϕ, and the zenith angle, θ, with $\mu = \cos\theta$. In (2.20), we assume a plane parallel atmosphere, and the vertical coordinate is the optical depth δ, a convenient variable when the energy source is outside the medium

$$\delta(p) = \int_{p}^{0} \beta_{\nu}^{ext}(p')\, dp' \tag{2.21}$$

$\beta_{\nu}^{ext}(p)$ is the extinction coefficient, equal to the sum of the scattering coefficient β_{ν}^{sca} of the aerosol (or cloud particle absorption coefficient β_{ν}^{abs}) and the purely molecular absorption coefficient k_{ν}. The diffuse radiance L_{ν} is governed by the radiation transfer equation

$$\mu \frac{d\mathcal{L}_{\nu}(\delta, \mu, \phi)}{d\delta} = \mathcal{L}_{\nu}(\delta, \mu, \phi) - \frac{\varpi_{\nu}(\delta)}{4} P_{\nu}(\delta, \mu, \phi, \mu_0, \phi_0) \mathcal{E}_{\nu}^{0} \exp(-\delta/\mu_r)$$
$$- \frac{\varpi_{\nu}(\delta)}{4} \int_{0}^{2\pi} d\phi' \left\{ \int_{-1}^{+1} \Phi_{\nu}(\delta, \mu, \phi, \mu', \phi') \mathcal{L}_{\nu}(\delta, \mu', \phi') d\mu' \right\} \tag{2.22}$$

$\mathcal{E}_{\nu}^{0}$ is the incident solar irradiance in the direction $\mu_0 = \cos\theta_0$, ϖ_{ν} is the single scattering albedo ($= \beta_{\nu}^{sca}/k_{\nu}$) and $\Phi(\delta, \mu, \phi, \mu', \phi')$ is the scattering phase function which defines the probability that radiation coming from direction (μ', ϕ') is scattered in direction (μ, ϕ). The shortwave part of the scheme, originally developed by *Fouquart and Bonnel* (1980) solves the radiation transfer equation and integrates the fluxes over the whole shortwave spectrum between 0.2 and 4 μm. Upward and downward fluxes are obtained from the reflectance and transmittances of the layers, and the photon-path-distribution method allows to separate the parametrization of the scattering processes from that of the molecular absorption.

2.3.1 Spectral integration

Solar radiation is attenuated by absorbing gases, mainly water vapour, uniformly mixed gases (oxygen, carbon dioxide, methane, nitrous oxide) and ozone, and scattered by molecules (Rayleigh scattering), aerosols and cloud particles. Since scattering and molecular absorption occur simultaneously, the exact amount of absorber along the photon path length is unknown, and band models of the transmission function cannot be used directly as in longwave radiation transfer (see Section 2.2). The approach of the photon path distribution method is to calculate the probability $\Pi(u)du$ that a photon contributing to the flux $\mathcal{F}_{cons}$ in the conservative case (i.e., no absorption, $\omega_{\nu} = 1$, $k_{\nu} = 0$) has encountered an absorber amount between u and $u + du$. With this distribution, the radiative flux at wavenumber ν is related to $\mathcal{F}_{cons}$ by

$$\mathcal{F}_{\nu} = \mathcal{F}_{cons} \int_{0}^{\infty} \Pi(u) \exp(-k_{\nu} u) du \tag{2.23}$$

and the flux averaged over the spectral interval $\Delta\nu$ can then be calculated with the help of any band model of the transmission function $t_{\Delta\nu}$

$$\mathcal{F} = \frac{1}{\Delta\nu} \int_{\Delta\nu} \mathcal{F}_{\nu} d\nu = \mathcal{F}_{cons} \int_{0}^{\infty} \Pi(u) t_{\Delta\nu}(u) d\nu \tag{2.24}$$

To find the distribution function $\Pi(u)$, the scattering problem is solved first, by any method, for a set of arbitrarily fixed absorption coefficients k_1, thus giving a set of simulated fluxes $\mathcal{F}_{k_1}$. An inverse Laplace transform is then performed on (2.23) (*Fouquart*, 1974). The main advantage of the method is that the actual distribution $\Pi(u)$ is smooth enough that (2.23) gives accurate results even if $\Pi(u)$ itself is not known accurately. In fact, $\Pi(u)$ need not be calculated explicitly as the spectrally integrated fluxes are

$$\mathcal{F} = \mathcal{F}_{\text{cons}} t_{\Delta\nu}(\langle u \rangle) \qquad \text{in the limiting case of weak absorption}$$

$$\mathcal{F} = \mathcal{F}_{\text{cons}} t_{\Delta\nu}(\langle u^{1/2} \rangle) \qquad \text{in the limiting case of strong absorption}$$

where $\langle u \rangle = \int_0^\infty \Pi(u)\, u \,\mathrm{d}u$ and $\langle u^{1/2} \rangle = \int_0^\infty \Pi(u)\, u^{1/2} \mathrm{d}u$.

The atmospheric absorption in the water vapour bands is generally strong, and the scheme determines an effective absorber amount u_{e} between $\langle u \rangle$ and $\langle u^{1/2} \rangle$ derived from

$$u_{\text{e}} = \ln(\mathcal{F}_{k_{\text{e}}}/\mathcal{F}_{\text{cons}})/k_{\text{e}} \tag{2.25}$$

where k_{e} is an absorption coefficient chosen to approximate the spectrally averaged transmission of the clear sky atmosphere

$$k_{\text{e}} = \frac{1}{u_{\text{tot}}/\mu_0} \ln(t_{\Delta\nu}(u_{\text{tot}}/\mu_o)) \tag{2.26}$$

where u_{tot} is the total amount of absorber in a vertical column and $\mu_0 = \cos\theta_0$. Once the effective absorber amounts of H_2O and uniformly mixed gases are found, the transmission functions are computed using Pade approximants

$$t_{\Delta\nu}(u) = \frac{\sum_{i=0}^{N} a_i u^{i-1}}{\sum_{j} b_j u^{j-1}} \tag{2.27}$$

Absorption by ozone is also taken into account, but since ozone is located at low pressure levels for which molecular scattering is small and Mie scattering is negligible, interactions between scattering processes and ozone absorption are neglected. Transmission through ozone is computed using (2.24) where u_{O_3} the amount of ozone is

$$u^{\text{d}}_{\text{O}_3} = M \int_p^0 \mathrm{d}u_{\text{O}_3} \qquad \text{for the downward transmission of the direct solar beam}$$

$$u^{\text{u}}_{\text{O}_3} = r \int_{p_s}^0 \mathrm{d}u_{\text{O}_3} + u^{\text{d}}_{\text{O}_3}(p_{\text{surf}}) \qquad \text{for the upward transmission of the diffuse radiation}$$

$r = 1.66$ is the diffusivity factor (see Section 2.2), and M is the magnification factor (*Rodgers,* 1967) used instead of r to account for the sphericity of the atmosphere at very small solar elevations

$$M = 35/\sqrt{\mu_0^2 + 1} \tag{2.28}$$

To perform the spectral integration, it is convenient to discretize the solar spectrum into subintervals in which the surface reflectance, molecular absorption characteristics, and cloud optical properties can be considered as constants. One of the main causes for such a spectral variation is the sharp increase in the reflectivity of the vegetation in the near-infrared. Also, water vapour does not absorb below 0.69 μm nor do liquid water clouds. Till June 2000, the ECMWF shortwave scheme considered only two spectral intervals, one for the visible (0.2 - 0.69 μm), one for the near-infrared (0.69-4.00 μm) parts of the solar spectrum. From June 2000 to April 2002, the near-infrared interval was sub-divided into three intervals (0.69 - 1.19 - 2.38 - 4.00 μm) to account better for the spectral variations of the cloud optical properties. Till April 2002, all the molecular absorption coefficients (for O_3, H_2O, uniformly mixed gases) were derived from statistical models of the transmission function using spectroscopic parameters derived from various versions of the HITRAN database (*Rothman et al.*, 1986, 1992). In April 2002, following the recomputation of all the molecular absorption coefficients from an updated version of the shortwave line-by-line model of *Dubuisson et al.* (1996) using spectroscopic data from *HAWKS* (2000), the ultraviolet and visible part of the spectrum are now considered in three spectral intervals (0.20 - 0.25 - 0.69 μm) making the scheme having a total of six spectral intervals over which the aerosol and cloud optical properties are also defined. The cut-off at 0.69 μm allows the scheme to be more computational efficient, in as much as the interactions between gaseous absorption (by water vapour and uniformly mixed gases) and scattering processes are accounted for only in the near-infrared interval(s).

2.3.2 Vertical integration

Considering an atmosphere where a fraction $C_{\mathrm{cld}}^{\mathrm{tot}}$ (as seen from the surface or the top of the atmosphere) is covered by clouds (the fraction $C_{\mathrm{cld}}^{\mathrm{tot}}$ depends on which cloud-overlap assumption is assumed for the calculations), the final fluxes are given as a weighted average of the fluxes in the clear sky and in the cloudy fractions of the column

$$\mathcal{F}^{-}(j) = C_{\mathrm{cld}}^{\mathrm{tot}}\, \mathcal{F}_{\mathrm{cld}}^{-}(j) + (1 - C_{\mathrm{cld}}^{\mathrm{tot}})\mathcal{F}_{\mathrm{clr}}^{-}$$

where the subscripts 'clr' and 'cld' refer to the clear-sky and cloudy fractions of the layer, respectively. In contrast to the scheme of *Geleyn and Hollingsworth* (1979), the fluxes are not obtained through the solution of a system of linear equations in a matrix form. Rather, assuming an atmosphere divided into homogeneous layers, the upward and downward fluxes at a given layer interface j are given by

$$\begin{aligned} \mathcal{F}^{-}(j) &= \mathcal{F}_0 \prod_{k=j}^{N} \mathcal{T}_{\mathrm{bot}}(k) \\ \mathcal{F}^{+}(j) &= \mathcal{F}^{-}(j)\mathcal{R}_{\mathrm{top}}(j-1) \end{aligned} \tag{2.29}$$

where $\mathcal{R}_{\mathrm{top}}(j)$ and $\mathcal{T}_{\mathrm{bot}}(j)$ are the reflectance at the top and the transmittance at the bottom of the j th layer. Computations of $\mathcal{R}_{\mathrm{top}}$'s start at the surface and work upward, whereas those of $\mathcal{T}_{\mathrm{bot}}$'s start at the top of the atmosphere and work downward. $\mathcal{R}_{\mathrm{top}}$ and $\mathcal{T}_{\mathrm{bot}}$ account for the presence of cloud in the layer

$$\begin{aligned} \mathcal{R}_{\mathrm{top}} &= C_{\mathrm{cld}}\mathcal{R}_{\mathrm{cld}} + (1 - C_{\mathrm{cld}})\mathcal{R}_{\mathrm{clr}} \\ \mathcal{T}_{\mathrm{bot}} &= C_{\mathrm{cld}}\mathcal{T}_{\mathrm{cld}} + (1 - C_{\mathrm{cld}})\mathcal{T}_{\mathrm{clr}} \end{aligned} \tag{2.30}$$

where C_{cld} is the cloud fractional coverage of the layer within the cloudy fraction C_{cld}^{tot} of the column.

2.3.2 (a) Cloudy fraction of the layer. $R_{t_{cdy}}$ and $T_{b_{cdy}}$ are the reflectance at the top and transmittance at the bottom of the cloudy fraction of the layer calculated with the Delta-Eddington approximation. Given δ_c, δ_a, and δ_g, the optical thicknesses for the cloud, the aerosol and the molecular absorption of the gases, respectively, and $(= k_e U)$, and g_c and g_a the cloud and aerosol asymmetry factors, $R_{t_{cdy}}$ and $T_{b_{cdy}}$ are calculated as functions of the total optical thickness of the layer

$$\delta = \delta_c + \delta_a + \delta_g \tag{2.31}$$

of the total single scattering albedo

$$\varpi^* = \frac{\delta_c + \delta_a}{\delta_c + \delta_a + \delta_g} \tag{2.32}$$

of the total asymmetry factor

$$g^* = \frac{\delta_c}{\delta_c + \delta_a} g_c + \frac{\delta_a}{\delta_c + \delta_a} g_a \tag{2.33}$$

of the reflectance $R_{\_}$ of the underlying medium (surface or layers below the j th interface), and of the cosine of an effective solar zenith angle $\mu_{eff}(j)$ which accounts for the decrease of the direct solar beam and the corresponding increase of the diffuse part of the downward radiation by the upper scattering layers

$$\mu_{eff}(j) = [(1 - C_{cld}^{eff}(j))/\mu + r\, C_{cld}^{eff}(j)]^{-1} \tag{2.34}$$

with $C_{cld}^{eff}(j)$ the effective total cloudiness over level j

$$C_{cld}^{eff}(j) = 1 - \prod_{i=\,\cdot\,}^{\cdot\,} (1 - C_{cld}(i) E(i)) \tag{2.35}$$

and

$$E(i) = 1 - \exp\left[-\frac{(1 - \varpi_c(i) g_c(i)^2)\delta_c(i)}{\mu}\right] \tag{2.36}$$

$\delta_c(i)$, $\varpi_c(i)$ and $g_c(i)$ are the optical thickness, single scattering albedo and asymmetry factor of the cloud in the i th layer, and r is the diffusivity factor. The scheme follows the Eddington approximation first proposed by *Shettle and Weinman* (1970), then modified by *Joseph et al.* (1976) to account more accurately for the large fraction of radiation directly transmitted in the forward scattering peak in case of highly asymmetric phase functions. Eddington's approximation assumes that, in a scattering medium of optical thickness δ^*, of single scattering albedo ω, and of asymmetry factor g, the radiance L entering (2.17) can be written as

$$L(\delta, \mu) = L_0(\delta) + \mu L_1(\delta) \tag{2.37}$$

In that case, when the phase function is expanded as a series of associated Legendre functions, all terms of order

greater than one vanish when (2.20) is integrated over μ and ϕ. The phase function is therefore given by

$$P(\Theta) = 1 + \beta_1(\Theta)\mu$$

where Θ is the angle between incident and scattered radiances. The integral in (2.20) thus becomes

$$\int_0^{2\pi} d\phi' \left\{ \int_{-1}^{+1} P(\mu, \phi, \mu', \phi') \mathcal{L}(\mu', \phi') d\mu' \right\} = 4\pi(\mathcal{L}_0 + \pi\mathcal{L}_1) \tag{2.38}$$

where

$$g = \frac{\beta_1}{3} = \frac{1}{2}\int_{-1}^{+1} P(\Theta)\mu \, d\mu$$

is the asymmetry factor.

Using (2.38) in (2.20) after integrating over μ and dividing by 2π, we get

$$\begin{aligned} \mu\frac{d}{d\delta}(\mathcal{L}_0 + \mu\mathcal{L}_1) = & -(\mathcal{L}_0 + \mu\mathcal{L}_1) + \varpi(\mathcal{L}_0 + g\mu\mathcal{L}_1) \\ & +1/4\varpi\mathcal{F}_0\exp(-\delta/\mu_0)(1 + 3g\mu_0\mu) \end{aligned} \tag{2.39}$$

We obtain a pair of equations for $\mathcal{L}_0$ and $\mathcal{L}_1$ by integrating (2.39) over μ

$$\begin{aligned} \frac{d\mathcal{L}_0}{d\delta} &= -3(1-\varpi)\mathcal{L}_0 + \frac{3}{4}\varpi\mathcal{F}_0\exp(-\delta/\mu_0) \\ \frac{d\mathcal{L}_1}{d\delta} &= -(1-\varpi g)\mathcal{L}_1 + \frac{3}{4}\varpi g\mu_0\mathcal{F}_0\exp(-\delta/\mu_0) \end{aligned} \tag{2.40}$$

For the cloudy layer assumed non-conservative ($\varpi < 1$), the solutions to (2.39) and (2.40), for $0 \le \delta \le \delta^*$, are

$$\begin{aligned} \mathcal{L}_0(\delta) &= C_1\exp(-K\delta) + C_2\exp(+K\delta) - \alpha\exp(-\delta/\mu_0) \\ \mathcal{L}_1(\delta) &= P\{C_1\exp(-K\delta) - C_2\exp(+K\delta) - \beta\exp(-\delta/\mu_0)\} \end{aligned} \tag{2.41}$$

where

$$\begin{aligned} K &= \{3(1-\varpi)(1-\varpi g)\}^{1/2} \\ P &= \{3(1-\varpi)/(1-\varpi g)\}^{1/2} \\ \alpha &= 3\varpi\mathcal{F}_0\mu_0\{1 + 3g(1-\varpi)\}/\{4(1-K^2\mu_0^2)\} \\ \beta &= 3\varpi\mathcal{F}_0\mu_0\{1 + 3g(1-\varpi)\mu_0^2\}/(4(1-K^2\mu_0^2)) \end{aligned}$$

The two boundary conditions allow to solve the system for C_1 and C_2; the downward directed diffuse flux at the

top of the atmosphere is zero, i.e.,

$$\mathcal{F}^{-}(0) = \left[\mathcal{L}_0(0) + \frac{2}{3}\mathcal{L}_1(0)\right] = 0$$

which translates into

$$(1 + 2P/3)C_1 + (1 - 2P/3)C_2 = \alpha + 2\beta/3 \tag{2.42}$$

The upward directed flux at the bottom of the layer is equal to the product of the downward directed diffuse and direct fluxes and the corresponding diffuse and direct reflectance ($\mathcal{R}_d$ and $\mathcal{R}_{\_}$, respectively) of the underlying medium

$$\begin{aligned}\mathcal{F}^{+}(\delta^*) &= \left\{\mathcal{L}_0(\delta^*) - \frac{2}{3}\mathcal{L}_1(\delta^*)\right\} \\ &= \mathcal{R}_{\_}\left\{\mathcal{L}_0(\delta^*) + \frac{2}{3}\mathcal{L}_1(\delta^*)\right\} + \mathcal{R}_d\mu_0\mathcal{F}_0\exp(-\delta^*/\mu_0)\end{aligned}$$

which translates into

$$\begin{aligned}&\{1 - \mathcal{R}_{\_} - 2(1 + \mathcal{R}_{\_})P/3\}C_1\exp(-K\delta^*) \\ &+\{1 - \mathcal{R}_{\_} + 2(1 + \mathcal{R}_{\_})P/3\}C_2(+K\delta^*) \\ &=\{(1 - \mathcal{R}_{\_})\alpha - 2(1 + \mathcal{R}_{\_})\beta/3 + \mathcal{R}_d\mu_0\mathcal{F}_0\}\exp(-\delta^*/\mu_0)\end{aligned} \tag{2.43}$$

In the Delta-Eddington approximation, the phase function is approximated by a Dirac delta function forward-scatter peak and a two-term expansion of the phase function

$$P(\theta) = 2f(1 - \mu) + (1 - f)(1 + 3g'\mu)$$

where f is the fractional scattering into the forward peak and g' the asymmetry factor of the truncated phase function. As shown by *Joseph et al.* (1976), these parameters are

$$\begin{aligned}f &= g^2 \\ g' &= g/(g + 1)\end{aligned} \tag{2.44}$$

The solution of the Eddington's equations remains the same provided that the total optical thickness, single scattering albedo and asymmetry factor entering (2.39)–(2.43) take their transformed values

$$\begin{aligned}\delta'^* &= (1 + \varpi f)\delta^* \\ \omega' &= \frac{(1 - f)\varpi}{1 - \varpi f}\end{aligned} \tag{2.45}$$

Practically, the optical thickness, single scattering albedo, asymmetry factor and solar zenith angle entering (2.39)-(2.42) are δ^*, ϖ^*, g^* and μ_{eff} defined in (2.33) and (2.34).

2.3.2 (b) Clear-sky fraction of the layers. In the clear-sky part of the atmosphere, the shortwave scheme accounts for scattering and absorption by molecules and aerosols. The following calculations are practically done twice, once for the clear-sky fraction ($1 - C_{\text{cld}}^{\text{tot}}$) of the atmospheric column with μ equal to μ_0, simply modified for the effect of Rayleigh and aerosol scattering, the second time for the clear-sky fraction of each individual layer within the fraction $C_{\text{cld}}^{\text{tot}}$ of the atmospheric column containing clouds, with μ equal to μ_e.

As the optical thickness for both Rayleigh and aerosol scattering is small, $\mathcal{R}_{\text{clr}}(j-1)$ and $\mathcal{T}_{\text{clr}}(j)$, the reflectance at the top and transmittance at the bottom of the *j* th layer can be calculated using respectively a first and a second-order expansion of the analytical solutions of the two-stream equations similar to that of *Coakley and Chylek* (1975). For Rayleigh scattering, the optical thickness, single scattering albedo and asymmetry factor are respectively δ_R, $\varpi_R = 1$, and $g_R = 0$, so that

$$\begin{aligned} \mathcal{R}_R &= \frac{\delta_R}{2\mu + \delta_R} \\ \mathcal{T}_R &= \frac{2\mu}{(2\mu + \delta_R)} \end{aligned} \tag{2.46}$$

The optical thickness δ_R of an atmospheric layer is simply

$$\delta_R = \delta_R^* \{p(j) - p(j-1)\} / p_{\text{surf}} \tag{2.47}$$

where δ^*_R is the Rayleigh optical thickness of the whole atmosphere parametrized as a function of the solar zenith angle (*Deschamps et al.*, 1983)

For aerosol scattering and absorption, the optical thickness, single scattering albedo and asymmetry factor are respectively δ_a, ϖ_a, with $1 - \varpi_a \ll 1$ and g_a, so that

$$\begin{aligned} \text{den} = 1 &+ \{1 - \varpi_a + \text{back}(\mu_e)\varpi_a\}(\delta_a/\mu_e) \\ &+ (1 - \varpi_a)\{1 - \varpi_a + 2\text{back}(\mu_e)\varpi_a\}(\delta_a^2/\mu_a^2) \end{aligned} \tag{2.48}$$

$$\begin{aligned} \mathcal{R}(\mu_e) &= \frac{(\text{back}(\mu_e)\varpi_a\delta_a)/\mu_a}{\text{den}} \\ \mathcal{T}(\mu_e) &= 1/\text{den} \end{aligned} \tag{2.49}$$

where $\text{back}(\mu_e) = (2 - 3\mu_e g_a)/4$ is the backscattering factor.

Practically, $\mathcal{R}_{\text{clr}}$ and $\mathcal{T}_{\text{clr}}$ are computed using (2.49) and the combined effect of aerosol and Rayleigh scattering comes from using modified parameters corresponding to the addition of the two scatterers with provision for the highly asymmetric aerosol phase function through Delta-approximation of the forward scattering peak (as in (2.40)–(2.41))

$$\begin{aligned}\delta^{+} &= \delta_R + \delta_a(1-\varpi_a g_a^2)\\ g^{+} &= \frac{g_a}{1+g_a}\frac{\delta_a}{(\delta_R+\delta_a)}\\ \varpi^{+} &= \frac{\delta_R}{\delta_R+\delta_a}\varpi_R + \frac{\delta_a}{\delta_R+\delta_a}\frac{\varpi_a(1-g_a^2)}{1-\varpi_a g_a^2}\end{aligned} \tag{2.50}$$

As for their cloudy counterparts, $\mathcal{R}_{clr}$ and $\mathcal{T}_{clr}$ must account for the multiple reflections due to the layers underneath

$$\mathcal{R}_{clr} = \mathcal{R}(\mu_e) + \mathcal{R}_{-}\mathcal{T}(\mu_e)/(1-\mathcal{R}^{*}\mathcal{R}_{-}) \tag{2.51}$$

and $\mathcal{R}_{-}$ is the reflectance of the underlying medium $\mathcal{R}_{-} = \mathcal{R}_{\uparrow}(j-1)$ and r is the diffusivity factor.

Since interactions between molecular absorption and Rayleigh and aerosol scattering are negligible, the radiative fluxes in a clear-sky atmosphere are simply those calculated from (2.27) and (2.45) attenuated by the gaseous transmissions (2.25).

2.3.3 Multiple reflections between layers

To deal properly with the multiple reflections between the surface and the cloud layers, it should be necessary to separate the contribution of each individual reflecting surface to the layer reflectance and transmittances in as much as each such surface gives rise to a particular distribution of absorber amount. In case of an atmosphere including N cloud layers, the reflected light above the highest cloud consists of photons directly reflected by the highest cloud without interaction with the underlying atmosphere, and of photons that have passed through this cloud layer and undergone at least one reflection on the underlying atmosphere. In fact, (2.22) should be written

$$\mathcal{F} = \sum_{i=0}^{N} \mathcal{F}_{cl} \int_{0}^{\infty} \mathcal{P}_1(\mathcal{U}) t_{\Delta\nu}(\mathcal{U}) d\nu \tag{2.52}$$

where $\mathcal{F}_{cl}$ and $\mathcal{P}_1(\mathcal{U})$ are the conservative fluxes and the distributions of absorber amount corresponding to the different reflecting surfaces.

Fouquart and Bonnel (1980) have shown that a very good approximation to this problem is obtained by evaluating the reflectance and transmittance of each layer (using (2.39) and (2.45)) assuming successively a non-reflecting underlying medium ($\mathcal{R}_{-} = 0$), then a reflecting underlying medium ($\mathcal{R}_{-} \neq 0$). First calculations provide the contribution to reflectance and transmittance of those photons interacting only with the layer into consideration, whereas the second ones give the contribution of the photons with interactions also outside the layer itself.

From those two sets of layer reflectance and transmittances ($\mathcal{T}_{t0}, \mathcal{T}_{b0}$) and ($\mathcal{R}_{\uparrow\neq}\ \mathcal{T}_{b\neq}$) respectively, effective absorber amounts to be applied to computing the transmission functions for upward and downward fluxes are then derived using (2.23) and starting from the surface and working the formulas upward

$$
\begin{aligned}
U^{-}_{e0} &= \ln(\mathcal{T}_{b0}/\mathcal{T}_{bc})/k_e \\
U^{-}_{e\neq} &= \ln(\mathcal{T}_{b\neq}/\mathcal{T}_{bc})/k_e \\
U^{+}_{e0} &= \ln(\mathcal{R}_{t0}/\mathcal{R}_{tc})/k_e \\
U^{+}_{e\neq} &= \ln(\mathcal{R}_{t\neq}/\mathcal{R}_{tc})/k_e
\end{aligned}
\tag{2.53}
$$

where $\mathcal{R}_{tc}$ and $\mathcal{T}_{bc}$ are the layer reflectance and transmittance corresponding to a conservative scattering medium.

Finally the upward and downward fluxes are obtained as

$$\mathcal{F}^{+}(j) = \mathcal{F}_0\{\mathcal{R}_{t0}t_{\Delta v}(\mathcal{U}^{+}_{e0}) + (\mathcal{R}_{t\neq} - \mathcal{R}_{t0})t_{\Delta v}(\mathcal{U}^{+}_{e\neq})\} \tag{2.54}$$

$$\mathcal{F}^{-}(j) = \mathcal{F}_0\{\mathcal{T}_{b0}t_{\Delta v}(\mathcal{U}^{+}_{e0}) + (\mathcal{T}_{b\neq} - \mathcal{T}_{b0})t_{\Delta v}(\mathcal{U}^{-}_{e\neq})\} \tag{2.55}$$

2.3.4 Cloud shortwave optical properties

As seen in Sub-section 2.3.2 (a), the cloud radiative properties depend on three different parameters: the optical thickness δ_c, the asymmetry factor g_c, and the single scattering albedo ϖ_c.

Presently the cloud optical properties are derived from *Fouquart* (1987) for the water clouds, and *Ebert and Curry* (1992) for the ice clouds

δ_c is related to the cloud liquid water amount $\mathcal{U}_{LWP}$ by

$$\delta_c = \frac{3\mathcal{U}_{LWP}}{2r_e}$$

where r_e is the mean effective radius of the size distribution of the cloud water droplets. Presently r_e is parametrized as a linear function of height from 10 μm at the surface to 45 μm at the top of the atmosphere, in an empirical attempt at dealing with the variation of water cloud type with height. Smaller water droplets are observed in low-level stratiform clouds whereas larger droplets are found in mid-level cumuliform water clouds.

In the two-, four-, and six- spectral interval versions of the shortwave radiation scheme, the optical properties of liquid water clouds are defined from *Fouquart* (1987) and those for ice clouds from *Ebert and Curry* (1992). Alternative optical properties are also available for liquid water clouds (*Slingo*, 1989) and ice clouds (*Fu*, 1996).

The effective radius of the liquid water cloud particles is computed from the cloud liquid water content using the diagnostic formulation of *Martin et al.* (1994) and specified concentrations of cloud concentration nuclei over land and ocean. For ice clouds, the effective dimension of the cloud particles is diagnosed from temperature using a revision of the formulation by *Ou and Liou* (1995).

2.4 HORIZONTAL INTERPOLATION

As stated in the introduction, the cost of the radiation scheme described in the previous sections is prohibitive if it were used to compute the radiative fluxes at every time step and every grid point of the model.

In order to cut down the computing costs, the full radiation scheme is only called every 3 hours (every 1 hour during the first 12 hours used for data assimilation) (the so-called full radiation time steps) and on a reduced grid interpolated from the full physical grid. A spatial and temporal interpolation thus provides the relevant interaction of the

shortwave radiative fluxes with the solar zenith angle at every time step and every grid point.

2.4.1 Temporal interpolation

To do so, a shortwave transmissivity is defined at each model level such that

$$\mathcal{F}_s = \tau_e \mathcal{S}_0 \tag{2.56}$$

where $\mathcal{F}_s$ is the net solar (shortwave) flux and $\mathcal{S}_0$ is the solar flux at the top of the atmosphere. $\mathcal{F}_s$ is defined only for a full radiation time step. At every time step, the net solar fluxes are computed therefore from the transmissivity derived for the last full radiation time step, using (2.56) with the correct solar angle for every grid point. The net longwave fluxes at kept at the values given by the full radiation calculation.

2.4.2 Spatial interpolation

Full radiation computations are now performed using the so-called halo configuration that can be defined according to needs for the various spatial resolutions.

The previous spatial sampling (operational till cycle 26R1), was done only in the longitudinal direction. It was going from one out of four points prevalent in sub-tropical and tropical latitudes and reduced gradually to every point in polar areas. On output, lagrangian cubic interpolation was used. The scheme worked efficiently on vector systems with less than 100 processors and scalar systems with about 1000 processors. The only real problem was the complexity of the message passing, a direct result of the use of a non-standard grid for radiation calculations.

The new interface for radiation computations was developed to address this complexity, and uses a standard IFS model grid, but with a coarser resolution than the current model grid. Further, interpolation between model and radiation grids are performed using the interfaces already existing within the IFS for the semi-lagrangian interpolation, and as a result should reduce future code maintenance. By using such a standard grid for radiation computations, there is no longer a load balance issue, as each processor is given an equal number of grid points for model and radiation grids.

A new grid is computed, independent of that for the rest of the physics, over which input fields are averaged using the standard interpolation routines. Then radiation computations are done, and output fluxes are interpolated back to the reduced grid, at times of full radiation computations. This new halo-related grid can be chosen differently with the forecast application (seasonal runs, EPS, high-resolution 10-day forecasts). Table 2.1 presents the various basic model resolutions together with the resolution made available, by default, for radiation computations by the new interface, whereas Table 2.2 presents the speed-up factor introduced by the various radiation configurations corresponding to horizontal resolutions used for different applications.

TABLE 2.1 POSSIBLE RESOLUTIONS OF THE NEW INTERPOLATION SCHEME FOR RADIATION COMPUTATIONS FOR THE VARIOUS DYNAMICAL RESOLUTIONS OF THE ECMWF FORECAST SYSTEM

Res	95	159	255	319	399	511	639	799	1023
NDLONx	192	320	512	640	800	1024	1280	1600	2048

NDLON is the maximum number of longitude points for the reference configuration with radiative (and other physics) computations at all grid points, 2, 3 and 4 correspond to a larger grid for radiative computations. Default values for model configurations from cy26r3 are in bold. Note that default T95 does not use a larger grid for radiation. The maximum number of longitude points for the radiative computations can be obtained from the equivalent value of Res. A maximum of 42 and 128 longitude points is respectively used for radiative computations for RadRes = 21 and 63.

TABLE 2.1 POSSIBLE RESOLUTIONS OF THE NEW INTERPOLATION SCHEME FOR RADIATION COMPUTATIONS FOR THE VARIOUS DYNAMICAL RESOLUTIONS OF THE ECMWF FORECAST SYSTEM

RadRes									
2	**95**	**95**	159	255	255	399	399	511	799
3	21	63	**95**	**159**	**159**	**255**	**319**	**399**	**511**
4	N/A	N/A	63	95	95	159	159	255	399

NDLON is the maximum number of longitude points for the reference configuration with radiative (and other physics) computations at all grid points, 2, 3 and 4 correspond to a larger grid for radiative computations. Default values for model configurations from cy26r3 are in bold. Note that default T95 does not use a larger grid for radiation. The maximum number of longitude points for the radiative computations can be obtained from the equivalent value of Res. A maximum of 42 and 128 longitude points is respectively used for radiative computations for RadRes = 21 and 63.

TABLE 2.2 SPEED-UP FACTOR OF THE VARIOUS RADIATION CONFIGURATIONS RELATIVE TO A COMPUTATION AT ALL GRID POINTS (CONFIGURATION 1), FOR DIFFERENT HORIZONTAL RESOLUTIONS.

Res	95	159	255	319	511
-1	2.76	2.89	2.28	2.89	2.61
2	**1.00**	**2.47**	2.03	1.47	1.52
3	5.60	4.88	**4.23**	**3.47**	**3.48**
4	N/A	N/A	4.60	7.73	7.28

-1 is the previous operational configuration with sampling up to one point out of four in each latitude band, 2, 3 and 4 correspond to the relevant resolution in Table 2.1. Default values for model configurations from cy26r3 are in bold.

2.5 INPUT TO THE RADIATION SCHEME

2.5.1 Model variables

Temperature values are needed at the boundaries of the layers, where the fluxes are computed. They are derived from the full level temperatures with a pressure weighted interpolation

$$T_{k+1/2} = T_k \frac{p_k(p_{k+1}-p_{k+1/2})}{p_{k+1/2}(p_{k+1}-p_k)} + T_{k+1}\frac{p_{k+1/2}(p_{k+1/2}-p_k)}{p_{k+1/2}(p_{k+1}-p_k)} \tag{2.57}$$

At the bottom of the atmosphere, either the surface temperature or the temperature at 2 m is used, while at the top of the atmosphere the temperature is extrapolated from the first full level and second half level temperatures.

2.5.2 Clouds

Cloud fraction, and liquid/ice water content is provided in all layers by the cloud scheme.

2.5.3 Aerosols

The aerosol climatology used in the operational model up to cycle 26R1 was given as annual mean geographical distributions defined from T5 spectral coefficients, for different aerosol types, respectively, maritime, continental,

urban and desert, plus a uniformly distributed stratospheric background aerosols, with fixed vertical distributions, following *Tanre et al.* (1984). In the last fifteen years, chemical and/or transport models have addressed the life cycles of various aerosol types and attempted an inventory of their spatio-temporal distributions. Out of these studies, a new climatology for the annual cycle of the aerosol distribution of various aerosol types has been compiled by *Tegen et al.* (1997), which has been implemented in the ECMWF forecast system from cycle 26R3 onwards. Table 3 describes the characteristics of the aerosol components for each tropospheric aerosol type and Table 4 compares the maximum optical thicknesses in the old and new climatologies.

TABLE 2.3 CHARACTERISTICS OF THE AEROSOL COMPONENTS FOR EACH TROPOSPHERIC AEROSOL TYPE IN THE NEW CLIMATOLOGY FOR CYCLE 26R3 OF THE ECMWF MODEL (ADAPTED FROM *Hess et al.*, 1998)

Type	RH (%)	Component	Number (cm^{-1})	Volume ($\mu m^3/m^3$)	Mass ($\mu g/m^3$)	Density (g/cm^3)
"Continental" organic	80					
		Insoluble	4.00E-01	4.75E+06	9.49E+00	2.00
		Water soluble	7.00E+03	1.57E+07	1.99E+01	1.27
		soot	8.30E+03	4.96E+05	4.96E-01	1.00
"Maritime" sulphate	95					
		Water soluble	1.50E+03	7.45E+06	8.35E+00	1.12
		sea salt (accum.)	2.00E+01	1.64E+08	1.72E+02	1.05
		sea salt (coarse)	3.20E-03	9.85E+05	1.04E+00	1.05
"Desert" dust-like	50					
		Water soluble	2.00E+03	2.81E+06	4.00E+00	1.42
		Mineral (nuclei)	2.70E+02	2.88E+06	7.49E+00	2.60
		Mineral (accum.)	3.05E+01	6.47E+07	1.69E+02	2.60
		Mineral (coarse)	1.42E-01	1.77E+07	4.60E+01	2.60
"Urban" black carbon	80					
		Insoluble	1.50E+00	1.78E+07	3.56E+01	2.00
		Water soluble	2.80E+04	6.28E+07	7.97E+01	1.27
		Soot	1.30E+05	7.78E+06	7.78E+01	1.00

Type: First definition (e.g., continental) is the aerosol component as known within both the ECMWF model and the OPAC software; second definition (e.g., organic) is the 3D distribution to which it is linked in *Tegen et al.* climatology. RH is the relative assumed for the computations of the relevant optical properties. The *nuclei*, *accumulation*, and *coarse* modes refer to various size ranges for the component particles.

TABLE 2.4 MAXIMUM OPTICAL THICKNESS IN THE TWO AEROSOL CLIMATOLOGIES

OLD	Annual	January	July	NEW
Continental	0.2	0.235	0.231	Organic
Maritime	0.05	0.099	0.232	Sulphate
Desert	1.9	0.184	1.01	Dust-like
Urban	0.1	0.039	0.039	Black carbon
Background trop.	0.03			
Background stratos	0.045	0.045	0.045	Background stratos.

Aerosol types of the new and old climatologies are paired according to the dominant components in each mix

2.5.4 Carbon dioxide, ozone and trace gases

Carbon dioxide, methane, nitrous oxide, CFC-11 and CFC-12 have constant volume concentrations of 353 ppm, 1.72 ppm, 0.31 ppm, 280 ppt, and 484 ppt respectively (IPCC/SACC, 1990), except in ERA-40 for the variation in concentrations is derived from (IPCC/SACC, 1995).

Two climatologies are available for the ozone distribution. In the first one (NOZOCL = 0), the ozone mixing ratio q_{O_3} depends on height, latitude, longitude and season. Its vertical distribution is assumed to be such that its integral from 0 to the pressure p is

$$\int_0^p q_{O_3} \mathrm{d}p = \frac{a}{1 + (b/p)^{3/2}} \tag{2.58}$$

The constants a and b are related to the total amount of ozone and the height of its maximum mixing ratio. They are imposed in terms of a limited series of spherical harmonics (T10) for the geographical distribution and a Fourier series for the seasonal variation. The total amount of ozone was taken from *London et al.* (1976) and the altitude of the maximum concentration was derived from *Wilcox and Belmont* (1977). Plots of these values can be found in the Appendix. In the second climatology (NOZOCL = 1), the ozone mixing ratio q_{O_3} depends on height, latitude and month, and is taken from *Fortuin and Langematz* (1995).

2.5.5 Ground albedo and emissivity

The background land albedo, α_{sb}, is interpolated to the model grid from the monthly mean values of a snow-free albedo produced for the combined 1982–1990 years. The albedo for that dataset was computed using the method of Sellers et al. (1996), but with new maps of soil reflectance, new values of vegetation reflectance and the biophysical parameters described in Los et al. (2000). More information on the original data and plots of the monthly mean albedo are shown in Chapter 10.

Spectral albedos for parallel and diffuse radiation are needed by the radiative code. In addition, the surface energy balance equation (see Chapter 3 on vertical diffusion) needs a spectrally integrated parallel+diffused albedo, specified for each independent surface functional unit, tile. The procedure is summarized in Table 2.5. Over open water, the surface albedo for direct parallel radiation is a fit to low-flying aircraft measurements over the ocean given by Taylor et al. (1996)

$$\alpha_{sp} = \frac{0.037}{1.1\mu_0^{1.4} + 0.15} \tag{2.59}$$

For sea ice, monthly values based on Ebert and Curry (1993) albedos for the Arctic Ocean are interpolated to the forecast time. The bare sea ice albedo value in Ebert and Curry is taken as a representative value for summer, and the dry snow albedo value is used for the winter months. Values for the Antarctic are shifted by six months. Separate values for visible and near-infrared spectral bands are used. The time-varying snow albedo (α_{sn}, see Chapter 7), is used for the exposed snow tile only. Finally, the average of the diffuse and parallel albedos are spectrally integrated for each tile.

TABLE 2.5 DIFFUSE AND PARALLEL ALBEDO AND WINDOW EMISSIVITY FOR EACH TILES

Tile	1	2	3	4	5	6	7	8
Description	Open sea	Sea ice	Interception layer	Low vegetation	Exposed snow	High vegetation	Shaded snow	Bare ground
Diffuse albedo	0.06	Ebert and Curry (1993)	α_{sb}	α_{sb}	α_{sn}	α_{sb}	0.15	α_{sb}
Parallel albedo	Taylor et al. (1996)	Ebert and Curry (1993)	α_{sb}	α_{sb}	α_{sn}	α_{sb}	0.15	α_{sb}
Window emissivity	0.99	0.98	0.96	0.93–0.96	0.98	0.93–0.96	0.93–0.96	0.93–0.96

The thermal emissivity of the surface outside the 800–1250 cm^{-1} spectral region is assumed to be 0.99 everywhere. In the window region, the spectral emissivity is constant for open water, sea ice, the interception layer and exposed snow tiles. For low and high vegetation and for shaded snow the emissivity depends on the water content in the top soil layer. Emissivity decreases linearly from 0.96 for soils at or above field capacity to 0.93 for soils at or below permanent wilting point. The same formulation is used for bare ground, except for desert areas ($\alpha_{sb} > 0.3$), where a value of 0.93 is used independently of the soil water content. Finally, a broadband emissivity is obtained by convolution of the spectral emissivity and the Planck function at the skin temperature.

2.5.6 Solar zenith angle

Equations to compute the annual variation of the solar constant I, the solar declination δ_s and the difference between solar time and official time can be found in *Paltridge and Platt* (1976). These equations are used to give the cosine of the solar angle at the ground. Because of the curvature of the earth, the zenith angle is not quite constant along the path of a sun ray. Hence a correction is applied to μ_0^a to give an average μ_0 for the atmosphere:

$$\mu_0 = \frac{\frac{H}{a}}{\sqrt{(\mu_0^a)^2 + \frac{H}{a}\left(2 + \frac{H}{a}\right)} - (\mu_0^a)^2} \tag{2.60}$$

where a is the earth radius and H is the atmospheric equivalent height. H/a is fixed at 0.001277.

2.6 THE RADIATION CODE

Routine RADHEAT or RADHEATN (depending whether the diagnostic or prognostic cloud scheme is used) is called at every time step to compute the radiative fluxes and heating using the solar zenith angle computed in CPGLAG and emissivities and transmissivities (PEMTU, PTRSOL) computed at full radiation time steps in RADINT. or RADINTG (see 2.6.2). The other routines are called either once at the beginning of the run (SUECRAD and below) or once per full radiation step at the first row (ECRADFR and below), or at every full radiation time step for all rows. In this section, we briefly describe the function of each routine.

TABLE 2.6 SPECTRAL DISTRIBUTION OF THE ABSORPTION BY ATMOSPHERIC GASES IN RRTM

Spectral intervals cm-1	Number of g-points	Gases included	
		Troposphere	Stratosphere
10-250	8	H_2O	H_2O
250-500	14	H_2O	H_2O
500-630	16	H_2O, CO_2	H_2O, CO_2
630-700	14	H_2O, CO_2	O_3, CO_2
700-820	16	H_2O, CO_2, CCl_4	O_3, CO_2, CCl_4
820-980	8	H_2O, CFC11, CFC12	CFC11, CFC12
980-1080	12	H_2O, O_3	O_3
1080-1180	8	H_2O, CFC12, CFC22	O_3, CFC12, CFC22
1180-1390	12	H_2O, CH_4	CH_4
1390-1480	6	H_2O	H_2O
1480-1800	8	H_2O	H_2O
1800-2080	8	H_2O	
2080-2250	4	H_2O, N_2O	
2250-2380	2	CO_2	CO_2
2380-2600	2	N_2O, CO_2	
2600-3000	2	H_2O, CH_4	

N.B.: CCl_4 and CFC22 are presented not accounted for in the ECMWF model.

2.6.1 Set-up routines

- SUECRAD provides the interface with the user, via the namelist NAERAD. It defines the constants of Table 2.6 and sets the configuration for the radiative computations (from SUPHEC).
- ECRADFR modifies the frequency of full radiative computations (from CNT4).
- SUAERL and SUAERSN set up the longwave and shortwave radiative characteristics of the aerosols (from SUECRAD).
- SUECRAD defines the geographical distribution of aerosols, in terms of spectral coefficients (from UPDTIER).
- SUAERV defines the globally averaged vertical distribution of the aerosols (from SUECRAD).
- SUCLOP sets up the longwave and shortwave radiative properties of the ice and water clouds (from SUECRAD).

- SUECOZO computes the Legendre coefficients for the ozone distribution according to the time of the year, using the Fourier coefficients defined in DATA statements (from UPDTIER).
- SULWN sets up the coefficients for the longwave radiative computations (from SUECRAD).
- SURDI sets up the concentrations of radiatively active gases and security parameters for the radiative computations (from SUECRAD).
- SUSAT sets up position and altitude of geostationary satellites in case of diagnostic simulation of radiances by the model radiation scheme (from SUECRAD).
- SUSWN sets up the coefficients for the shortwave radiative computations (from SUECRAD).
- UPDTIER updates the time for full radiative computations (from ECRADFR).
- The routines SUAERH , SUECOZO are called only once per full radiation step, at the first row.
- SURRTAB precomputes the array linking gaseous optical thickness and the transmission function (RRTM). (called from SUECRAD).
- SURRTFTR includes all coefficients related to the g -point configuration (RRTM). (called from SUECRAD).
- SURRTPK defines the limits of the spectral intervals, and the coefficients of the spectrally defined and spectrally integrated Planck functions (RRTM). (called from SUECRAD).
- SURRTRF defines the pressure and temperature reference profiles used for the tabulation of the absorption coefficients (RRTM). (called from SUECRAD).
- RRTM_CMBGBn, for each of the 16 spectral intervals, remaps the absorption coefficients from 16 to the final number of g -points (called from RRTM_INIT_140GP).
- RRTM_INIT_140GP performs the g -point reduction from 16 per band to a band-dependant number (column 2 in Table 1). It also computes the relative weighting for the new g -point combinations (called from SUECRAD).
- RRTM_KGBn contain the various absorption coefficients for all gases relevant to the different spectral bands.

2.6.2 Main routines

- RADINT or RADINTG is called by RADDRV to launch the full radiation computations, depending on whether the pre-CY26R1 sampling configuration or the CY26R1 halo configuration is used for spatial interpolation (see 2.4.2). Zonal mean diagnostic of the temperature, clouds and albedo are computed. Temperature is vertically interpolated. Depending on the value of the variable NRINT an interpolation of all input variables to a coarser grid may be carried out. It may be necessary to subdivide the latitude belt in a few parts for the actual calculation of radiative fluxes because of storage space limitations. For this reason a loop over these parts follows. Inside this loop a call to routine RADLSW provides solar and thermal fluxes for a subset of points of that latitude row. These fluxes are converted into transmissivities and emissivities and after completion of the whole latitude circle they are transferred to the full grid when the calculations are carried out with the coarse resolution (NRINT>1).
- RADLSW is the driver routine of the solar and thermal fluxes by calling specialized routines SW for shortwave radiation and either RRTM_RRTM_140GP or LW for longwave radiation.

2.6.3 Specialized routines

- RADSRF is called from RADPAR/CALLPAR to compute surface albedo and emissivity. It computes the gridpoint diffuse and parallel spectral albedos and a spectrally integrated albedo (for postprocessing). It also computes the emissivity inside and outside the window region, and the

spectrally integrated emissivity. Finally, it computes spectrally integrated tile albedos to be used by the surface energy balance routine (see Chapter 3 on vertical diffusion).

- LW organizes the longwave computation by calling in turn LWU, LWBV, LWC.
- LWU computes the effective absorber amounts including the pressure and temperature dependencies in the spectral intervals of the longwave radiation scheme.
- LWBV calls LWB and LWV
- LWB computes the Planck function with relation to temperature for all levels and spectral intervals.
- LWV organizes the vertical integration by calling LWVN which deals with the contribution to the flux of the layers adjacent to the level of computation of flux, LWVD which deals with the contribution from the more distant layers, and LWVB which computes the contribution of the boundary terms.
- LWTT and LWTTM compute the relevant transmission functions needed in LWVN, LWVD, and LWVB.
- LWC introduces the effect of clouds on the longwave fluxes.
- SW organizes the shortwave computation by calling in turn SWU, SW1S, and SW2S.
- SWU computes the effective absorber amounts including the pressure and temperature dependencies of the absorption.
- SW1S and SW2S deal with the shortwave radiation transfer in the two spectral intervals used to describe the solar spectrum. They both call SWCLR, which deals with the conservative scattering processes (Rayleigh) and the scattering / absorption by aerosols in the totally clear sky part of the atmospheric column, then SWR which deals with the same processes for the clear sky layers in an otherwise cloudy column, and SWDE which computes the reflectivity and transmissivity of a layer including non-conservative scatterers (cloud particles) with the Delta-Eddington approximation.
- SWTT and SWTT1, computes the relevant transmission functions.
- RRTM_RRTM_140GP organizes the longwave computation by calling in turn, within a loop on the individual vertical columns, RRTM_ECRT_140GP, RRTM_SETCOEF_140GP, RRTM_GASABS1A_140GP and RRTM_RTRN1A_140GP.
- RRTM_ECRT_140GP defines the surface spectral emissivity, and the spectral aerosol thickness, and the layer absorber amounts and cloud quantities as used in RRTM
- RRTM_SETCOEF_140GP computes the indices and frcations related to the pressure and temperature interpolations. It also calculates the values of the integrated Planck function for each spectral band at the level and layer temperatures.
- RRTM_GASABS1A_140GP launches the calculation of the spectrally defined optical thickness for gaseous absorption. It calls RRTM_TAUMOLn
- RRTM_RTRN1A_140GP computes the downward then upward fluxes, using a diffusivity-type approximation for the angle integration. Cloud overlap is treated with a generalized maximum/ random overlap method. Adjacent layers are treated with maximum overlap, non-adjacent cloud groups are treated with random overlap. For adjacent cloud layers, cloud information is carried from the previous two layers.

2.6.4 Heating rate computation

- RADHEAT or RADHEATN, depending whether the diagnostic or the prognostic cloud scheme is used, recomputes at each time step the net radiative fluxes from the layers' effective emissivity and transmissivity, using the actual temperature and solar zenith angle. It also computes the downward longwave and shortwave radiation at the surface.

APPENDIX A LIST OF SYMBOLS

B_ν	Planck function integrated over the half sphere with the factor invoving π absorbed: in units of flux (W m^{-2})
C_{cld}	fractional cloud cover
c_p	specific heat at constant pressure of moist air
$c_{p_{dry}}$	specific heat at constant pressure of dry air
$c_{p_{vap}}$	specific heat at constant pressure of water vapour
F_ν^0	incident solar radiance in the direction θ_0
$\mathcal{F}$	radiative flux
f	fractional scattering into the forward peak
g	acceleration of gravity
g	asymmetry factor for aerosol scattering
k	absorption coefficient
L_ν	monchromatic radiance at wavenumber ν
M	magnification factor ($= 35/\sqrt{(\mu_0^2 + 1)}$)
m_{O_3}	ozone mixing ratio
P	scattering phase function
p	pressure
$\Pi(u)\mathrm{d}u$	probability of a photon encountering an absorber amount between u and $u + \mathrm{d}u$
q	specific humidity
r	diffusivity factor ($= \sec\theta$)
r_e	mean effective radius of cloud water droplets
$\mathcal{R}$	reflectance
S_0	solar flux at the top of the atmosphere
$\mathcal{T}$	transmittance
T	temperature
t_ν	monchromatic transmission at wavenumber ν
u	absorber amount
α	surface albedo
β_ν^{abs}	cloud particle absorbtion coefficient
β_ν^{ext}	extinction coefficient
β_ν^{sca}	scattering coefficient
δ_g	molecular absorption of gases
δ	optical depth
ε_{cld}	cloud emissivity
μ	$= \cos\theta$
ν	wavenumber
ϖ_ν	single scattering albedo ($= \beta_\nu^{sca}/k_\nu$)
Φ	scattering phase function
φ	azimuth angle
θ	zenith angle
θ_0	direction of incident solar beam
Θ	angle between incident and scattered radiances

Part IV: PHYSICAL PROCESSES

CHAPTER 3 Turbulent diffusion and interactions with the surface

Table of contents

3.1 INTRODUCTION

The parametrization scheme described in this chapter represents the turbulent transfer of heat, momentum and moisture between the surface and the lowest model level and the turbulent transport of the same quantities between model levels. The scheme computes the physical tendencies of the four prognostic variables (u , v , T and q) due to the vertical exchange by turbulent (non-moist) processes. These tendencies are obtained as the difference between the results of an implicit time-step from t to $t + 1$. All the diagnostic computations (such as the calculation of the exchange coefficients, etc.) are done at time t . The surface boundary condition is formulated separately for 8 different tiles: water, ice, wet skin, low vegetation, exposed snow, high vegetation, snow under vegetation, and bare soil. The different tiles have their own surface energy balance and their own skin temperature. In this version

of the IFS, the mixture of land and ocean tiles is still not used, i.e. a grid box is either 100% ocean (water + ice) or 100% land (tile 3 to 8). Details about tiles are given in Chapter 7.

The equation for the vertical diffusion of any conservative quantity ψ is:

$$\frac{\partial \psi}{\partial t} = \frac{1}{\rho}\frac{\partial}{\partial z}\left(\rho K_\psi \frac{\partial \psi}{\partial z}\right) = \frac{1}{\rho}\frac{\partial J_\psi}{\partial z} \tag{3.1}$$

The vertical turbulent flux J_ψ (positive downwards) is written using a first-order turbulence closure, where K_ψ is the exchange coefficient. The goal of the vertical diffusion parametrization is to define the exchange coefficients and then to solve equation (3.1) with the following boundary conditions:

$$\begin{aligned} &K_\psi \frac{\partial \psi}{\partial z} = 0 \qquad \text{at} \qquad p = p_{\text{top}} \\ &K_\psi \frac{\partial \psi}{\partial z} \rightarrow \sum_{i=1}^{N_T} F_i C_{\psi i} |U(z)| \, (\psi(z) - \psi_{surfi}) \text{as } z \rightarrow 0 \end{aligned} \tag{3.2}$$

where p_{top} is the pressure at the top of the atmosphere. For heat and moisture the surface boundary condition is provided tile by tile and fluxes are averaged over the N_T tiles, weighted by their fraction F_i . The transfer coefficient $C_{\psi i}$ at the lowest model level depends upon the static stability. The variable ψ_{surf} represents the value of ψ at the surface. For heat and moisture, 8 tiles are used (see Chapter 9). For wind, a single tile is used with a no slip condition at the surface.

The vertical diffusion process is applied to the two horizontal wind components, u and v , the specific humidity q and the dry static energy s , where

$$s = c_{pdry}(1 + \delta q)T + gz = c_p T + \phi \tag{3.3}$$

where $\delta = c_{pvap}/c_{pdry} - 1$ and c_{pdry} , c_{pvap} , and c_p are the specific heats at constant pressure of dry air, water vapour and moist air, respectively, and ϕ is the geopotential.

The problem is simplified by assuming that ϕ remains constant with respect to time during the turbulent diffusion process (even if in reality T variations would modify $z(p)$). Exchange coefficients (with the dimension of a pressure thickness) are then computed for momentum and for heat (sensible plus latent) (the subscripts 'M , 'H ' and 'Q' are used to identify the exchange coefficient for momentum, heat and humidity), with different formulations for the stable and the unstable case (depending on the sign of a stability parameter, either the Obukhov length or the bulk Richardson number in the surface layer). The implicit linear equations for the fluxes of momentum, firstly for u and v and secondly for s and q , are solved by a Gaussian-elimination/back-substitution method.

The surface boundary condition is applied between the downward scanning elimination and the upward scanning back substitution. It involves a no-slip condition for u and v and the tile-by-tile solution of the surface energy balance for the boundary condition of s and q . The water tile is an exception as it ignores the surface energy balance and uses the specified SST and the saturation specific humidity as boundary conditions.

Finally, the tendency of the variable temperature is computed, modified by the effects of local dissipation (it is assumed that there is no storage of turbulence kinetic energy) and moisture diffusion on c_p . The tiled surface fluxes of heat and moisture are also computed for later use by the surface scheme.

3.2 THE SURFACE LAYER

The surface layer approximation is applied between the lowest model level (about 10 m above the surface in the 60-level model) and the surface and for each tile separately. It is assume that the turbulent fluxes are constant with height and equal to the surface values. They can be expressed, using Monin–Obukhov similarity theory, in terms of the gradients of wind, dry static energy and specific humidity, which are assumed to be proportional to universal gradient functions of a stability parameter:

$$\begin{aligned} \frac{\kappa z}{u_*}\frac{\partial u}{\partial z} &= \Phi_{\mathrm{M}}\left(\frac{z}{\mathcal{L}}\right) \\ \frac{\kappa z}{s_*}\frac{\partial s}{\partial z} &= \Phi_{\mathrm{H}}\left(\frac{z}{\mathcal{L}}\right) \\ \frac{\kappa z}{q_*}\frac{\partial q}{\partial z} &= \Phi_{\mathrm{Q}}\left(\frac{z}{\mathcal{L}}\right) \end{aligned} \tag{3.4}$$

The scaling parameters u_*, s_* and q_* are expressed in terms of surface fluxes:

$$\begin{aligned} \rho u_*^2 &= J_M \\ \rho u_* s_* &= J_s \\ \rho u_* q_* &= J_q \end{aligned} \tag{3.5}$$

The stability parameter $\mathcal{L}$ is the Obukhov length defined as

$$\mathcal{L} = -u_*^3 / \left(\frac{\kappa g}{T_l} Q_{0\mathrm{v}}\right) \qquad \text{with} \qquad Q_{0\mathrm{v}} = \frac{u_* s_* - (c_{p_{\mathrm{vap}}} - c_{p_{\mathrm{dry}}}) T_l u_* q_*}{c_p} + \varepsilon T_l u_* q_* \tag{3.6}$$

$Q_{0\mathrm{v}}$ is the virtual temperature flux in the surface layer, κ is the Von Kármán constant ($= 0.4$), T_l is a reference temperature taken as a near-surface temperature (the temperature of the lowest atmospheric level) and $\varepsilon = (R_{\mathrm{vap}}/R_{\mathrm{dry}}) - 1$, where R_{vap} and R_{dry} are the gas constants for water vapour and dry air, respectively.

In the surface layer, the gradient functions (3.4) can be integrated to profiles

$$u = \frac{\tau_x}{\kappa \rho u_*}\left\{\log\left(\frac{z_l + z_{0\mathrm{M}}}{z_{0\mathrm{M}}}\right) - \Psi_{\mathrm{M}}\left(\frac{z_l + z_{0\mathrm{M}}}{\mathcal{L}}\right) + \Psi_{\mathrm{M}}\left(\frac{z_{0\mathrm{M}}}{\mathcal{L}}\right)\right\} \tag{3.7}$$

$$v = \frac{\tau_y}{\kappa \rho u_*}\left\{\log\left(\frac{z_l + z_{0\mathrm{M}}}{z_{0\mathrm{M}}}\right) - \Psi_{\mathrm{M}}\left(\frac{z_l + z_{0\mathrm{M}}}{\mathcal{L}}\right) + \Psi_{\mathrm{M}}\left(\frac{z_{0\mathrm{M}}}{\mathcal{L}}\right)\right\} \tag{3.8}$$

$$s - s_{\mathrm{surf}} = \frac{J_s}{\kappa \rho u_*}\left\{\log\left(\frac{z_l + z_{0\mathrm{M}}}{z_{0H}}\right) - \Psi_H\left(\frac{z_l + z_{0\mathrm{M}}}{\mathcal{L}}\right) + \Psi_H\left(\frac{z_{0H}}{\mathcal{L}}\right)\right\} \tag{3.9}$$

$$q - q_{\mathrm{surf}} = \frac{J_q}{\kappa \rho u_*}\left\{\log\left(\frac{z_l + z_{0\mathrm{M}}}{z_{0Q}}\right) - \Psi_H\left(\frac{z_l + z_{0\mathrm{M}}}{\mathcal{L}}\right) + \Psi_H\left(\frac{z_{0Q}}{\mathcal{L}}\right)\right\} \tag{3.10}$$

z_{0M}, z_{0H} and z_{0Q} are the roughness lengths for momentum, heat and moisture. The stability profile functions Ψ are derived from the gradient functions (3.4) with the help of the relationship $\Phi = 1 - \zeta(\partial\Psi/\partial\zeta)$. These profiles are used for the surface atmosphere interaction as explained in the following sections and also for the interpolation between the lowest model level and the surface (postprocessing of 10 m wind and 2m temperature and moisture).

In extremely stable situations, i.e. for very small positive $\mathcal{L}$, the ratio $z/\mathcal{L}$ is large, resulting in unrealistic profile shapes with standard stability functions. Therefore the ratio $z/\mathcal{L}$ is limited to 5 by defining a height h such that $h/\mathcal{L} = 5$. If $z < h$, then the profile functions described above, are used up to $z = h$ and the profiles are assumed to be uniform above that. This modification of the profiles for exceptionally stable situations (no wind) is applied to the surface transfer formulation as well as to the interpolation for postprocessing.

3.2.1 Surface fluxes

Surface fluxes for heat and moisture are computed separately for the different tiles, so most of the surface layer computations loop over the tile index. Here a general description is given of the aerodynamic aspects of the transfer between the surface and the lowest model level. The description of the individual tiles can be found in Chapter 7.

Assuming that the first model level above the surface is located in the surface boundary layer at a specified height z_l, the gradient functions (3.4) can be integrated to profiles for wind, dry static energy and specific humidity. The surface fluxes are expressed in terms of differences between parameters at level z_l and surface quantities (identified by the subscript 'surf'; the tile index has been omitted in this general description).

$$\begin{aligned} J_M &= \rho C_{\mathrm{M}} |U_l|^2 \\ J_s &= \rho C_{\mathrm{H}} |U_l| (s_l - s_{\mathrm{surf}}) \\ J_q &= \rho C_{\mathrm{Q}} |U_l| (\alpha_l q_l - \alpha_{surf} q_{\mathrm{surf}}) \end{aligned} \tag{3.11}$$

where $q_{surf} = q_{sat}(T_{surf})$, α_l and α_{surf} are provided by the land scheme, $s_{surf} = c_{p_{\mathrm{dry}}}(1 + \delta q_{sa})T_{surf}$, and q_{sa} is the apparent surface humidity also provided by the land surface scheme (the humidity equation simplifies over water where $\alpha_l = 1$, $\alpha_{surf} = 1$ and $q_{sa} = q_{surf}$.

The transfer coefficients can be expressed as follows

$$C_{\mathrm{M}} = \frac{\kappa^2}{\left[\log\left(\frac{z_l + z_{0\mathrm{M}}}{z_{0\mathrm{M}}}\right) - \Psi_{\mathrm{M}}\left(\frac{z_l + z_{0\mathrm{M}}}{\mathcal{L}}\right) + \Psi_{\mathrm{M}}\left(\frac{z_{0\mathrm{M}}}{\mathcal{L}}\right)\right]^2} \tag{3.12}$$

$$C_{\mathrm{H}} = \frac{\kappa^2}{\left[\log\left(\frac{z_l + z_{0\mathrm{M}}}{z_{0\mathrm{M}}}\right) - \Psi_{\mathrm{M}}\left(\frac{z_l + z_{0\mathrm{M}}}{\mathcal{L}}\right) + \Psi_{\mathrm{M}}\left(\frac{z_{0\mathrm{M}}}{\mathcal{L}}\right)\right]\left[\log\left(\frac{z_l + z_{0\mathrm{M}}}{z_{0\mathrm{H}}}\right) - \Psi_{\mathrm{H}}\left(\frac{z_l + z_{0\mathrm{M}}}{\mathcal{L}}\right) + \Psi_{\mathrm{H}}\left(\frac{z_{0\mathrm{H}}}{\mathcal{L}}\right)\right]} \tag{3.13}$$

$$C_{\mathrm{Q}} = \frac{\kappa^2}{\left[\log\left(\frac{z_l + z_{0\mathrm{M}}}{z_{0\mathrm{M}}}\right) - \Psi_{\mathrm{M}}\left(\frac{z_l + z_{0\mathrm{M}}}{\mathcal{L}}\right) + \Psi_{\mathrm{M}}\left(\frac{z_{0\mathrm{M}}}{\mathcal{L}}\right)\right]\left[\log\left(\frac{z_l + z_{0\mathrm{M}}}{z_{0\mathrm{Q}}}\right) - \Psi_{\mathrm{Q}}\left(\frac{z_l + z_{0\mathrm{M}}}{\mathcal{L}}\right) + \Psi_{\mathrm{Q}}\left(\frac{z_{0\mathrm{Q}}}{\mathcal{L}}\right)\right]} \tag{3.14}$$

The wind speed $|U_l|$ is expressed as

$$|U_l|^2 = u_l{}^2 + v_l{}^2 + w_*^2 \tag{3.15}$$

with w_* the free convection velocity scale defined by

$$w_* = \left(z_i \frac{g}{T_l} Q_{ov}\right)^{1/3} \tag{3.16}$$

The parameter z_i is a scale height of the boundary layer depth and is set to constant value of 1000 m, since only the order of magnitude matters. The additional term in equation (3.15) represents the near surface wind induced by large eddies in the free-convection regime. When the surface is heated, this term guarantees a finite surface wind-forcing in the transfer law even for vanishing u_l and v_l, and prevents $|U_l|$ and $\mathcal{L}$ from becoming zero. *Beljaars* (1994) showed that this empirical term, when added into the standard Monin–Obukhov scaling, is in agreement with scaling laws for free convection. When used with the roughness lengths defined below, it provides a good fit to observational data, both over land and over sea.

3.2.2 Stability functions

The empirical forms of the dimensionless gradient functions Φ (equations (3.4)) have been deduced from field experiments over homogeneous terrain.

(a) In unstable conditions, $(\zeta = z/\mathcal{L} < 0)$, the gradient functions proposed by Dyer and Hicks are used (*Dyer*, 1974; *Hogström*, 1988):

$$\begin{aligned} \Phi_M(\zeta) &= (1 - 16\zeta)^{-1/4} \\ \Phi_H(\zeta) &= \Phi_Q(\zeta) = (1 - 16\zeta)^{-1/2} \end{aligned} \tag{3.17}$$

These functions can be integrated to the universal profile stability functions, Ψ, (*Paulson,* 1970):

$$\begin{aligned} \Psi_M(\zeta) &= \frac{\pi}{2} - 2\,\mathrm{atan}(x) + \log\frac{(1+x)^2 \cdot (1+x^2)}{8} \\ \Psi_H(\zeta) &= \Psi_Q(\zeta) = 2\log\left\{\frac{1+x^2}{2}\right\} \end{aligned} \tag{3.18}$$

with $x = (1 - 16\zeta)^{1/4}$. The ψ-functions are used in the surface layer and the ϕ-functions for unstable stratification are used above the surface layer for local closure.

(b) For stable conditions, $(\zeta = z/\mathcal{L} > 0)$, the code contains gradient function Φ_M as documented by *Hogström* (1988), and Φ_H as derived from the Ellison and Turner relation for the ratio Φ_M/Φ_H:

$$\begin{aligned} \Phi_M(\zeta) &= 1 + 5\zeta \\ \Phi_H(\zeta) &= \Phi_Q(\zeta) = (1 + 4\zeta)^2 \end{aligned} \tag{3.19}$$

These functions were meant to be used for local closure above the surface layer, but are not used at all in the current model version, because Richardson number dependent functions are used instead (see section on exchange coefficients above the surface layer).

The stable profile functions as used in the surface layer, are assumed to have the empirical forms proposed by *Holtslag and De Bruin* (1988), with a modification to allow for the effects of a critical flux Richardson number for large ζ:

$$\begin{aligned}\Psi_{\mathrm{M}}(\zeta) &= -b\left(\zeta-\frac{c}{d}\right)\exp(-d\zeta)-a\zeta-\frac{bc}{d}\\ \Psi_{\mathrm{H}}(\zeta) &= \Psi_{\mathrm{Q}}(\zeta) = -b\left(\zeta-\frac{c}{d}\right)\exp(-d\zeta)-\left(1+\frac{2}{3}a\zeta\right)^{1.5}-\frac{bc}{d}+1\end{aligned} \tag{3.20}$$

where $a = 1$, $b = 2/3$, $c = 5$, and $d = 0.35$.

3.2.3 Computation of the Obukhov length

The transfer coefficients needed for the surface fluxes require the estimation of stability parameter ζ, itself a function of the surface fluxes. Therefore, an implicit equation, relating ζ to bulk Richardson number Ri_{bulk}, is solved:

$$Ri_{\mathrm{bulk}} = \zeta\cdot\frac{\left[\log\left(\frac{z_l+z_{0\mathrm{M}}}{z_{0\mathrm{H}}}\right)-\Psi_{\mathrm{H}}\left(\frac{z_l+z_{0\mathrm{M}}}{\mathcal{L}}\right)+\Psi_{\mathrm{H}}\left(\frac{z_{0\mathrm{H}}}{\mathcal{L}}\right)\right]}{\left[\log\left(\frac{z_l+z_{0\mathrm{M}}}{z_{0\mathrm{M}}}\right)-\Psi_{\mathrm{M}}\left(\frac{z_l+z_{0\mathrm{M}}}{\mathcal{L}}\right)+\Psi_{\mathrm{M}}\left(\frac{z_{0\mathrm{M}}}{\mathcal{L}}\right)\right]^2} \tag{3.21}$$

with

$$Ri_{\mathrm{bulk}} = \left(\frac{g}{\theta_v}\right)\frac{z_l(\theta_{\mathrm{v}l}-\theta_{\mathrm{vsurf}})}{|U_l|^2} \tag{3.22}$$

where $\theta_{\mathrm{v}l}$ and θ_{vsurf} are the virtual potential temperatures at level z_l and at the surface, and θ_{v} is a virtual potential temperature within the surface layer. Equation (3.22) can be expressed in terms of dry static energy:

$$Ri_{\mathrm{bulk}} = \frac{gz_l}{|U_l|^2}\left[\frac{2(s_l-s_{\mathrm{surf}})}{(s_l+s_{\mathrm{surf}}-\phi_l)}-(\delta-\varepsilon)(q_l-q_{\mathrm{surf}})\right] \tag{3.23}$$

Knowing Ri_{bulk} at time t, a first guess of the Obukhov length is made from fluxes computed at the previous time step. Equation (3.21) is solved numerically using the Newton iteration method to retrieve ζ.

In contrast to the previous formulation used in the model (*Louis et al.*, 1982), the present scheme allows a consistent treatment of different roughness lengths for momentum, heat and moisture. The revised stability functions also reduce diffusion in stable situations resulting in more shallow stable boundary layers.

3.2.4 Roughness lengths

The integration constants $z_{0\mathrm{M}}$, $z_{0\mathrm{H}}$ and $z_{0\mathrm{Q}}$, in the equations for the transfer coefficients C_{M}, C_{H} and C_{Q}, (equations (3.12)–(3.14)) are called roughness lengths because they are related to the small scale inhomogeneities of the surface that determine the air–surface transfer.

- Over land, roughness lengths are assumed to be fixed climatological fields as described in Chapter 9. They are derived from land-use maps, with an extra contribution dependent on the variance of subgrid orography.

- Over sea, the specification of surface roughness lengths is particularly important. Because of the fixed boundary conditions for temperature and moisture the sea is, in principle, an infinite source of energy to the model. The surface roughness lengths are expressed by (*Beljaars,* 1994):

$$\begin{aligned} z_{0M} &= \alpha_M \frac{\nu}{u_*} + \alpha_{Ch} \frac{u_*^2}{g} \\ z_{0H} &= \alpha_H \frac{\nu}{u_*} \\ z_{0Q} &= \alpha_Q \frac{\nu}{u_*} \end{aligned} \tag{3.24}$$

These expressions account for both low and high wind regimes:

- At low wind speed the sea surface becomes aerodynamically smooth and the sea surface roughness length scales with the kinematic viscosity $\nu (= 1.5 \cdot 10^{-5} m^2 s^{-1})$.
- At high wind speed the Charnock relation is used. The chosen constants are $\alpha_M = 0.11$, $\alpha_H = 0.40$, and $\alpha_Q = 0.62$ (*Brutsaert*, 1982). The Charnock coefficient, α_{Ch}, is set equal to 0.018 for the uncoupled model, and is provided by the wave model in coupled mode.

The smooth-surface parametrization is retained in high wind speed regimes for heat and moisture because observations indicate that the transfer coefficients for heat and moisture have very little wind-speed dependence above 4 ms^{-1} (*Miller et al.,* 1992*; Godfrey and Beljaars, 1991)*. In Eqs. (3.24), friction velocity u_*, is calculated from

$$u_* = C_M^{1/2} (u_l^2 + v_l^2 + w_*^2)^{1/2} \tag{3.25}$$

with w_* from equation (3.16) using fluxes from the previous time step.

3.3 THE EXCHANGE COEFFICIENTS ABOVE THE SURFACE LAYER

3.3.1 General

A first order closure specifies the turbulent flux of a given quantity ψ at a given model level proportional to the vertical gradient of that quantity:

$$J_\psi = \rho K_\psi \frac{\partial \psi}{\partial z} \tag{3.26}$$

The exchange coefficients K_ψ are estimated at half model levels. The computation of the exchange coefficients depends on the stability regimes (locally and at the surface) and on the vertical location above the surface. Fig. 3.1 summarizes the various areas where each scheme (non-local diffusion from Troen and Mahrt, local diffusion dependent on the Richardson number, local diffusion with Monin–Obukhov functions) is applied. First, the local Richardson number is computed in each vertical layer:

$$
\begin{aligned}
|\Delta U|^2_{k+1/2} &= (u_k - u_{k+1})^2 + (v_k - v_{k+1})^2 \\
\left(\frac{\Delta s_v}{c_p T}\right)_{k+1/2} &= \frac{2(s_k - s_{k+1})}{(s_k - \phi_k + s_{k+1} - \phi_{k+1})} - (\delta - \varepsilon)(q_k - q_{k+1}) \\
\mathrm{Ri}_{k+1/2} &= (\phi_k - \phi_{k+1}) \frac{\{(\Delta s_v)/(c_p T)\}_{k+1/2}}{|\Delta U|^2_{k+1/2}}
\end{aligned}
\tag{3.27}
$$

Given the value of Ri, in stable local conditions the stability parameter $\zeta = z/L$ is deduced from precomputed tables giving $\zeta = \zeta(\mathrm{Ri})$. A cubic spline interpolation is performed (*Press et al.* 1992, pp107-111). In unstable local conditions, we simply set $\zeta = \mathrm{Ri}$.

3.3.2 The exchange coefficients

3.3.2 (a) Turbulence length scale.

The mixing lengths $l_M = l_H = \kappa z$ used in the surface layer are bounded in the outer layer by introducing asymptotic length scales $\lambda_M \beta$ and $\lambda_H \beta$ (*Blackadar*, 1962)

$$
\begin{aligned}
\frac{1}{l_M} &= \frac{1}{\kappa z} + \frac{1}{\lambda_M \beta} \\
\frac{1}{l_H} &= \frac{1}{\kappa z} + \frac{1}{\lambda_H \beta}
\end{aligned}
\tag{3.28}
$$

The underlying idea is that vertical extent of the boundary layer limits the turbulence length scale. Since the results in the boundary layer are not very sensitive to the exact value of the asymptotic length scales, these parameters are chosen to be constants:

$$
\lambda_H = \lambda_M = 150 \text{ m} . \tag{3.29}
$$

Parameter β is 1 in the boundary layer but reduces the length scales above the boundary layer in order to prevent excessive mixing to occur in and around the jet stream. The following expression is used

$$
\beta = \beta_o + \frac{(1 - \beta_o)}{1 + \left(\frac{z}{H_{min}}\right)^2} \tag{3.30}
$$

where $\beta_o = 0.2$ and $H_{min} = 4000m$.

*3.3.2 (b) M–O similarity with Ri< 0 (*Area 1 in Fig. 3.1).

In this regime, the exchange coefficients K_ψ are based on local similarity (Nieuwstadt, 1984) stating that the expressions of the surface layer similarity can be used in the outer layer (strictly speaking only valid for stable condtions):

$$K_{\mathrm{M}} = \frac{l_{\mathrm{M}}^2}{\Phi_{\mathrm{M}}^2} \cdot \left|\frac{\partial U}{\partial z}\right|$$
$$K_{\mathrm{H}} = \frac{l_{\mathrm{H}}^2}{\Phi_{\mathrm{M}}\Phi_{\mathrm{H}}} \left|\frac{\partial U}{\partial z}\right| \tag{3.31}$$

Here it is used for the unstable regime above the boundary layer, basically to provide strong vertical mixing in statically unstable situations.

3.3.2 (c) Revised Louis scheme for Ri > 0 (Area 1 in Fig. 3.1).

The use of Eq. (3.31) to define the exchange coefficients in the stable regime was found to be detrimental to the scores of the model (*Beljaars*, 1995) because of insufficient turbulent exchange in the lower troposphere. Therefore a revised version of the Louis scheme is used (Beljaars *and Viterbo*, 1999; *Viterbo et al.*, 1999):

$$K_{\mathrm{M}} = l_{\mathrm{M}}^2 \left|\frac{\partial U}{\partial z}\right| f_{\mathrm{M}}(\mathrm{Ri})$$
$$K_{\mathrm{H}} = l_{\mathrm{H}}^2 \left|\frac{\partial U}{\partial z}\right| f_{\mathrm{H}}(\mathrm{Ri}) \tag{3.32}$$

The functional dependencies of f_{M} and f_{H} with Ri are:

$$f_{\mathrm{M}}(\mathrm{Ri}) = \frac{1}{1 + 2b\mathrm{Ri}(1 + d\mathrm{Ri})^{-1/2}}$$
$$f_{\mathrm{H}}(\mathrm{Ri}) = \frac{1}{1 + 2b\mathrm{Ri}(1 + d\mathrm{Ri})^{1/2}} \tag{3.33}$$

with $b = 5$ and $d = 1$ (these functions are revised versions of the *Louis et al.*, 1982 functions and were introduced in September 1995 in order to enhance turbulent transport in stable layers, see *Viterbo et al.*, 1999).

3.3.2 (d) Unstable at the surface (Area 2 in Fig. 3.1). In unstable surface conditions ($Q_{0\mathrm{v}} < 0$), the exchange coefficients are expressed as integral profiles for the entire convective mixed layer. This K-profile closure is based on the form proposed by *Troen and Mahrt* (1986). This approach is more suitable than the local diffusion one when the length scale of the largest transporting turbulent eddies have a similar size as the boundary layer height itself (unstable and convective conditions). It also allows for an explicit entrainment parametrization in the capping inversion (*Beljaars and Viterbo*, 1999).

First a characteristic turbulent velocity scale w_{turb} is computed:

$$w_{\mathrm{turb}} = (u_*^3 + 0.6w_*^3)^{1/3} \tag{3.34}$$

The velocities u_* and w_* are defined by equations (3.25) and (3.16) respectively.

Since the most energetic transporting scales of turbulent motion in the convective boundary layer are thermals, their strength is defined by a temperature excess with respect to their surrounding. The virtual dry static energy excess is written as

$$s_{v\mathrm{turb}} = (-2c_{p\mathrm{dry}})\frac{Q_{0\mathrm{v}}}{w_{\mathrm{turb}}} \tag{3.35}$$

The profile is scanned to find the first virtual dry static energy minimum above the surface s_{vmin} at level z_{kmin}. The the profile is further scanned to find mixed-layer depth, z_{i}, defined in terms of the first level k where $s_{vk} > s_{vmin} + s_{v\mathrm{turb}}$, and $z_{\mathrm{i}} = 0.5(z_k + z_{k+1})$.

- *Area 2.1 in Fig. 3.1* . In the surface layer above the first atmospheric level, $z_l < z < 0.1z_{\mathrm{i}}$, the exchange coefficients are prescribed as follows

$$\begin{aligned} K_{\mathrm{M}} &= \kappa z u_* \left(1 - \frac{z}{z_{\mathrm{i}}}\right)^2 \frac{1}{\Phi_{\mathrm{M}}} \\ K_{\mathrm{H}} &= \kappa z u_* \left(1 - \frac{z}{z_{\mathrm{i}}}\right)^2 \frac{1}{\Phi_{\mathrm{H}}} \end{aligned} \tag{3.36}$$

- *Area 2.2 in Fig. 3.1* . In the unstable outer layer ($0.1z_i < z \le z_i$), similar expressions are used:

$$\begin{aligned} K_{\mathrm{M}} &= kzw_{\mathrm{turb}} \left(1 - \frac{z}{z_{\mathrm{i}}}\right)^2 \\ K_{\mathrm{H}} &= kzw_{\mathrm{turb}} \left(1 - \frac{z}{z_{\mathrm{i}}}\right)^2 \frac{\Phi_{\mathrm{M}}}{\Phi_{\mathrm{H}}} \end{aligned} \tag{3.37}$$

  The Prandtl number $\mathrm{Pr} = \Phi_{\mathrm{M}}/\Phi_{\mathrm{H}}$ is evaluated at $z = 0.1z_{\mathrm{i}}$.

- *Entrainment zone*. Entrainment at the top of the convective boundary layer is taken into account explicitly. The buoyant flux at $z = z_{\mathrm{i}}$ is assumed to be proportional to the surface heat flux:

$$(Q_{\mathrm{v}})_{z=z_{\mathrm{i}}} = -C_{\mathrm{entr}} Q_{0\mathrm{v}} \tag{3.38}$$

  where the entrainment constant C_{entr} is determined from experimental data. The numerical value of 0.2 is chosen from *Driedonks and Tennekes* (1984).

Knowing the flux at the top of the mixed layer, the exchange coefficient can be expressed as:

$$\begin{aligned} &\hat{K}_{\mathrm{H}} = -C_{\mathrm{entr}} Q_{0\mathrm{v}} \frac{\Delta z}{\Delta \theta_{\mathrm{v}}} \qquad \text{with} \\ &(\Delta\theta_{\mathrm{v}})_{k+1/2} = \frac{1}{c_{p\mathrm{dry}}}\{s_k - s_{k+1} - 0.5(\delta - \varepsilon)(q_k - q_{k+1})(s_k + s_{k+1})\} \end{aligned} \tag{3.39}$$

Then at $z = z_{\mathrm{i}}$:

$$K_{\mathrm{H}} = \max(K_{\mathrm{H}}, \hat{K}_{\mathrm{H}}) \tag{3.40}$$

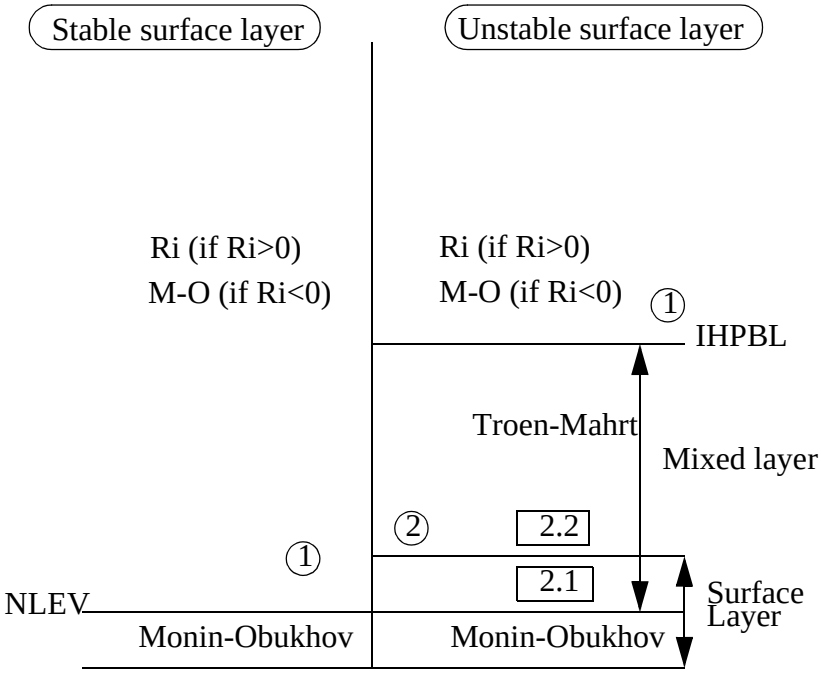

Figure 3.1 Schematic diagram of the different regions of the boundary layer.

Instead of the exchange coefficients $(K)_{k+1/2}$ themselves, the scaled quantities $(K)^*_{k+1/2}$ are computed

$$K^*_{k+1/2} = K_{k+1/2}\alpha\rho_{k+1/2}\left[\frac{2g\Delta t}{(\Delta z)_{k+1/2}}\right] \tag{3.41}$$

where α is the implicitness factor of the finite difference scheme (see equation (3.44)).

3.4 SOLUTION OF THE VERTICAL DIFFUSION EQUATIONS

The equations for turbulent transfer are solved with the tendencies from the adiabatic (subscript 'dyn') and radiative processes (subscript 'rad') as source terms in the right hand side:

$$\frac{\partial\psi}{\partial t} = g\frac{\partial J_\psi}{\partial p} + \left.\frac{\partial\psi}{\partial t}\right|_{\text{dyn}} + \left.\frac{\partial\psi}{\partial t}\right|_{\text{rad}} \tag{3.42}$$

Since the thickness of the model layers Δz is small near the ground, the time-stepping procedure must be implicit in order to avoid numerical instability when $K\Delta t/(\Delta z)^2 > 1$. However, the interaction with the adiabatic and radiative processes is treated implicitly, and *Janssen et al.* (1992) have shown that if the tendencies are not added to the right hand side of equation (3.42) a time step dependent equilibrium, and a too low numerical drag coefficient for high wind speeds, arise. By applying a 'fractional-steps' method (*Beljaars*, 1991), the discretization of equation (3.42) becomes, for $1 < k < l$,

$$\left.\frac{\partial\psi}{\partial t}\right|_{\text{diff}} = \frac{\psi^{t+1} - \{\psi^t + \Delta\psi_{\text{dyn}} + \Delta\psi_{\text{rad}}\}}{\Delta t}$$
$$= \frac{g}{p_{k+1/2} - p_{k-1/2}}\left\{\rho_{k+1/2}K^t_{k+1/2}\left(\frac{\hat{\psi}_{k+1} - \hat{\psi}_k}{z_{k+1} - z_k}\right) - \rho_{k-1/2}K^t_{k-1/2}\left(\frac{\hat{\psi}_k - \hat{\psi}_{k-1}}{z_k - z_{k-1}}\right)\right\} \tag{3.43}$$

where

$$\hat{\psi} = \alpha\psi^{t+1} + (1-\alpha)\psi^t \tag{3.44}$$

The parameter α determines the implicitness of the scheme. For $\alpha = 0$ the scheme is explicit, for $\alpha = 0.5$ we have a Crank–Nicholson and for $\alpha = 1$ we have an implicit backward scheme. In the model, $\alpha = 1.5$, to avoid non-linear instability from the K-coefficients. The exchange coefficients are computed from the mean variables at $t-1$.

The previous equation can be written as

$$-\frac{K^*_{k-1/2}}{\Delta p_k}\left(\frac{\hat{\psi}_{k-1}}{\alpha}\right) + \left[1 + \frac{K^*_{k+1/2}}{\Delta p_k} + \frac{K^*_{k-1/2}}{\Delta p_k}\right]\left(\frac{\hat{\psi}_k}{\alpha}\right) - \frac{K^*_{k+1/2}}{\Delta p_k}\cdot\left(\frac{\hat{\psi}_{k+1}}{\alpha}\right)$$
$$= \frac{\psi^t_k}{\alpha} + \Delta\psi_{\text{dyn}} + \Delta\psi_{\text{rad}} \tag{3.45}$$

leading to the inversion of a tridiagonal matrix to solve for $\hat{\psi}/\alpha$. The coefficients K^* are defined from (3.41).

At the lowest level ($k = l$) the equation includes the surface fluxes which are obtained by averaging over N_T tiles:

$$\frac{\hat{\psi}_l}{\alpha} = \frac{\psi^t_l}{\alpha} + \Delta\psi_{\text{dyn}} + \Delta\psi_{\text{rad}} - K^*_{l-1/2}\cdot\frac{\hat{\psi}_l - \hat{\psi}_{l-1}}{\alpha\Delta p_l} + \sum_{i=1}^{N_T} F_i\frac{C^*_{\psi i}}{\alpha\Delta p_l}\{A_{li}\hat{\psi}_l - A_{\text{surfi}}\hat{\psi}_{\text{surfi}}\} \tag{3.46}$$

with $C_{\psi i}{}^* = C^{t-1}_{\psi i}|U_l|g\rho\alpha\Delta t$ and

$$\begin{array}{llll} \Psi = 0 & ,A_l = 1 & ,A_{surf} = 1 & ,N_T = 1 \text{ for } \psi = u, v \\ \psi_{\text{surfi}} = s_{skini} & ,A_{li} = 1 & ,A_{surfi} = 1 & ,N_T = 8 \text{ for } \psi = s \\ \psi_{\text{surfi}} = q_{\text{sat}}(T_{\text{skini}}) & ,A_{li} = \alpha_{li} & ,A_{surfi} = \alpha_{surfi} & ,N_T = 8 \text{ for } \psi = q \end{array} \tag{3.47}$$

Eq. (3.46) can be re-written

$$-\frac{K^*_{l-1/2}}{\Delta p_l}\left(\frac{\hat{\psi}_{l-1}}{\alpha}\right) + \left[1 + \sum_{i=1}^{N_T} F_i\frac{C^*_{\psi i}A_{li}}{\Delta p_l} + \frac{K^*_{l-1/2}}{\Delta p_l}\right]\left(\frac{\hat{\psi}_l}{\alpha}\right)$$
$$= \frac{\psi^t_l}{\alpha} + \Delta\psi_{\text{dyn}} + \Delta\psi_{\text{rad}} - \sum_{i=1}^{N_T} F_i\frac{C^*_{\psi i}A_{\text{surfi}}}{\Delta p_l}\left(\frac{\hat{\psi}_{\text{surfi}}}{\alpha}\right) \tag{3.48}$$

The implicit value at the surface $\hat{\psi}_{\text{surfi}}$ on the right hand side is obtained from coupling this last equation with the calculation of the surface energy budget through the computation of the skin surface temperature (see equation (3.62) in Section 3.5).

At the top of the atmosphere ($k = 1$) turbulent fluxes at set to zero and we have

$$\frac{\hat{\psi}_1}{\alpha} = \frac{\hat{\psi}_1^t}{\alpha} + \Delta\psi_{\text{dyn}} + \Delta\psi_{\text{rad}} - K^*_{-1/2}\frac{\hat{\psi}_1 - \hat{\psi}_0}{\alpha\Delta p_1} \tag{3.49}$$

which can be re-written

$$-\frac{K^*_{-1/2}}{\Delta p_1}\frac{\hat{\psi}_0}{\alpha} + \left(1 + \frac{K^*_{-1/2}}{\Delta p_1}\right)\frac{\hat{\psi}_1}{\alpha} = \frac{\psi_1^t}{\alpha} + \Delta\psi_{\text{dyn}} + \Delta\psi_{\text{rad}} \tag{3.50}$$

The tridiagonal matrix equation is solved by a downward elimination scan followed by an upward back substitution (*Press et al.*, 1992, pp 42-43).

3.5 THE SKIN TEMPERATURE

The surface energy balance is satisfied independently for the tiles by calculating the skin temperature for each tile. The skin layer represents the vegetation layer, the top layer of the bare soil, or the top layer of the snow pack, has no heat capacity and therefore responds instantaneously to changes in e.g. radiative forcing. In order to calculate the skin temperature, the surface energy balance equation is linearized for each tile leading to an expression for the skin temperature. This procedure is equivalent to the Penmann-Monteith approach which can be derived by eliminating the skin temperature from the surface energy balance equation assuming that the net radiation minus ground heat flux is known (e.g. Brutsaert, 1982). The approach followed here is an extension to the Penmann-Monteith derivation in the sense that it allows for coupling with the underlying soil (or snow, ice). Because of the short time scale associated with the skin layer, the equation for its temperature is solved implicitly together with the vertical diffusion in the boundary layer.

The following general discussion applies to each tile but the parameters are tile dependent as discussed in the land surface part of the documentation (Chapter 7). The surface energy balance equation can be written as:

$$\Re_{\text{SW}} + \Re_{\text{LW}} + H + LJ_q = \Lambda_{\text{skin}}(T_{\text{skin}} - T_s) \tag{3.51}$$

where $\Re_{\text{SW}}$ and $\Re_{\text{LW}}$ are the net shortwave and longwave radiation fluxes at the surface and the right hand side represents the ground heat flux through coupling with the underlying soil, snow or ice with temperature T_s. The turbulent sensible and latent heat fluxes are

$$H = J_s - c_{pdry}T_{skin}\delta J_q \tag{3.52}$$

$$J_s = \rho C_{\text{H}}|U_l|\{s_l - s_{skin}\} \tag{3.53}$$

$$J_q = \rho C_Q|U_l|\{\alpha_l q_l - \alpha_{surf}q_{sat}(T_{skin})\} \tag{3.54}$$

In order to solve for the skin temperature implicitly, the surface energy balance is solved together with the vertical diffusion equations. After the downward elimination scan of the tridiagonal system of equations (3.45) a relation

is obtained between the lowest model level values and the surface values, i.e. between $\hat{q}_l$ and $\hat{q}_{sat}(\hat{T}_{skin})$, and between $\hat{s}_l$ and $\hat{s}_{skin}$:

$$\hat{s}_l = Z_{\mathrm{AS}}\hat{s}_{\mathrm{skin}} + Z_{\mathrm{BS}} \tag{3.55}$$

$$\hat{q}_l = Z_{\mathrm{AQ}}q_{\mathrm{sat}}(\hat{T}_{\mathrm{skin}}) + Z_{\mathrm{BQ}} \tag{3.56}$$

Since the vertical diffusion equation is formulated in terms of the time extrapolated parameters (indicated by a hat, see equation (3.44)), the skin temperature has to be extrapolated as well. Eliminating the lowest model level parameters and linearizing with respect to previous time step skin temperature leads to

$$H = \rho C_{\mathrm{H}}|U_l|\{(Z_{\mathrm{AS}}-1)\hat{s}_{\mathrm{skin}} + Z_{\mathrm{BS}}\} - c_{pdry}\hat{T}_{skin}\delta J_q \tag{3.57}$$

$$J_q = \rho C_{\mathrm{Q}}|U_l|\left\{a_l(Z_{\mathrm{AQ}}-a_{\mathrm{surf}})\left[q_{\mathrm{sat}}(T^t_{\mathrm{skin}}) + \frac{\partial q_{\mathrm{sat}}}{\partial T}(\hat{T}_{\mathrm{skin}} - T^t_{\mathrm{skin}})\right] + a_l Z_{\mathrm{BQ}}\right\} \tag{3.58}$$

Also $\hat{s}_{\mathrm{skin}}$ needs to be expressed in surface variables. For this purpose the moisture correction in c_p is evaluated from the previous time level:

$$\hat{s}_{skin} = c_p\hat{T}_{skin} \tag{3.59}$$

$$c_p = c_{pdry}\{1 + \delta\alpha_{surf}q_{sat}(T^t_{skin}) + \delta(1-\alpha_l)q^t_l\} \tag{3.60}$$

The net long-wave radiation at the surface is linearized with respect to skin temperature at the previous radiation time step (indicated by superscript $trad$, which can be up to 3 hours earlier):

$$\hat{\Re}_{LW} = \Re^{trad}_{LW} - 4(T^{trad}_{\mathrm{skin}})^3(\hat{T}_{\mathrm{skin}} - T^{trad}_{\mathrm{skin}}) \tag{3.61}$$

Substituting $\hat{s}_{skin}$ in (3.57) and replacing H and J_q in surface energy balance equation (3.51) by equations (3.57) and (3.58) leads to an expression for skin temperature $\hat{T}_{\mathrm{skin}}$ at the extrapolated time level.

$$\begin{aligned}\hat{T}_{\mathrm{skin}} = \Big[&\Lambda_{\mathrm{skin}}T_{\mathrm{s}} + \Re_{\mathrm{SW}} + \Re^{trad}_{LW} + 4(T^{trad}_{\mathrm{skin}})^4 + \rho C_{\mathrm{H}}|U|Z_{\mathrm{BS}} + \\ &\rho C_Q(L - c_{pd}T^t_{skin}\delta)|U_l|\left((a_lZ_{\mathrm{AQ}} - a_{surf})\left(q_{\mathrm{sat}}(T^t_{\mathrm{skin}}) - \frac{\partial q_{\mathrm{sat}}}{\partial T}T^t_{\mathrm{skin}}\right) + a_lZ_{\mathrm{BQ}}\right)\Big] \\ &\left[4(T^{trad}_{\mathrm{skin}})^3 - \rho C_{\mathrm{H}}|U_l|(Z_{\mathrm{AS}}-1)c_p - \rho C_{\mathrm{Q}}|U_l|(L - c_{pd}T^t_{skin}\delta)(a_lZ_{\mathrm{AQ}} - a_{\mathrm{surf}})\frac{\partial q_{\mathrm{sat}}}{\partial T} + \Lambda_{\mathrm{skin}}\right]^{-1}\end{aligned} \tag{3.62}$$

with c_p from equation (3.60). Following the downward elimination scan of the tridiagonal matrices for s and q, equation (3.62) is solved for all the tiles, using the appropriate parameters for each tile (note that also the transfer coefficients and therefore coefficients Z_{Aq}, Z_{Bq}, Z_{As}, Z_{Bs} are tile dependent). The resulting skin temperatures are used in (3.48) with the corresponding weights of the tiles as a boundary condition before doing the upward scanning back-substitution.

This procedure is fully implicit for the dominant tile in the sense that atmospheric and skin variables are in equilibrium at the new time level. However, equilibrium for non-dominant tiles is not necessarily achieved. It can happen that the surface fluxes from the dominant tile changes the temperature and moisture substantially at the lowest model level. If the fluxes to another tile (with small fraction) happen to be very different, this tile will not see the correct atmospheric state in the computation of the skin temperature. A full implicit coupling would require the solution of a matrix problem involving the skin temperatures of all the tiles simultaneously.

3.6 TENDENCY CALCULATIONS AND ENERGY DISSIPATION

Total wind and specific humidity tendencies after the vertical diffusion (including also the dynamics and the radiation) are

$$\begin{aligned} \frac{\partial u}{\partial t} &= \frac{u^{t+1}-u^{t}}{\Delta t} \\ \frac{\partial v}{\partial t} &= \frac{v^{t+1}-v^{t}}{\Delta t} \\ \frac{\partial q}{\partial t} &= \frac{q^{t+1}-q^{t}}{\Delta t} \end{aligned} \tag{3.63}$$

The kinetic energy lost by the mean flow through the diffusion process, E_{diss}, is

$$E_{\text{diss}} = 2\Delta t \cdot \left.\frac{\partial u}{\partial t}\right|_{\text{diff}} \left(\frac{u^{t+1}+u^{t}}{2}\right) + 2\Delta t \cdot \left.\frac{\partial v}{\partial t}\right|_{\text{diff}} \left(\frac{v^{t+1}+v^{t}}{2}\right) \tag{3.64}$$

The kinetic energy lost is assumed to be transformed locally into internal energy. This procedure by-passes the subgrid scale energy cascade, but it allows to have a closed energy cycle in the model (the term is generally small)

$$\left.\frac{\partial T}{\partial t}\right|_{\text{diff+dyn+rad}} = \frac{1}{2\Delta t}\left[\frac{s^{t+1}-\phi+E_{\text{diss}}}{c_{p\text{dry}}(1+\varepsilon q^{t+1})} - T^{t}\right] \tag{3.65}$$

3.7 SHORTER TIME STEP IN THE VERTICAL DIFFUSION SCHEME

The vertical diffusion scheme is called three times in every physics time step, with a time step of 1/3 of the standard time step.

3.8 DIAGNOSTIC COMPUTATIONS FOR POSTPROCESSING

3.8.1 Diagnostic boundary layer height

Because of its importance for applications (e.g. in air pollution modelling), the boundary layer height is diagnosed and made available for postprocessing. The parametrization of the mixed layer (and entrainment) already uses a model level index as boundary layer height, but in order to get a continuous field, also in neutral and stable situations the parcel lifting method (or bulk Richardson method) proposed by *Troen and Mahrt* (1986) is used as a diagnostic, independent of the turbulence parametrization. Boundary layer height h_{BL} is defined as the level where

the bulk Richardson number, based on the difference between quantities at that level and the lowest model level, reaches the critical value $Ri_{cr} = 0.25$. The bulk Richardson is computed from the following set of equations

$$\begin{aligned}
|\Delta U|^2 &= (u_{hbl} - u_l)^2 + (v_{hbl} - v_l)^2 \\
s_{vl} &= c_{pdry} T_l (1 + \varepsilon q_l) + g z_l \\
s_{vhbl} &= c_{pdry} T_{hbl} (1 + \varepsilon q_{hbl}) + g h_{bl} \\
\Delta s &= 8.5 c_{pdry} u_* Q_{0v} / \mathrm{w}_s \\
w_s &= \{u_*^3 + 0.6(g/T) Q_{0v} h_{bl}\}^{1/3} \qquad unstable \\
w_s &= u_* \qquad stable \\
\mathrm{Ri}_b &= h_{bl} \frac{2g(s_{vhbl} - s_{vl} - \Delta s)}{(s_{vhbl} + s_{vl} - g h_{bl} - g z_l)|\Delta U|^2}
\end{aligned} \tag{3.66}$$

where index l indicates the lowest model level and h_{bl} indicates the boundary layer height i.e the level where $Ri_b = Ri_{cr}$. The virtual dry static energy from the lowest level s_{vl} is increased with a turbulent part Δs and compared to the virtual dry static energy at boundary layer height h_{bl}. The boundary layer height is found by a vertical scan from the surface upwards. If the boundary layer height is found to be between two levels a linear interpolation is done to find the exact position. Since the boundary layer height is needed for w_s, the upward scan is done twice. The first one uses $h_{BL} = 1000m$ in the expression for w_s; the second scan uses the result of the first scan.

3.8.2 Wind at 10 m level

Wind at the 10 m level is computed for postprocessing because it is the standard level for SYNOP observations. It can be obtained rather easily by vertical interpolation between the lowest model level and the surface, making use of profile functions (3.7) and (3.8). This procedure is appropriate over the ocean or in areas where the surface is smooth and homogeneous. However, the postprocessed field is meant to be comparable to wind from SYNOP observations and for observations over land WMO requires SYNOP stations to be in open terrain in order to be well exposed to wind. So the SYNOP wind observations are not necessarily compatible with the wind that is representative for a large area (i.e. a grid box from the model). Over inhomogeneous terrain, the problem can be particularly serious, because the "aerodynamic roughness length" in the model is adjusted to provide sufficient drag at the surface which is dominated by the rough elements. This approach leads to a low area-averaged wind speed which is not comparable to the "open-terrain" wind speed as observed by WMO stations.

In order to make the postprocessed wind compatible with SYNOP observations, the concept of exposure correction is introduced. The open-terrain wind is obtained by taking the wind information from such a height above the surface that it is less influenced by the underlying terrain. This height is called the blending height h_{blend}. and for the the interpolation to 10 m an aerodynamic roughness length is used that is typical for open terrain with grassland.

The interpolation procedure is as follows. First the blending height and the interpolation roughness length are set dependent on the model roughness length field:

$$\begin{aligned}
h_{\mathrm{blend}} = 75\,, \quad z_{0MWMO} = 0.03 \quad , \quad F_{\mathrm{blend}} &= (u_{\mathrm{blend}}^2 + v_{\mathrm{blend}}^2)^{1/2} \text{ if } z_{0M} > 0.03 \\
h_{\mathrm{blend}} = z_l \quad , \quad z_{0MWMO} = z_{0M} \quad F_{\mathrm{blend}} &= (u_l^2 + v_l^2)^{1/2} \text{ if } z_{0M} < 0.03
\end{aligned} \tag{3.67}$$

$$F_{10} = F_{\text{blend}} \frac{\log\left(\frac{z_{10}+z_{0MWMO}}{z_{0MWMO}}\right) - \Psi_M\left(\frac{z_{10}+z_{0MWMO}}{\mathcal{L}}\right) + \Psi_M\left(\frac{z_{0MWMO}}{\mathcal{L}}\right)}{\log\left(\frac{z_{\text{blend}}+z_{0MWMO}}{z_{0MWMO}}\right) - \Psi_M\left(\frac{z_{\text{blend}}+z_{0MWMO}}{\mathcal{L}}\right) + \Psi_M\left(\frac{z_{0MWMO}}{\mathcal{L}}\right)} \tag{3.68}$$

where $z_{10} = 10m$, F_{blend} is the horizontal wind speed at the blending height either interpolated from model levels to 75 m or copied from the lowest model level, and F_{10} is the resulting horizontal windspeed at 10 m. The wind speed from equation (3.68) is converted to components making use of the wind direction from the lowest model level.

3.8.3 Temperature and humidity at the 2 m level

Computation of temperature and moisture at the 2 m level is based on interpolation between the lowest model level and the surface making use of the same profile functions as in the parametrization of the surface fluxes. The following expressions are derived from equations (3.9) and (3.10)

$$s_2 = s_{\text{surf}} + (s_l - s_{surf}) \frac{\log\left(\frac{z_2+z_{0\text{M}WMO}}{z_{0HWMO}}\right) - \Psi_H\left(\frac{z_2+z_{0\text{M}WMO}}{\mathcal{L}}\right) + \Psi_H\left(\frac{z_{0HWMO}}{\mathcal{L}}\right)}{\log\left(\frac{z_l+z_{0\text{M}WMO}}{z_{0HWMO}}\right) - \Psi_H\left(\frac{z_l+z_{0\text{M}WMO}}{\mathcal{L}}\right) + \Psi_H\left(\frac{z_{0HWMO}}{\mathcal{L}}\right)} \tag{3.69}$$

$$q_2 = q_{\text{surf}} + (q_l - q_{surf}) \frac{\log\left(\frac{z_2+z_{0\text{M}WMO}}{z_{0QWMO}}\right) - \Psi_H\left(\frac{z_2+z_{0\text{M}WMO}}{\mathcal{L}}\right) + \Psi_H\left(\frac{z_{0QWMO}}{\mathcal{L}}\right)}{\log\left(\frac{z_l+z_{0\text{M}WMO}}{z_{0QWMO}}\right) - \Psi_H\left(\frac{z_l+z_{0\text{M}WMO}}{\mathcal{L}}\right) + \Psi_H\left(\frac{z_{0QWMO}}{\mathcal{L}}\right)} \tag{3.70}$$

with $z_2 = 2m$, $z_{0HWMO} = z_{0QWMO} = 0.003$ if $z_{0M} > 0.03$, and otherwise $z_{0HWMO} = z_{0H}$ and $z_{0QWMO} = z_{0Q}$. Temperature T_2 is derived from s_2 and q_2 with equation (3.3). Also the dew point is computed from q_2 and surface pressure. The dew point uses the saturation formulation with respect to water to be consistent with WMO reporting practise. If the resulting dew point is lower than temperature T_2, the dew point is set equal to temperature.

3.8.4 Wind gusts

The computation of gusts is intended to be compatible with WMO observing practise for wind extremes. In order to get uniform observations, WMO defines a wind gust as the maximum of the wind averaged over 3 second intervals.

First the friction and the horizontal wind speed at the 10 m level are computed from the lowest model level (no exposure correction)

$$u_* = \frac{F_l}{\log\left(\frac{z_l+z_{0M}}{z_{0M}}\right) - \Psi_M\left(\frac{z_l+z_{0M}}{\mathcal{L}}\right) + \Psi_M\left(\frac{z_{0M}}{\mathcal{L}}\right)} \tag{3.71}$$

$$F_{M10} = \frac{u_*}{\kappa}\left[\log\left(\frac{z_{10}+z_{0M}}{z_{0M}}\right) - \Psi_M\left(\frac{z_{10}+z_{0M}}{\mathcal{L}}\right) + \Psi_M\left(\frac{z_{0M}}{\mathcal{L}}\right)\right]$$

To simulate gusts, the standard deviation of the horizontal wind is estimated on the basis of the similarity relation by *Panofsky et al.* (1977)

$$\sigma_u = 2.29u_* \cdot \left(1 + \frac{0.5z_i}{12\,\mathcal{L}}\right)^{1/3} \quad \text{for } \mathcal{L} < 0$$
$$\sigma_u = 2.29u_* \quad \text{for } \mathcal{L} > 0 \tag{3.72}$$

with $z_i = 1000m$. The difference between the gust and F_{M10} is proportional to σ_u , where the multiplier has been determined from universal turbulence spectra for a 50% exceeding probability of the three-second wind gust (see *Beljaars,* 1987). The resulting wind gust is

$$F_{\text{gust}} = F_{M10} + C_{ugn1}\sigma_u \tag{3.73}$$

with parameter $C_{ugn1} = C_{ugn}$ for open terrain and $C_{ugn} = 7.71$. To correct for extremem gusts over mountainous terrain, where the roughness length is extreme, the following expression is used

$$C_{ugn1} = \frac{1}{\kappa}\ln\left(\frac{5\exp(\kappa C_{ugn}) + z_{0M}}{5 + z_{0M}}\right)$$

From the controlling parameters it is clear that the effects of surface friction (through surface roughness) and stability are captured. However, the approach is not adequate for gusts in baroclinic situations and gusts due to strong convective events. Parameter F_{gust} is computed every time step and its maximum since the last postprocessing time is written out for archiving.

3.9 CODE

Vertical diffusion, which affects temperature, velocities and specific humidity, is performed in subroutine **VDFMAIN** called by VDFOUTER which, in turn, is called by CALLPAR. VDFOUTER calls VDFMAIN three times with 1/3 of the normal time step (these two routines have identical arguments so VDFMAIN can be called directly if the vertical diffusion is only needed once per time step).

At the start of the model integration the following setup routines are called to initialize modules specific to the vertical diffusion code:

- SUVDF. Setup routine for a number of parametrization constants.
- SUVDFS. Setup routine for constants and tables related to the stability functions. Stability functions are included as statement functions from fcvds.h.
- SUVEG. Setup routine for vegetation and tile parameters.

The main subroutine (VDFMAIN) does a sequence of computations and subroutine calls:

- The tiled surface fluxes and tiled skin temperatures are cycled from time step to time step (fluxes are needed for the first guess of stability parameters), but are not available at the start of the forecast. For the first time step, neutral transfer coefficients are used to estimate momentum fluxes, the tiled skin temperatures are set equal to the grid box averaged skin temperature from the initial condition, and the sensible and latent heat fluxes needed as a first guess for the Obukhov length computation are set to zero.

- VDFUPDZ0. This routine computes roughness lengths for momentum, heat and moisture over ocean surfaces according to equation (3.24). It also computes surface buoyancy flux and Obukhov length from the fluxes of the previous time level.
- The dry static energy is computed on model levels.
- A grid box average of the surface albedo is computed from the tile albedo and the tile fractions.
- VDFSURF. This routine prepares the surface boundary conditions for temperature and humidity and is called for every tile. The following quantities are computed: the surface specific humidity at saturation, the derivative of the saturation humidity curve at the surface, surface dry static energy, and vegetation stomatal resistances (see Chapter 7).
- VFDEXCS. This routine determines the drag transfer coefficients between the surface and the lowest model level with the thermal stability expressed as function of the Obukhov length. It is called for every tile. The implicit relation between $z/\mathcal{L}$ and the Richardson number Ri_{bulk} is solved iteratively (using the Newton method with the derivative approximated in finite differences). Pre-computed tables defined in subroutine SUVDFS are used to obtain the first guess in stable conditions (Ri>*0*) at the first time step. Transfer coefficients are multiplied by a constant factor $\rho\alpha 2\Delta tg$.
- VDFEVAP. This routine computes for each tile the equivalent evapo-transpiration efficiency and the corresponding parameters α_l and α_{surf} defined by the land surface scheme (see chapter 7). Dry static energy at the surface at time level t is estimated as well.
- VDFSFLX. This routine computes surface fluxes for each tile (heat flux, evaporation, momentum flux and virtual heat flux) at time t for later use in similarity functions and for the estimation of the diagnostic boundary layer depth.
- VDFDPBL. This routine diagnoses the boundary layer height for time level t . This boundary layer height is for postprocessing only and is not used by the parametrization.
- VDFEXCU. This routine determines the turbulent diffusion coefficients between the model levels above the surface layer. In unstable surface conditions, the depth of a mixed layer is estimated where the diffusion coefficients are expressed according to equations (3.36) and (3.37). Above the mixed layer, the diffusion coefficients are expressed from local similarity theory with equations (3.31) if Ri<0. In layers with Ri>*0*, diffusion coefficients are expressed as function of the Richardson number according to equation (3.32). The entrainment rate at the top of the mixed layer is computed according to (3.40).
- VDFDIFM. This routine solves the diffusion equation for momentum, by Gaussian elimination of the tridiagonal matrices.
- VDFDIFH. This routine solves the diffusion equations for dry static energy and specific humidity. A downward elimination scan is done through the tridiagonal matrices, and coefficients z_{AS}, z_{BS}, z_{AQ}, and z_{BQ} are computed for each tile. Then, subroutine VDFTSK is called for each tile to compute the skin temperatures from the surface energy balance equation. Subsequently the tiled skin temperatures are used as a boundary condition and the back-sustitution is performed.
- VDFINCR. This routine computes the tendencies of the prognostic variables and estimates the kinetic energy dissipation.
- VDFTFLX. This routine computes the tile fluxes at the new time levels. These are also the fluxes to be used in the land surface scheme. Averaging over the tiles is also done for diagnostic purposes and postprocessing.
- VDFPPCFL. This routine computes the surface 2 metre temperature and humidity (dew point and specific humidity), and the wind at 10 m.
- VDFPPGUST. This routine computes wind gusts as they are typically observed by standard WMO SYNOP stations.

APPENDIX A LIST OF SYMBOLS

C_{H}	transfer coefficient for heat
C_{M}	transfer coefficient for momentum (drag coefficient)
C_{Q}	transfer coefficient for moisture
c_p	specific heat at constant pressure of moist air
c_{pdry}	specific heat at constant pressure of dry air
c_{pvap}	specific heat at constant pressure of water vapour
E_{diss}	kinetic energy lost by the diffusion process
f	Coriolis parameter
F_{blend}	horizontal wind speed at blending height (for pp of 10 m wind)
F_{10}	horizontal wind speed at 10 m level (for pp)
g	acceleration of gravity
h_{BL}	diagnosed boundary layer height
h_{blend}	blending height (for pp of 10 m wind)
J_ψ	vertical turbulent flux of ψ
J_q	surface humidity flux
J_s	surface flux of dry static energy
J_M	surface momentum flux
K_ψ	turbulent exchange coefficient for ψ
K_{H}	turbulent exchange coefficient for heat
K_{M}	turbulent exchange coefficient for momentum
K_{Q}	turbulent exchange coefficient for moisture
$\mathcal{L}$	Obukhov length
L	latent heat of vaporization/sublimation
l_{H}	mixing length for heat
l_{M}	mixing length for momentum
N_T	number of tiles
p	pressure
Pr	Prandtl number
q	specific humidity
q_*	$= J_q/(\rho u_*)$
$Q_{0\mathrm{v}}$	virtual temperature flux in the surface layer
q_{sat}	saturation specific humidity
R_{dry}	gas constant for dry air
R_{vap}	gas constant for water vapour
$\Re_{\mathrm{LW}}$	net long wave radiation at the surface
$\Re_{\mathrm{SW}}$	net short wave radiation at the surface
$\mathrm{RH}_{\mathrm{surf}}$	relative humidity at the surface
Ri	local Richardson number
$\mathrm{Ri}_{\mathrm{bulk}}$	bulk Richardson number for the surface layer
s	dry static energy
s_v	virtual dry static energy
s_*	$= J_s/(\rho u_*)$
T	temperature
t	time

$\|U\|$	horizontal wind speed
u , v	horizontal wind components
u_*	friction velocity = $(J_{\mathrm{M}}/\rho)^{1/2}$
w_*	free convection velocity scale
w_{turb}	turbulent velocity scale
$z_{0\mathrm{M}}$	roughness length for momentum (aerodynamic roughness length)
$z_{0\mathrm{H}}$	roughness length for heat
$z_{0\mathrm{Q}}$	roughness length for moisture
z_{i}	scale height of the boundary layer
z_l	height of the lowest model level l
z_{0MWMO}	roughness length for momentum at SYNOP station
z_{0HWMO}	roughness length for heat at SYNOP station
z_{0QWMO}	roughness length for moisture at SYNOP station
z_2	height of sreen level observation (2 m)
z_{10}	height of surface wind observation (10 m)
α	implicitness factor for diffusion equation
α_{Ch}	Charnock parameter
β	scaling parameter for asymptotic mixing length
Δt	time step
Δz	vertical grid length
δ	$c_{pvap}/c_{pdry} - 1$
ε	$= (R_{\mathrm{vap}}/R_{\mathrm{dry}}) - 1$
θ_{v}	virtual potential temperature
κ	Von Kármán's constant
λ	asymptotic mixing length
Λ_{skin}	conductivity of
ν	kinematic viscosity
ρ	density
σ_u	standard deviation of horizontal wind
ζ	$= z/L$
ϕ	geopotential
Φ_M	universal gradient stability function for wind
Φ_H	universal gradient stability function for temperature
Φ_Q	universal gradient stability function for moisture
ψ	symbolic reference to a conservative quantity
Ψ_M	universal profile stability function for wind
Ψ_H	universal profile stability function for temperature
Ψ_Q	universal profile stability function for moisture

Subscripts:

i	tile index
k	level index (counted from model top downwards)
l	referring to lowest model level
$skin$	referring to the skin layer
$surf$	referring to the surface

Superscrips:

t	index for old time level, indicating beginning of time step
$t + 1$	index for new time level, indicating end of time step
$trad$	index referring to the latest full radiation time step

Special symbols:

$\hat{\psi}$	implicit variable ψ defined by equation (3.44)

Part IV: PHYSICAL PROCESSES

CHAPTER 4 Subgrid-scale orographic drag

Table of contents

4.1 GENERAL PRINCIPLES

The influence of subgridscale orography on the momentum of the atmosphere, and hence on other parts of the physics, is represented by a combination of lower-troposphere drag created by orography assumed to intersect model levels, and vertical profiles of drag due to the absorbtion and/or reflection of vertically propagating gravity waves generated by stably stratified flow over the subgridscale orography. The scheme is described in detail in *Lott and Miller* (1996).

The scheme is based on ideas presented by *Baines and Palmer* (1990), combined with ideas from bluff-body dynamics. The assumption is that the mesoscale-flow dynamics can be described by two conceptual models, whose relevance depends on the non-dimensional height of the mountain via.

$$H_{\mathrm{n}} = \frac{NH}{|U|} \tag{4.1}$$

where H is the maximum height of the obstacle, U is the wind speed and N is the Brunt–Väisälä frequency of the incident flow.

At small H_{n} all the flow goes over the mountain and gravity waves are forced by the vertical motion of the fluid. Suppose that the mountain has an elliptical shape and a height variation determined by a parameter b in the along-ridge direction and by a parameter a in the cross-ridge direction, such that $\gamma = a/b \leq 1$, then the geometry of the mountain can be written in the form

$$h(x,y) = \frac{H}{1 + x^2/a^2 + y^2/b^2} \ . \tag{4.2}$$

In the simple case when the incident flow is at right angles to the ridge the surface stress due to the gravity wave

has the magnitude

$$\tau_{wave} = \rho_0 b G B(\gamma) N U H^2 \tag{4.3}$$

provided that the Boussinesq and hydrostatic approximations apply. In Eq. (4.3) G is a function of the mountain sharpness (*Phillips* 1984), and for the mountain given by Eq. (4.2), $G \approx 1.23$. The term $B(\gamma)$ is a function of the mountain anisotropy, γ, and can vary from $B(0) = 1$ for a two-dimensional ridge to $B(1) = \pi/4$ for a circular mountain.

At large H_n, the vertical motion of the fluid is limited and part of the low-level flow goes around the mountain. As is explained in Section 4.2, the depth, Z_{blk}, of this blocked layer, when U and N are independent of height, can be expressed as

$$Z_{blk} = H \times \max\left(0, \frac{H_n - H_{n_{crit}}}{H_n}\right) \tag{4.4}$$

where $H_{n_{crit}}$ is a critical non-dimensional mountain height of order unity. The depth Z_{blk} can be viewed as the upstream elevation of the isentropic surface that is raised exactly to the mountain top. In each layer below Z_{blk} the flow streamlines divide around the obstacle, and it is supposed that flow separation occurs on the obstacle's flanks. Then, the drag, $D_{blk}(z)$, exerted by the obstacle on the flow at these levels can be written as

$$D_{blk}(z) = -\rho_0 C_d l(z) \frac{U|U|}{2} \tag{4.5}$$

Here $l(z)$ represents the horizontal width of the obstacle as seen by the flow at an upstream height z and C_d, according to the free streamline theory of jets in ideal fluids, is a constant having a value close to unity (*Kirchoff* 1876; *Gurevitch* 1965). According to observations, C_d can be nearer 2 in value when suction effects occur in the rear of the obstacle (*Batchelor* 1967). In the proposed parametrization scheme this drag is applied to the flow, level by level, and will be referred to as the drag of the 'blocked' flow, D_{blk}. Unlike the gravity-wave-drag scheme, the total stress exerted by the mountain on the 'blocked' flow does not need to be known *a priori*. For an elliptical mountain, the width of the obstacle, as seen by the flow at a given altitude $z < Z_{blk}$, is given by

$$l(z) = 2b\left(\frac{Z_{blk} - z}{z}\right)^{1/2} \tag{4.6}$$

In Eq. (4.6), it is assumed that the level Z_{blk} is raised up to the mountain top, with each layer below Z_{blk} raised by a factor H/Z_{blk}. This leads, effectively, to a reduction of the obstacle width, as seen by the flow when compared with the case in which the flow does not experience vertical motion as it approaches the mountain. Then applying Eq. (4.5) to the fluid layers below Z_{blk}, the stress due to the blocked-flow drag is obtained by integrating from $z = 0$ to $z = Z_{blk}$, viz.

$$\tau_{blk} \approx C_d \pi b \rho_0 Z_{blk} \frac{U|U|}{2}. \tag{4.7}$$

However, when the non-dimensional height is close to unity, the presence of a wake is generally associated with upstream blocking and with a downstream foehn. This means that the isentropic surfaces are raised on the windward side and become close to the ground on the leeward side. It we assume that the lowest isentropic surface passing over the mountain can be viewed as a lower rigid boundary for the flow passing *over* the mountain, then the

distortion of this surface will be seen as a source of gravity waves and, since this distortion is of the same order of magnitude as the mountain height, it is reasonable to suppose that the wave stress will be given by Eq. (4.3), whatever the depth of the blocked flow, Z_{blk}, although it is clearly an upper limit to use the total height, H. Then, the total stress is the sum of a wave stress, τ_{wave}, and a blocked-flow stress whenever the non-dimensional mountain height $H_{\mathrm{n}} > H_{\mathrm{n_{crit}}}$, i.e.

$$\tau \approx \tau_{\mathrm{wave}} \left\{ 1 + \frac{\pi C_{\mathrm{d}}}{2GB(\gamma)} \max\left(0, \frac{H_{\mathrm{n}} - H_{\mathrm{n_{crit}}}}{H_{\mathrm{n}}^2} \right) \right\}. \tag{4.8}$$

The addition of low-level drag below the depth of the blocked flow, Z_{blk}, enhances the gravity-wave stress term in Eq. (4.8) substantially.

In the present scheme the value of C_{d} is allowed to vary with the aspect ratio of the obstacle, as in the case of separated flows around immersed bodies (*Landweber* 1961), while at the same time setting the critical number $H_{\mathrm{n_{crit}}}$ equal to 0.5 as a constant intermediate value. Note also that for large H_{n}, Eq. (4.8) overestimates the drag in the three-dimensional case, because the flow dynamics become more an more horizontal, and the incidence of gravity waves is diminished accordingly. In the scheme a reduction of this kind in the mountain-wave stress could have been introduced by replacing the mountain height given in Eq. (4.3) with a lower 'cut-off' mountain height, $H(H_{\mathrm{n_{crit}}}/H_{\mathrm{n}})$. Nevertheless, this has not been done. Cases with large non-dimensional mountain heights are often associated with low-level wave breaking, and hence the main impact of adopting of a cut-off mountain height would be a reduction of this low-level drag.

4.2 DESCRIPTION OF THE SCHEME

Following *Baines and Palmer* (1990), the subgrid-scale orography over one grid-point region is represented by four parameters μ, γ, σ and θ which stand for the standard deviation, the anisotropy, the slope and the geographical orientation of the orography, respectively. These four parameters have been calculated from the US Navy (USN) $(10' \times 10')$ data-set.

The scheme uses values of low-level wind velocity and static stability which are partitioned into two parts. The first part corresponds to the incident flow which passes over the mountain top, and is evaluated by averaging the wind, the Brunt–Väisälä frequency and the fluid density between μ and 2μ above the model mean orography. Following *Wallace et al.* (1983), 2μ is interpreted as the envelope of the subgrid-scale mountain peaks above the model orography. The wind, the Brunt–Väisälä frequency and the density of this part of the low-level flow will be labelled U_H, N_H and ρ_H, respectively. The second part is the 'blocked' flow, and its evaluation is based on a very simple interpretation of the non-dimensional mountain height H_{n}. To first order in the mountain amplitude, the obstacle excites a wave, and the sign of the vertical displacement of a fluid parcel is controlled by the wave phase. If a fluid parcel ascends the upstream mountain flank over a height large enough to significantly modify the wave phase, its vertical displacement can become zero, and it will not cross the mountain summit. In this case the blocking height, Z_{blk}, is the highest level located below the mountain top for which the phase change between Z_{blk} and the mountain top exceeds a critical value $H_{\mathrm{n_{crit}}}$, i.e.

$$\int_{Z_{\mathrm{bl;k}}}^{3\mu} \frac{N}{U_{\mathrm{p}}} \, \mathrm{d}z \geq H_{\mathrm{n_{crit}}} \tag{4.9}$$

In the inequality (4.9), the wind speed, $U_{\mathrm{p}}(z)$, is calculated by resolving the wind, $U(z)$, in the direction of the

flow U_H. Then, if the flow veers or backs with height, (4.9) will be satisfied when the flow becomes normal to U_H. Levels below this 'critical' altitude define the low-level blocked flow. The inequality (4.9) will also be satisfied below inversion layers, where the parameter N is very large. These two properties allow the new parametrization scheme to mimic the vortex shedding observed when pronounced inversions occur (*Etling* 1989). The upper limit in the equality (4.9) was chosen to be 3μ, which is above the subgrid-scale mountain tops. This ensures that the integration in equality (4.9) does not lead to an underestimation of Z_{blk}, which can occur because of the limited vertical resolution when using 2μ as an upper limit (a better representation of the peak height), but this upper limit could be relaxed given better vertical resolution.

In the following subsection the drag amplitudes will be estimated combining formulae valid for elliptical mountains with real orographic data. Considerable simplifications are implied and the calculations are, virtually, scale analyses relating the various amplitudes to the sub-grid parameters.

4.2.1 Blocked-flow drag

Within a given layer located below the blocking level Z_{blk}, the drag is given by Eq. (4.5). At a given altitude z, the intersection between the mountain and the layer approximates to an ellipse of eccentricity

$$(a', b') \approx (a, b)\left(\frac{Z_{\text{blk}} - z}{z + \mu}\right)^{\frac{1}{2}}, \tag{4.10}$$

where, by comparison with Eq. (4.6), it is also supposed that the level $z = 0$ (i.e. the model mean orography) is at an altitude μ above the mountain valleys. If the flow direction is taken into account, the length $l(z)$ can be written approximately as

$$l(z) \approx 2 \max\,(b\cos\psi, a\sin\psi)\left(\frac{Z_{\text{blk}} - z}{z + \mu}\right)^{\frac{1}{2}} \tag{4.11}$$

where ψ is the angle between the incident flow direction and the normal ridge direction, θ, For one grid-point region and for uniformly distributed subgrid-scale orography, the incident flow encounters $L/(2a)$ obstacles is normal to the ridge $(\psi = 0)$, whereas if it is parallel to the ridge $(\psi = \pi/2)$ it encounters $L/(2b)$ obstacles, where L is the length scale of the grid-point region. If we sum up these contributions, the dependence of Eq. (4.11) on a and b can be neglected, and the length $l(z)$ becomes

$$l(z) = L\left(\frac{Z_{\text{blk}} - z}{z + \mu}\right)^{\frac{1}{2}}. \tag{4.12}$$

Furthermore, the number of consecutive ridges (i.e. located one after the other in the direction of the flow) depends on the obstacle shape: there are approximately $L/(2b)$ successive obstacles when the flow is along the ridge, and $L/(2a)$ when it is normal to the ridge. If we take this into account, together with the flow direction, then

$$l(z) = \frac{L^2}{2}\left(\frac{Z_{\text{blk}} - z}{z + \mu}\right)^{\frac{1}{2}} \max\left(\frac{\cos\psi}{a}, \frac{\sin\psi}{b}\right). \tag{4.13}$$

Relating the parameters a and b to the subgrid-scale orography parameters $a \approx \mu/\sigma$ and $a/b \approx \gamma$ and, allowing the drag coefficient to vary with the aspect ratio of the obstacle as seen by the incident flow, we have

$$r = \frac{\cos^2\psi + \gamma\sin^2\psi}{\gamma\cos^2\psi + \sin^2\psi} , \tag{4.14}$$

and the drag per unit area and per unit height can be written

$$D_{\rm blk}(z) = -C_{\rm d}\ \max\left(2-\frac{1}{r}\ ,0\right)\rho\frac{\sigma}{2\mu}\left(\frac{Z_{\rm blk}-z}{z+\mu}\right)^{\frac{1}{2}}\ \max(\cos\psi\ ,\ \gamma\sin\psi)\frac{U|U|}{2}\ . \tag{4.15}$$

The drag coefficient is modulated by the aspect ratio of the obstacle to account for the fact that $C_{\rm d}$ is twice as large for flow normal to an elongated obstacle as it is for flow round an isotropic obstacle. The drag tends to zero when the flow is nearly along a long ridge because flow separation is not expected to occur for a configuration of that kind. It can be shown that the term $\max(\cos\psi\ ,\ \gamma\sin\psi)$ is similar to a later form used for the directional dependence of the gravity-wave stress. For simplicity, this later form has been adopted, i.e.

$$D_{\rm blk}(z) = C_{\rm d}\ \max\left(2-\frac{1}{r},0\right)\rho\frac{\sigma}{2\mu}\left(\frac{Z_{\rm blk}-z}{z+\mu}\right)^{\frac{1}{2}}\ (B\cos^2\psi + C\sin^2\psi)\frac{U|U|}{2} \tag{4.16}$$

where the constants $B(\gamma)$ and $C(\gamma)$ are defined below. The difference between Eq. (4.15) and Eq. (4.16) has been shown to have only a negligible impact on all aspects of the model's behaviour,

In practice, Eq. (4.16) is suitably resolved and applied to the component from of the horizontal momentum equations. This equation is applied level by level below $Z_{\rm blk}$ and, to ensure numerical stability, a quasi-implicit treatment is adopted whereby the wind velocity U in Eq. (4.16) is evaluated at the updated time $t + {\rm d}t$, while the wind amplitude, $|U|$, is evaluated at the previous time step.

4.2.2 Gravity-wave drag

This gravity-wave part of the scheme is based on the work of *Miller et al.* (1989) and *Baines and Palmer* (1990), and takes into account some three-dimensional effects in the wave stress amplitude and orientation. For clarity and convenience, a brief description is given here. On the assumption that the subgrid-scale orography has the shape of one single elliptical mountain, the mountain wave stress can be written as (*Phillips* 1984)

$$(\tau_1,\tau_2) = \rho_H U_H N_H H^2 b G(B\ \cos^2\psi_H + C\ \sin^2\psi_H\ ,\ (B-C)\ \sin\psi\ \cos\ \psi_H) \tag{4.17}$$

where $B = 1-0.18\gamma-0.04\gamma^2$, $C = 0.48\gamma+0.3\gamma^2$ and G is a constant of order unity. Furthermore, when b or a are significantly smaller than the length L, characteristic of the gridpoint region size, there are, typically, $L^2/(4ab)$ ridges inside the grid-point region. Summing all the associated forces we find the stress per unit area, viz.

$$(\tau_1,\tau_2) = \rho_H U_H N_H \mu\sigma G\{B\ \cos^2\psi_H + C\ \sin^2\psi_H\ ,\ (B-C)\ \sin\psi_H\ \cos\psi_H\} \tag{4.18}$$

where H has been replaced by 2μ, and a by μ/σ.

It is worth noting that, since the basic parameters ρ_H, U_H, N_H are evaluated for the layer between μ and 2μ above the mean orography that defines the model's lower boundary, there will be much less diurnal cycle in the stress than in previous formulations that used the lowest model levels for this evaluation. The vertical distribution of the gravity-wave stress will determine the levels at which the waves break and slow down the synoptic flow.

Since this part of the scheme is active only above the blocked flow, this stress is now constant from the bottom model level to the top of the blocked flow, $Z_{\rm blk}$. Above $Z_{\rm blk}$, up to the top of the model, the stress is constant until the waves break. This occurs when the total Richardson number, Ri, falls below a critical value $\mathrm{Ri}_{\rm crit}$, which is of order unity. When the non-dimensional mountain height is close to unity, this algorithm will usually predict wave breaking at relatively low levels; this is not surprising since the linear theory of mountain gravity waves predicts low-level breaking waves at large non-dimensional mountain heights (*Miles and Huppert* 1969). In reality, the depth over which gravity-wave breaking occurs is more likely to be related to the vertical wavelength of the waves. For this reason, when low-level wave breaking occurs in the scheme, the corresponding drag is distributed (above the blocked flow), over a layer of thickness Δz, equal to a quarter of the vertical wavelengths of the waves, i.e.

$$\int_{Z_{\rm blk}}^{Z_{\rm blk}+\Delta z} \frac{N}{U_{\rm p}}\,\mathrm{d}z \approx \frac{\pi}{2} \tag{4.19}$$

Above the height $Z_{\rm blk} + \Delta z$ are waves with an amplitude such that $\mathrm{Ri} > \mathrm{Ri}_{\rm crit}$.

4.3 SPECIFICATION OF SUBGRID-SCALE OROGRAPHY

For completeness, the following describes how the subgrid-scale orography fields were computed by *Baines and Palmer* (1990). The mean topographic height above mean sea level over the gridpoint region (GPR) is denoted by $\bar{h}$, and the coordinate z denotes elevation above this level. Then the topography relative to this height $h(x,y) - \bar{h}$ is represented by four parameters, as follows

- *(i)* The net variance, or standard deviation, μ, of $h(x,y)$ in the grid-point region. This is calculated from the US Navy data-set, or equivalent, as described by *Wallace et al.* (1983). The quantity μ gives a measure of the amplitude and 2μ approximates the physical envelope of the peaks.
- *(ii)* A parameter γ which characterizes the anisotropy of the topography within the grid-point region.
- *(iii)* An angle ψ, which denotes the angle between the direction of the low-level wind and that of the principal axis of the topography.
- *(iv)* A parameter σ which represents the mean slope within the grid-point region.

The parameters γ and ψ may be defined from the topographic gradient correlation tensor

$$H_{ij} = \overline{\frac{\partial h}{\partial x_i}\frac{\partial h}{\partial x_j}},$$

where $x_1 = x$, and $x_2 = y$, and where the terms be calculated (from the USN data-set) by using all relevant pairs of adjacent gridpoints within the grid-point region. This symmetric tensor may be diagonalized to find the directions of the principal axes and the degree of anisotropy. If

$$K = \frac{1}{2}\left\{\overline{\left(\frac{\partial h}{\partial x}\right)^2} + \overline{\left(\frac{\partial h}{\partial y}\right)^2}\right\},\quad L = \frac{1}{2}\left\{\overline{\left(\frac{\partial h}{\partial x}\right)^2} - \overline{\left(\frac{\partial h}{\partial y}\right)^2}\right\} \text{ and } M = \overline{\frac{\partial h}{\partial x}\frac{\partial h}{\partial y}}\ , \tag{4.20}$$

the principal axis of H_{ij} is oriented at an angle θ to the x-axis, where θ is given by

$$\theta = \frac{1}{2}\arctan(M/L)\,. \tag{4.21}$$

This gives the direction where the topographic variations, as measured by the mean-square gradient, are largest. The corresponding direction for minimum variation is at right angles to this. Changing coordinates to x', y' which are oriented along the principal axes $x' = x\cos\theta + y\sin\theta$ and $y' = y\cos\theta - x\sin\theta$, the new values of K, L and M relative to these axes, denoted K', L' and M', are given by

$$K' = K,\quad L' = (L^2 + M^2)^{\frac{1}{2}} \quad \text{and} \quad M' = 0\,,$$

where K, L and M are given by Eq. (4.20). The anisotropy of the orography or 'aspect ratio'. γ is then defined by the equations

$$\begin{aligned}\gamma^2 &= \overline{\left(\frac{\partial h}{\partial y'}\right)^2} \Big/ \overline{\left(\frac{\partial h}{\partial x'}\right)^2} \\ &= \frac{K' - L'}{K' + L'} = \frac{K - (L^2 + M^2)^{1/2}}{K + (L^2 + M^2)^{1/2}}\end{aligned} \tag{4.22}$$

If the low-level wind vector is directed at an angle φ to the x-axis, then the angle ψ is given by

$$\psi = \theta - \varphi\,. \tag{4.23}$$

The slope parameter, σ, is defined as

$$\sigma^2 = \overline{\left(\frac{\partial h}{\partial x'}\right)^2}\,, \tag{4.24}$$

i.e. the mean-square gradient along the principal axis.

4.4 CODE

The code mirrors the basic form of the scheme. Hence there is a routine defining all the basic input values for the evaluations of drag, wave stress etc.; a routine to calculate the vertical distribution of wave stress; and a principal routine which computes the wave stress at the surface and the total momentum tendencies, including that from the low-level drag.

The orography parametrization is called from CALLPAR as GWDRAG which in turn calls GWSETUP, and GWPROFIL.

4.4.1 GWSETUP

This defines various reference model levels for controlling the vertical structure of the calculations, and sets up a number of derived atmospheric variables and geometric calculations required to run the scheme:

(a) The definition of the Brunt–Väisälä frequency on half levels

$$N^2{}_{k-1/2} = \frac{2g^2}{c_{p_{\rm dry}}(T_k + T_{k-1})}\left\{1 - c_{p_{\rm dry}}\rho_{k-1/2}\frac{(T_k - T_{k-1})}{(p_k - p_{k-1})}\right\} \tag{4.25}$$

(b) The definition of the mean wind components in the layer $\mu < z < 2\mu$ (where μ is the standard deviation of the subgridscale orographic height)

$$U_{\rm LOW} = \frac{\sum_{k=\mu}^{k=2\mu} U_k \Delta p_k}{\sum \Delta p_k} \tag{4.26}$$

and similarly for $V_{\rm LOW}$; likewise the mean static stability, $N_{\rm LOW}$, and the mean density, $\rho_{\rm LOW}$ are calculated.

(c) The calculation of necessary geometry pertaining to geographical orientation of subgridscale orography and wind direction,

$$\varphi_k = \tan^{-1}\left(\frac{V_k}{U_k}\right) \tag{4.27}$$

$$\psi_k = \theta - \varphi_k \tag{4.28}$$

$$\bar{\varphi} = \tan^{-1}\left(\frac{V_{\rm LOW}}{U_{\rm LOW}}\right) \tag{4.29}$$

and $\bar{\psi} = \theta - \bar{\varphi}$, where θ is the orientation of ridges relative to east, and the calculation of *Phillips* (1984) parameters

$$B = 1 - 0.18\gamma - 0.04\gamma^2 \ , \quad C = 0.48\gamma + 0.3\gamma^2 \ , \tag{4.30}$$

where γ is the anisotropy of the subgridscale orography.

(d) The calculation of the vertical wind-profile in the plane of the gravity wave stress. Defining

$$\hat{U}_k = \frac{U_{\rm LOW}}{|\mathbf{V}_{\rm LOW}|}U_k + \frac{V_{\rm LOW}}{|\mathbf{V}_{\rm LOW}|}V_k$$

and similarly for $\hat{V}_k$, where $\mathbf{V}_{\rm LOW} = (U_{\rm LOW}, V_{\rm LOW})$,
then the wind profile is defined level-by-level as

$$V_k^G = (\hat{U}_k D_1 + \hat{V}_k D_2)(D_1^2 + D_2^2)^{1/2} \ , \tag{4.31}$$

where $D_1 = B - (B - C)\sin^2\bar{\psi}$ and $D_2 = (B - C)\sin\bar{\psi}\cos\bar{\psi}$; the values of V_k^G are also used to compute half level values $V_{k+1/2}^G$ etc. by linear interpolation in pressure.

(e) The calculation of basic flow Richardson Number

$$\overline{Ri}_{k-1/2} = N^2_{k-1/2}\left\{\frac{p_k - p_{k-1}}{g\rho_{k-1/2}\,(V^G_k - V^G_{k-1})}\right\}^2$$

(f) The calculation of the depth of the layer treated as 'blocked' (i. e. experiencing a direct drag-force due to the subgrid-scale orography). This is given by the value of $Z_{\rm blk}$ that is the solution to the finite-difference form of the equation

$$\int_{Z_{\rm blk}}^{3\mu} \frac{N_k}{\hat{U}_k}\,{\rm d}z \geq F_{\rm c} \tag{4.32}$$

where $F_{\rm c}$ is a constant defined later.

(g) The calculation of the layer in which low-level wave-breaking occurs (i. e. the layer experiencing gravity wave breaking (if any) immediately above the 'blocked' layer). This is given by the value of Δz that is the solution to the finite difference form of the equation

$$\int_{Z_{\rm blk}}^{Z_{\rm blk}+\Delta z} \frac{N_k}{\hat{U}_k}\,{\rm d}z = \frac{\pi}{2}; \tag{4.33}$$

the value of $(Z_{\rm blk} + \Delta z)$ is not allowed to be less than 4μ.

(h) The calculation of the assumed vertical profile of the subgridscale orography needed for the 'blocking' computations

$$z^{\rm DEP}_k = \sqrt{\frac{Z_{\rm blk} - z_k}{z_k + \mu}} \tag{4.34}$$

4.4.2 GWPROFIL

This computes the vertical profile of gravity-wave stress by constructing a local wave Richardson number which attempts to describe the onset of turbulence due to the gravity waves becoming convectively unstable or encountering critical layers. This wave Richardson number can be written in the form

$$\tilde{\rm Ri} = \overline{\rm Ri}\left\{\frac{1-\alpha}{(1+\overline{\rm Ri}^{1/2}\alpha)^2}\right\},$$

where $\overline{\rm Ri}$ is the Richardson number of the basic flow. The parameter $\alpha = N|\delta z|/U_\tau$ in which $|\delta z|$ represents the amplitude of the wave and U_τ is the wind speed resolved in the direction of $\tau_{\rm wave}$. By requiring that $\tilde{Ri}$ never falls below a critical value $\tilde{\rm Ri}_{\rm crit}$ (currently equal to 0.25), values of wave stress are defined progressively from the top of the blocked layer upwards.

When low-level breaking occurs the relevant depth is assumed to be related to the vertical wavelength. Hence a linear (in pressure) decrease of stress is included over a depth Δz given by the solution of Eq. (4.32). The linear decrease of stress is written as

$$\tau(p_k) = \tau_{Z_{\rm blk}} + (\tau_* - \tau_{Z_{\rm blk}})\frac{(p_k - p_{Z_{\rm blk}})}{(p_* - p_{Z_{\rm blk}})} \tag{4.35}$$

where the asterisk subscript indicates that the value is at the level $(Z_{\rm blk} + \Delta z)$.

4.4.3 GWDRAG

This is the main routine. After calling GWSETUP, it defines the gravity-wave stress amplitude in the form,

$$\tau_{\rm wave} = k\rho_{\rm LOW}\sigma\mu\ (U^2{}_{\rm LOW} + V^2{}_{\rm LOW})^{1/2}\ (D^2{}_1 + D^2{}_2)^{1/2}\ N_{\rm LOW} \tag{4.36}$$

(where k is a constant defined later and σ is the mean slope of the subgrid-scale orography) and then calls GWPROCIL. The tendencies due to the wave stresses are then calculated in the form gravity-wave stress amplitude in the form,

$$\tau_{\rm wave} = k\rho_{\rm LOW}\sigma\mu\ (U^2{}_{\rm LOW} + V^2{}_{\rm LOW})^{1/2}\ (D^2{}_1 + D^2{}_2)^{1/2}\ N_{\rm LOW} \tag{4.37}$$

where k is a constant defined later and σ is the mean slope of the subgrid-scale orography.

$$\left(\frac{\partial u}{\partial t}\right)_{\rm wave} = -g\frac{(\dot{\tau}_{k+1} - \tau_k)}{(p_{k+1} - p_k)}\, f(\psi) \tag{4.38}$$

where $f(\psi)$ is the necessary geometric function to generate components, (similarly for $(\partial v/\partial t)_{\rm wave}$).

Next the low-level blocking calculations are carried out for levels below $z_{\rm b}$. These are done level-by-level as follows. Writing the low-level deceleration in the form

$$\left(\frac{\partial u}{\partial t}\right)_{\rm blk} = -C_{\rm d}\ \max\left(2 - \frac{1}{r}, 0\right)\frac{\sigma}{2\mu}\sqrt{\frac{Z_{\rm blk} - z}{z + \mu}}\ (B\ \cos^2\psi + C\ \sin^2\psi)\ \frac{U|U|}{2}\,, \tag{4.39}$$

where $r = (\cos^2\psi + \gamma\ \sin^2\psi)/(\gamma\ \cos^2\psi + \sin^2\psi)$ and B and C have been defined earlier, Eq. (4.39) is evaluated in the following partially implicit manner by writing it in the form

$$\left(\frac{\partial u}{\partial t}\right)_{\rm blk} = \frac{\tilde{U}^{n+1} - U^{n-1}}{2\Delta t} = -A\ |U^{n-1}|\tilde{U}^{n+1}$$

then $\tilde{U}^{n+1} = U^{n-1}/(1+\beta)$ and $\beta = A\ |U^{n-1}|\ 2\Delta t$. Hence

$$\left(\frac{\partial u}{\partial t}\right)_{\rm blk} = -\left(\frac{\beta}{1+\beta}\right)\frac{U^{n-1}}{2\Delta t}$$

This calculation is done level-by-level.

Finally the tendencies are incremented. This includes local dissipation heating in the form

$$\left(\frac{\partial T}{\partial t}\right) = \frac{1}{c_p}\frac{\rm DISS}{2\Delta t}$$

where $\text{DISS} = \frac{1}{2}\left\{(U^{n-1})^2 + (V^{n-1})^2 - \left(\widehat{U}\right)^2 - \left(\widehat{V}\right)^2\right\}$, and $\widehat{U} = U^{n-1} + 2\Delta t\left(\frac{\partial u}{\partial t}\right)_{sgsor}$ etc.

APPENDIX A LIST OF SYMBOLS

a	half mountain width in x-direction
B	function of the mountain anisotropy
b	half mountain width in y-direction
C_{d}	drag coefficient
D_{blk}	drag due to flow in blocked layer
G	function of the mountain sharpness
H	maximum mountain height ($=2\mu$)
$h(x,y)$	mountain height profile
H_{n}	non-dimensional mountain height ($=NH/\lvert U\rvert$)
$H_{\mathrm{n_{crit}}}$	critical non-dimensional mountain height
L	length scale of the grid-point region
$l(z)$	horizontal width of mountain seen by the upstream flow
N	Brunt–Väisälä frequency
N_H	Brunt–Väisälä frequency of un-blocked flow evaluated at height $H(=2\mu)$
Ri	Richardson number
$\mathrm{Ri}_{\mathrm{crit}}$	critical Richardson number
U	wind speed in x-direction
U_H	wind speed of incident un-blocked flow evaluated at height $H(=2\mu)$
U_{p}	component of the wind speed in the direction of U_H
U_τ	component of wind speed in the direction of the stress τ
V	wind speed in y-direction
Z_{blk}	depth of blocked layer
γ	anisotropy of the orography ($=a/b\le 1$)
θ	orientation of the orography
μ	standard deviation of orography
ρ_0	density of air at the surface
ρ_H	density of the un-blocked flow evaluated at height $H(=2\mu)$
σ	slope of the orography
τ_{blk}	stress due to blocked flow
τ_{wave}	surface stress due to gravity waves
ψ	angle between incident flow and orographic principal axis

IFS documentation

Part 4: PHYSICAL PROCESSES

CHAPTER 5 Convection

Table of contents

5.1 INTRODUCTION

Cumulus convection is parametrized by a bulk mass flux scheme which was originally described in *Tiedtke* (1989). The scheme considers deep, shallow and mid-level convection. Clouds are represented by a single pair of entraining/detraining plumes which describes updraught and downdraught processes. Momentum and tracer transport is also included.

5.2 LARGE-SCALE BUDGET EQUATIONS

The contributions from cumulus convection to the large-scale budget equations of heat moisture, momentum, and chemical tracers are

$$\left.\begin{aligned}
\left(\frac{\partial \bar{s}}{\partial t}\right)_{cu} &= g\frac{\partial}{\partial p}[M_{up}s_{up} + M_{down}s_{down} - (M_{up} + M_{down})\bar{s}] \\
&\quad + L(c_{up} - e_{down} - e_{subcld}) - (L_{subl} - L_{vap})(\mathrm{M_{elt}} - F_{rez}) \\
\left(\frac{\partial \bar{q}}{\partial t}\right)_{cu} &= g\frac{\partial}{\partial p}[M_{up}q_{up} + M_{down}q_{down} - (M_{up} + M_{down})\bar{q}] \\
&\quad -(c_{up} - e_{down} - e_{subcld}) \\
\left(\frac{\partial \bar{u}}{\partial t}\right)_{cu} &= g\frac{\partial}{\partial p}[M_{up}u_{up} + M_{down}u_{down} - (M_{up} + M_{down})\bar{u}] \\
\left(\frac{\partial \bar{v}}{\partial t}\right)_{cu} &= g\frac{\partial}{\partial p}[M_{up}v_{up} + M_{down}v_{down} - (M_{up} + M_{down})\bar{v}] \\
\left(\frac{\partial \bar{C}^i}{\partial t}\right)_{cu} &= g\frac{\partial}{\partial p}[M_{up}C^i{}_{up} + M_{down}C^i{}_{down} - (M_{up} + M_{down})\bar{C}^i]
\end{aligned}\right\} \qquad (5.1)$$

where M_{up}, M_{down} are the net contributions from all clouds to the updraught and downdraught mass fluxes, c_{up} and e_{down} are the condensation/sublimation in the updraughts, and the evaporation in the downdraughts . s_{up}, s_{down}, q_{up}, q_{down}, u_{up}, u_{down}, v_{up}, v_{down}, $C^i{}_{up}$ and $C^i{}_{down}$ are the weighted averages of the dry static energy $\bar{s}$, the specific humidity $\bar{q}$, the horizontal wind components $\bar{u}$ and $\bar{v}$ and the passive chemical tracer $\bar{C}^i$ from all updraughts and downdraughts within a grid box (although individual convective elements are not considered) obtained from the bulk cloud model described below. L_{subl} and L_{vap} are latent heats of sublimation and vaporization, and L is the effective latent heat for an ice–water mix (an empirical function of temperature). e_{subcld} is the evaporation of precipitation in the unsaturated sub-cloud layer , $\mathrm{M_{elt}}$ is the melting rate of snow and $\mathrm{F_{rez}}$ is the freezing rate of condensate in the convective updraught. In addition to (5.1) the precipitation fluxes are defined as

$$P^{\mathrm{rain}}(p) = \int_{Ptop}^{P} (G^{\mathrm{rain}} - e^{\mathrm{rain}}_{\mathrm{down}} - e^{\mathrm{rain}}_{\mathrm{subcld}} + \mathrm{M_{elt}})\frac{dp}{g}; \quad P^{\mathrm{snow}}(p) = \int_{Ptop}^{P} \langle G^{\mathrm{snow}} - e^{\mathrm{snow}}_{\mathrm{down}} - e^{\mathrm{snow}}_{\mathrm{subcld}} - \mathrm{M_{elt}}\rangle\frac{dp}{g} \qquad (5.2)$$

where P^{rain} and P^{snow} are the fluxes of precipitation in the forms of rain and snow at level p. G^{rain} and G^{snow} are the conversion rates from cloud water into rain and cloud ice into snow, and *Melt* denotes melted precipitation. The evaporation of precipitation in the downdraughts e_{down}, and below cloud base e_{subcld}, have been split into water and ice components, $e^{\mathrm{rain}}_{\mathrm{down}}$, $e^{\mathrm{snow}}_{\mathrm{down}}$, $e^{\mathrm{rain}}_{\mathrm{subcld}}$, and $e^{\mathrm{snow}}_{\mathrm{subcld}}$. The microphysical terms in Eqs. (5.1) -(5.2) referring to the updraught are explained in detail in Section 5.6, those refering to the downdraught are defined in Eq. (5.16) .

5.3 CLOUD MODEL EQUATIONS

5.3.1 Updraughts

The updraught of the cloud ensemble is assumed to be in a steady state. Then the bulk equations for mass, heat, moisture, cloud water content, momentum and tracers are

$$
\left.
\begin{aligned}
-g\frac{\partial M_{\mathrm{up}}}{\partial p} &= E_{\mathrm{up}} - D_{\mathrm{up}} \\
-g\frac{\partial (M_{\mathrm{up}} s_{\mathrm{up}})}{\partial p} &= E_{\mathrm{up}}\bar{s} - D_{\mathrm{up}} s_{\mathrm{up}} + L c_{\mathrm{up}} \quad , \qquad -g\frac{\partial (M_{\mathrm{up}} q_{\mathrm{up}})}{\partial p} = E_{\mathrm{up}}\bar{q} - D_{\mathrm{up}} q_{\mathrm{up}} - c_{\mathrm{up}} \\
-g\frac{\partial (M_{\mathrm{up}} l_{\mathrm{up}})}{\partial p} &= -D_{\mathrm{up}} l_{\mathrm{up}} + c_{\mathrm{up}} - G \quad , \qquad -g\frac{\partial M_{\mathrm{up}} r_{\mathrm{up}}}{\partial p} = -D_{\mathrm{up}} r_{\mathrm{up}} + G - S_{\mathrm{fallout}} \\
-g\frac{\partial (M_{\mathrm{up}} u_{\mathrm{up}})}{\partial p} &= E_{\mathrm{up}}\bar{u} - D_{\mathrm{up}} u_{\mathrm{up}} \quad , \qquad -g\frac{\partial (M_{\mathrm{up}} v_{\mathrm{up}})}{\partial p} = E_{\mathrm{up}}\bar{v} - D_{\mathrm{up}} v_{\mathrm{up}} \\
-g\frac{\partial (M_{\mathrm{up}} C^{i}{}_{\mathrm{up}})}{\partial p} &= E_{\mathrm{up}}\bar{C}^{i} - D_{\mathrm{up}} C^{i}{}_{\mathrm{up}}
\end{aligned}
\right\} \qquad (5.3)
$$

where E_{up} and D_{up} are the rates of mass entrainment and detrainment, l_{up} is the updraught cloud water/ice$ABCDEF$ content, and r_{up} is precipitating rain and snow. The vertical integration of (5.3) requires knowledge of the cloud-base mass flux and of the mass entrainment and detrainment rates. The cloud-base mass flux is determined for the various types of convection from the closure assumptions discussed in Section 5.4.

Entrainment of mass into convective plumes is assumed to occur (1) through turbulence exchange of mass through the cloud edges, and (2) through organized inflow; and detrainment is assumed to occur (1) through turbulent exchange and (2) through organized outflow at cloud top. The superscripts (1) and (2) are used to denote the components of the entrainment and detrainment due to turbulent and organized exchanges, respectively

$$
E_{\mathrm{up}} = E^{(1)}_{\mathrm{up}} + E^{(2)}_{\mathrm{up}} \ , \ D_{\mathrm{up}} = D^{(1)}_{\mathrm{up}} + D^{(2)}_{\mathrm{up}} \qquad (5.4)
$$

5.3.1 (a) Entrainment and detrainment rates. Turbulent entrainment and detrainment rates (s^{-1}) are parametrized as

$$
E^{(1)}_{\mathrm{up}} = \varepsilon^{(1)}_{\mathrm{up}} \frac{M_{\mathrm{up}}}{\bar{\rho}} \qquad D^{(1)}_{\mathrm{up}} = \delta^{(1)}_{\mathrm{up}} \frac{M_{\mathrm{up}}}{\bar{\rho}} \qquad (5.5)
$$

where the fractional entrainment/detrainment (m^{-1}) depend inversely on cloud radii in the updraughts (R_{up}) (*Simpson and Wiggert*, 1969; *Simpson*, 1971):

$$
\varepsilon^{(1)}_{\mathrm{up}} = \frac{0.2}{R_{\mathrm{up}}} \quad , \quad \delta^{(1)}_{\mathrm{up}} = \frac{0.2}{R_{\mathrm{up}}} \qquad (5.6)
$$

By assuming typical cloud sizes for the various types of convection, average values of fractional entrainment/detrainment are defined; deep convection is assumed to have a larger radius and so a smaller entrainment rate than shallow convection. In order to keep the scheme simple, fixed values of fractional turbulent entrainment/detrainment for each of the various types of convection are used:

$$
\varepsilon^{(1)}_{\mathrm{up}} = \delta^{(1)}_{\mathrm{up}} = \begin{cases} 1.2 \times 10^{-4}\,\mathrm{m}^{-1} & \text{for penetrative and midlevel convection} \\ 3 \times 10^{-4}\,\mathrm{m}^{-1} & \text{for shallow convection} \end{cases} \qquad (5.7)
$$

For penetrative convection and mid-level convection a small value typical for tropical thunder clouds (*Simpson*, 1971) is imposed, in order not to inhibit the penetration of clouds to large heights. For shallow convection a value typical for the larger trade wind cumuli is used (*Nitta*, 1975). In order to take into account enhanced turbulence in the lower part of the clouds, ε_{up} and δ_{up} are increased in the lowest 150hPa of the cloud in the case of deep and shallow convection. The enhancement factor varies linearly from 4 at cloud base to 1 at 150hPa above cloud base. Turbulent entrainment is only applied over the lowest half of the cloud layer.

5.3.1 (b) Organized entrainment and detrainment. Organized entrainment is applied to deep and mid-level convection. The vertical distribution of the updraught mass flux above cloud base is determined by assuming that there is organized entrainment which is directly proportional to the large-scale moisture convergence as

$$E_{\mathrm{up}}^{(2)} = -\frac{1}{\bar{q}}\left(\bar{\mathbf{V}} \cdot \nabla \bar{q} + \bar{\omega}\frac{\partial \bar{q}}{\partial p}\right) \tag{5.8}$$

Organized entrainment is only considered in the lower part of the cloud layer where large-scale convergence is encountered, that is, below the level of strongest vertical ascent. The idea to link the cloud mass flux directly to the large-scale moisture convergence has first been advocated as a parametrization by *Lindzen* (1981) who indicated that it may provide vertical profiles of mass flux and convective heating in good agreement with observations. The assumption (5.8) ensures that the vertical distribution of the convective mass flux follows that of the large-scale ascent which is partly supported by diagnostic studies for tropical convection (e.g. *Cheng et al.*, 1980; *Johnson*, 1980).

Organized detrainment is estimated from the vertical variation of the updraught vertical velocity w_{up}, which is estimated from the budget equation for the updraught kinetic energy written in height coordinates

$$\frac{\partial K_{\mathrm{up}}}{\partial z} = -\frac{\mu_{\mathrm{up}}}{M_{\mathrm{up}}}(1 + \beta C_{\mathrm{d}})2K_{\mathrm{up}} + \frac{1}{f(1+\gamma)}g\frac{T_{\mathrm{v,\,up}} - \bar{T}_{\mathrm{v}}}{\bar{T}_{\mathrm{v}}} \tag{5.9}$$

with

$$K_{\mathrm{up}} = \frac{w_{\mathrm{up}}^2}{2} \tag{5.10}$$

where K_{up} is the updraught kinetic energy, $T_{\mathrm{v,\,up}}$ is the virtual temperature of the updraught and $\bar{T}_{\mathrm{v}}$ the virtual temperature of the environment. μ_{up} is a mixing coefficient which is equal to the entrainment rate (E_{up}), or the detrainment rate (D_{up}) if this is larger. As entrainment is set to zero in the upper part of the cloud layer, use of detrainment in this region better represents the effect of mixing and vertical pressure gradients in the upper part of deep convective clouds, reducing vetical velocity and reducing overshoot of convective towers into the lower stratosphere.

$\gamma = 0.5$ is the virtual mass coefficient (*Simpson and Wiggert* 1969), the factor $f = 2$ is introduced because the flow is highly turbulent (*Cheng* et al. 1980) and for the drag coefficient a value of $C_{\mathrm{d}} = 0.506$ is used (*Simpson and Wiggert* 1969). The value for β is 1.875. The cloud base value of the updraught velocity is chosen as 1 m s^{-1}.

w_{up} enters the scheme in several ways: (i) for the generation and fallout of rain (Section 5.6), (ii) to determine the penetration above the zero-buoyancy level and the top of cumulus updraughts (where w_{up} reduces to zero),and (iii) to specify detrainment below the top of the updraught.

Organized detrainment is estimated by equating the decrease in updraught vertical velocity due to negative buoyancy at the top of the cloud to the decrease in mass flux with height:

$$\frac{M_{\mathrm{up}}(z)}{M_{\mathrm{up}}(z+\Delta z)} = \sqrt{\frac{K_{\mathrm{up}}(z)}{K_{\mathrm{up}}(z+\Delta z)}}\,. \tag{5.11}$$

This assumes that the cloud area remains constant in the detraining layer and neglects the vertical variation of buoyancy. Eq. (5.11) defines the reduction of mass flux with height, which combined with the updraught continuity equation (Eq. (5.3)) gives the organised detrainment rate.

5.3.2 Downdraughts

Downdraughts are considered to be associated with convective precipitation from the updraughts and originate from cloud air influenced by the injection of environmental air. Following *Fritsch and Chappell* (1980) and *Foster* (1958), the Level of Free Sinking (LFS) is assumed to be the highest model level (below the level of minimum moist static energy) where a mixture of equal parts of cloud and saturated environmental air at the wet-bulb temperature becomes negative buoyant with respect to the environmental air. The downdraught mass flux is assumed to be directly proportional to the upward mass flux. Following *Johnson* (1976, 1980) the mass flux at the LFS is specified from the updraught mass flux at cloud base as

$$(M_{\mathrm{down}})_{\mathrm{LFS}} = -\eta (M_{\mathrm{up}})_{\mathrm{base}} \qquad \text{with} \qquad \eta = 0.3 \tag{5.12}$$

The vertical distribution of the downdraught mass flux, dry static energy, moisture, horizontal momentum and passive tracers below the LFS are determined by entraining/detraining plume equations similar to those for the updraught;

$$\left.\begin{aligned} g\frac{\partial M_{\mathrm{down}}}{\partial p} &= E_{\mathrm{down}} - D_{\mathrm{down}} \\ g\frac{\partial (M_{\mathrm{down}} s_{\mathrm{down}})}{\partial p} &= E_{\mathrm{down}}\bar{s} - D_{\mathrm{down}} s_{\mathrm{down}} + L e_{\mathrm{down}}\,, \qquad g\frac{\partial (M_{\mathrm{down}} q_{\mathrm{down}})}{\partial p} = E_{\mathrm{down}}\bar{q} - D_{\mathrm{down}} q_{\mathrm{down}} + e_{\mathrm{down}} \\ g\frac{\partial (M_{\mathrm{down}} u_{\mathrm{down}})}{\partial p} &= E_{\mathrm{down}}\bar{u} - D_{\mathrm{down}} u_{\mathrm{down}}\,, \qquad g\frac{\partial (M_{\mathrm{down}} v_{\mathrm{down}})}{\partial p} = E_{\mathrm{down}}\bar{v} - D_{\mathrm{down}} v_{\mathrm{down}} \\ g\frac{\partial (M_{\mathrm{down}} C^{i}{}_{\mathrm{down}})}{\partial p} &= E_{\mathrm{down}}\bar{C}^{i} - D_{\mathrm{down}} C^{i}{}_{\mathrm{down}} \end{aligned}\right\} \tag{5.13}$$

e_{down} is the evaporation of convective rain to maintain a saturated descent; the moistening and cooling of the environmental air injected at the LFS is also due to evaporating rain.

Entrainment and detrainment in downdraughts are highly uncertain as relevant data are not available. As for the updraught, both turbulent and organized entrainment/detrainment are considered.

5.3.2 (a) Turbulent entrainment and detrainment. For turbulent mixing

$$\varepsilon^{(1)}_{\mathrm{down}} = \delta^{(1)}_{\mathrm{down}} = 2\times 10^{-4} m^{-1} \tag{5.14}$$

5.3.2 (b) Organized entrainment and detrainment. Organized entrainment for the downdraught is based upon a formulation suggested by *Nordeng* (1994);

$$\varepsilon_{\text{down}}^{(2)} = \frac{\left\{ g\frac{T_{\text{v,down}} - T_{\text{down}} r_{\text{down}} - \overline{T}_{\text{v}}}{\overline{T}_{\text{v}}} \right\}}{z} \qquad (5.15)$$
$$(w_{\text{down}}^{\text{LFS}})^2 - \int \left\{ g\frac{T_{\text{v,down}} - T_{\text{down}} r_{\text{down}} - \overline{T}_{\text{v}}}{\overline{T}_{\text{v}}} \right\} \mathrm{d}z$$

where $w_{\text{down}}^{\text{LFS}}$ is the vertical velocity in the downdraught at the LFS (set to -1 m s^{-1}). The total evaporation rate in the downdraft corresponds to the total downdraft precipitation rate that is simply given as

$$\sum_{\text{k=LFS}}^{\text{nlev}} e_{\text{down}} = \sum_{k\ =\ \text{LFS}}^{\text{nlev}} \frac{g}{\Delta p}(q_{\text{down,k}} - \hat{q}_{\text{down,k}}) M_{\text{down,k}} \qquad (5.16)$$

where $q_{\text{down,k}}$ is the value of the downdraft humidity computed from (5.13) without saturation adjustment, and $\hat{q}_{\text{down,k}}$ is the humidity after the saturation adjustment. The value of the rain water content in the downdraft used in (5.15) is estimated as $r_{\text{down}} = e_{\text{down}} g/(\Delta p M_{\text{up}})$, for the definition of the pressure thickness Δp of layer k see Eq. (5.48).

Organized detrainment from the downdraught occurs when either the downdraught becomes positively buoyant or approaches the surface. If the downdraught remains negatively buoyant until it reaches the surface then the mass flux is decreased linearly over the lowest 60 hPa of the atmosphere. However, if a downdraught becomes positively buoyant during its descent, it is detrained over one level, except where this occurs at cloud base. In this case the downdraught fluxes are decreased linearly (deep convection) or quadratically (mid-level convection) to zero at the surface.

5.4 Convection Initiation and Convective Types

The first important task of a convection parameterization is to decide if convection is active or not in a model grid column. This is done in a very simplified "first-guess" updraught computation that implies the determination of the cloud base level, i.e. the Lifting Condensation Level (LCL), and of the properties of the cloud (updraught) at cloud base. Furthermore, in using a bulk mass flux scheme, as opposed to a scheme which considers an ensemble of convective clouds (such as that of *Arakawa and Schubert*, 1974), some determination of convective cloud type must be made so that appropriate choices can be made for the cloud properties.

The scheme first tests for the occurrence of shallow convection by computing the ascent of a surface parcel. The following simplified updraught equation is applied

$$\frac{\partial \phi_{\text{up}}}{\partial z} = \varepsilon_{\text{up}}^{\text{ini}}(\overline{\phi} - \phi_{\text{up}}) \qquad (5.17)$$

where ϕ stands either for the dry static energy or the total water specific humidity. As proposed by Jakob and Siebesma (2003) the entrainment rate for the test parcel for shallow convection is set to $\varepsilon_{\text{up}}^{\text{ini}} = 0.5\left(\frac{0.55}{z} + 1\times10^{-4}\right)$. Additionally, a temperature ΔT_{up} and moisture excess Δq_{up} with respect to the environment is given to the test parcel at the lowest model level depending on the surface sensible and latent turbulent heat fluxes

$$\Delta T_{\rm up}^{\rm shal} = -1.5\frac{J_s}{\bar{\rho} c_p w_*}, \qquad \Delta q_{\rm up}^{\rm shal} = -1.5\frac{J_q}{\bar{\rho} L w_*}, \tag{5.18}$$

where the convective-scale velocity w_* is given as

$$w_* = 1.2\left(u_*^3 - 1.5\frac{gz\kappa}{\bar{\rho}\bar{T}}\left[\frac{J_s}{c_p} + 0.61\bar{T}\frac{J_v}{L}\right]\right)^{\frac{1}{3}}, \tag{5.19}$$

with κ =0.4 the von Kármán constant; the friction velocity u_* is set to a constant value of 0.1 m s^{-1}. The convective-scale velocity w_* is also used to initialise the updraft vertical velocity at the first model level. A grid column is then identified as shallow convective if a LCL is found for the surface parcel, if the updraft vertical velocity at the LCL (obtained by solving the kinetic energy equation (5.9)) is positive, and if the cloud thickness is smaller than 200 hPa.

Next, the occurence of deep convection is tested for by repeating the updraught computations but starting at the next higher model level. However, the entrainment rate is now set as for the first full updraught computation (5.7), i.e. $\varepsilon_{\rm up}^{\rm ini} = \varepsilon_{\rm up}^{(1)}$, simplified microphysics is taken into account by removing at each level 50% of the condensed water; the initial parcel perturbations are specified as

$$\Delta T_{\rm up}^{\rm deep} = 0.2{\rm K}, \qquad \Delta q_{\rm up}^{\rm deep} = 1\times10^{-4}{\rm kg\ kg}^{-1}, \tag{5.20}$$

and the updraught vertical velocity at the departure level is initialised to 1 ms^{-1}. Furthermore, in the lowest 60 hPa of the atmosphere that typically correspond to the mixed-layer depth over oceanic regions, the updraught values of the dry static energy (or humidity) at the departure level *k* are initialised as $s_{\rm up,k} = \tilde{s}_k + c_p\Delta T_{\rm up}^{\rm deep}$, where the tilde symbol represents a 50 hPa layer average, instead of $s_{\rm up,k} = \bar{s}_k + c_p\Delta T_{\rm up}^{\rm deep}$ as for departure levels above the assumed 60 hPa mixed-layer. The idea behind is that deep convection requires a sufficiently deep source layer, this procedure also avoids spurious convection in the early morning hours when the surface-layer undergoes strong heating. A grid-column is then identified as deep-convective, if a LCL is found and the resulting cloud (the top being defined as the level where the updraught vertical velocity vanishes) is thicker than 200 hPa. If this criterion is verified the cloud is identified as deep and the results obtained for the shallow convective test parcel are ignored (only one cloud type can exist). If no deep convective cloud is found for the given departure level, the procedure is repeated starting from the next higher model level and so on until the departure level of the test parcel is more than 350 hPa above ground. A summary of this procedure, and a discussion of the consequences for the simulation of the diurnal cycle of convection over land is given in *Bechtold et al.* (2004).

Finally, if neither deep nor shallow convection has been found, elevated (or mid-level) convection is tested for (see subsection 5.4.3) . Also, at the end of this procedure and if a column has been identified as convective, the computed values of the updraught vertical velocity, dry static energy, liquid water and specific humidity at cloud base are used to initialise the following full updraught computation at cloud base. The updraught values of the horizontal wind components at cloud base are simply set to the environmental values at the level just below (see subsection 5.9).

In the following, the determination of the convective activity (as controlled by the cloud-base mass flux) is discussed separately for each type of convection.

5.4.1 Deep convection

Following *Fritsch and Chappell* (1980) and *Nordeng* (1994), the cloud base mass flux for deep convection is esti-

mated from assuming that convection acts to reduce the convective available potential energy (CAPE) towards zero over a specified time scale τ;

$$\frac{\partial \mathrm{CAPE}}{\partial t} = -\frac{\mathrm{CAPE}}{\tau} = \int_{z_{\mathrm{base}}}^{z_{\mathrm{top}}} \frac{g}{\overline{T}_{\mathrm{v}}}\left(\frac{\partial \overline{T}_{\mathrm{v}}}{\partial t}\right)^{\mathrm{cum}} \mathrm{d}z \approx \int_{z_{\mathrm{base}}}^{z_{\mathrm{top}}} \frac{M_{\mathrm{cld}}}{\overline{\rho}} \frac{g}{\overline{T}_{\mathrm{v}}}\left(\frac{\partial \overline{T}_{\mathrm{v}}}{\partial z}\right) \mathrm{d}z \tag{5.21}$$

where

$$M_{\mathrm{cld}} = M_{\mathrm{up}} + M_{\mathrm{down}} = \alpha [M_{\mathrm{up}}]_{\mathrm{base}} + \beta [M_{\mathrm{down}}]_{\mathrm{LFS}} \tag{5.22}$$

where α and β describe the vertical variation of the updraught and downdraught mass flux due to entrainment and detrainment and the subscript 'base' refers to cloud-base quantities. As the downdraught mass flux at the LFS is linked to the updraught mass flux at cloud base (Eq. (5.12)) then,

$$M_{\mathrm{cld}} = [M_{\mathrm{up}}]_{\mathrm{base}} (\alpha - \beta\eta) \tag{5.23}$$

Using Eq. (5.23) in Eq. (5.21) results in an expression for the "final" cloud base mass flux,

$$[M_{\mathrm{up}}]_{\mathrm{base}} = \frac{\frac{CAPE}{\tau}}{g \int_{z_{\mathrm{base}}}^{z_{\mathrm{top}}} (\alpha - \beta\eta) \frac{g}{\overline{\rho}\overline{T}_{\mathrm{v}}} \frac{\partial \overline{T}_{\mathrm{v}}}{\partial z} \mathrm{d}z} = \frac{\frac{CAPE}{\tau}}{g \int_{z_{\mathrm{base}}}^{z_{\mathrm{top}}} \frac{M_{\mathrm{cld}}^{n-1}}{M_{\mathrm{base}}^{n-1}} \frac{1}{\overline{\rho}\overline{T}_{\mathrm{v}}} \frac{\partial \overline{T}_{\mathrm{v}}}{\partial z} \mathrm{d}z} \tag{5.24}$$

where M_{cld}^{n-1} is the cloud mass flux from the first full updraught (n-1=1) computation that has been initialised with a unit cloud base mass flux $M_{\mathrm{base}}^{n-1} = 0.1\Delta p_{\mathrm{base}}/(g\Delta t)$, with Δt the model time step, and where CAPE is estimated from the parcel ascent incorporating the effects of water loading,

$$\mathrm{CAPE} = \int_{z_{\mathrm{base}}}^{z_{\mathrm{top}}} g\left(\frac{T_{\mathrm{v,up}} - \overline{T}_{\mathrm{v}}}{\overline{T}_{\mathrm{v}}} - l_{\mathrm{up}}\right) \mathrm{d}z \tag{5.25}$$

Using these estimates the updraught mass flux at cloud base is recomputed and downdraught mass fluxes rescaled. A second updraught ascent is then computed to revise the updraught properties.

The adjustment time scale τ is rather arbitrary but experience suggests that to prevent grid-scale saturation it must be of order

$$M_{\mathrm{cld}} \approx -\frac{\overline{\omega}}{g} = \overline{\rho w} \tag{5.26}$$

where $\overline{w}$ is the grid-scale vertical velocity. The magnitude of the grid-scale vertical velocity increases with increasing resolution, and therefore the relaxation timescale is also made dependent on model resolution. At resolutions smaller than T319 it is set to 1 hour, and at resolutions ranging from T319 to T511 it is set to 20 minutes so that the adjustment time is close to or larger than the model time step. For future horizontal resolutions of T799 an

adjustment time scale of 10 minutes is foreseen.

5.4.2 Shallow convection

Here we consider cumulus convection, which predominantly occurs in undisturbed flow, that is in the absence of large-scale convergent flow. Typical examples are trade-wind cumuli under a subsidence inversion, convection occurring in the ridge region of tropical easterly waves and daytime convection over land. This type of convection seems to be effectively controlled by sub-cloud layer turbulence. In fact, most of the diagnostic studies carried out for trade-wind cumuli show that the net upward moisture flux at cloud-base level is nearly equal to the turbulent moisture flux at the surface (*Le Mone and Pennell*, 1976). In regions of cold air flowing over relatively warm oceans the strong sensible heat flux has been found to be of significant importance. We therefore derive the mass flux at cloud base on a balance assumption for the sub-cloud layer based on the moist static energy budget;

$$[M_{\mathrm{up}}(h_{\mathrm{up}}-\bar{h})]_{\mathrm{base}} = -\int_{\mathrm{surf}}^{\mathrm{base}} \left(\bar{\mathbf{V}}\cdot\nabla\bar{h} + \bar{\omega}\frac{\partial}{\partial p}\bar{h} - c_p\left(\frac{\partial}{\partial t}\bar{T}\right)_{\mathrm{rad}} + \frac{\partial}{\partial p}(\overline{\omega' h'})_{\mathrm{turb}}\right)\frac{dp}{g} \tag{5.27}$$

with

$$\bar{h} = c_p\bar{T} + L\bar{q} + gz \tag{5.28}$$

The moisture supply to the shallow cumulus is largely through surface evaporation as the contributions from large-scale convergence are either small or even negative, such as in the undisturbed trades where dry air is transported downward to lower levels.

An initial estimate for the updraught base mass flux is obtained using Eq. (5.27). If downdraughts occur (relatively rare for shallow convection due to the low precipitation rates), then a revised estimate is made accounting for the impact of downdraughts upon the sub-cloud layer, the l.h.s. of Eq. (5.27) being replaced by

$$[M_{\mathrm{up}}(h_{\mathrm{up}}-\bar{h})]_{\mathrm{base}} + [M_{\mathrm{down}}(h_{\mathrm{down}}-\bar{h})]_{\mathrm{base}} = [M_{\mathrm{up}}(h_{\mathrm{up}}-\bar{h})]_{\mathrm{base}} - [\beta\eta M_{\mathrm{up}}(h_{\mathrm{down}}-\bar{h})]_{\mathrm{base}} \tag{5.29}$$

Again downdraught properties are obtained using the original estimate of the updraught base mass flux and then rescaled by the revised value. For the updraught a second ascent is calculated using the revised value of the base mass flux.

No organized entrainment is applied to shallow convection. As turbulent entrainment and detrainment rates are equal, the mass flux remains constant with height until reducing at cloud top by organized detrainment.

5.4.3 Mid-level convection

Mid-level convection, that is, convective cells which have their roots not in the boundary layer but originate at levels above the boundary layer, often occur at rain bands at warm fronts and in the warm sector of extratropical cyclones (*Browning et al.* 1973; *Houze et al*. 1976; *Herzegh and Hobbs* 1980). These cells are probably formed by the lifting of low level air until it becomes saturated (*Wexler and Atlas* 1959) and the primary moisture source for the clouds is from low-level large-scale convergence (*Houze et al.* 1976). Often a low-level temperature inversion exists that inhibits convection from starting freely from the surface; therefore convection seems to be initiated by lifting low-level air dynamically to the level of free convection. This occurs often in connection with mesoscale circulations which might be related to conditionally symmetric instability (*Bennets and Hoskins* 1979; *Bennets and Sharp* 1982) or a wave-CISK mechanism (*Emanuel* 1982).

Although it is not clear how significant the organization of convection in mesoscale rain bands is for the large-scale flow, a parametrization should ideally account for both convective and mesoscale circulations. Such a parametrization, however, is presently not available and we must therefore rely on simplified schemes. Here we use a parametrization which in a simple way considers the finding of the diagnostic studies mentioned above. We assume that mid-level convection can be activated in a height range between 5×10^2 m $< z < 1\times10^4$m when there is a large-scale ascent, and the environmental air is sufficiently moist, i.e. of relative humidity in excess of 80%

The convective mass flux at cloud base is set equal to the vertical mass transport by the large-scale flow at that level:

$$\bar{\rho}_{\text{base}}\ \overline{w}_{\text{base}} = (M_{\text{up}})_{\text{base}} + (M_{\text{down}})_{\text{base}} = (M_{\text{up}})_{\text{base}}(1-\beta\eta) \tag{5.30}$$

following the notation of Subsection 5.4.1 above. Again two estimates of the updraught base mass flux are made; first neglecting downdraughts, followed by a revised estimate if downdraughts occur. The closure ensures that the amount of moisture which is vertically advected through cloud base by the large-scale ascent is fully available for generation of convective cells.

5.5 SUB-CLOUD LAYER

The first level at which convective mass, momentum and thermodynamic fluxes are estimated is cloud base. To represent the effects of convective updraughts on the sub-cloud layer a simple scaling of cloud base fluxes is applied in which they decrease to zero at the surface through the sub-cloud layer.

Care must be taken to ensure that fluxes of liquid water are zero below cloud base. Through the cloud base level an interpolation of the fluxes of liquid water static energy and total water content is used to estimate fluxes of dry static energy and water vapour mixing ratio in the level immediately below cloud base;

$$\begin{aligned}(Ms)_{\text{up}}^{\text{base+1}} &= (Z^n)(Ms)_{\text{up}}^{\text{base}} - L(Ml)_{\text{up}}^{\text{base}}\\ (Mq)_{\text{up}}^{\text{base+1}} &= (Z^n)(Mq)_{\text{up}}^{\text{base}} + (Ml)_{\text{up}}^{\text{base}}\\ (Ml)_{\text{up}}^{\text{base+1}} &= 0\end{aligned} \tag{5.31}$$

where $\phi^{\text{base+1}}$ refers to the value of ϕ at the level immediately below cloud base. Z is given by

$$Z = \left(\frac{p_{\text{surf}} - p_{\text{base+1}}}{p_{\text{surf}} - p_{\text{base}}}\right)^m \tag{5.32}$$

and p_{surf} is the surface pressure.

For deep and shallow convection m is set to 1 (implying a linear decrease in the flux with pressure below cloud base) while for mid-level convection m is equal to 2 (implying a quadratic reduction in flux below cloud base).

For the remainder of the sub-cloud layer, fluxes at level 'B+1' are reduced to zero at the surface using Z recomputed as

$$Z = \left(\frac{p_{\text{surf}} - p_k}{p_{\text{surf}} - p_{\text{base+1}}}\right)^m \tag{5.33}$$

where p_k is the pressure at level model k.

The cloud-mass and momentum fluxes in the sub-cloud layer are treated in a similar manner.

5.6 CLOUD MICROPHYSICS

5.6.1 Condensation rate in updraughts

The updraught condensation rate c_{up} is computed through a saturation adjustment

$$c_{\mathrm{up}} = \frac{g}{\Delta p}(q_{\mathrm{up}} - \hat{q}_{\mathrm{up}})M_{\mathrm{up}} \tag{5.34}$$

where q_{up} is the value of the specific humidity before the saturation adjustment, and $\hat{q}_{\mathrm{up}}$ is the specific humidity at saturation after the adjustment.

5.6.2 Freezing in convective updraughts

We assume that condensate in the convective updraughts freezes in the temperature range $250.16\mathrm{K} < T < 273.16\mathrm{K}$ maintaining a mixed phase within that range according to (6.6) (see Chapter 6 'Clouds and large-scale precipitation').

5.6.3 Generation of precipitation

The conversion from cloud water/ice to rain/snow is treated in a consistent way with that in the large-scale precipitation scheme by using a formulation following *Sundqvist* (1978)

$$G^{\mathrm{precip}} = \frac{M_{\mathrm{up}}}{\bar{\rho}} \frac{c_0}{0.75 w_{\mathrm{up}}} l_{\mathrm{up}}[1 - \exp\{-(l_{\mathrm{up}}/l_{\mathrm{crit}})^2\}] \tag{5.35}$$

where $c_0 = 1.5 \times 10^{-3}\mathrm{s}^{-1}$ and $l_{\mathrm{crit}} = 0.5\ \mathrm{g\ kg}^{-1}$. w_{up} is the updraught vertical velocity and is limited to a maximum value of 10 m s^{-1} in Eq. (5.35). This value of the autoconversion coefficient is higher than in previous cycles where it was around $c_0 = 1 \times 10^{-3}\ \mathrm{s}^{-1}$. With this value the updraft condensate content is probably still overestimated. However, with even larger values of the conversion coefficient the precipitation efficiency of the convection scheme would be too high, and the detrainment of cloud condensate too low.

Sundqvist (1978) takes into account the Bergeron-Findeisen process for temperatures below $-5°\mathrm{C}$ through a temperature dependent modification of c_0 and l_{crit};

$$\begin{aligned} c'_0 &= c_0 c_{\mathrm{BF}} \\ l'_{\mathrm{crit}} &= l_{\mathrm{crit}} c_{\mathrm{BF}} \end{aligned} \tag{5.36}$$

where

$$\begin{aligned} c_{\mathrm{BF}} &= 1 + 0.5\sqrt{\max(T_{\mathrm{BF}} - T_{\mathrm{up}}, T_{\mathrm{BF}} - T_{\mathrm{ice}})} \quad \text{for } T < T_{\mathrm{BF}} \\ c_{\mathrm{BF}} &= 1 \quad \text{for } T > T_{\mathrm{BF}} \end{aligned} \tag{5.37}$$

$T_{BF} = 268.16\text{K}$,and $T_{ice} = 260\text{K}$.

Eq. (5.35) is integrated analytically in the vertical.

5.6.4 Fallout of precipitation

The fallout of rain water/snow is parametrized as (e.g. *Kuo and Raymond*, 1980)

$$S_{fallout} = \frac{g}{\Delta p} M_{up} \frac{V}{w_{up}} r_{up} \tag{5.38}$$

where Δp is the model layer depth. The terminal velocity V is parametrized as (*Liu and Orville*, 1969)

$$V = 21.18 r_{up}^{0.2} \tag{5.39}$$

Since the fall speed of ice particles is smaller than that of water droplets, only half the value of V calculated with Eq. (5.32) is used for ice. In estimating the fallout of precipitation in the mixed phase region of the cloud a weighted mean of the fall speed for ice and water precipitation is used. Eq. (5.38) is integrated analytically in the vertical

5.6.5 Evaporation of rain

The evaporation rate of convective rain below cloud base is activated when the relative humidity *RH* in the environment drops below 80 %. It is parametrized following *Kessler* (1969), where the evaporation is assumed to be proportional to the saturation deficit $(\bar{q}_{sat} - \bar{q})$ and to be dependent on the density of rain ρ_{rain} (g m^{-3})

$$e_{subcld} = \alpha_1 (\text{RH}\ \bar{q}_{sat} - \bar{q}) \rho_{rain}^{13/20} \tag{5.40}$$

where α_1 is a constant being zero for $\bar{q} > \text{RH}\ \bar{q}_{sat}$.

As the density of rain ρ_{rain} is not given by the model it is convenient to express it in terms of the rain intensity R $(\text{g m}^{-2}\text{s}^{-1})$ as

$$R = \rho_{rain} V_{rain} \tag{5.41}$$

where V_{rain} is the mean fall speed of rain drops which again is parametrized following *Kessler* (1969).

$$V_{rain} = \alpha_2 \rho_{rain}^{1/8} / \sqrt{p/p_{surf}} \tag{5.42}$$

(Note that this is different from the formulation used in the estimation of the fallout of precipitation).

Considering that the convective rain takes place only over a fraction C_{conv} of the grid area, the evaporation rate at level k becomes

$$e_{subcld} = C_{conv} \alpha_1 (\text{RH} \bar{q}_{sat} - \bar{q}) \left[\frac{\sqrt{p/p_{surf}}}{\alpha_2} \frac{R}{C_{conv}} \right]^{\alpha_{33}} \tag{5.43}$$

where the constants have the following values (*Kessler*, 1969)

$$\alpha_1 = 5.44 \times 10^{-4}\ s^{-1} \qquad \alpha_2 = 5.09 \times 10^{-3} \qquad \alpha_3 = 0.5777$$

and where for the fractional area of precipitating clouds a constant value of $C_{conv} = 0.05$ is assumed.

5.6.6 Melting and freezing of precipitation

Melting of snow falling across the freezing level T_0 is parametrized by a simple relaxation towards T_0;

$$M_{elt} = \frac{c_p}{L_f}\frac{(\bar{T} - T_0)}{\tau} \tag{5.44}$$

where M_{elt} is the rate of melting and τ_{melt} is a relaxation time scale which decreases with increasing temperature

$$\tau_{melt} = \frac{5 \times 3600}{\{1 + 0.5(\bar{T} - T_0)\}} \tag{5.45}$$

The parametrization may produce melting over a deeper layer than observed (*Mason* 1971) but this has been intentionally introduced to account implicitly for the effects of vertical mixing which may develop in response to the production of negative buoyancy.

5.7 LINK TO CLOUD SCHEME

Before the introduction of the prognostic cloud scheme (see Chapter 6 'Clouds and large-scale precipitation') water detrained from convection ($D_{up} l_{up}$) was evaporated instantaneously. However with the prognostic cloud scheme water detrained from convection is a source of cloud mass increasing the cloud fraction and water content of clouds;

$$\begin{aligned} \frac{\partial a}{\partial t} &= (1 - a) D_{up} l_{up} \\ \frac{\partial \bar{l}}{\partial t} &= D_{up} l_{up} \end{aligned} \tag{5.46}$$

where a is the cloud fraction and $\bar{l}$ the grid-box mean cloud water.

5.8 MOMENTUM TRANSPORT

Equation set (5.3) includes a treatment of the vertical transport of horizontal momentum by convection. Studies have shown that for deep convection momentum transports are overestimated by the plume models unless the effects of cloud scale horizontal pressure gradients are included (*Gregory et al.* 1997b). For unorganised convection the effects of the pressure gradients are to adjust the in-cloud winds towards those of the large-scale flow. This can be represented by an enhanced turbulent entrainment rate in the cloud momentum equations. To ensure mass continuity the turbulent detrainment rate is also increased by an equivalent amount. As the air entrained as detrained have differing properties this adjusts the in-cloud wind back towards the large-scale value.

Hence for deep and mid-level convection the turbulent entrainment and detrainment used in the updraught momentum equation are

$$\begin{aligned}\varepsilon_{up}^{(1),(u,v)} &= \varepsilon_{up}^{(1)} + \lambda\varepsilon_{up}^{(1)} \\ \delta_{up}^{(1),(u,v)} &= \delta_{up}^{(1)} + \lambda\delta_{up}^{(1)}\end{aligned} \tag{5.47}$$

where $\varepsilon_{up}^{(1)}$ and $\delta_{up}^{(1)}$ are given by equation (5.7).

When $\varepsilon_{up}^{(1)} > 0$ (below the mid-level of the cloud) $\lambda = 2$, while if $\varepsilon_{up}^{(1)} = 0$ (in the upper part of the cloud) then $\lambda = 3$. *Gregory* (1997) suggests that the above formulation provides an adequate description of the effects of cloud scale pressure gradients in cases of deep convection. For shallow convection and downdraughts it is assumed that the effects of the pressure gradient term can be neglected and no enhancement of the entrainment rates in the momentum equations is applied. This formulation limits the momentum transports to be downgradient. Upgradient transports by highly organized convective systems (e.g. African squall lines) are not captured by this method.

The definition of the horizontal wind in the updraught and downdraught at cloud base and LFS is not well known. For the updraught the value at cloud base is set to the environmental value just below cloud base. For the downdraught the initial values at the LFS are set equal to the average values of the winds in the updraught and those of the large-scale flow.

5.9 VERTICAL DISCRETIZATION OF THE MODEL EQUATIONS

The flux divergence in the large-scale budget equations (5.1) (5.1) and in the cloud equations (5.3) and (5.13) are approximated by centred finite differences as

$$g\frac{\partial(M\phi)}{\partial p} = \frac{g}{\Delta p}(M_{k+1/2}\phi_{k+1/2} - M_{k-1/2}\phi_{k-1/2}) \quad , \Delta p = p_{k+1/2} - p_{k-1/2} \tag{5.48}$$

Furthermore, the updraught/downdraught Eqs. (5.3) and (5.13) including the entrainment/detrainment terms are discretized as

$$\begin{aligned}\frac{g}{\Delta p}(M_{up,k-1/2}\phi_{up,k-1/2} - M_{up,k+1/2}\phi_{up,k+1/2}) &= E_{up}\bar{\phi}_{k+1/2} - D_{up}\phi_{up,k+1/2} \\ \frac{g}{\Delta p}(M_{down,k+1/2}\phi_{down,k+1/2} - M_{down,k-1/2}\phi_{down,k-1/2}) &= E_{down}\bar{\phi}_{k-1/2} - D_{down}\phi_{down,k-1/2}\end{aligned} \tag{5.49}$$

The updraught equation is solved for $\phi_{up,k-1/2}$ and the downdraught equation for $\phi_{down,k+1/2}$. Note that with the definition (5.5) the terms E_{down} and D_{down} are negative. For the horizontal wind components and for tracers, the half-level environmental values are defined as shifted full-level values, i.e. $\bar{\phi}_{k+1/2} = \bar{\phi}_k$ and $\bar{\phi}_{k-1/2} = \bar{\phi}_{k-1}$. For temperature (dry static energy) and humidity, the half-level environmental values are determined by downward extrapolation from the next full level above along a cloud-ascent through that level:

$$\left.\begin{aligned}\bar{T}_{k+1/2} &= \bar{T}_k + \left(\frac{\partial \bar{T}}{\partial p}\right)_{h_{sat}}(p_{k+1/2} - p_k) \\ \bar{q}_{k+1/2} &= \bar{q}_k + \left(\frac{\partial \bar{q}}{\partial p}\right)_{h_{sat}}(p_{k+1/2} - p_k)\end{aligned}\right\} \tag{5.50}$$

where $h_{sat} = c_p T + gz + Lq_{sat}$ is the saturation moist static energy. Using an extrapolation like (5.50) for calculating the subsidence of environmental air assures smooth profiles, and is also more consistent with the calculation

of the updraughts where cloud air is transported upwards through level $k + 1/2$ with the thermal state below that level and equally with the downdraughts which depend only on values of s and q above that level. Similarly, because of (5.48) the subsidence of environmental air through the same level accounts now only for thermal properties above that level. The choice of a moist adiabat for extrapolation is dictated by the property of the moist static energy which is, by convection in the absence of downdraughts, only changed through the fluxes of moist static energy

$$\left(\frac{\partial \bar{h}}{\partial t}\right)_{\mathrm{cu}} = g\frac{\partial}{\partial p}[M_{\mathrm{up}}(h_{\mathrm{up}} - \bar{h})] \tag{5.51}$$

As the lines of the saturation moist static energy h_{sat} through point $(p_{k+1/2}, T_{k-1/2})$ and the updraught moist static energy are almost parallel, apart from entrainment effects, the difference $h_{\mathrm{up}} - \bar{h}$ is little affected by the vertical discretization.

The ascent in the updraughts is obtained by vertical integration of (5.3). Starting at the surface the condensation level (equal to the lowest half-level which is saturated or supersaturated and where updraught velocity is positive) is determined from an adiabatic ascent. The cloud profile above cloud base is determined layer by layer by first doing a dry adiabatic ascent with entrainment and detrainment included and then adjusting temperature and moisture towards a saturated state, taking into account condensation and freezing processes. The buoyancy of the parcel is calculated taking into account the effects of cloud and precipitation water loading i.e.

$$B = T_{\mathrm{up}}(1 + 0.608q_{\mathrm{up}} - l_{\mathrm{up}} - r_{\mathrm{up}}) - \bar{T}(1 + 0.608q_{\mathrm{e}}) \tag{5.52}$$

Special care has to be taken in the discretization of (5.9) because of overshooting effects. A centred differencing scheme is used so that

$$\begin{aligned}\frac{K_{\mathrm{up},\,k-1/2} - K_{\mathrm{up},k+1/2}}{z_{k-1/2} - z_{k+1/2}} = {} & \frac{E_{\mathrm{up},\,k}}{M_{\mathrm{up},\,k+1/2}}(1 + \beta C_{\mathrm{d}})\{K_{\mathrm{up},\,k-1/2} + K_{\mathrm{up},\,k+1/2}\} + \\ & \frac{1}{f(1+\gamma)}\frac{1}{2}g\left[\frac{\{T_{\mathrm{v,\,up}} - \bar{T}_{\mathrm{v}}\}_{k-1/2}}{\{T_{\mathrm{v}}\}_{k-1/2}} + \frac{\{T_{\mathrm{v,\,up}} - \bar{T}_{\mathrm{v}}\}_{k+1/2}}{\{T_{\mathrm{v}}\}_{k+1/2}}\right]\end{aligned} \tag{5.53}$$

Finally, we mention that for numerical reasons the environmental air must not be convectively unstably stratified:

$$\bar{s}_{k-1/2} \geq \bar{s}_{k+1/2} \tag{5.54}$$

In fact, one of the forecasts with the ECMWF global model became numerically unstable when (5.27) was not imposed.

5.10 TEMPORAL DISCRETIZATION

The convective tendencies for the environmental values are obtained by an explicit solution of the advection equation (5.1) written in flux form

$$\left(\frac{\partial \bar{\phi}}{\partial t}\right)_{\mathrm{cu}} = \frac{\bar{\phi}_k^{\mathrm{n+1}} - \bar{\phi}_k^{\mathrm{n}}}{\Delta t} = \frac{g}{\Delta p}[M_{\mathrm{up}}\phi_{\mathrm{up}} + M_{\mathrm{down}}\phi_{\mathrm{down}} - (M_{\mathrm{up}} + M_{\mathrm{down}})\bar{\phi}^{\mathrm{n}}]\Big|_{k-1/2}^{k+1/2} \tag{5.55}$$

as the tendency (or the new environmental value $\bar{\phi}$ at time n+1) only depends on quantities known at time step n. However, in order for the explicit solution to be stable it must satisfy the Courant-Friedrich-Levy (CFL) criterion, and therefore the mass flux values should be limited to

$$M_{\text{up}} + M_{\text{down}} \leq \frac{\Delta p}{g \Delta t} \tag{5.56}$$

It turned out that this mass flux limit is frequently reached in the case of shallow convection and long model time steps of order Δt >1800 s, and that the application of this mass flux limiter contributed to a sensitivity of model results to the model time step. Therefore, from model cycle 26r3 onwards it was decided to relax this mass flux limiter to three times the value given by the CFL criterion in the case of shallow convection and for model time steps $\Delta t > 1800$s - as a further restriction this relaxed mass flux limiter is only applied to temperature and humidity, but not to the horizontal winds.

With cycle 28r3 onwards an implicit solution is also available for chemical tracers, and is also planned to apply this solution to the horizontal winds. The implicit formulation reads

$$\left(\frac{\partial \bar{\phi}}{\partial t}\right)_{\text{cu}} = \frac{\bar{\phi}_k^{\text{n+1}} - \bar{\phi}_k^{\text{n}}}{\Delta t} = \frac{g}{\Delta p}[M_{\text{up}}\phi_{\text{up}} + M_{\text{down}}\phi_{\text{down}} - (M_{\text{up}} + M_{\text{down}})\bar{\phi}^{\text{n+1}}]\Big|_{k-1/2}^{k+1/2} \tag{5.57}$$

With the "shifted" vertical discretization for Tracers and horizontal winds, this equation constitues a bi-diagonal linear system with unknowns $\bar{\phi}_k^{\text{n+1}}$ and $\bar{\phi}_{k-1}^{\text{n+1}}$. The implicit solution provides smoother and non-local vertical profiles of tendencies through its inherent diffusivity.

5.11 STRUCTURE OF CODE

The parametrization of cumulus convection is performed in subroutines shown in Fig. 5.1 .CUCALLN
Provides interface of routines for cumulus parametrization. It takes the input values through arguments from CALLPAR and returns updated tendencies of T, q, l, u, v and chemical Tracers, as well as convective precipitation rates.

CUMASTRN
Master routine for convection scheme.

CUININ
Initializes variables for convection scheme (including vertical interpolation to the half model levels).

CUBASEN
First Guess updraught. Calculates condensation level, and sets updraught base variables and first guess cloud type.

CUASCN
Calculates ascent in updraughts. CUASCN is called twice, the second time after downdraughts have been calculated taking account of the CAPE adjustment closure for deep convection and downdraughts for mid-level and shallow convection Routines CUENTR and CUBASMCN are called from CUASCN.

CUENTR
Calculated entrainment and detrainment rates.

CUBASMCN
Calculates cloud base properties of mid-level convection.

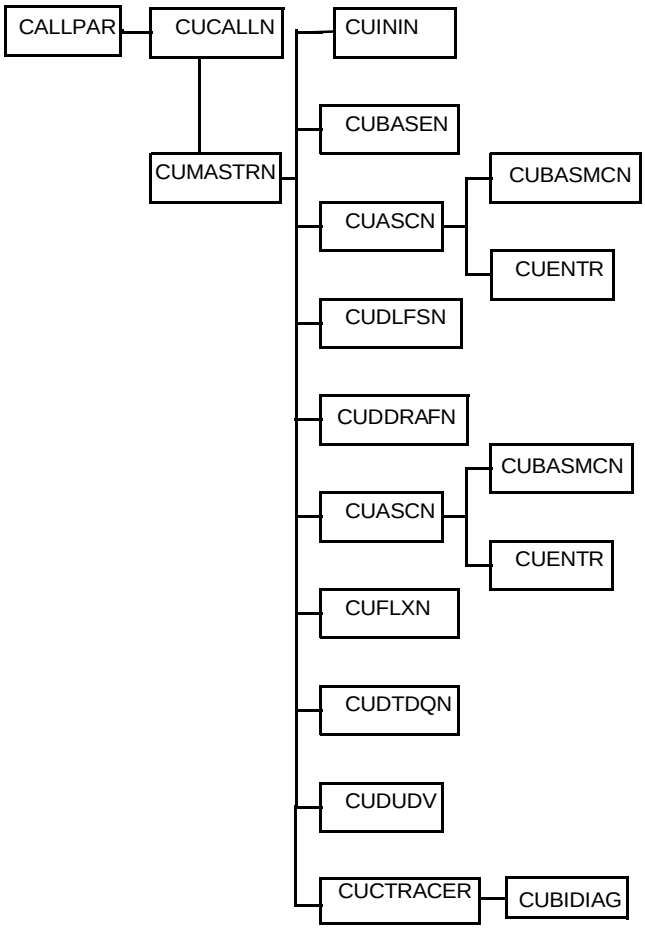

Figure 5.1 Structure of convection scheme

CUDLFSN

Calculates the level of free sinking for downdraughts.

CUDDRAFN

Calculates the downdraught descent.

CUFLXN

Calculates final convective fluxes and surface precipitation rates taking into account of melting/freezing and the evaporation of falling precipitation.

CUDTDQN

Calculates the tendencies of T and q from convection.

CUDUDV

Calculates the tendencies of u and v from convection

CUADJTQ

Calculates super/sub saturation and adjusts T and q accordingly.

CUCTRACER

Calculates convective tendencies for chemical Tracers.

CUBIDIAG
Solver for bi-diagonal linear equation system.

EXTERNALS
Subroutine SATUR for calculating saturation mixing ratio.

PARAMETERS
Defined in subroutine SUCUM called from INIPHY.

APPENDIX A LIST OF SYMBOLS

CAPE	Convective available potential energy
C^i	Convective chemical Tracer no i
C^i_{down}	Convective Tracer concentration in updraught
C^i_{down}	Convective Tracer concentration in downdraught
C_{d}	Drag coefficient
$\mathcal{C}_{\text{conv}}$	Fraction of grid square occupied by convection
c_p	Specific at constant pressure for dry air
c_{up}	Condensation/sublimation in the updraughts
D_{up}	Rate of mass detrainment in the updraughts
D_{down}	Rate of mass detrainment in the downdraughts
E_{up}	Rate of mass entrainment in the updraughts
E_{down}	Rate of mass entrainment in the downdraughts
e^{rain}	Evaporation of rain
e_{down}	Evaporation of precipitation (rain and snow) in the downdraughts
$e^{\text{rain}}_{\text{down}}$	Evaporation of rain in the downdraughts
$e^{\text{snow}}_{\text{down}}$	Evaporation of snow in the downdraughts
$\tilde{e}_{\text{subcld}}$	Evaporation of precipitation (rain and snow) in the unsaturated sub-cloud layer
$\tilde{e}^{\text{rain}}_{\text{subcld}}$	Evaporation of rain in the unsaturated sub-cloud layer
$\tilde{e}^{\text{snow}}_{\text{subcld}}$	Evaporation of snow in the unsaturated sub-cloud layer
F_{rez}	Freezing rate of condensate in the updraughts
G^{precip}	Conversion rate from cloud (water+ice) into precipitation (rain+snow)
G^{rain}	Conversion rate from cloud water into rain
G^{snow}	Conversion rate from cloud ice into snow
$\bar{h}$	Moist static energy (= $c_p T + L\bar{q} + gz$) in the environment
$\bar{h}_{\text{sat}}$	Saturated moist statice energy in the environment
h_{up}	Moist static energy in the updraughts
h_{down}	Moist static energy in the downdraughts
J_s	Surface turbulent sensible heat flux
J_q	Surface turbulent latent heat flux
K_{up}	Kinetic energy in the updraughts
L	Effective latent heat for an ice/water mix

L_{fus}	Latent heat of fusion
L_{subl}	Latent heat of sublimation
L_{vap}	Latent heat of vaporization
LCL	Lifting Condensation Level
CFL	Courant-Friedrich-Levy criterium
l_{up}	Cloud water/ice content in the updraughts
M_{elt}	Melting rate of snow
M_{cld}	Net mass flux in the convective clouds (updraughts + downdraughts)
M_{up}	Net mass flux in the downdraughts
M_{down}	Net mass flux in the downdraughts
P^{rain}	Net flux of precipitation in the form of rain
P^{snow}	Net flux of precipitation in the form of snow
p	pressure
$\bar{q}$	Specific humidity of the environment
q_{up}	Specific humidity in the updraughts
q_{down}	Specific humidity in the downdraughts
R	Rain intensity
RH	Relative humidity
r_{up}	Precipitation (rain+snow) in the updraughts
r_{down}	Precipitation (rain+snow) in the downdraughts
S_{fallout}	Fall-out of rain/snow
s	Dry static energy in the environment
s_{up}	Dry static energy in the updraughts
s_{down}	Dry static energy in the downdraughts
T_{v}	Virtual temperature in the environment
$T_{\text{v,up}}$	Virtual temperature in the updraughts
u	u component of wind in the environment
u_{up}	u component of wind in the updraughts
u_{down}	u component of wind in the downdraughts
V	Mean terminal velocity of precipitation (rain+snow)
V_{rain}	Mean terminal velocity of rain drops
$\bar{v}$	v component of wind in the environment
v_{up}	v component of wind in the updraughts
v_{down}	v component of wind in the downdraughts
$\bar{w}$	Vertical velocity in the environment
w_{up}	Vertical velocity in the updraughts
w_*	Convective velocity scale
δ	Detrainment per unit length
ε	Entrainment per unit length
ρ	Density of air
ρ_{rain}	Density of rain
τ	Adjustment time scale
ω	Omega (large-scale) vertical velocity
Δp	Pressure difference between two model half-levels
Δt	Model time step

IFS documentation
Part IV: PHYSICAL PROCESSES

CHAPTER 6 Clouds and large-scale precipitation

Table of contents

6.1 THEORY

Cloud and large-scale precipitation processes are described by prognostic equations for cloud liquid water/ice and cloud fraction and diagnostic relations for precipitation. The scheme is described in detail in *Tiedtke* (1993).

6.1.1 Definitions

6.1.1 (a) Specific cloud water content and cloud fraction. The grid-mean specific cloud water/ice content is defined as

$$l = \frac{1}{V}\int_{V} \frac{\rho_w}{\rho}\, dV\,, \tag{6.1}$$

where ρ_w is the density of cloud water, ρ is the density of moist air and V is the volume of the grid box. The

fraction of the grid box covered by clouds is defined as

$$a = \frac{1}{V}\int_V \delta \, \mathrm{d}V, \qquad \delta = \begin{cases} 1, & \text{in clouds} \\ 0, & \text{otherwise} \end{cases} \tag{6.2}$$

Furthermore, the definition of the specific cloud water content per cloud area (in-cloud water/ice content) is

$$l_{\mathrm{cld}} = \frac{l}{a} . \tag{6.3}$$

6.1.1 (b) Saturation specific humidity. The saturation specific humidity is expressed as a function of saturation water vapour pressure as

$$q_{\mathrm{sat}} = \frac{\frac{R_{\mathrm{dry}}}{R_{\mathrm{vap}}} e_{\mathrm{sat}}(T)}{p - \left(1 - \frac{R_{\mathrm{dry}}}{R_{\mathrm{vap}}}\right) e_{\mathrm{sat}}(T)} , \tag{6.4}$$

where the saturation water vapour pressure is expressed with the Teten's formula

$$e_{\mathrm{sat}}(T) = a_1 \exp\left\{ a_3 \left(\frac{T - T_0}{T - a_4} \right) \right\} , \tag{6.5}$$

where a_3 and a_4 are different depending on the sign of $(T - T_0)$ (i.e. water or ice phase with $T_0 = 273.16$ K)

6.1.1 (c) Mixed phase. In the scheme only one variable for condensed water species is used. The distinction between the water and ice phase is made as a function of temperature. The fraction of water in the total condensate is described as

$$\begin{aligned} \alpha &= 0 && T \le T_{\mathrm{ice}} , \\ \alpha &= \left(\frac{T - T_{\mathrm{ice}}}{T_0 - T_{\mathrm{ice}}} \right)^2 && T_{\mathrm{ice}} < T < T_0 , \\ \alpha &= 1 && T \ge T_0 . \end{aligned} \tag{6.6}$$

T_{ice} and T_0 represent the threshold temperatures between which a mixed phase is allowed to exist and are chosen as $T_{\mathrm{ice}} = 250.16$ K and $T_0 = 273.16$ K. The saturation thermodynamics are calculated according to the mixture of water and ice obtained with Eq. (6.6) so that the saturation specific humidity becomes

$$q_{\mathrm{sat}} = \alpha q_{\mathrm{sat(w)}} + (1 - \alpha) q_{\mathrm{sat(i)}} , \tag{6.7}$$

where $q_{\mathrm{sat(w)}}$ and $q_{\mathrm{sat(i)}}$ are the saturation specific humidities with respect to water and ice, respectively. The latent heat of phase changes is described as

$$L = \alpha L_{\mathrm{vap}} + (1 - \alpha) L_{\mathrm{subl}} . \tag{6.8}$$

6.1.2 Basic equations

With these definitions and the usual assumption that clouds encountered extend vertically over the whole model layer depth the equations for the time change of the grid-box averaged cloud water/ice content and the cloud fraction are obtained as

$$\frac{\partial l}{\partial t} = A(l) + S_{\text{conv}} + S_{\text{bl}} + S_{\text{strat}} - \mathcal{E}_{\text{cld}} - G_{\text{prec}} - \frac{1}{\rho}\frac{\partial}{\partial z}(\rho\overline{w'l'})_{\text{entr}} \tag{6.9}$$

and

$$\frac{\partial a}{\partial t} = A(a) + \delta a_{\text{conv}} + \delta a_{\text{bl}} + \delta a_{\text{strat}} - \delta a_{\text{evap}} \tag{6.10}$$

The terms on the right-hand side of Eq. (6.9) and Eq. (6.10) represent the following processes:

- $A(l)$, $A(a)$ — transport of cloud water/ice and cloud area through the boundaries of the grid volume
- S_{conv}, δa_{conv} — formation of cloud water/ice and cloud area by convective processes
- S_{bl}, δa_{bl} — formation of cloud water/ice and cloud area by boundary-layer turbulence
- S_{strat}, δa_{strat} — formation of cloud water/ice and cloud area by stratiform condensation processes
- $\mathcal{E}_{\text{cld}}$ — rate of evaporation of cloud water/ice
- G_{prec} — generation of precipitation from cloud water/ice
- $(1/\rho)\partial(\rho\overline{w'l'})_{\text{entr}}/\partial z$ — dissipation of cloud water/ice by cloud top entrainment
- δa_{evap} — rate of decrease of cloud area due to evaporation.

The large-scale budget equations for specific humidity q, and dry static energy $s = c_p T + gz$ after introduction of the scheme are modified to

$$\frac{\partial q}{\partial t} = A(q) - S_{\text{bl}} - S_{\text{strat}} + \mathcal{E}_{\text{cld}} + \mathcal{E}_{\text{prec}} - \frac{1}{\rho}\frac{\partial}{\partial z}(\rho\overline{w'q'})_{\text{entr}} \tag{6.11}$$

and

$$\begin{aligned}\frac{\partial s}{\partial t} = {} & A(s) + L(S_{\text{bl}} + S_{\text{strat}} - \mathcal{E}_{\text{cld}} - \mathcal{E}_{\text{prec}}) - L_{\text{fus}}\mathcal{M} - \frac{1}{\rho}\frac{\partial}{\partial z}(\rho\overline{w's'})_{\text{entr}} \\ & + c_p\{(1-a)\mathcal{R}_{\text{clear}} + a\mathcal{R}_{\text{cld}}\}\end{aligned} \tag{6.12}$$

where $A(q)$ and $A(s)$ represent all processes except those related to clouds and radiation. L_{fus} is the latent heat of freezing, $\mathcal{M}$ is the rate of snow-melt, $\mathcal{R}_{\text{clear}}$ and $\mathcal{R}_{\text{cld}}$ are the radiative heating rates in cloud-free and cloudy areas. The flux-divergence terms represent the effects of cloud top entrainment.

6.1.3 Definition of the source and sink terms

6.1.3 (a) Convection. Clouds formed by convective processes are parametrized by considering them to be condensates produced in cumulus updraughts and detrained into the environmental air. This approach, besides being part of the cloud parametrization, represents also an important extension of the model's cumulus parametrization. It is applied for all types of convection, namely deep, shallow and mid-level. The source of cloud water/ice content is

$$S_{\text{conv}} = \frac{D_{\text{up}}}{\rho}(l_{\text{up}} - l) + \frac{M_{up}}{\rho}\frac{\partial l}{\partial z} \tag{6.13}$$

and the source of cloud area is described as

$$\delta a_{\text{conv}} = (1-a)\frac{D_{\text{up}}}{\rho} + \frac{M_{up}}{\rho}\frac{\partial a}{\partial z}\,, \tag{6.14}$$

where D_{up} is the detrainment of mass from cumulus updraughts, l_{up} is the specific cloud water/ice content in cumulus updraughts and M_{up} is the updraught mass flux (see chapter 5). The factor $(1-a)$ in Eq. (6.14) appears because updraught air detrains simultaneously into cloud-free air as well as into already existing clouds.

6.1.3 (b) Boundary layer clouds. This part of the scheme considers stratocumulus clouds at the top of convective boundary layers. They are distinguished from shallow cumuli by making the assumption, that the cloud depth must not exceed one model-layer depth. All clouds deeper than one layer are represented as convective clouds by the cumulus convection scheme. The scheme follows the mass-flux approach, so that the cloud transport for moisture is written as

$$F_q = \rho\tilde{w}(q_{\text{up}} - q_{\text{down}})\,, \tag{6.15}$$

where q_{up} and q_{down} are updraught and downdraught specific humidity, respectively, and $\rho\tilde{w}$ $(= \rho a_{\text{up}} w_{\text{up}})$ is the cloud mass flux, w_{up} being the updraught velocity and a_{up} the fractional area of updraughts. Note that in contrast to convection, stratocumulus cloud circulations contain roughly equal ascending and descending branches. The cloud-base mass flux is determined by reformulating the moisture transport at cloud base produced by the boundary layer parametrization J_q (see Sections 3.3 and 3.4 of Chapter 3 'Turbulent diffusion and interactions with the surface') into the mass-flux concept so that

$$(\rho\hat{w})_{\text{base}} = \frac{J_q}{q_0 - \{a(q_{\text{sat}} + l_{\text{cld}})_{\text{top}} + (1-a)q_{\text{top}}\}}\,. \tag{6.16}$$

The subscripts '0' and 'top' refer to model levels near the surface and close to the cloud top (i.e. next level above cloud base), respectively, indicating that the updraughts start close to the surface and the downdraughts close to the cloud top. Above cloud base the assumption is made that $\tilde{w}$ decreases linearly to zero at cloud top. The net generation of cloud water/ice due to condensation in updraughts and evaporation in downdraughts then becomes

$$S_{\text{bl}} = -\frac{1}{\rho}\frac{\partial(\rho\tilde{w})}{\partial z}(l_{\text{up}} - a l_{\text{down}})\,, \tag{6.17}$$

and the source of cloud air in terms of cloud cover is

$$\delta a_{\text{bl}} = -\frac{1}{\rho}\frac{\partial(\rho\hat{w})}{\partial z}(1-a)\,. \tag{6.18}$$

6.1.3 (c) Formation of stratiform clouds. Here the formation of clouds by non-convective processes (e.g. large-scale lifting of moist air, radiative cooling etc.) is considered. The parametrization is based on the principle that condensation processes are determined by the rate at which the saturation specific humidity decreases. This rate is linked to vertical motions and diabatic cooling through

$$\frac{\mathrm{d}q_{\mathrm{sat}}}{\mathrm{d}t} = \left(\frac{\mathrm{d}q_{\mathrm{sat}}}{\mathrm{d}p}\right)_{\mathrm{ma}} (\overline{w} + gM_{\mathrm{Cu}}) + \left(\frac{\mathrm{d}q_{\mathrm{sat}}}{\mathrm{d}T}\right)\left(\frac{\mathrm{d}T}{\mathrm{d}t}\right)_{\mathrm{diab}}, \tag{6.19}$$

where $(\mathrm{d}q_{\mathrm{sat}}/\mathrm{d}p)_{\mathrm{ma}}$ is the change of q_{sat} along a moist adiabat through point (p, T), w is the area-mean generalized vertical velocity, gM_{Cu} is the cumulus-induced subsidence between the updraughts, and $(\mathrm{d}T/\mathrm{d}t)_{\mathrm{diab}}$ is the net temperature tendency due to radiative and turbulent processes. Two cases of condensation are distinguished

(a) in already existing clouds and

(b) the formation of new clouds

$$c_{\mathrm{cld}} = c_1 + c_2 \,. \tag{6.20}$$

Condensation in already existing clouds is described as

$$c_1 = -a\frac{\mathrm{d}q_{\mathrm{sat}}}{\mathrm{d}t} \qquad \frac{\mathrm{d}q_{\mathrm{sat}}}{\mathrm{d}t} < 0 \,. \tag{6.21}$$

New clouds are assumed to form, when the grid-averaged relative humidity exceeds a threshold value which is defined as a function of height as

$$\begin{aligned}
&\mathrm{RH}_{\mathrm{crit}} = \mathrm{RH}_{\mathrm{c}} + (1 - \mathrm{RH}_{\mathrm{c}})\left(\frac{\sigma - \sigma_1}{1 - \sigma_1}\right)^2 && \sigma_1 < \sigma \\
&\mathrm{RH}_{\mathrm{crit}} = \mathrm{RH}_{\mathrm{c}} && \sigma_{\mathrm{trop}} + (\Delta\sigma)_{\mathrm{d}} < \sigma < \sigma_{\mathrm{d}} \\
&\mathrm{RH}_{\mathrm{crit}} = \mathrm{RH}_{\mathrm{c}} + (1 - \mathrm{RH}_{\mathrm{c}})\left(\frac{\sigma_{\mathrm{trop}} + (\Delta\sigma)_{\mathrm{d}} - \sigma}{(\Delta\sigma)_{\mathrm{d}}}\right)^2 && \sigma_{\mathrm{trop}} < \sigma < \sigma_{\mathrm{trop}} + (\Delta\sigma)_{\mathrm{d}} \\
&\mathrm{RH}_{\mathrm{crit}} = 1 && \sigma < \sigma_{\mathrm{trop}}
\end{aligned} \tag{6.22}$$

where $\mathrm{RH}_{\mathrm{c}} = 0.8$, $\sigma = p/p_{\mathrm{surf}}$ with p being the pressure and p_{surf} the pressure at the surface, $\sigma_1 = 0.8$, σ_{trop} is the height of the tropopause in σ-coordinates and $(\Delta\sigma)_{\mathrm{d}} = 0.2$. The increase in cloud cover is determined by how much of the cloud-free area exceeds saturation in one time step which in turn depends on the moisture distribution in the cloud-free area and how fast saturation is approached. The moisture is assumed to be evenly distributed within the range $[\{q^{\mathrm{env}} - (q_{\mathrm{sat}} - q^{\mathrm{env}})\}, q_{\mathrm{sat}}]$ around the mean environmental value q^{env}, while the approach to saturation is determined by $\mathrm{d}q_{\mathrm{sat}}/\mathrm{d}t$. The increase in cloud cover then becomes

$$\delta a_{\mathrm{strat}} = \frac{-(1-a)}{(q_{\mathrm{sat}} - q^{env})}\frac{\mathrm{d}q_{\mathrm{sat}}}{\mathrm{d}t} \qquad \frac{\mathrm{d}q_{\mathrm{sat}}}{\mathrm{d}t} < 0 \,, \tag{6.23}$$

which can be expressed in terms of grid averages (using the definition $q = aq_{\mathrm{sat}} + (1-a)q^{\mathrm{env}}$) as

$$\delta a_{\mathrm{strat}} = -(1-a)^2\frac{1}{(q_{\mathrm{sat}} - q)}\frac{\mathrm{d}q_{\mathrm{sat}}}{\mathrm{d}t} \qquad \frac{\mathrm{d}q_{\mathrm{sat}}}{\mathrm{d}t} < 0 \,. \tag{6.24}$$

For the application of Eq. (6.24) at values of q close to saturation, the constraint $\delta a_{\mathrm{strat}} < (1-a)/\Delta t$ is imposed to ensure realistic values of a.

The generation of cloud water/ice in newly formed clouds is then

$$c_2 = -\frac{1}{2}\delta a_{\text{strat}}\frac{\mathrm{d}q_{\text{sat}}}{\mathrm{d}t} \qquad \frac{\mathrm{d}q_{\text{sat}}}{\mathrm{d}t} < 0\,, \tag{6.25}$$

where δa_{strat} is the fractional cloud cover produced in the time step by Eq. (6.24).

6.1.3 (d) Evaporation of cloud water/ice. The scheme describes evaporation of clouds by two processes in connection with large-scale and cumulus-induced descent and diabatic heating and by turbulent mixing of cloud air with unsaturated environmental air.

$$\mathcal{E}_{\text{cld}} = \mathcal{E}_1 + \mathcal{E}_2\,. \tag{6.26}$$

The first process is accounted for in the same way as stratiform cloud formation except that $\mathrm{d}q_{\text{sat}}/\mathrm{d}t > 0$. Hence

$$\mathcal{E}_1 = a\frac{\mathrm{d}q_{\text{sat}}}{\mathrm{d}t} \qquad \frac{\mathrm{d}q_{\text{sat}}}{\mathrm{d}t} > 0\,. \tag{6.27}$$

Assuming a homogeneous horizontal distribution of liquid water in the cloud, the cloud fraction remains unaltered by this process except at the final stage of dissipation where it reduces to zero.

$$\delta a_{\text{evap}} = \frac{a}{\Delta t} \qquad \text{if } l \to 0 \tag{6.28}$$

The parametrization of cloud dissipation as cloud air mixes with environmental air is described as a diffusion process proportional to the saturation deficit of the environmental air:

$$\mathcal{E}_2 = aK(q_{\text{sat}} - q)\,, \tag{6.29}$$

where the diffusion coefficient is

$$K = 2.10^{-6}\ \text{s}^{-1}\,. \tag{6.30}$$

The decrease in cloud cover is parametrized as

$$\delta a_{\text{evap}} = \frac{\mathcal{E}_2}{l_{\text{cld}}}\,, \tag{6.31}$$

where l_{cld} is the specific cloud water/ice content per cloud area as defined in Eq. (6.3). Note that because of Eq. (6.3) the parametrizations Eq. (6.29) and Eq. (6.31) imply a reduction in cloud area while l_{cld} remains unchanged.

6.1.3 (e) Cloud top entrainment. Fluxes of heat, moisture, cloud water/ice, and momentum through cloud top due to the cloud top entrainment process are described as

$$(\overline{w'\Phi'})_{\text{entr}} = -w_{\text{e}}\Delta\Phi\,, \tag{6.32}$$

where w_{e} is the entrainment velocity. Additionally Φ stands for the transported variables of s_{v} (the virtual dry static energy), total water (the sum of water vapour and cloud water) or the velocity fields, and Δ stands for the change of Φ between two model levels. The parametrization of cloud top entrainment is currently only used if the

level above a cloudy model level is entirely cloud free and if Δs_v is positive (stable layer). There are two parametrized contributions to the entrainment velocity

$$w_e = w_{e,1} + w_{e,2}. \tag{6.33}$$

(i) *Clouds at the top of convective boundary layers.* In the case of clouds at the top of convective boundary layers the parametrization of the entrainment velocity follows *Deardorff* (1976). The entrainment velocity is represented as

$$w_{e,1} = -\frac{(\overline{w's_v'})_H}{\Delta s_v}, \tag{6.34}$$

where

$$-(\overline{w's_v'})_H = \alpha\frac{1}{H}\int_0^H \overline{w's_v'}\,dz \tag{6.35}$$

is the average buoyancy flux in the mixed layer of height H and $\alpha = 0.5$.

(ii) *All cloud tops.* The second contribution to the entrainment velocity is parametrized as

$$w_{e,2} = \beta\frac{c_p\Delta\mathcal{F}_{LW}}{\Delta s_v}, \tag{6.36}$$

where $\Delta\mathcal{F}_{LW}$ is the longwave radiative flux divergence and $\beta = 0.5$.

Cloud water/ice transported into the cloud free layer above by entrainment is assumed to evaporate immediately until the layer becomes saturated, at which point the process is inhibited.

6.1.3 (f) Precipitation processes. Similar to radiation, precipitation processes are treated separately in clear and cloudy skies. This owes to the fact that the microphysical processes in these two regions are very distinct from each other, with conversion, collection and accretion processes being relevant in clouds whereas evaporation of precipitation is the relevant process outside clouds. Therefore the precipitation flux is written as

$$P = P^{cld} + P^{clr} \tag{6.37}$$

with

$$P^{cld} \equiv \frac{1}{A}\int P \cdot H(l)\,dA \tag{6.38}$$

and

$$P^{clr} \equiv \frac{1}{A}\int P \cdot (1 - H(l))\,dA \tag{6.39}$$

where the step function, $H(l)$, marks the portion of the grid-cell containing cloud with a condensate specific humidity $l > 0$ and A is the area of the grid-cell.

The precipitation fraction in the gridbox is then described as

$$a_P = a_P^{cld} + a_P^{clr} \tag{6.40}$$

with

$$a_P^{cld} \equiv \frac{1}{A}\int H(l)H(P)dA \tag{6.41}$$

and

$$a_P^{clr} \equiv \frac{1}{A}\int (1-H(l))H(P)dA\,. \tag{6.42}$$

Precipitation sources are represented differently for pure ice clouds and for mixed phase and pure water clouds.

$$G_{\text{prec}} = G_i + G_{mw} \tag{6.43}$$

The distinction is made as a function of temperature according to Eq. (6.6). The rain and snow formed is removed from the column immediately but can evaporate, melt and interact with the cloud water in the layers it passes through.

(i) *Pure ice clouds.* The precipitation process in ice clouds is treated separately for two classes of particles. The separation is made by size at a threshold of 100 μm. First the ice water content in particles smaller than 100 μm is determined following a parametrization proposed by McFarquhar and Heymsfield (1997) as

$$IWC_{<100} = \frac{1}{1000}\cdot min\left[IWC_{tot}, b_1\left(\frac{IWC_{tot}}{IWC_0}\right)^{b_2}\right], \tag{6.44}$$

where

$$IWC_{tot} = \frac{\rho l_{cld}}{1000} \tag{6.45}$$

is the total ice water content in g m^{-3}, IWC_0 is set to 1 g m^{-3}, b_1=0.252 g m^{-3} and b_2= 0.837. The The ice content in particles larger than 100 μm is then given by

$$IWC_{>100} = 1000\cdot IWC_{tot} - IWC_{<100} \tag{6.46}$$

The small ice particles $IWC_{<100}$ (now in kg m^{-3}) are given a small terminal fall speed of $w_{<100}^{ice} = 0.15$ ms^{-1} while large ice particles have a variable fall speed given by

$$w_{>100}^{ice} = c_1 IWC_{>100}^{c_2} \tag{6.47}$$

based on *.fHeymsfield and Donner* (1990). The constants currently chosen are c_1=2.3 and c_2=0.16. This relationship ensures that the mean ice fall speed increases with the grid mean ice water content, and asymptotes reasonably to a small non-zero fall speed as the ice mass tends towards zero.

1)

Given the fall speed and the separation by particle size the contribution to G_{prec} from pure ice clouds is

$$G_i = -\frac{1}{\rho}\frac{\partial}{\partial z}(w_{<100}^{ice} IWC_{<100} + w_{>100}^{ice} IWC_{>100}), \tag{6.48}$$

With the current explicit advection scheme that only allows transport to adjacent layers within one timestep it is not advisable to advect the cloud cover associated with ice sedimentation below cloud base, since the cloud boundary would subsequently advect at velocity determined by the CFL stability criterion. Thus, the ice sedimentation process does not affect the cloud cover and ice is only advected to the layer below in regions that are already cloudy. Ice settling into clear portions of the layer below (calculated according to the cloud overlap rules) is converted directly into snow which falls out the column within one timestep (see Subsection 6.2.3). This removal of snow implies a larger effect mean fall speed of ice, which is why the fall speed relationship for large ice particles uses a tuning constant that is reduced relative to the observations of *Heymsfield and Donner* (1990). Note that the minus sign in the first term of the right hand side of (6.48) appears since the fall velocity of ice is assumed to be positive downwards.

(ii) *Mixed phase and pure water clouds*. For mixed phase and pure water clouds a parametrization following *Sundqvist* (1978) is used. The generation of precipitation is written as

$$G_{mw} = a c_0 l_{\text{cld}} \left[1 - \exp\left\{-\left(\frac{l_{\text{cld}}}{l_{\text{crit}}}\right)^2\right\}\right] \tag{6.49}$$

where c_0^{-1} represents a characteristic time scale for conversion of cloud droplets into drops and l_{crit} is a typical cloud water content at which the release of precipitation begins to be efficient. These disposable parameters are adjusted as follows

$$c_0 = c_0^* F_1 F_2 \tag{6.50}$$

and

$$l_{\text{crit}} = \frac{l_{\text{crit}}^*}{F_1 F_2} \tag{6.51}$$

to take into account the effect of collection of cloud droplets by raindrops falling through the cloud (F_1) and the Bergeron–Findeisen mechanism (F_2). Here F_1 and F_2 are defined as

$$F_1 = 1 + b_1\sqrt{P_{\rm loc}} \tag{6.52}$$

and

$$F_2 = 1 + b_2\sqrt{(T_{\rm BF} - T)} \qquad \text{if } T_{\rm ice} < T < T_{\rm BF} \tag{6.53}$$

where $P_{\rm loc}$ is the local cloudy precipitation rate ($P_{\rm loc} = P^{cld}/a_P^{cld}$) and $T_{\rm BF}$ is the temperature at which the Bergeron–Findeisen mechanism starts to enhance the precipitation. The values for the constants are those used by *Sundqvist* (1978), namely $T_{\rm BF} = 268$ K, $b_1 = 100$, $b_2 = 0.5$, $c_0^* = 10^{-4}\,{\rm s}^{-1}$, and $l_{\rm crit}^* = 0.3$ g kg^{-1}.

(iii) *Evaporation of precipitation.* The parametrization of rain and snow evaporation is uncertain. A scheme following *Kessler* (1969) is used. It describes the evaporation rate as

$$\mathcal{E}_{\rm prec} = \{a_P^{clr} \times 5.44\times10^{-4}\}(q_{\rm sat} - q) \times \left\{\left(\frac{p}{p_0}\right)^{1/2} \frac{1}{5.9\times10^{-3}} \frac{P^{clr}}{a_P^{clr}}\right\}^{0.577} \tag{6.54}$$

where a_P^{clr} is the clear-sky precipitation fraction. Evaporation of rain/snow only takes place when the grid mean relative humidity is below a threshold value. The choice of the threshold value is not straightforward for numerical reasons. Here, the assumption is made that the clear-sky relative humidity (= grid mean relative humidity in the absence of clouds) that can be reached by evaporation of precipitation is a function of the fractional coverage with precipitation of the clear sky part of the grid-box. Hence, the threshold value is parametrized as

$$RH_{crit,E_P} = 0.7 + 0.3\frac{a_P^{clr}}{1 - a}. \tag{6.55}$$

(iv) *Melting of snow.* The melting of snow is parametrized by allowing the part of the grid box that contains precipitation to cool to $T_{\rm melt}$ over a time scale τ, i.e.,

$$\mathcal{M} = (a_P^{cld} + a_P^{clr})\frac{c_p}{L_{\rm fus}} \frac{T - T_{\rm melt}}{\tau}, \tag{6.56}$$

where $T_{\rm melt} = 0°C$ and

$$\tau = \frac{5h}{1 + 0.5(T - T_{\rm melt})}.$$

6.2 NUMERICS

6.2.1 Integration of the equations for cloud water/ice and cloud cover

As cloud processes are rapidly varying in time, care must be taken when Eq. (6.9) and Eq. (6.10) are integrated over the relatively large model time steps. Therefore terms that depend linearly on a and l are integrated analytically. Eq. (6.9) and Eq. (6.10) can be written as

$$\frac{\partial l}{\partial t} = C - Dl \tag{6.57}$$

where C is defined by Eq. (6.13), Eq. (6.17), Eq. (6.21), Eq. (6.25), Eq. (6.27) and Eq. (6.29) and D is defined by Eq. (6.48) or Eq. (6.49) respectively, and

$$\frac{\partial a}{\partial t} = (1-a)A - aB + C_a \tag{6.58}$$

with A , B , and C_a defined by Eq. (6.14), Eq. (6.18), Eq. (6.24), Eq. (6.28) and Eq. (6.31). Analytical integration of Eq. (6.57) and Eq. (6.58) yields

$$a(t+\Delta t) = a(t)\exp\{-(A+B)\Delta t\} + \frac{A+C_a}{A+B}[1-\exp\{-(A+B)\Delta t\}] \tag{6.59}$$

and

$$l(t+\Delta t) = l(t)\exp(-D\Delta t) + \frac{C}{D}\{1-\exp(-D\Delta t)\} \tag{6.60}$$

Both the cloud water and cloud cover equations (Eq. (6.59) and Eq. (6.60)) use identical profiles of temperature, humidity and cloud quantities to calculate every individual source and sink term. These are "first-guess" profiles: beginning of timestep values that have been subsequently modified to take into account the tendencies due to physics parametrizations such as deep and shallow convection, radiation and vertical diffusion processes. The fact that all processes considered by the cloud scheme use identical profiles implies these processes are assumed to act concurrently. An additional cosmetic benefit is that this approach allows a far greater modulisation of the code, significantly facilitating its legibility.

Fast processes are considered implicitly. Further details are provided below, but briefly, the processes that are now treated implicitly for cloud cover are:

- convective detrainment
- generation by cooling
- generation at the top of stratocumulus layers
- destruction by turbulent mixing

For the cloud water the implicit processes are:

- advection by convective subsidence
- generation/destruction by cooling/warming
- cloud top entrainment
- sedimentation of ice
- warm and mixed phase precipitation generation

The choice of numerical treatment is often based on pragmatism, and no perfect solution exists for a model such as the IFS using high vertical resolution with relatively long timesteps. Since some terms in Eq. (6.59) and Eq. (6.60) are treated explicitly, there is nothing to prevent values of cloud water or cloud cover from "overshooting" during one timestep, in other words that unphysical values may result. Previously, these were handled by simply clipping the final tendencies for each layer to maintain the cloud variables within physically reasonable limits. However, this approach can lead to significant conservation errors. For example, if ice sedimentation combined with other linear sink terms reduces the IWC below zero over a time step, and the final combined tendency is sub-

sequently clipped to correct this, the ice sedimentation source term for layer below has to take this into account to prevent an artificial net creation of total water. The present treatment therefore calculates the precise point during the timestep at which the cloud water or cover reaches zero (or additionally one in the case of cloud cover) and then limits the source and sink terms to equal precisely the advect transport terms for the remainder of the timestep. This approach ensures conservation of total water, and gives an effective balance between linear and nonlinear terms (i.e. no processes are given priority).

6.2.2 Calculation of $\mathrm{d}q_{\mathrm{sat}}/\mathrm{d}t$

Special care has to be taken in the numerical calculation of $\mathrm{d}q_{\mathrm{sat}}/\mathrm{d}t$ from Eq. (6.19). Since the saturation water vapour pressure depends exponentially on temperature, straightforward numerical integration of Eq. (6.19) would produce large truncation errors. Therefore the average of $\mathrm{d}q_{\mathrm{sat}}/\mathrm{d}t$ over the time step is determined by the means of moist adjustment (e.g. *Haltiner and Williams* 1980). This is achieved by first extrapolating the cloud temperature to time-level $t + \Delta t$ and then adjust temperature and moisture toward saturation conditions.

6.2.3 Convective cloud source

The vertical discretization of equations (6.13) and (6.14) is achieved with a simple upstream scheme, i.e.,

$$S_{\mathrm{conv}} = \frac{D_{\mathrm{up,k}}}{\rho_k}(l_{\mathrm{up,k+1/2}} - l_k) - gM_{up,\,k-1/2}\frac{l_{k-1} - l_k}{p_{k-1} - p_k} \tag{6.61}$$

and

$$\delta a_{\mathrm{conv}} = \frac{D_{\mathrm{up,k}}}{\rho_k}(1 - a_k) - gM_{up,\,k-1/2}\frac{a_{k-1} - a_k}{p_{k-1} - p_k}\ . \tag{6.62}$$

Although two of the terms in equation (6.62) depend linearly on l_k it was decided to treat the convective source (like any other source of condensate) fully explicitly, i.e., (6.62) is added into (6.57) as a contribution to C_k only. For cloud fraction it is obvious that the first term on the right hand side of (6.63) can be added to A_k in equation (6.58) whereas the second term can be split into a contribution to B_k and $C_{a,k}$.

6.2.4 Stratiform cloud source

It is evident from (6.24) that the stratiform source of cloud cover is quadratically dependent on $(1-a)$ and can therefore not easily be integrated analytically following (6.58). To overcome this problem one factor of $(1-a)$ is integrated into A_k, i.e., treated explicitly, before carrying out the analytic integration of (6.58), i.e.,

$$A_{k,strat} = \frac{1 - a_k}{(q_{\mathrm{sat},k} - q_k)}\left(\frac{\mathrm{d}q_{\mathrm{sat}}}{\mathrm{d}t}\right)_k . \tag{6.63}$$

6.2.5 Precipitation fractions

The method to determine a_P^{cld} and a_P^{clr} is as follows. If precipitation is generated in a level through the processes of autoconversion or ice sedimentation, it is assumed to be generated at all portions of the cloud uniformly and thus at the base of level *k*, $a_{P,k}^{cld} = a_k$. The precipitation generated in this cloudy region is given by:

$$\Delta P_k^{cld} \equiv \frac{1}{A}\int\left(\frac{1}{g}\int_{p_{k-1/2}}^{p_{k+1/2}} G_{prec}\cdot H(l)dp'\right)dA \ , \tag{6.64}$$

and the cloudy precipitation flux at the base of level *k* is given by $P_k^{cld} = \tilde{P}_k^{cld} + \Delta P_k^{cld}$, where the twiddle symbol indicates the value of P^{cld} at the top of level *k*. Because the cloud is assumed to be internally homogenous, (6.64) simplifies to $a_k G_{prec}(p_{k+1/2} - p_{k-1/2})/g$, where S_p^{cld} is the generation rate of precipitation inside the cloud. If only accretion occurs in the clouds of level *k*, $a_{P,k}^{cld}$ equals $\tilde{a}_{P,k}^{cld}$, the fractional area that contains cloudy precipitation flux at the top of level *k*.

Because the clear precipitation flux is assumed to be horizontally uniform, evaporation does not alter the area containing clear precipitation flux such that $a_{P,k}^{clr} = \tilde{a}_{P,k}^{clr}$. Only in the case that all of the clear precipitation flux evaporates in level *k* does $a_{P,k}^{clr} = 0$. The clear-sky precipitation flux at the base of level *k* is given by $P_k^{clr} = \tilde{P}_k^{clr} + \Delta P_k^{clr}$, where $\tilde{P}_k^{clr}$ is the clear-sky precipitation flux at the top of level *k*, and

$$\Delta P_k^{clr} = \frac{1}{A}\int\left(\frac{1}{g}\int_{p_{k-1/2}}^{p_{k+1/2}} E_{prec}\cdot(1-H(l))dp'\right)dA = \tilde{a}_{P,k}^{clr} E_{prec}(p_{k+1/2} - p_{k-1/2})/g \ , \tag{6.65}$$

where E_{prec} represents precipitation evaporation. Note that precipitation evaporation is a function of $\tilde{P}_k^{clr}$ guaranteeing that precipitation generated in a level cannot evaporate in the same level. This will guarantee consistency with the assumption that clouds where present fill the vertical extent of the grid cell and that horizontal transfer of precipitation mass from cloudy to clear regions of the grid cell is not possible.

At the interfaces between levels, precipitation mass that is in cloud of the upper level may fall into clear air of the lower level, or precipitation mass that is in clear air of the upper level may fall into cloud of the lower level. Thus at level interfaces an algorithm is needed to transfer precipitation and its area between the cloudy and clear portions of the grid box. The algorithm is constructed by determining the amount of area associated with each transfer and then transferring precipitation fluxes between clear and cloudy components according to the assumption that the precipitation flux is horizontally uniform but with different values in the clear and cloudy regions containing precipitation.

There are four possible areas to be defined (see schematic in Figure ??): the area in which cloudy precipitation flux falls into cloud of the lower level, the area in which cloudy precipitation flux falls into clear air of the lower level, the area in which clear precipitation flux falls into clear air of the lower level, and the area in which clear precipitation flux falls into cloud of the lower level. To determine these areas, the cloud overlap assumption is applied to determine the relative horizontal placements of clouds in the upper and lower levels. For the ECMWF model, the cloud overlap assumption is expressed in terms of an equation which relates the total horizontal area *C* covered by clouds in levels 1 to *k* (where *k* = 1 is the top level of the model), to the total horizontal area cover by clouds in levels 1 to *k*-1:

$$(1 - C_k) = (1 - C_{k-1})\cdot\frac{1 - max(a_k, a_{k-1})}{1 - min(a_{k-1}, 1-\delta)}, \tag{6.66}$$

where δ is a tiny number set to 10^{-6}. Equation (6.66) gives maximum overlap for clouds in adjacent levels and random overlap for clouds separated by clear levels. From this equation, one can determine the portion of clouds of the lower level which is not overlapped by clouds at all higher levels; this area, $\Delta C = C_k - C_{k-1}$, cannot have any precipitation falling into it. Using this assumption, the area for which cloudy precipitation flux falls into clear air of the level below is given by:

$$\Delta a_{cld \to clr} = a^{cld}_{P,k-1} - min(a_k - \Delta C, a^{cld}_{P,k-1}) \,. \tag{6.67}$$

Equation (6.67) makes the further assumption that there is maximum overlap between the area covered by cloudy precipitation at the base of the upper level and the portion of the lower level cloud which lies beneath clouds in higher levels, $a_k - \Delta C$. With the assumption that the precipitation flux is horizontally uniform, the amount of cloudy precipitation flux of the upper level that falls into clear air of the level below is:

$$\Delta P_{cld \to clr} = \frac{\Delta a_{cld \to clr}}{a^{cld}_{P,k-1}} \cdot P^{cld}_{k-1} \,. \tag{6.68}$$

The area in which clear precipitation flux of the upper level falls into cloud of the level below is:

$$\Delta a_{clr \to cld} = max(0., min(a^{clr}_{P,k-1}, a_k - \Delta C - a_{k-1})) \,, \tag{6.69}$$

which assumes maximum overlap between the portion of the cloud in the lower level *k* which has cloud at some higher level other than *k*-1, and the area covered by the clear precipitation flux. Again, with the assumption that the precipitation flux is horizontally uniform, the amount of clear precipitation flux of the upper level that falls into cloud of the level below is:

$$\Delta P_{clr \to cld} = \frac{\Delta a_{clr \to cld}}{a^{clr}_{P,k-1}} \cdot P^{clr}_{k-1} \,. \tag{6.70}$$

Finally, the areas and fluxes at the top of level *k* can be related to those at the base of level *k*-1 by:

$$\tilde{a}^{cld}_{P,k} = a^{cld}_{P,k-1} + \Delta a_{clr \to cld} - \Delta a_{cld \to clr} \,, \tag{6.71}$$

$$\tilde{a}^{clr}_{P,k} = a^{clr}_{P,k-1} - \Delta a_{clr \to cld} + \Delta a_{cld \to clr} \,, \tag{6.72}$$

$$\tilde{P}^{cld}_{k} = P^{cld}_{k-1} + \Delta P_{clr \to cld} - \Delta P_{cld \to clr} \,, \tag{6.73}$$

$$\tilde{P}^{clr}_{k} = P^{clr}_{k-1} - \Delta P_{clr \to cld} + \Delta P_{cld \to clr} \,. \tag{6.74}$$

From these equations it is obvious that total precipitation area, $a^{cld}_P + a^{clr}_P$, and precipitation flux, $P^{cld} + P^{clr}$, are conserved at level interfaces.

6.2.6 Precipitation sources

After the integration of Eq. (6.60) the fallout of condensate (represented by the term Dl in Eq. (6.57)) out of model level k is determined as

$$G_{\text{fallout},k} = \frac{l_k(t) - l_k(t + \Delta t)}{\Delta t} + C_k \,. \tag{6.75}$$

The condensate falling out of model level k is then distributed into rain, snow or cloud ice in the level below using

the following assumptions:

(i) *Pure water clouds.* In the case of pure water clouds ($T_k \geq T_0$) all condensate falling out of a model level is converted into rain, i.e.,

$$G_{\text{rain},k} = G_{\text{fallout},k} \quad . \tag{6.76}$$

(ii) *Mixed phase clouds.* In the case of mixed phase clouds ($T_{\text{ice}} < T_k < T_0$) all condensate falling out of a model level is converted into rain or snow whereby the partitioning between the two phases is determined using Eq. (6.6), i.e.,

$$G_{\text{rain},k} = \alpha_k G_{\text{fallout},k} \tag{6.77}$$

and

$$G_{\text{snow},k} = (1-\alpha_k) G_{\text{fallout},k} \, . \tag{6.78}$$

(iii) *Pure ice clouds.* In the case of pure ice clouds ($T_k \leq T_{\text{ice}}$) the condensate falling out of a model level is partitioned into a source of cloud ice in the level below and snow. As stated above ice falling into clear sky is converted into snow, while ice in falling into cloud remains cloud ice. The cloud mask remains unaffected by this process. This is implemented in the code as follows. First (6.44) is solved to determine the ice water content in particles smaller than 100 μm. Then (6.60) is solved for layer k using the mass weighted fallspeed:

$$D_k = -g \frac{\rho_k (\alpha_{<100} w^{ice}_{<100,\,k} + (1-\alpha_{<100}) w^{ice}_{>100,\,k})}{p_{k-\frac{1}{2}} - p_{k+\frac{1}{2}}} , \tag{6.79}$$

where

$$\alpha_{<100,\text{k}} = \frac{IWC_{<100,\text{k}}}{IWC_{tot,\,k}} . \tag{6.80}$$

Of the ice water content falling into layer k the part falling into overlapping cloud area is treated as source of cloud ice. The area of cloud overlap is determined as

$$a_{ovlp,\,k} = min(a_k - \Delta C, a_{k-1}) , \tag{6.81}$$

where ΔC is the change of total cloud cover from layer $k-1$ to layer k as described above.

6.2.7 Evaporation of precipitation

Since the evaporation of precipitation has a threshold value of relative humidity at which the process should cease to exist (see equation (6.55)) an implicit treatment is applied when solving (6.54). If (6.54) is written as

$$\frac{\partial q}{\partial t} = \beta (q_s - q), \tag{6.82}$$

the implicit solution becomes

$$\Delta q = \frac{\beta \Delta t (q_s^n - q^n)}{1 + \beta \Delta t \left[1 + \frac{L}{c_p} \left(\frac{dq_s}{dT} \right)^n \right]}, \tag{6.83}$$

where n refers to the time level at the beginning of timestep Δt. (6.88) ensures that evaporation of precipitation never leads to $q^{n+1} > q_s^{n+1}$. To ensure the maximum relative humidity after evaporation does not exceed the threshold value defined in (6.55) the maximum change in specific humidity is calculated as

$$(\Delta q)_{max} = \frac{RH_{crit,E_P} \cdot q_s^n - q^n}{1 + RH_{crit,E_P} \frac{L}{c_p} \left(\frac{dq_s}{dT} \right)^n}. \tag{6.84}$$

The smaller of the values given by (6.88) and (6.89) is then chosen as the true value of evaporation of precipitation.

6.2.8 Cloud top entrainment

After parametrizing the entrainment flux as in Eq. (6.32) and the entrainment velocity as in Eq. (6.33) the tendency equations for the two levels involved in the entrainment process are solved simultaneously using an implicit formulation.

The tendency equation for the cloudy model level, k, can be written as

$$\left(\frac{\partial \Phi}{\partial t} \right)_k = g \frac{F_{\Phi, k-\frac{1}{2}} - F_{\Phi, k+\frac{1}{2}}}{p_{k-\frac{1}{2}} - p_{k+\frac{1}{2}}}, \tag{6.85}$$

where $F_{\Phi, k-1/2}$ is the flux of Φ taken at half-level $k-1/2$. A similar equation can be written for the level immediately above the cloud, $k-1$. Since only the transport between levels k and $k-1$ are considered only the flux at half level $k-1/2$ is non-zero. The solution for Φ at both model levels for time $n+1$ given the values at time n can then be found by solving the system of two linear equations

$$\Phi_k^{n+1} - \Phi_k^n = -g \Delta t \frac{w_e (\Phi_{k-1}^{n+1} - \Phi_k^{n+1})}{p_{k-\frac{1}{2}} - p_{k+\frac{1}{2}}} \tag{6.86}$$

and

$$\Phi_{k-1}^{n+1} - \Phi_{k-1}^n = g \Delta t \frac{w_e (\Phi_{k-1}^{n+1} - \Phi_k^{n+1})}{p_{k-\frac{3}{2}} - p_{k-\frac{1}{2}}}. \tag{6.87}$$

In order to keep the mixing of the various quantities self-consistent, the following procedure is now employed. Equation (6.87) is first solved for the total water (sum of vapour and cloud water). An implicit limit is applied such that the mixing tendency asymptotes to zero as the clear sky layer above the cloud deck approaches saturation. The resulting tendency is then converted into a implicit sink term for equation (6.60) by dividing the tendency by the initial cloud water at time n:

$$D_{entr} = \frac{q_k^{n+1} + l_k^{n+1} - q_k^n + l_k^n}{l_k^n}. \tag{6.88}$$

This modified treatment ensures that the cloud top entrainment processes is given the same priority as the other source and sink terms. Moreover, by including it in the cloud water equation, the sink term also correctly asymptotes to zero as the cloud water in uppermost cloud layer reduces to zero. Thus the present cloud top mixing treatment has realistic and numerically robust behaviour for both limits: saturation above cloud top or destruction of cloud water at the cloud top. Note that, like ice sedimentation and convective subsidence processes, cloud top entrainment is also effectively an advective term, and must also be handled in a manner than guarantees conservation of total water. When equation (6.60) has been solved, and the limiters for overshoots have been applied, the "final" effective entrainment velocity w_e over the timestep is obtained by inverting equation (6.86), using the final tendency of cloud water and the mid time step total water inversion strength

$$w_e^{final} = \frac{p_{k-\frac{1}{2}} - p_{k+\frac{1}{2}}}{g((l+q)_{k-1}^{n+0.5} - (l+q)_k^{n+0.5})} \frac{(l_{entr}^{n+1} - l_{entr}^n)}{\Delta t} \tag{6.89}$$

The mixing of the virtual dry static energy, and the horizontal velocity components is then calculated implicitly using equations (6.86) and (6.87), inserting this "final" value of the entrainment velocity that is consistent with the cloud water history.

6.2.9 Final moist adjustment

In the case where semi-Lagrangian advection is not used, a final test for supersaturation is performed after the calculation of the liquid water/ice tendency and the corresponding tendencies of temperature and moisture. If any supersaturation is found the grid box is re-adjusted to saturation (using the moist adjustment formulation) and the moisture excess is converted into precipitation. When the semi-Lagrangian advection scheme is utilized however, this final supersaturation check is performed by a separate routine that is applied on the effective profiles of temperature and humidity after all physical and explicit dynamical contributions have been computed. See Section 3.10 of Chapter 3 "Semi-Lagrangian formulation" for a more detailed description of the applied saturation check. Note, that small amounts of non-physical supersaturation due to numerical approximations may remain in the postprocessed fields.

6.3 CODE

The parametrization of cloud and large-scale precipitation processes is performed in the following routines:

CLDPP

This routine prepares the cloud variables for radiation calculations and calculates total, high, mid-level and low cloud cover for postprocessing. These are obtained using the maximum-random overlap assumption over the relevant vertical atmospheric slab. In sigma coordinates these slabs are defined as follows,

Low clouds: $P > 0.8P_s$

Medium clouds: $0.45P_s \le P \le 0.8P_s$

High clouds: $P < 0.45P_s$

CLOUDSC

This routine carries out all calculations necessary to solve Eq. (6.9) and Eq. (6.10). As stated above, recent developments in the numerical treatment has allowed the code to be greatly modularized. The calculations are carried out in the following order:

Section 1: Calculate initial input profiles

Section 2: Setup

- initial setup including calculation of
  - q_{sat}
  - tropopause height for Eq. (6.22)
  - mixed layer buoyancy integral as defined in Eq. (6.35)

Section 3: Sources and sinks

- convective source terms including freezing if different mixed phase assumptions are used for convection and large-scale processes (Eq. (6.13) and Eq. (6.14))
- entrainment velocity due to longwave cooling (Eq. (6.36))
- generation of clouds at top of convective boundary layer (Eq. (6.17) and Eq. (6.18))
- erosion of clouds by turbulent mixing (Eq. (6.29) and Eq. (6.31))
- calculation of $\mathrm{d}q_{\mathrm{sat}}/\mathrm{d}t$ (see section 6.2.2)
- large-scale evaporation (Eq. (6.27))
- large-scale cloud formation (Eq. (6.21), Eq. (6.24), and Eq. (6.25))

Section 4: Precipitation generation

- precipitation overlap
- ice sedimentation
- warm rain and mixed phased processes

Section 5: Solvers for cloud cover and water

- analytical integration of the equation for a (Eq. (6.59))
- analytical integration of the equation for l (Eq. (6.60))
- apply limiters calculation modified cloud advection processes

Section 6: Solver-dependent physics

- mixing due to cloud-top entrainment of static energy and horizontal winds
- melting of snow (Eq. (6.56))
- evaporation of precipitation (Eq. (6.54))

Section 7: Update tendencies

- final tendency calculations of all thermodynamic quantities

Sections 8: Flux calculations for diagnostics

APPENDIX A LIST OF SYMBOLS

$A(\ )$	advective transport through the boundaries of the grid box
a	fraction of grid box covered by clouds
a_{prec}	fraction of grid box covered by precipitation

$a_{\rm up}$	fractional area of updraughts
$c_{\rm cld}$	condensation rate
c_p	specific heat at constant pressure
$D_{\rm up}$	detrainment in the cumulus updraughts
$\mathcal{E}_{\rm cld}$	rate of evaporation of cloud water/ice
$\mathcal{E}_{\rm prec}$	rate of evaporation of precipitation
$e_{\rm sat}$	saturation water vapour
$\mathcal{F}_{\rm LW}$	longwave radiative flux divergence
F_q	moisture transport by clouds
g	acceleration of gravity
$G_{\rm fallout}$	generation of precipitation that falls out from one level to another
$G_{\rm prec}$	generation of precipitation from cloud water/ice
$G_{\rm rain}$	generation of precipitation in the form of rain
$G_{\rm snow}$	generation of precipitation in the form of snow
H	mixed-layer height
J_q	surface humidity flux
K	diffusion coefficient
L	latent heat
$L_{\rm fus}$	latent heat of fusion
$L_{\rm subl}$	latent heat of sublimation
$L_{\rm vap}$	latent heat of vaporization
l	grid-mean specific cloud liquid-water and ice content
$l_{\rm cld}$	specific cloud water content per cloud area
$l_{\rm down}$	specific cloud water/ice content in the cumulus downdraughts
$l_{\rm up}$	specific cloud water/ice content in the cumulus updraughts
$\mathcal{M}$	rate of snowment
$M_{\rm Cu}$	cumulus-induced subsidence mass flux
P	precipitation rate
$P_{\rm loc}$	local precipitation rate
p	pressure
$q^{\rm env}$	environmental specific humidity
$q_{\rm down}$	specific humidity in the convective downdraughts
$q_{\rm sat}$	saturation specific humidity
$q_{\rm sat(i)}$	saturation specific humidity with respect to ice
$q_{\rm sat(w)}$	saturation specific humidity with respect to water
$q_{\rm up}$	specific humidity in the convective updraughts
$\mathcal{R}_{\rm cld}$	radiative heating rate in cloudy air
$\mathcal{R}_{\rm clear}$	radiative heating rate in cloud-free air
$R_{\rm dry}$	gas constant for dry air
$R_{\rm vap}$	gas constant for water vapour
$\rm RH_c$	= 0.8
$\rm RH_{crit}$	threshold value of the relative humidity
$S_{\rm conv}$	formation of cloud water/ice by convective processes
$S_{\rm strat}$	formation of cloud water/ice by stratiform condensation processes
$S_{\rm bl}$	formation of cloud water/ice by boundary-layer processes
s	dry static energy
$s_{\rm v}$	virtual dry static energy

T	temperature
T_0	= 273.16 K
T_{BF}	= 268 K temperature at which the Bergeron–Findeison enhances the precipitation
T_{ice}	= 250.16 K
T_{melt}	= 0°C
$\overline{w}$	area-mean generalized vertical velocity
$\hat{w}$	$\rho\hat{w} = \rho a_{up} w_{up}$ is the cloud mass flux
w_e	entrainment velocity
w_{ice}	terminal fall speed of ice particles
w_{up}	updraught velocity
α	fraction of condensate held as liquid water
δa_{bl}	rate of increase of cloud area by boundary-layer processes
δa_{conv}	rate of increase of cloud area by convective processes
δa_{strat}	rate of increase of cloud area by stratiform condensation processes
δa_{evap}	rate of decrease of cloud area due to evaporation
ρ	density of moist air
ρ_w	density of cloud water

Part IV: PHYSICAL PROCESSES

CHAPTER 7 Surface parametrization

Table of contents

7.1 INTRODUCTION

The parametrization scheme described in this chapter represents the surface fluxes of energy and water and, where appropriate, corresponding sub-surface quantities. Fig. 7.1 summarizes the main features of the land part of the model; hereafter the scheme will be referred to as the TESSEL (Tiled ECMWF Scheme for Surface Exchanges over Land) scheme. At the interface between the surface and the atmosphere, each grid-box is divided into fractions (tiles), with up to 6 fractions over land (bare ground, low and high vegetation, intercepted water, shaded and ex-

posed snow) and up to 2 fractions over sea and freshwater bodies (open and frozen water). Each fraction has its own properties defining separate heat and water fluxes used in an energy balance equation solved for the tile skin temperature. Special attention is devoted to the different physical mechanisms limiting evaporation of bare ground and vegetated surfaces.

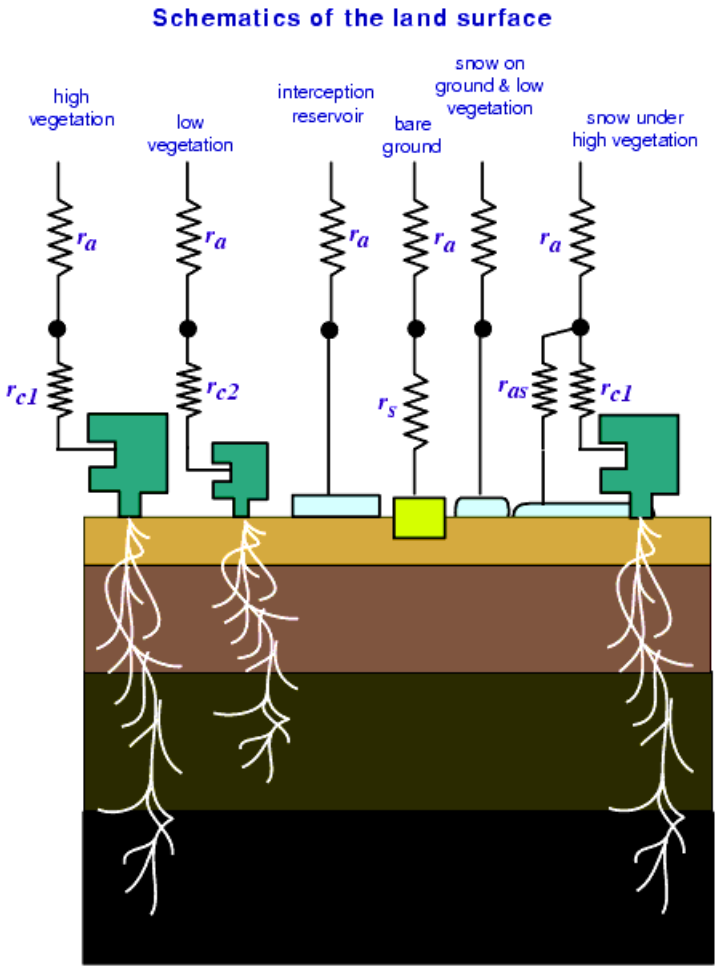

Figure 7.1 Schematic representation of the structure of TESSEL land-surface scheme

Over land, the skin temperature is in thermal contact with a four-layer soil or, if there is snow present, a single layersnow mantle overlying the soil. The snow temperature varies due to the combined effect of top energy fluxes, basal heat flux and the melt energy. The soil heat budget follows a Fourier diffusion law, modified to take into account the thermal effects of soil water phase changes. The energy equation is solved with a net ground heat flux as the top boundary condition and a zero-flux at the bottom.

Snowfall is collected in the snow mantle, which in turn is depleted by snowmelt, contributing to surface runoff and soil infiltration, and evaporation. A fraction of the rainfall is collected by an interception layer, where the remaining fraction (throughfall) is partitioned between surface runoff and infiltration. Subsurface water fluxes are determined by Darcy's law, used in a soil water equation solved with a four-layer discretization shared with the heat budget equation. Top boundary condition is infiltration plus surface evaporation, free drainage is assumed at the bottom; each layer has an additional sink of water in the form of root extraction over vegetated areas.

Finally, open water points have a fixed surface temperature. When present, frozen water occupies a fraction of the

grid box, with a prognostic ice temperature evolving in the forecast following the heat budget of a four-layer ice model in thermal contact with an underlying ocean at freezing temperature.

7.2 TILES AND SURFACE FLUXES

7.2.1 Tile and vegetation characteristics

Grid-box surface fluxes are calculated separately for the different subgrid surface fractions (or "tiles"), leading to a separate solution of the surface energy balance equation and skin temperature for each of these tiles. This is an analogue of the "mosaic" approach of *Koster and Suarez* (1992). Note that the tiles at the interface soil–atmosphere are in energy and hydrological contact with one single atmospheric profile above and one single soil profile below. Each grid box is divided into 8 fractions: two vegetated fractions (high and low vegetation without snow), one bare soil fraction, three snow/ice fractions (snow on bare ground/low vegetation, high vegetation with snow beneath, and sea-ice, respectively), and two water fractions (interception reservoir, ocean/lakes). The tile for "high vegetation with snow beneath" is a combined tile with a separate energy balance and evaporation model for the high vegetaton and the underlying snow. A mixture of land and water (ocean/inland water) tiles is not allowed, i.e. a grid box is either 100% land or 100% sea.

In each grid box two vegetation types are present: a high and a low vegetation type. An external climate database, based on the Global Land Cover Characteristics (GLCC) data that has been derived using one year of Advanced Very High Resolution Radiometer (AVHRR) data and ancillary information (*Loveland et al.* 2000; http://edcdaac.usgs.gov/glcc/glcc.html; see also Chapter 10). The nominal resolution is 1 km. The data used provides for each pixel a biome classification based on the Biosphere–Atmosphere Transfer Scheme (BATS) model (Dickinson *et al.* 1993), and four parameters have been derived for each grid box: dominant vegetation type, T_H and T_L, and the area fraction, A_H and A_L, for each of the high- and low-vegetation components, respectively.

The coverage C_i for the tile i depends on the type and relative area of low and high vegetation, and the presence of snow and intercepted water. In the absence of snow and interception, the vegetation coverage of high (c_H) and low (c_L) vegetation are calculated as $A_H c_{veg}(T_H)$ and $A_L c_{veg}(T_L)$, respectively, with c_{veg} a vegetation type dependent coverage (see Table 7.1). The bare ground fraction c_B is the residual.

$$\begin{aligned} c_H &= A_H c_{veg}(T_H) \\ c_L &= A_L c_{veg}(T_L) \\ c_B &= (1 - c_H - c_L) \end{aligned} \tag{7.1}$$

Each vegetation type is characterized by a series of (fixed) parameters as detailed in Table 7.1:

- A minimum canopy resistance, $r_{s,min}$;
- A leaf area index, LAI;
- A vegetation coverage, c_{veg};
- A coefficient, g_D, for the dependence of the canopy resistance, r_c, on water vapour pressure deficit;
- The root distribution over the soil layers, specified by an exponential profile involving attenuation coefficients, a_r,and b_r;

The numerical values for the parameters of Table 1 are based both on experiments conducted as described in van den Hurk *et al.* (2000) and on literature review, in particular *Mahfouf et al.* (1995), *Manzi and Planton* (1994), *Giard and Bazile* (2000), *Dorman and Sellers* (1989), *Bonan* (1994), *Pitman et al.* (1991), and *Zeng et al.* (1998).

TABLE 7.1 VEGETATION TYPES AND PARAMETER VALUES (SEE TEXT). H/L REFER TO THE DISTINCTION BETWEEN HIGH AND LOW VEGETATION.

Index	Vegetation type	H/L	$r_{s,min}$ ($s\ m^{-1}$)	LAI ($m^2 m^{-2}$)	c_{veg}	g_D (hPa^{-1})	a_r	b_r
1	Crops, mixed farming	L	180	3	0.90	0	5.558	2.614
2	Short grass	L	110	2	0.85	0	10.739	2.608
3	Evergreen needleleaf trees	H	500	5	0.90	0.03	6.706	2.175
4	Deciduous needleleaf trees	H	500	5	0.90	0.03	7.066	1.953
5	Evergreen broadleaf trees	H	175	5	0.90	0.03	5.990	1.955
6	Deciduous broadleaf trees	H	240	6	0.99	0.03	7.344	1.303
7	Tall grass	L	100	2	0.70	0	8.235	1.627
8	Desert	-	250	0.5	0	0	4.372	0.978
9	Tundra	L	80	1	0.50	0	8.992	8.992
10	Irrigated crops	L	180	3	0.90	0	5.558	2.614
11	Semidesert	L	150	0.5	0.10	0	4.372	0.978
12-	Ice caps and glaciers	-	-	-	-	-	-	-
13	Bogs and marshes	L	240	4	0.60	0	7.344	1.303
14	Inland water	-	-	-	-	-	-	-
15	Ocean	-	-	-	-	-	-	-
16	Evergreen shrubs	L	225	3	0.50	0	6.326	1.567
17	Deciduous shrubs	L	225	1.5	0.50	0	6.326	1.567
18	Mixed forest/woodland	H	250	5	0.90	0.03	4.453	1.631
19	Interrupted forest	H	175	2.5	0.90	0.03	4.453	1.631
20	Water and land mixtures	L	150	4	0.60	0	-	-

The presence of snow and intercepted water dynamically modifies the coverage fractions. The coverage of snow, c_{sn}, is linearly related to the snow mass per unit area (abreviated to snow mass in the following), S (units 10^3($kg\ m^{-2}$) or m). The interception reservoir fraction, c_l, is given by W_l / W_{lm}, with W_{lm}, the maximum value for the intercepted water in the grid box, defined from the leaf area index contributions from the high and low vegetation tiles. The water contents of the interception reservoir, W_l (units m), and S are prognostic quantities in the model. Snow cover is assumed to be overlying vegetation and bare ground with the same fraction. The interception reservoir occupies an identical fraction of all snow-free tiles.

$$
\begin{aligned}
c_{\mathrm{sn}} &= \min\left(1, \frac{S}{S_{\mathrm{cr}}}\right) \\
W_{\mathrm{lm}} &= W_{\mathrm{lmax}}[c_{\mathrm{B}} + c_{\mathrm{H}} \cdot LAI(T_{\mathrm{H}}) + c_{\mathrm{L}} \cdot LAI(T_{\mathrm{L}})] \\
c_{l} &= \min\left(1, \frac{W_{\mathrm{l}}}{W_{\mathrm{lm}}}\right)
\end{aligned}
\tag{7.2}
$$

In the expressions above the minimum snow mass that ensures complete coverage of the grid box is $S_{\mathrm{cr}} = 0.015\mathrm{m}$ and the maximum water over a single layer of leaves or over bare ground is $W_{\mathrm{lmax}} = 0.0002\ \mathrm{m}$. The leaf area index LAI, is specified in Table 7.1 as a function of surface type. The full set of fractional tile coverages is given by Eqs. (7.3) and (7.4), where the indexing of the tiles is detailed in Table 7.2. Since a mixture of land and ocean tiles is not allowed, a grid box is either 100% water (open water and ice, with ice fraction c_{i}):

$$
\begin{aligned}
C_1 &= 1 - c_{\mathrm{i}} \\
C_2 &= c_{\mathrm{i}} \\
C_i &= 0, \ i \in [3, N_{\mathrm{T}}]
\end{aligned}
\tag{7.3}
$$

or 100% land (tiles 3 to N_{T}, where $N_{\mathrm{T}}=8$ is the number of tiles):

$$
\begin{aligned}
C_1 &= C_2 = 0 \\
C_3 &= (1 - c_{\mathrm{sn}}) \cdot c_{\mathrm{l}} \\
C_4 &= (1 - c_{\mathrm{sn}}) \cdot (1 - c_{\mathrm{l}}) \cdot c_{\mathrm{L}} \\
C_5 &= c_{\mathrm{sn}} \cdot (1 - c_{\mathrm{H}}) \\
C_6 &= (1 - c_{\mathrm{sn}}) \cdot (1 - c_{\mathrm{l}}) \cdot c_{\mathrm{H}} \\
C_7 &= c_{\mathrm{sn}} \cdot c_{\mathrm{H}} \\
C_8 &= (1 - c_{\mathrm{sn}}) \cdot (1 - c_{\mathrm{l}}) \cdot (1 - c_{\mathrm{L}} - c_{\mathrm{H}})
\end{aligned}
\tag{7.4}
$$

Apart from the fractional gridbox coverage, each tile has a couple of additional parameters (see Table 7.2):

- The skin conductivity, Λ_{sk}, provides the thermal connection between the skin level and the soil or snow deck. For high vegetation, Λ_{sk}, is different for a stable and unstable stratification of the temperature gradient between the skin level and the upper soil or snow layer. This difference is considered to represent the asymmetric coupling between the ground surface and the tree canopy layer: an effective convective transport within the tree trunk space for unstable conditions, and a limited turbulent exchange for stable stratification (*Bosveld et al.* 1999).
- A small fraction $f_{R_{\mathrm{s}}}$ of net short-wave radiation that is transmitted directly to the top soil or snow layer. The remaining fraction of the short-wave radiation (1 - $f_{R_{\mathrm{s}}}$) is absorbed by the skin layer.

Finally, the surface albedo, α_{i}, is similar for all land tiles within a grid box except for those covered with snow (see the snow scheme description below). The climate database provides the snow-free background albedo on a monthly basis. Long-wave emissivity, ε, outside the window region is equal to 0.99 for all tiles; emissivity in the window region is tile dependent and varies between 0.93 and 0.98 (see Table 2.5 in Section 2.5.5 for more details). The remaining surface characteristics (roughness length for momentum, $z_{0\mathrm{m}}$, and heat, $z_{0\mathrm{h}}$) are similar for all land tiles within a grid box and specified in the climate database (Chapter 10).

TABLE 7.2 TILE SPECIFIC VALUES.

Index	Tile	Λ_{sk} unstable ($W\ m^{-2}K^{-1}$)	Λ_{sk} stable ($W\ m^{-2}K^{-1}$)	f_{Rs}	Resistance scheme
1	Open water	∞	∞	0	Potential
2	Ice water	58	58	0	Potential
3	Interception reservoir	10	10	0.05	Potential
4	Low vegetation	10	10	0.05	Resistance
5	Snow on low vegetation/bare ground	7	7	0	Potential
6	High vegetation	$\Lambda_{a,u} + 5$	$\Lambda_{a,s} + 5$	0.03	Resistance
7	High vegetation with snow beneath	$\Lambda_{a,u} + 5$	$\Lambda_{a,s} + 5$	0.03	Canopy and snow resistance
8	Bare ground	15	15	0	Resistance

The resistance scheme describes the way of coupling with the atmosphere: *Potential* denotes atmospheric resistance only; *Resistance* denotes aerodynamic resistance in series with a canopy or soil resistance; *Canopy and snow resistance* denotes a canopy resistance for the vegetation and an extra aerodynamic coupling to the snow surface (see Figs. 7.1 – 7.2 and Subsection 7.2.2). For tiles 6 and 7, $\Lambda_{a,u} = 15 W\ m^{-2}K^{-1}$ and $\Lambda_{a,s} = 10 W\ m^{-2}K^{-1}$ represent the aerodynamic coupling between the canopy and the soil in the unstable and stable cases, respectively, and the factor 5 represents the longwave radiative exchanges. *Unstable/stable* refers to the temperature gradient between the skin layer and the top soil or snow layer.

7.2.2 Surface heat and evaporation fluxes

A resistance parameterization is used to calculate the turbulent fluxes. Momentum exchange is parameterized with the same roughness length for all tiles, but with a different stability correction for each tile. The resistance scheme for water vapour and heat exchanges is different for different tiles (see Fig. 7.2). For ocean, sea ice and snow on low vegetation, the turbulent fluxes of heat and water vapour are given by

$$H_i = \rho_a c_p |U_L| C_{H,i}(T_L + g z_L - T_{sk,i}) \tag{7.5}$$

$$E_i = \rho_a |U_L| C_{H,i}[q_L - q_{sat}(T_{sk,i})] \tag{7.6}$$

with ρ_a the air density, c_p the heat capacity of moist air, g the acceleration fo gravity, $|U_L|$, T_L, q_L, z_L the wind speed, temperature, humidity and height of the lowest atmospheric model level, and $C_{H,i}$ the turbulent exchange coefficient, that varies from tile to tile because of different atmospheric stabilities. See Chapter 3 for a description of the exchange coefficients where different roughness lengths for heat and momentum are assumed and a Monin–Obukhov formulation is adopted for the stability dependence.

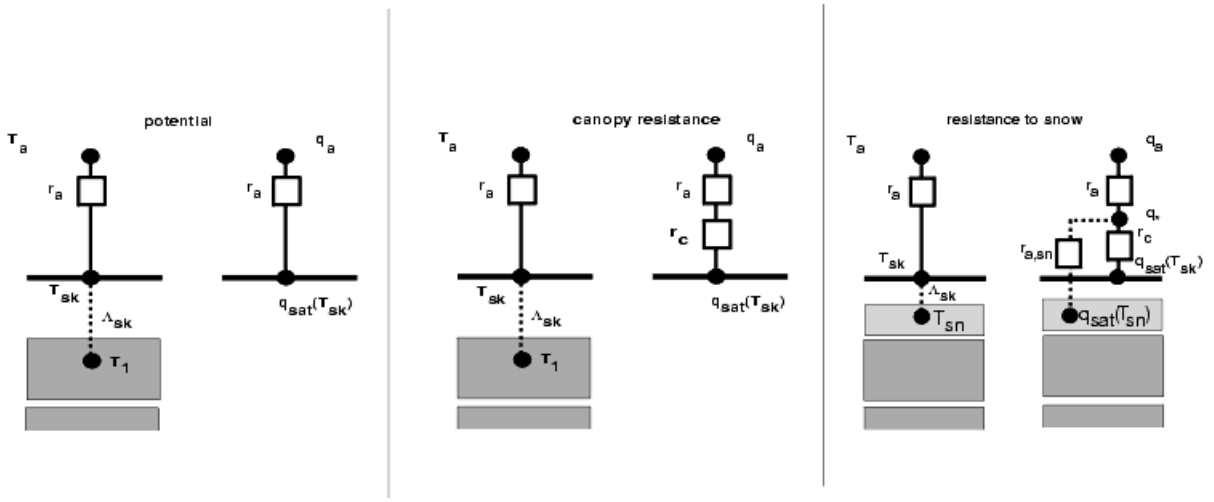

Figure 7.2 Resistance scheme for three categories of coupling. *Potential* refers to ocean, sea ice and and snow on low vegetation; *(Canopy) resistance* to dry low and dry high vegetation, bare soil, and interception reservoir when potential evaporation exceeds the maximum reservoir content; *Resistance to snow* to snow under high vegetation.

For high and low vegetation, an additional canopy resistance r_c is added:

$$E_i = \frac{\rho_a}{r_a + r_c}[q_L - q_{sat}(T_{sk,i})] \tag{7.7}$$

with $r_a = (|U_L| C_{H,i})^{-1}$ and i indicating the high or low vegetation tiles. r_c is a function of downward shortwave radiation R_s, leaf area index LAI, average unfrozen root soil water $\bar{\theta}$, atmospheric water vapour deficit D_a and a minimum stomatal resistance $r_{s,min}$, following *Jarvis* (1976):

$$r_c = \frac{r_{S,min}}{LAI} f_1(R_s) f_2(\bar{\theta}) f_3(D_a) \tag{7.8}$$

f_1 is a hyperbolic function of downward short-wave radiation only:

$$\frac{1}{f_1(R_s)} = \min\left[1, \frac{bR_s + c}{a(bR_s + 1)}\right] \tag{7.9}$$

where $a = 0.81$, $b = 0.004\ \mathrm{W^{-1}m^2}$ and $c = 0.05$.

Function f_2 is defined as

$$\frac{1}{f_2(\bar{\theta})} = \begin{cases} 0 & \bar{\theta} < \theta_{pwp} \\ \dfrac{\bar{\theta} - \theta_{pwp}}{\theta_{cap} - \theta_{pwp}} & \theta_{pwp} \le \bar{\theta} \le \theta_{cap} \\ 0 & \bar{\theta} > \theta_{cap} \end{cases} \tag{7.10}$$

where the soil moisture at permanent wilting point and at field capacity, θ_{pwp} and θ_{cap}, respectively, are defined in Table 7.5. $\bar{\theta}$ is a weighted average of the unfrozen soil water

$$\bar{\theta} = \sum_{k=1}^{4} R_k \max[f_{\mathrm{liq},k}\theta_k, \theta_{pwp}] \tag{7.11}$$

where R_k is the the fraction of roots in layer k and the fraction of unfrozen soil water, $f_{\mathrm{liq},k} = 1 - f_{fr}(T_k)$, is a parameterized function of the soil temperature of layer k, T_k, as specified in Section 7.5.2. Table 7.1 lists the coefficients a_r and b_r which are used to calculate the root fraction R_k according to *Zeng et al.* (1998):

$$R_k = 0.5[\exp(-a_r z_{k-1/2}) + \exp(-b_r z_{k-1/2}) - \exp(-a_r z_{k+1/2}) - \exp(-b_r z_{k+1/2})] \tag{7.12}$$

where $z_{k+1/2}$ is the depth of the bottom of layer k (in m; $z_{1/2} = 0$ m). Contributions from levels exceeding the column depth are added to the deepest soil layer in order to ensure that $\sum R_k = 1$. Table 7.3 lists the distribution of the roots over the four soil layers.

.

TABLE 7.3 ROOT DISTRIBUTION PER VEGETATION TYPE (IN %) OVER THE FOUR LAYERS. VEGETATION INDEXES REFER TO Table 7.1.

Vegetation index	1	2	3	4	5	6	7	8	9	10	11	13	16	17	18	19
Layer 1	24	35	26	26	24	25	27	100	47	24	17	25	23	23	19	19
Layer 2	41	38	39	38	38	34	27	0	45	41	31	34	36	36	35	35
Layer 3	31	23	29	29	31	27	27	0	8	31	33	27	30	30	36	36
Layer 4	4	4	6	7	7	14	9	0	0	4	19	11	11	11	10	10

A dependence on atmospheric humidity deficit (D_a=$e_{sat}(T_L)$-e_L, with e the vapour pressure) is included according to

$$\frac{1}{f_3(D_a)} = \exp(-g_D D_a) \tag{7.13}$$

where g_D depends on the vegetation type (Table 7.1), and is non-zero for high vegetation only.

Evaporation from the interception reservoir is given by Eq. (7.6) only when the amount of water in the interception reservoir, W_l, is sufficient to sustain potential evaporation during the entire time step Δt. If W_l is limited, an additional resistance r_l, analogue to r_c in Eq. (7.7), is introduced. r_l is calculated from the potential evaporation of the previous time step. Note that this type of flux-limiter is a time-step dependent feature of the model numerics.

Bare-soil evaporation uses a resistance approach, an analogue to the canopy transpiration formulation (Eq. (7.7)). The soil evaporation resistance, r_{soil}, is

$$r_{soil} = r_{soil,min} f_2(f_{liq}\theta_1) \tag{7.14}$$

with f_2 given by Eq. (7.10), and $r_{soil,min}$ = 50 s m^{-1}. By this parameterization, evaporation from bare ground is treated similar to a single leaved canopy with a minimum resistance $r_{soil,min}$, extracting water from the upper soil layer only, and not experiencing any additional stress due to limited radiation or dry air. Eq. (7.14) shuts off evaporation when the top soil moisture reaches permanent wilting point. When compared to observations over semi-arid areas, an alternative relative humidity formulation (*Mahfouf and Noilhan* 1991; *Viterbo and Beljaars* 1995), that does not have a similar limitation, gave excessive evaporation (*van den Hurk et al.* 2000).

A special treatment is included in the calculation of evaporation over high vegetation with snow underneath (see Fig. 7.2). Evaporation takes place from both the canopy component in the tile ($E_{veg,7}$) and from the snow lying under the vegetation. The canopy evaporation uses a canopy resistance and saturation specific humidity at the canopy skin temperature, while the snow evaporation $E_{sn,7}$ is parameterized with an additional constant aerodynamic resistance $r_{a,sn}$ and saturation specific humidity at snow temperature T_{sn}. The evpaoration from tile 7 is the combination of the canopy transpiration and the snow evaporation:

$$E_7 = \rho_a \frac{q_L - q_*}{r_a} = \rho_a \frac{q_* - q_{sat}(T_{sn})}{r_{a,sn}} + \rho_a \frac{q_* - q_{sat}(T_{sk})}{r_c} \tag{7.15}$$

where q_* is the humidity at the connection point of the three resistances (Fig. 7.2). After elimination of q_*, E_7 can be rewritten as:

$$E_7 = \rho_a \frac{q_L - q_{sat}(T_{sk})}{r_a + r_c + r_c \frac{r_a}{r_{a,sn}}} + \rho_a \frac{q_L - q_{sat}(T_{sn})}{r_a + r_{a,sn} + r_{a,sn} \frac{r_a}{r_c}} \tag{7.16}$$

The first term in the equation above is interpreted as $E_{veg,7}$ and is treated in the standard way (i.e., implicit in the tile skin temperature). The second term is interpreted as evaporation from snow ($E_{sn,7}$) and is handled explicitly. The values of $r_{a,sn}$ depend on the stability of the subcanopy layer and are functions of $\Lambda_{a,u}$ and $\Lambda_{a,s}$ (see Table 7.2); $r_{a,sn}$ = 67 s m^{-1} and $r_{a,sn}$ = 220 s m^{-1} for an unstable and stable subcanopy layer, respectively. In spring, the latent heat flux of that tile, $L_v E_{veg,7} + L_s E_{sn,7}$ will be dominated by snow evaporation since the frozen soil under the snow deck will lead to very large values of r_c.

The grid box total sensible and latent heat fluxes are expressed as an area weighted average:

$$H = \sum_{i=1}^{\cdot} C_i H_i \tag{7.17}$$

$$E = \sum_{i=1}^{\cdot} C_i E_i \tag{7.18}$$

with H_i given by Eq. (7.5), and E_i by Eq. (7.6) for ocean, sea-ice and snow on low vegetation, Eq. (7.7) for dry high and low vegetation, the interception reservoir (with r_c replaced by r_l) and for bare soil (with r_c replaced by r_{soil}) and Eq. (7.16) for high vegetation with underlying snow.

7.3 THE SURFACE ENERGY BALANCE AND COUPLING TO THE SOIL

A skin temperature T_{sk} forms the interface between the soil and the atmosphere. As detailed in Section 3.5, it is

calculated for each grid box tiles separately, by scanning the surface energy balance solver over the 8 tiles, assuming a complete coverage of the specific tile. For a single tile, this procedure is very similar to the derivation of the Penman–Monteith equation in which the skin temperature is eliminated from the surface energy balance equation. The numerical approach used in TESSEL has the advantage that the feedback of skin temperature on net radiation and ground heat flux is included (see Section 3.5). The input radiation and reference atmospheric temperature (T_L), specific humidity (q_L) and wind speed (U_L) are identical for each tile. The surface fluxes "seen" by the atmosphere are calculated as an area-weighted average over the tiles (see Eqs. (7.17) and (7.18)). For the high vegetation with snow underneath, the skin temperature is that of the high vegetation; the temperature of the underlying snow is calculated separately.

The energy balance equation solved for each tile takes into account partial absorption of net short-wave radiation, $1\text{-}f_{Rs,i}$, in the skin layer (see Table 7.2). The remaining energy is directly passed to the soil or snow:

$$(1-f_{Rs,i})(1-\alpha_i)R_s + \varepsilon(R_T - \sigma T_{sk,i}^4) + H_i + L_{v,s}E_i = \Lambda_{sk,i}(T_{sk,i} - T_1) \qquad (7.19)$$

where i denotes the tile index, R_s and R_T are downward short-wave radiation and long-wave radiation, respectively, σ is the Stefan–Bolzman constant, T_1 the temperature of the upper soil or snow layer, H_i the sensible heat flux, and $L_{v,s}E_i$ the latent heat flux from the skin layer, and $\Lambda_{sk,i}$, the skin conductivity for tile i. Latent heat of evaporation, L_v, is used for all evaporation terms except snow evaporation, while L_s, the latent heat of sublimation, is used for evaporation of snow (i.e., tile 5 and the contribution $E_{sn,7}$ from tile 7, defined by Eq. (7.16)).

The tiled surface is thermally coupled to the snow deck, when present, and to a single soil profile. The net flux into the soil is a weighted average of the flux from each tile.

The solution of Eq. (7.19) is performed inside the code for turbulent exchanges in the atmosphere (Chapter 3). The atmospheric vertical diffusion equations yield a tridiagonal system of equations, with the coupling to the skin temperature given by the matrix row corresponding to the lowest model level. The first step for the solution of the system of equations, an LU decomposition, is followed by the solution of Eq. (7.19) before back-substitution. Details of the computations can be found in Chapter 3.

7.4 SNOW

The snow scheme represents an additional "layer" on top of the upper soil layer, with an independent, prognostic, thermal and mass contents. The snow pack is represented by a single snow temperature, T_{sn} and the snow mass per unit area (snow mass for short) S. The net energy flux at the top of the snow pack, G_{sn}^T, is the residual of the skin energy balance from the snow covered tiles and the snow evaporation from the tile with high vegetation over snow (Eq. (7.15)). The basal heat flux, G_{sn}^B, is given by equation a resistance formulation modified in case of melting. The absorbed energy is used to change the snow temperature or melt the snow, when T_{sn} exceeds the melting point.

The heat capacity of the snow deck is a function of its depth and the snow density, which is a prognostic quantity depending on snow age following (*Douville et al.* 1995). The snow thermal conductivity changes with changing snow density. The snow albedo changes exponentially with snow age. For snow on low vegetation it ranges between 0.50 for old snow and 0.85 for fresh snow (to which it is reset whenever the snow fall exceeds 1 mm hr^{-1}). The albedo for high vegetation with snow underneath is fixed at 0.15.

7.4.1 Snow mass and energy budget

The snow mass budget reads as:

$$\rho_w \frac{\partial S}{\partial t} = F + c_{sn}(E_{sn} - M_{sn}) \tag{7.20}$$

where F is snowfall (units kg m^{-2}s^{-1}), S is snow mass (sometimes referred as snow water equivalent) grid-averaged (units 103 kg m^{-2}), ρ_w is the water density (units kg m^{-3}), E_{sn} and M_{sn} are snow evaporation and melting, respectively (units kg m^{-2}s^{-1}), and c_{sn} is the snow fraction (see Eq. (7.2)), i.e. the sum of tiles 5 and 7 (see Eq. (7.4)). In Eq. (7.20) and in the remaining of this section, all surface fluxes are per unit area and apply only to the snow area (i.e. tile 5 and 7). The snow equivalent water S applies to the entire grid square and therefore occurs in the equation divided by the total snow fraction. The snow flux from the atmospheric model, F, is again for the entire grid square. As a general rule, all quantities with subscript sn will refer to the snow area. In Eq. (7.20), the snow evaporation is defined as

$$c_{sn}E_{sn} = c_5E_5 + c_7E_{sn,\,7} \tag{7.21}$$

Snow mass and snow depth are related by

$$D_{sn} = \frac{\rho_w}{\rho_{sn}} \frac{S}{c_{sn}} \tag{7.22}$$

where D_{sn} is snow depth for the snow-covered area (units m; D_{sn} is NOT a grid-averaged quantity) and ρ_{sn} is the snow density (units kg m^{-3}).

The snow energy budget reads as

$$(\rho C)_{sn} D_{sn} \frac{\partial T_{sn}}{\partial t} = (\rho C)_{sn} \frac{\rho_w}{\rho_{sn}} \frac{S}{c_{sn}} \frac{\partial T_{sn}}{\partial t} \approx (\rho C)_i \frac{\rho_w}{\rho_i} \frac{S}{c_{sn}} \frac{\partial T_{sn}}{\partial t} = R^N_{sn} + L_s E_{sn} + H_{sn} - G^B_{sn} - Q_{sn} \tag{7.23}$$

where $(\rho C)_i$ and $(\rho C)_{sn}$ are the ice and snow volumetric heat capacities, respectively (units J m^{-3}K^{-1}), ρ_i is the ice density (units kg m^{-3}, R^N_{sn} is the net radiation absorbed by the snow pack (units W m^{-2}), L_s is the latent heat of sublimation (units J kg^{-1}), H_{sn}, G^B_{sn}, and Q_{sn} represent, respectively, the snow sensible heat flux, basal heat flux (at the bottom of the snow pack), and energy exchanges due to melting (units W m^{-2}). Eq. (7.23) neglects the thermal energy brought by precipitation. The snow is composed of an ice fraction, a liquid water fraction and an air fraction, ν_i, ν_w and ν_a, respectively, where typically $0.3 < \nu_a < 0.9$ and the liquid water fraction is significantly different from zero in melting conditions. The following approximations are made in Eq. (7.23)

$$\begin{aligned}
(\rho C)_{sn} &= \nu_i(\rho C)_i + \nu_w(\rho C)_w + \nu_a(\rho C)_a \approx \nu_i(\rho C)_i + \nu_w(\rho C)_w \\
\rho_{sn} &= \nu_i\rho_i + \nu_w\rho_w + \nu_a\rho_a \approx \nu_i\rho_i + \nu_w\rho_w \\
\frac{(\rho C)_{sn}}{\rho_{sn}} &\approx \frac{\nu_i(\rho C)_i + \nu_w(\rho C)_w}{\nu_i\rho_i + \nu_w\rho_w} \approx \frac{(\rho C)_i}{\rho_i}
\end{aligned} \tag{7.24}$$

The melting term couples the mass and energy equation

$$Q_{sn} = L_f M_{sn} = -L_f \frac{\rho_w}{c_{sn}} \frac{\partial S}{\partial t}\bigg|_m \tag{7.25}$$

where L_f is the latent heat of fusion (units J kg^{-1}) and the subscrit m represents melting.

7.4.2 Prognostic snow density and albedo

Following *Douville et al.* (1995) snow density is assumed to be constant with depth and to evolve exponentially towards a maximum density (*Verseghy*, 1991). First a weighted average is taken between the current density and the minimum density for fresh snow

$$\rho^*_{sn} = \frac{S\rho^t_{sn} + (\Delta t F/\rho_w)\rho_{min}}{S + (\Delta t F/\rho_w)} \tag{7.26}$$

The exponential relaxation reads

$$\rho^{t+1}_{sn} = (\rho^*_{sn} - \rho_{max})\exp(-\tau_f \Delta t/\tau_1) + \rho_{max} \tag{7.27}$$

where timescales $\tau_1 = 86400$ s, and $\tau_f = 0.24$ corresponding to an e-folding time of about 4 days, with minimum density $\rho_{min} = 100$ kg m^{-3} and maximum density $\rho_{max} = 300$ kg m^{-3} (see Table 7.4).

TABLE 7.4 SNOW-RELATED PARAMETERS

Symbol	Parameter	Value
D^{max}_{sn}	Maximum snow thermal depth	0.07 m
S_{cr}	Threshold value for grid box coverage of snow	0.015 m
α_{min}	Minimum albedo of exposed snow	0.50
α_{max}	Maximum albedo of exposed snow	0.85
$\alpha_{sn,f}$	Albedo of shaded snow	0.2
λ_i	Ice heat conductivity	2.2 W m^{-1}K^{-1}
ρ_{min}	Minimum snow density	300 k gm^{-3}
ρ_{max}	Maximum snow density	100 k gm^{-3}
ρ_i	Ice density	920 kgm^{-3}
$(\rho C)_i$	Ice volumetric heat capacity	2.05 10^6 J m^{-3} K^{-1}
τ_a	Linear coefficient for decrease of albedo of non-melting snow	0.008
τ_f	Coefficient for exponential decrease of snow density and melting snow albedo	0.24
τ_1	Length of day	86400 s

Snow albedo in exposed areas evolves according to the formulation of *Baker et al.* (1990), Verseghy (1991) and *Douville et al.* (1995). For non melting-conditions:

$$\alpha^{t+1}_{sn} = \alpha^t_{sn} - \tau_a \Delta t/\tau_1 \tag{7.28}$$

where $\tau_a = 0.008$, which will decrease the albedo by 0.1 in 12.5 days. For melting conditions $M_{sn} > 0$:

$$\alpha^{t+1}_{sn} = (\alpha^t_{sn} - \alpha_{min})\exp(-\tau_f \Delta t/\tau_1) + \alpha_{min} \tag{7.29}$$

where $\alpha_{min} = 0.5$ and $\alpha_{max} = 0.85$. If snowfall $F > 1$ kg m^{-2}hr^{-1}, the snow albedo is reset to the maximum value,

$\alpha_{sn}^{t+1} = \alpha_{max}$.

The above formulae are inadequate to describe the evolution of the surface albedo of snow cover with high vegetation. Observations suggest a dependence on forest type but, by and large, the albedo changes from a value around 0.3 just after a heavy snowfall to a value around 0.2 after a few days (see *Betts and Ball* (1997) and the discussion in *Viterbo and Betts* (1999)). This change reflects the disappearance of intercepted snow, due to melt (for sufficiently warm temperatures) or wind drift (for cold temperatures). Ways of describing those two mechanisms would involve either a separate albedo variable for the snow in the presence of high vegetation, or the introduction of an interception reservoir for snow. In the absence of any of the two, we define $\alpha_{sn,f} = 0.2$ for the snow in the presence of high vegetation. This value was chosen to match the overall forest albedo in the presence of snow from the results of *Viterbo and Betts* (1999).

7.4.3 Additional details

7.4.3 (a) Limiting of snow depth in the snow energy equation. Initial experimentation with the snow model revealed that the time evolution of snow temperature was very slow over Antartica. The reason is rather obvious; the snow depth over Antartica is set to a climatological value of 10 m which can respond only very slowly to the atmospheric forcing due to its large thermal inertia. In previous model versions, the properties of layer 1 were replaced by snow properties when snow was present, which kept the timescale short. A physical solution would have been to introduce a multilayer snow model, with e.g. four layers to represent timescales from one day to a full annual cycle. As a shortcut, a limit is put on the depth of the snow layer in the thermal budget, $D_{sn}^{max} = 0.07$ m. The energy equation reads:

$$\begin{aligned}(\rho C)_{sn} D^*_{sn} \frac{\partial T_{sn}}{\partial t} &= R_{sn}^{N} + L_s E_{sn} + H_{sn} - G_{sn}^{B} - Q_{sn} \\ D^*_{sn} &= \min(D_{sn}, D_{sn}^{max})\end{aligned} \tag{7.30}$$

7.4.3 (b) Basal heat flux and thermal coefficients. The heat flux at the bottom of the snow pack is written as a finite difference in the following way:

$$G_{sn}^{B} = \frac{T_{sn} - T_1}{r_{sn}} \tag{7.31}$$

where r_{sn} is the resistance between the middle of the snow pack and the middle of soil layer 1, with two components: the resistance of the lower part of the snow pack and the resistance of the top half of soil layer 1:

$$r_{sn} = 0.5\frac{D^*_{sn}}{\lambda_{sn}} + \frac{1}{\Lambda_{sk,8}} \tag{7.32}$$

where the second term is the skin layer conductivity for bare soil (tile 8), which can be seen as an approximation of $0.5(D_1/\lambda_T)$. The snow thermal conductivity, is related to the ice thermal conductivity according to *Douville et al.* (1995):

$$\lambda_{sn} = \lambda_i \left(\frac{\rho_{sn}}{\rho_i}\right)^{1.88} \tag{7.33}$$

Table 7.4 contains the numerical values of the ice density and ice heat conductivity.

7.4.3 (c) Numerical solution for non-melting situations. The net heat flux that goes into the top of the snow deck is an output of the vertical diffusion scheme

$$H_{sn}^{N} = R_{sn}^{N} + L_{sub}E_{sn} + H_{sn} \tag{7.34}$$

In the absence of melting, the solution of Eq. (7.30) is done implicitly. The preliminary snow temperature, prior to the checking for melting conditions, T^*_{sn}, is given by

$$A_1\frac{T^*_{sn} - T^t_{sn}}{\Delta t} = H_{sn}^{N} - \frac{T^*_{sn} - T_1}{r_{sn}} \tag{7.35}$$

$$\begin{aligned} A_1 &= \min\left[(\rho C)_i\frac{\rho_w}{\rho_i}\frac{S}{c_{sn}}, A_1^{max}\right] \\ A_1^{max} &= (\rho C)_i\frac{\rho_w}{\rho_i}D_{sn}^{max} \end{aligned} \tag{7.36}$$

where superscript t refers to the current time step and superscript * to the preliminary value at the next time step. The solution for T^*_{sn} is obtained from

$$T^*_{sn}\left(1 + \frac{\Delta t}{r_{sn}A_1}\right) = T^t_{sn} + \frac{\Delta t}{A_1}\left(H_{sn}^{N} + \frac{T^t_1}{r_{sn}}\right) \tag{7.37}$$

The basal snow heat flux to be used as input for the thermal budget of the soil (in the snow covered fraction only) is

$$G_{sn}^{B} = \frac{T^*_{sn} - T_1}{r_{sn}} \tag{7.38}$$

Finally, a preliminary new value for the snow mass, S^*, is computed from snow fall and snow evaporation

$$\rho_w\frac{S^* - S^t}{\Delta t} = F + c_{sn}E_{sn} \tag{7.39}$$

7.4.4 Treatment of melting

7.4.4 (a) No melting occurs. If $T^*_{sn} < T_0$ no melting occurs and the preliminary values T^*_{sn} and S^* become the $t+1$ values, while the basal heat flux is given by Eq. (7.38).

7.4.4 (b) Melting conditions. If $T^*_{sn} > T_0$, snow melting occurs and the time step is divided in two fractions, $\Delta t = \Delta_1 t + \Delta_2 t$, where the first fraction, $\Delta_1 t$ brings the temperature to T_0 with no melting:

$$\Delta_1 t = \frac{A_1(T_0 - T^t_{sn})}{H_{sn}^{N} - (T_0 - T^t_1)/r_{sn}} \tag{7.40}$$

while, during the second fraction, $\Delta_2 t$, melting occurs with no resultant warming of the snow:

$$
\begin{aligned}
T^{t+1} &= T_0 \\
Q_{\mathrm{sn}} &= H_{\mathrm{sn}}^{\mathrm{N}} - G_{\mathrm{sn}}^{\mathrm{B}} \\
\rho_{\mathrm{w}} \frac{S^{t+1} - S^{*}}{\Delta_2 t} &= -c_{\mathrm{sn}} M_{\mathrm{sn}} = -c_{\mathrm{sn}} \frac{Q_{\mathrm{sn}}}{L_{\mathrm{f}}} = -c_{\mathrm{sn}} \frac{H_{\mathrm{sn}}^{\mathrm{N}} - G_{\mathrm{sn}}^{\mathrm{B}}}{L_{\mathrm{f}}}
\end{aligned}
\tag{7.41}
$$

If not all the snow melts, i.e., if $S^{t+1}>0$, the following heat flux is passed to the soil

$$
G_{\mathrm{sn}}^{\mathrm{B}} = \frac{T_0 - T_1}{r_{\mathrm{sn}}} \tag{7.42}
$$

When all the snow melts, i.e., if $S^{t+1}<0$, the melting time step is redefined as:

$$
\begin{aligned}
S^{t+1} &= 0 \\
\Delta_2 t &= \rho_{\mathrm{w}} L_{\mathrm{f}} \frac{S^{*}}{c_{\mathrm{sn}} (H_{\mathrm{sn}}^{\mathrm{N}} - G_{\mathrm{sn}}^{\mathrm{B}})} \\
\Delta_3 t &= 1 - (\Delta_1 t + \Delta_2 t)
\end{aligned}
\tag{7.43}
$$

and the basal heat flux is redefined as

$$
G_{\mathrm{sn}}^{\mathrm{B}} = \frac{\Delta_1 t + \Delta_2 t}{\Delta t} \frac{T_0 - T_1^{t}}{r_{\mathrm{sn}}} + \frac{\Delta_3 t}{\Delta t} H_{\mathrm{sn}}^{\mathrm{N}} \tag{7.44}
$$

7.5 SOIL HEAT TRANSFER

In the absence of internal phase changes, the soil heat transfer is assumed to obey the following Fourier law of diffusion

$$
(\rho C)_{\mathrm{soil}} \frac{\partial T}{\partial t} = \frac{\partial}{\partial z} \left[\lambda_T \frac{\partial T}{\partial z} \right] \tag{7.45}
$$

where $(\rho C)_{\mathrm{soil}}$ is the volumetric soil heat capacity $(\mathrm{J\,m^{-3}K^{-1}})$, T is the soil temperature (units K), z is the vertical coordinate—the distance from the surface, positive downwards—(units m), and λ_{T} is the thermal conductivity $(\mathrm{W\,m^{-1}K^{-1}})$. The above equation assumes that heat fluxes are predominantly in the vertical direction, that the effects of phase changes in the soil and the heat transfer associated with the vertical movement of water in the soil can be neglected (*de Vries* 1975), and that the effects of hysteresis can be neglected (*Milly* 1982).

The boundary condition at the bottom, no heat flux of energy, is an acceptable approximation provided that the total soil depth is large enough for the time-scales represented by the model or, in other words, the bottom of the soil is specified at a depth where the amplitude of the soil heat wave is a negligible fraction of its surface amplitude (see *de Vries* (1975) and next section).

7.5.1 Discretization and choice of parameters

TABLE 7.5 PARAMETERS IN THE LAND-SURFACE SCHEME. SEE Table 7.4 FOR SNOW-RELATED PARAMETERS.

Symbol	Parameter	Value
b	Clapp and Hornberger soil parameter	6.04
b_I	Interception efficiency	0.25
D_1	Depth of soil layer 1	0.07 m
D_2	Depth of soil layer 2	0.21 m
D_3	Depth of soil layer 3	0.72 m
D_4	Depth of soil layer 4	1.89 m
F_{cv}	Fraction of gridbox covered by convective rainfall	0.5
k	Heterogeneity factor for convective precipitation	0.5
T_{f1}	Highest temperature for existence of ice water	$T_0 + 1$
T_{f2}	Lowest temperature for existence of liquid water	$T_0 - 3$
W_{lmax}	Maximum water amount on single leaf	0.0002 m
γ_{sat}	Hydraulic conductivity at saturation	4.57×10^{-4} m s^{-1}
λ_{dry}	Heat conductivity of dry soil	0.190 W m^{-1}K^{-1}
λ_{sm}	Heat conductivity of soil matrix	3.44 W m^{-1}K^{-1}
λ_{w}	Heat conductivity of liquid water	0.57 W m^{-1}K^{-1}
$(\rho C)_{\mathrm{soil}}$	Volumetric soil heat capacity	2.19×10^6 J m^{-3}K^{-1}
θ_{sat}	Soil moisture at saturation	0.472 m^3 m^{-3}
θ_{cap}	Soil moisture at field capacity	0.323 m^{3}m^{-3}
θ_{pwp}	Soil moisture at permanent wilting point	0.171 m^{3}m^{-3}
ψ_{sat}	Matric potential at saturation	–0.338 m

For the solution of Eq. (7.45) the soil is discretized in four layers, of depths D_k, (k = 1, 2, 3, 4), the temperatures are defined at full layers (T_k), and the heat fluxes, at half layers ($\hat{G}_{k+1/2}$ is the heat flux, positive downwards, units W m^{-2}, at the interface between layer k and k + 1). An energy-conserving implicit algorithm is used, leading to a tridiagonal system of equations with solution detailed in Section 7.8.

The boundary condition at the bottom is:

$$G_{4+1/2} = 0 \tag{7.46}$$

At the top, the boundary condition is the soil heat flux at the surface, computed as a weighted average over the tiles. For the snow free tiles, the flux into the soil consists of two parts. Apart from the diffusion of heat governed by $\Lambda_{\mathrm{sk},i}(T_{\mathrm{sk,i}} - T_1)$ (see Eq. (7.19)), the net shortwave radiation not absorbed by the skin layer ($f_{\mathrm{Rs},i}$) provides energy to the soil. Table 7.2 lists the values of $\Lambda_{\mathrm{sk},i}$ and $f_{\mathrm{Rs},i}$ for each of the tiles. For the snow tiles, the heat flux into the soil is the snow basal flux, calculated using a resistance formulation and modified in the case of partial melting (see Eqs. (7.31), (7.38), (7.42), and (7.44)).

The net heat flux into the soil is given by:

$$G_{1/2} = \sum_{i} C_i[\Lambda_{\mathrm{sk},i}(T_{\mathrm{sk},i} - T_1) + f_{\mathrm{Rs},i}(1-\alpha_i)R_{\mathrm{s}}] + c_{\mathrm{s}}G^{\mathrm{B}}_{\mathrm{sn}} \quad , \tag{7.47}$$

where the summation scans all snow free tiles.

The volumetric soil heat capacity is assumed constant, with value 2.19×10^6 J m^{-3}K^{-1} (see Table 7.5 for a list of constants used by the model). The heat conductivity, λ, depends on the soil-water content following *Peters-Lidard et al.* (1998) (see also *Farouki* 1986; *Johansen* 1975) and is given by a combination of dry λ_{dry} and saturated λ_{sat} values, weighted by a factor known as the Kersten number, K_e:

$$\lambda = K_e(\lambda_{\mathrm{sat}} - \lambda_{\mathrm{dry}}) + \lambda_{\mathrm{dry}} \quad , \tag{7.48}$$

where $\lambda_{\mathrm{dry}} = 0.190$W m^{-1}K^{-1} and

$$\lambda_{\mathrm{sat}} = \lambda_{\mathrm{sm}}^{1-\theta_{\mathrm{sat}}}\lambda_{\mathrm{w}}^{\theta} \quad , \tag{7.49}$$

where the heat conductivity of the soil matrix, $\lambda_{\mathrm{sm}} = 3.44$W m^{-1}K^{-1} and the thermal conductivity of water is $\lambda_{\mathrm{w}} = 0.57$W m^{-1}K^{-1}. Eq. (7.49) represents a simplification of Peters-Lidard formulation, neglecting the changes in conductivity due to ice water and assuming the quartz content typical of a loamy soil. Finally, the Kersten number for fine soils was selected in *Peters-Lidard et al.* (1998):

$$K_e = \log_{10}\left[\max\left(0.1, \frac{\theta}{\theta_{\mathrm{sat}}}\right)\right] + 1 \tag{7.50}$$

The depths of the soil layers are chosen in an approximate geometric relation (see Table 7.5), as suggested in Deardorff (1978). *Warrilow et al.* (1986) have shown that four layers are enough for representing correctly all timescales from one day to one year. Using the numerical values of the heat capacity and soil depths defined in Table 7.5, the amplitude and phase response of the numerical solution of Eq. (7.45) were analysed by *Viterbo and Beljaars* (1995) for typical values of soil moisture in Eq. (7.48), and for harmonic forcings at the surface with periods ranging from half a day to two years. The analysis points to an error in the numerical solution of less than 20% in amplitude and 5% in phase for forcing periods between one day and one year.

7.5.2 Soil-water phase changes

At high and mid latitudes the phase changes of water in the soil have an important effect on the water and energy transfer in the soil. A proper consideration of the solid phase of soil water requires modifications including, in order of importance:

- *(a)* The thermal effects related to the latent heat of fusion/freezing (e.g. *Rouse* 1984);
- *(b)* Changes in the soil thermal conductivity due to the presence of ice (e.g. *Penner* 1970, not included in TESSEL as mentioned in the previous section);
- *(c)* Suppression of transpiration in the presence of frozen ground (e.g. *Betts et al.* 1998) and already described in Eq. (7.11); and
- *(d)* Soil water transfer dependent on a soil water potential including the effects of frozen water (e.g. *Lundin* 1989), represented in a proxy way by Eq. (7.66).

The latent-heat effects are described in the following. The main impact will be to delay the soil cooling in the beginning of the cold period, and to delay the soil warming in spring, although the latter effect is less important because it occurs when the solar forcing is significant. Both effects make the soil temperatures less responsive to the

atmospheric forcing and damp the amplitude of the annual soil temperature cycle. More details on the soil-freezing scheme and its impact on forecasts and the model climate are described in *Viterbo et al.* 1999.

The soil energy equation, Eq. (7.45), is modified in the presence of soil water phase changes as

$$(\rho C)_{\text{soil}}\frac{\partial T}{\partial t} = \frac{\partial}{\partial z}\left[\lambda_T \frac{\partial T}{\partial z}\right] + L_{\text{fus}}\rho_{\text{w}}\frac{\partial \theta_{\text{I}}}{\partial t} \tag{7.51}$$

where θ_{I} is the volumetric ice-water content. Without loss of generality, for the grid squares characteristic of NWP models it can be assumed that

$$\theta_{\text{I}} = \theta_{\text{I}}(\theta, T) = f(T)\theta \tag{7.52}$$

where θ is the total soil-water content (liquid + ice), and

$$\begin{aligned} f_{\text{fr}}(T) &= 0 \qquad && T > T_{\text{f1}} \\ 0 < f_{\text{fr}}(T) &< 1 \qquad && T_{f1} \le T \le T_{\text{f2}} \\ f_{\text{fr}}(T) &= 1 \qquad && T < T_{\text{f2}} \end{aligned} \tag{7.53}$$

where T_{f1} and T_{f2} are characteristic temperatures limiting the phase change regime. In reality, the values of T_{f1} and T_{f2} and the function $f_{\text{fr}}(T)$ have complicated dependencies on soil texture and composition (see e.g. *Williams and Smith* 1989), but here they are approximated in a simple way. For an idealized homogeneous, one-component soil, $f_{\text{fr}}(T)$ would be a step-function. The physical reasons for having an interval over which melting/freezing is active, rather than a threshold temperature, include (*Williams and Smith* 1989):

(a) Adsorption, resulting from forces between the mineral parts of the soil and the water;
(b) Capillarity, related to the fact that the water-free surface is not plane;
(c) Depression of the freezing point due to the effect of dissolved salts; and
(d) Soil heterogeneity.

To avoid an undesirable coupling between the temperature and water equations in the soil, Eq. (7.52) is simplified to

$$\theta_{\text{I}} = f_{\text{fr}}(T)\theta_{\text{f}} \tag{7.54}$$

where θ_{f} is a constant, representing the amount of soil water that can be frozen (thawed). For simplicity, $\theta_{\text{f}} = (c_{\text{H}} + c_{\text{L}})\theta_{\text{cap}}$. The scaling with the vegetated fractions is the simplest way of distinguishing between dry (vegetation-sparse areas, e.g. deserts) and wet (vegetated) areas. Combining Eq. (7.54) with Eq. (7.51) results in

$$\left[(\rho C)_{\text{soil}} - L_{\text{fus}}\rho_{\text{w}}\frac{\partial f_{\text{fr}}}{\partial T}\right]\frac{\partial T}{\partial t} = \frac{\partial}{\partial z}\left[\lambda_T \frac{\partial T}{\partial z}\right] \tag{7.55}$$

showing that the effect of freezing can be interpreted as an additional soil heat capacity, sometimes referred in the literature as the 'heat-capacity barrier' around freezing; not considering the process of soil water freezing/melting can lead to very large artificial temperature changes that do not occur in nature when sufficient soil water is available.

Finally, function $f_{\text{fr}}(T)$, is given by

$$f_{\mathrm{fr}}(T) = \begin{cases} 0 & T > T_{\mathrm{f1}} \\ 0.5\left\{1 - \sin\left[\dfrac{\pi(T - 0.5T_{\mathrm{f1}} - 0.5T_{\mathrm{f2}})}{T_{\mathrm{f1}} - T_{\mathrm{f2}}}\right]\right\} & T_{\mathrm{f2}} \le T \le T_{\mathrm{f1}} \\ 1 & T < T_{\mathrm{f2}} \end{cases} \tag{7.56}$$

with $T_{\mathrm{f1}} = T_0 + 1$, $T_{\mathrm{f1}} = T_0 - 3$.

7.6 SOIL-WATER BUDGET

The vertical movement of water in the unsaturated zone of the soil matrix obeys the following equation (see *Richards* (1931), *Philip* (1957), *Hillel* (1982), and *Milly* (1982) for the conditions under which Eqs. (7.57) and (7.58) are valid) for the volumetric water content θ:

$$\rho_{\mathrm{w}} \frac{\partial \theta}{\partial t} = -\frac{\partial F_{\mathrm{w}}}{\partial z} + \rho_{\mathrm{w}} S_{\theta} \tag{7.57}$$

ρ_{w} is the water density (kg m^{-3}), F_{w} is the water flux in the soil (positive downwards, kg m^{-2}s^{-1}), and S_{θ} is a volumetric sink term (m^{3}m$^{-3}s^{-1}$), corresponding to root extraction. Using Darcy's law, F_{w} can be specified as:

$$F_{\mathrm{w}} = \rho_{\mathrm{w}}\left(\lambda \frac{\partial \theta}{\partial z} - \gamma\right) \tag{7.58}$$

λ (m^{2}s^{-1}) and γ (m s^{-1}) are the hydraulic diffusivity and hydraulic conductivity, respectively.

Replacing (7.58) in (7.57), specifying $S_{\theta} = S_{\theta}(\theta, z)$, and defining parametric relations for λ and γ as functions of soil water, a partial differential equation for θ is obtained; it can be numerically integrated if the top boundary condition is precipitation minus evaporation minus surface runoff. The bottom boundary condition assumes free drainage. *Abramopoulos et al.* (1988) specified free drainage or no drainage, depending on a comparison of a specified geographical distribution of bedrock depth, with a model-derived water-table depth. For the sake of simplicity the assumption of no bedrock everywhere has been adopted.

7.6.1 Interception

The interception reservoir is a thin layer on top of the soil/vegetation, collecting liquid water by the interception of rain and the collection of dew, and evaporating at the potential rate. The water in the interception reservoir, W_{l}, obeys

$$\rho_{\mathrm{w}} \frac{\partial W_l}{\partial t} = c_{\mathrm{l}} E_{\mathrm{l}} + D + I \tag{7.59}$$

where $c_{\mathrm{l}} E_{\mathrm{l}}$ is the water evaporated by the interception reservoir (or dew collection, depending on its sign), D represents the dew deposition from other tiles, and I (kg m^{-2}s^{-1}) is the interception—the fraction of precipitation that is collected by the interception reservoir and is later available for potential evaporation. Because the interception reservoir has a very small capacity (a maximum of the order of 1 mm, see Eq. (7.2)), it can fill up or evaporate completely in one time step; special care has to be taken in order to avoid numerical problems when integrating Eq. (7.59). In addition, since E_{l} is defined in the vertical diffusion code, it might impose a rate of

evaporation that depletes entirely the interception layer in one time step. In order to conserve water in the atmosphere-intercepted water–soil continuum, the mismatch of evaporation of tile 3 plus dew deposition from the other tiles (which is not explicitely dealt with by the vertical diffusion) as seen by the vertical diffusion and the intercepted water has to be fed into the soil.

The equation is solved in three fractional steps: evaporation, dew deposition, and rainfall interception. The solver provides as outputs

(a) the inteception layer contents at time step $n + 1$, W_l^{n+1};
(b) Throughfall (ie, rainfall minus intercepted water); and
(c) The evaporation effectively seen by the intercepted layer in each tile i.

First, the upward evaporation ($E_l < 0$) contribution is considered; because $C_l E_l$ depends linearly on W_l (see Eq. (7.2)), an implicit version of the evaporating part of (7.59) is obtained by linearizing $C_l(W_l)E_l$:

$$\rho_w \frac{W_l^* - W_l^t}{\Delta t} = C_l(W_l^t)E_l + \frac{E_l}{W_{lm}}(W_l^* - W_l^t) \tag{7.60}$$

where W_l^* is the new value of interception-reservoir content after the evaporation process has been taken into account. After solving for W_l^*, a non-negative value of evaporation is obtained and the evaporation seen by this fractional time step is calculated

$$\begin{aligned} W_l^1 &= \max(0, W_l^*) \\ E^1 &= \rho_w \frac{W_l^1 - W_l^t}{\Delta t} \end{aligned} \tag{7.61}$$

The dew deposition is dealt with explicitely for each non-snow tile in succession, for tiles 3, 4, 6, 7, 8, where tile 7 is also considered because in the exposed snow tile, the canopy is in direct evaporative contact with the atmosphere. When the evaporative flux is downwards ($E_l > 0$)

$$\begin{aligned} W^2 &= W^1 + \min\left(W_{lm} - W^1, \frac{\Delta t}{\rho_w} c_i D_i\right) \\ D_i &= \rho_w \frac{W_{l,i}^2 - W_l^1}{\Delta t} \end{aligned} \tag{7.62}$$

where superscript 2 denotes the final value at the end of the this fractional time step.

The interception of rainfall is considered by applying the following set of equations to large-scale and convective rainfall

$$\begin{aligned} W_l^3 &= W_l^2 + \min\left(W_{lm} - W_l^2, \frac{\Delta t}{\rho_w} b_I (c_H + c_L) R_{ls}\right) \\ T_{ls} &= R_{ls} - \rho_w \frac{W_l^3 - W_l^2}{\Delta t} \\ W_l^{t+1} &= W_l^3 + \min\left(W_{lm} - W_l^3, \frac{\Delta t}{\rho_w} b_I (c_H + c_L) \frac{R_{cv}}{F_{cv}}\right) \\ T_{cv} &= R_{cv} - \rho_w \frac{W_l^{t+1} - W_l^3}{\Delta t} \end{aligned} \tag{7.63}$$

R_{cv}/F_{cv} is a modified convective rainfall flux, computed by applying the heterogeneity assumption that convective rainfall only covers a fraction $F_{cv} = 0.5$ of the grid box, $b_I = 0.25$ is a coefficient of efficiency of interception of rain. The total evaporation seen by the interception reservoir is D_i for tiles 4, 6, 7, and 8 and $c_l E_l + D_i$ for tile 3.

The interception reservoir model described in this section is probably the simplest water-conserving formulation based on Rutter's original proposition (*Rutter et al.* 1972; *Rutter et al.* 1975). For more complicated formulations still based on the Rutter concept see, for instance, *Mahfouf and Jacquemin* (1989), *Dolman and Gregory* (1992), and *de Ridder* (2001).

7.6.2 Soil properties

Integration of Eqs. (7.57) and (7.58) requires the specification of hydraulic conductivity and diffusivity as a function of soil-water content. *Mahrt and Pan* (1984) have compared several formulations for different soil types. The widely used parametric relations of *Clapp and Hornberger* (1978) (see also *Cosby et al.* 1984) are adopted:

$$\gamma = \gamma_{sat}\left(\frac{\theta}{\theta_{sat}}\right)^{2b+3}$$
$$\lambda = \frac{b\gamma_{sat}(-\psi_{sat})}{\theta_{sat}}\left(\frac{\theta}{\theta_{sat}}\right)^{b+2} \qquad (7.64)$$

b is a non-dimensional exponent, γ_{sat} and ψ_{sat} are the values of the hydraulic conductivity and matric potential at saturation, respectively. A minimum value is assumed for λ and γ corresponding to permanent wilting-point water content.

Cosby et al. (1984) tabulate best estimates of b, γ_{sat}, ψ_{sat} and θ_{sat}, for the 11 soil classes of the US Department of Agriculture (USDA) soil classification, based on measurements over large samples. Since the model described here specifies only one soil type everywhere, and because the determination of the above constants is not independent of the values of θ_{cap} and θ_{pwp}, the following procedure is adopted.

A comprehensive review of measurements of θ_{cap} and θ_{pwp} may be found in *Patterson* (1990). Starting from Patterson's estimates of θ_{cap} and θ_{pwp} for the 11 USDA classes, a mean of the numbers corresponding to the medium-texture soils (classes 4, 5, 7, and 8, corresponding to silt loam, loam, silty clay loam and clay loam, respectively) is taken. The resulting numbers are $\theta_{cap} = 0.3\dot{2}3$ m^3m^{-3} and $\theta_{pwp} = 0.171$ m^3m^{-3}. Averaging the values of *Cosby et al.* (1984) for soil moisture and soil-water conductivity at saturation for the same classes gives the numerical values $\gamma_{sat} = 5.57 \times 10^{-6}$ $m\,s^{-1}$ and $\theta_{sat} = 0.472$ m^3m^{-3}. The Clapp and Hornberger expression for the matric potential

$$\psi = \psi_{sat}\left(\frac{\theta}{\theta_{sat}}\right)^{-b} \qquad (7.65)$$

is used with $\psi(\theta_{pwp}) = -153$ m (–15 bar) and $\psi(\theta_{cap}) = -3.37$ m (–0.33 bar) (see *Hillel* 1982; *Jacquemin and Noilhan* 1990) to find the remaining constants b and ψ_{sat}. The results are $b = 6.04$ and $\psi_{sat} = -0.338$ m. The above process ensures a soil that has an availability corresponding to the average value of medium-texture soils, and yields a quantitative definite hydraulic meaning to θ_{cap} and θ_{pwp} compatible with the Clapp and Hornberger relations (see Table 7.2 for a summary of the soil constants).

Finally, the water transport in frozen soil is limited in the case of a partially frozen soil, by considering the effective hydraulic conductivity and diffusivity to be a weighted average of the values for total soil water and a very small

value (for convenience, taken as the value of Eq. (7.64) at the permanent wilting point) for frozen water. The soil properties, as defined above, also imply a maximum infiltration rate at the surface defined by the maximum downward diffusion from a saturated surface. If the throughfall exceeds the maximum infiltration rate, the excess precipitation is put into runoff. However, in practice the maximum infiltration rate is so large that this condition is never reached. Surface runoff is therefore only produced if the soil becomes saturated.

7.6.3 Discretization and the root profile

A common soil discretization is chosen for the thermal and water soil balance for ease of interpretation of the results, proper accounting of the energy involved in freezing/melting soil water, and simplicity of the code. Equations Eqs. (7.57) and (7.58) are discretized in space in a similar way to the temperature equations, ie, soil water and root extraction defined at full layers, θ_k and $\rho_{water} S_{\theta,k}$, and $F_{k+1/2}$ the flux of water at the interface between layer k and $k+1$. The resulting system of equations represents an implicit, water-conserving method.

For improved accuracy, the hydraulic diffusivity and conductivity are taken as (see *Mahrt and Pan* 1984)

$$\begin{aligned} \lambda_{k+1/2} &= (1-f_{fr}^*)\lambda[\max(\theta_k{}^n, \theta_{k+1}^n)] + f_{fr}^*\lambda(\theta_{pwp}) \\ \gamma_{k+1/2} &= (1-f_{fr}^*)\gamma[\max(\theta_k{}^n, \theta_{k+1}^n)] + f_{fr}^*\gamma(\theta_{pwp}) \end{aligned} \tag{7.66}$$

where $f_{fr}^* = \min[f_{fr}(\theta_k), f_{fr}(\theta_{k+1})]$. The boundary conditions are given by

$$\begin{aligned} F_{4+1/2} &= \rho_w \gamma_4 \\ F_{1/2} &= T + M_{sn} - Y_{sfc} + E_{1/2} \end{aligned} \tag{7.67}$$

The difference between throughfall T and surface runoff Y_{sfc} (kg m^{-2}s^{-1}) is the soil infiltration at the surface:

$$\begin{aligned} T &= T_{ls} + T_{cv} \\ Y_{sfc} &= max(0, T_{ls} + M_{sn} - I_{f,mx}) + \frac{\max(0, F_{cv}T_{cv} - I_{f,mx})}{F_{cv}} \\ I_{f,mx} &= \rho_w\left[\lambda_{1/2}\frac{(\theta_{sat}-\theta_1)}{0.5D_1} + \gamma_{1,2}\right] \end{aligned} \tag{7.68}$$

and $\lambda_{1/2} = f_{fr}^*\lambda(\theta_{pwp}) + (1-f_{fr}^*)\lambda(\theta_{sat})$, with a similar equation for $\gamma_{1/2}$. The evaporation at the top of the soil layer, $E_{1/2}$, is computed as the sum of the evaporations of tile 8 plus the contributions necessary to conserve water with the solver of the interception layer:

(a) tile 3 mismatch(after the evaporated water used by the interception reservoir for the given tile is subtracted) ; and

(b) when the evaporative fluxes are downward (i.e., dew deposition), the evaporation for tiles 4, 6 and the canopy evaporation of tile 7.

Root extraction is computed as

$$\rho_w S_{\theta,k} = \sum_i C_i \frac{E_i}{D_k}\frac{R_k\theta_k}{\sum_j R_j\theta_j} \tag{7.69}$$

where the sum over tiles i is done for tiles 4, 6, and 7 (for which only the transpiration is used) and the sum over j is done over all soil levels. In case of dew deposition (i.e., tile downward evaporative flux), $S_{\theta,k} = 0$.

7.7 SEA/LAKE ICE

Any non-land point (i.e., a grid point with land cover less or equal 0.5) can have two fractions, open water and ice. A surface analysis defines the ice fraction, c_{I}, and the temperature of the open water fraction; both quantities are kept constant during the forecast. No distinction is made between surface and skin temperature for the open water fraction (see Table 7.2).

The ice fraction is modelled as an ice slab, with open water underneath and a skin temperature for the thermal contact with the atmosphere. The main caveats in the sea ice parameterization are:

(a) Fixed depth of the slab (which can be relaxed once there is a reliable data set to specify its geographic distribution;

(b) Fixed fraction, which is a reasonable assumption for a 10-day forecast period, and avoids the need for the momentum balance of the ice and its complex rheology (see, e.g., *Flato and Hibler* 1992) and the definition of the ocean currents; and

(c) No snow accumulation on top of the ice (although one of the main effects of snow, i.e., a markedly different surface albedo, is partially emulated by the prescribed seasonal albedo in Table 2.6).

The ice heat transfer is assumed to obey the following Fourier law of diffusion

$$(\rho C)_{\mathrm{I}} \frac{\partial T_{\mathrm{I}}}{\partial t} = \frac{\partial}{\partial z}\left[\lambda_{\mathrm{I}} \frac{\partial T_{\mathrm{I}}}{\partial z}\right] \tag{7.70}$$

where $(\rho C)_{\mathrm{I}} = 1.88 \times 10^{6}\ \mathrm{J\ m^{-3}K^{-1}}$ is the volumetric ice heat capacity, T_{I} is the ice temperature, and $\lambda_{\mathrm{I}} = 2.03\ \mathrm{W\ m^{-1}K^{-1}}$ is the ice thermal conductivity. The boundary condition at the bottom is the temperature of the frozen water, $T_{\mathrm{fr}} = T_0 - 1.7$ and the top boundary condition is the net heat flux at the surface, obtained from the solution of the ice skin thermal budget.

Eq. (7.70) is solved with the ice disretized in four layers, with the depth of the top three layers as in the soil model and the depth of the bottom layer defined as

$$D_{\mathrm{I},4} = D_{\mathrm{I}} - \sum_{j=1}^{3} D_{\mathrm{I},j} \tag{7.71}$$

and the total depth of the ice slab, D_{I}, is prescribed as 1.5 m. In order to ensure a constant ice fraction, the solution of the ice thermal budget is capped to the ice melting temperature, $T_{\mathrm{ml}} = T_0$ at all levels. The details of the numerical discretization can be found in Section 7.8.

7.8 NUMERICAL SOLUTION OF THE SURFACE EQUATIONS

7.8.1 Recap of the analytical equations

The water budget (Eqs. (7.57)–(7.58), with boundary conditions given by Eq. (7.67)), the soil energy budget (Eq. (7.45), with boundary conditions given by Eqs. (7.46)–(7.47)) and the ice energy budget (Eq. (7.70)) can be rewritten in a generalised form as:

$$\frac{\partial \Psi}{\partial t} = \frac{1}{C}\frac{\partial}{\partial z}\left(\lambda\frac{\partial \Psi}{\partial z} - \gamma\right) + S_\Psi \tag{7.72}$$

The meaning of the different variables in each individual equations is summarized Table 7.6, together with the respective upper and lower boundary conditions, F_Ψ.

TABLE 7.6 VARIABLES IN THE GENERALIZED SOIL/ICE TEMPERATURE AND WATER EQUATION.

Equation	Ψ	C	λ	γ	S_Ψ	UBC	LBC
Soil moisture	θ	1	λ_θ	γ_θ	S_θ	$F_\theta = If - c_8 E_8$	$F_\theta = \gamma_\theta$
Soil temperature	T	$(\rho C)_{eff}$	λ_T	0	0	$F_T = H^N$	$F_T = 0$
Ice temperature	T_I	$(\rho C)_I$	λ_I	0	0	$F_I = H^N$	$T_{Ns+1} = T_{0,I}$

UBC and LBC stand for upper and lower boundary condition, respectively

7.8.2 Implicit numerical solution

Eq. (7.72) is time discretized in the following way:

$$\frac{\Psi^{t+1} - \Psi^t}{\Delta t} = \frac{1}{C}\frac{\partial}{\partial z}\left(\lambda\frac{\partial \tilde{\Psi}}{\partial z} - \gamma\right) + S_\Psi \tag{7.73}$$

where

$$\tilde{\Psi} = \alpha_{\text{impl}}\Psi^{t+1} + (1 - \alpha_{\text{impl}})\Psi^t \tag{7.74}$$

and the semi-implicit coefficient, $\alpha_{\text{impl}} = 1$. If the prognostic variable Ψ is defined at full levels and the fluxes F_Ψ are defined at half-levels (the interface between layers), Eq. (7.73) can be discretized in space to give:

$$\begin{aligned}
\frac{\hat{\Psi} - \Psi^t}{\alpha_{\text{impl}}} &= \frac{\Delta t}{C_k}\left(\frac{\lambda_{k-1/2}(\hat{\Psi}_{k-1} - \hat{\Psi}_k)}{\Delta z_k \Delta z_{k-1/2}} - \frac{\lambda_{k-1/2}(\hat{\Psi}_k - \hat{\Psi}_{k+1})}{\Delta z_k \Delta z_{k+1/2}} + \frac{\gamma_{k-1/2} - \gamma_{k+1/2}}{\Delta z_k}\right) + \Delta t S_{\Psi,k} \qquad k = 2, \ldots, Ns-1 \\
\frac{\hat{\Psi} - \Psi^t}{\alpha_{\text{impl}}} &= \frac{\Delta t}{C_k}\left(\frac{F_\Psi^T}{\Delta z_k} - \frac{\lambda_{k-1/2}(\hat{\Psi}_k - \hat{\Psi}_{k+1})}{\Delta z_k \Delta z_{k+1/2}} + \frac{\gamma_{k-1/2} - \gamma_{k+1/2}}{\Delta z_k}\right) + \Delta t S_{\Psi,k} \qquad k = 1 \\
\frac{\hat{\Psi} - \Psi^t}{\alpha_{\text{impl}}} &= \frac{\Delta t}{C_k}\left(\frac{\lambda_{k-1/2}(\hat{\Psi}_{k-1} - \hat{\Psi}_k)}{\Delta z_k \Delta z_{k-1/2}} - \underbrace{\frac{\lambda_{k-1/2}(\hat{\Psi}_k - \hat{\Psi}_{k+1})}{\Delta z_k \Delta z_{k+1/2}}}_{I} + \frac{\gamma_{k-1/2} - \gamma_{k+1/2}}{\Delta z_k}\right) + \Delta t S_{\Psi,k} \qquad k = Ns
\end{aligned} \tag{7.75}$$

where the horizontal brace means that the term exists only for the ice temperature equation (because of the bottom temperature boundary condition for ice) and Δz_k, z_k, $z_{k-1/2}$, and $z_{k+1/2}$ represent the thickness of layer k, and the depths of its centre, the top and the bottom interface, respectively:

$$\begin{aligned}
\Delta z_k &= D_k = z_{k+1/2} - z_{k-1/2} \\
\Delta z_{k+1/2} &= z_{k+1} - z_k
\end{aligned} \tag{7.76}$$

Eq. (7.75) leads to a triadiagonal system of equations:

$$
\begin{aligned}
&\frac{\hat{\Psi}_{k-1}}{\alpha_{\text{impl}}}\left(\frac{\hat{\lambda}_{k-1/2}}{C_k\Delta z_k}\right)+\frac{\hat{\Psi}_k}{\alpha_{\text{impl}}}\left(1+\frac{\hat{\lambda}_{k-1/2}}{C_k\Delta z_k}+\frac{\hat{\lambda}_{k+1/2}}{C_k\Delta z_k}\right)-\frac{\hat{\Psi}_{k+1}}{\alpha_{\text{impl}}}\left(\frac{\hat{\lambda}_{k+1/2}}{C_k\Delta z_k}\right)\\
&\qquad=\left(\frac{\Psi_k^t}{\alpha_{\text{impl}}}+\Delta t\left(\frac{\gamma_{k-1/2}-\gamma_{k+1/2}}{C_k\Delta z_k}\right)+\Delta t S_{\Psi,k}\right) \qquad k=2,\ldots,Ns-1\\
&\frac{\hat{\Psi}_k}{\alpha_{\text{impl}}}\left(1+\frac{\hat{\lambda}_{k+1/2}}{C_k\Delta z_k}\right)-\frac{\hat{\Psi}_{k+1}}{\alpha_{\text{impl}}}\left(\frac{\hat{\lambda}_{k+1/2}}{C_k\Delta z_k}\right)-\frac{F_\Psi^T}{C_k\Delta z_k}\\
&\qquad=\frac{\Psi_k^t}{\alpha_{\text{impl}}}+\Delta t\left(\frac{\gamma_{k-1/2}-\gamma_{k+1/2}}{C_k\Delta z_k}\right)+\Delta t S_{\Psi,k} \qquad k=1\\
&-\frac{\hat{\Psi}_{k-1}}{\alpha_{\text{impl}}}\left(\frac{\hat{\lambda}_{k-1/2}}{C_k\Delta z_k}\right)+\frac{\hat{\Psi}_k}{\alpha_{\text{impl}}}\left(1+\frac{\hat{\lambda}_{k-1/2}}{C_k\Delta z_k}+\underbrace{\frac{\hat{\lambda}_{k+1/2}}{C_k\Delta z_k}}_{I}\right)-\underbrace{\frac{\hat{\Psi}_{k+1}}{\alpha_{\text{impl}}}\left(\frac{\hat{\lambda}_{k+1/2}}{C_k\Delta z_k}\right)}_{I}\\
&\qquad=\frac{\Psi_k^t}{\alpha_{\text{impl}}}+\Delta t\left(\frac{\gamma_{k-1/2}-\gamma_{k+1/2}}{C_k\Delta z_k}\right)+\Delta t S_{\Psi,k} \qquad k=Ns
\end{aligned}
\tag{7.77}
$$

with the generalized modified diffusivities, $\hat{\lambda}_{k-1/2}$, defined as:

$$
\begin{aligned}
&\hat{\lambda}_{k-1/2}=\frac{\Delta t\,\alpha_{\text{impl}}\lambda_{k-1/2}}{\Delta z_{k-1/2}}\\
&I\begin{cases}\Delta z_{Ns+1/2}=D_{Ns}/2\\ \hat{\Psi}_{Ns+1}=T_{0,I}\end{cases}
\end{aligned}
\tag{7.78}
$$

where D_{Ns} is the depth of the deepest soil layer. The discretization above conserves water (energy) and is linearly stable. The coefficients λ and γ are a function of variable at the current time step, Ψ^n.

7.9 CODE

The surface parameterization computations are shared between the vertical diffusion routine (VDFMAIN, see Chapter 3) and the main surface routine, SRFMAIN. In VDFMAIN, the tile fluxes and skin temperatures are computed: After the elimination part of the tridiagonal system of equations is computed, the energy budget for each tile is computed before back-substition.

At the start of the model integration, the following setup routine is called to initialize a module specific to the soi-code:

- SUSOIL. Setup routine for soil/snow/ice constants.

The main subroutine of the surface code (SRFMAIN) is called from CALLPAR, with: (a) values of the surface prognostic equations at time step n, convective and large scale rainfall and snowfall, tile evaporation, sensible and latent heat fluxes, and temperatures, net surface longwave flux, tile net shortwave flux as inputs; and (b) tendencies for the surface prognostic variables, plus a comprehensive set of diagnostic arrays as outputs. SRFMAIN does a sequence of computations and subroutine calls:

- SRFSN. Solution of the snow energy and water budget and computation of the next time step density and albedo fields. Inputs: snow depth, temperature, density and albedo at the current time step, soil temperature, shortwave and longwave radiation fluxes, snowfall, and tile fluxes. Outputs: snow depth, temperature, density and albedo at the next time step, meltwater flux, and basal heat flux.
- SRFRCG. Computes apparent soil heat capacity, ie including effects of soil freezing. Inputs: soil temperature and vegetation covers. Output is volumetric heat capacity.
- SRFT. Solution of the soil heat budget. Inputs: Soil temperature, soil moisture, longwave radiative flux, snow basal heat flux, volumetric heat capacity, tile evaporation, sensible heat flux and shortwave radiative flux. Output: Soil temperature at the next time step. First the modified heat diffusivity, the soil energy per unit area and the right-hand sice of the system of equations are computed. The generalized surface tridiagonal solver, SRFWDIF, is called to solve for the semi-implicit variable, $\hat{T}/\alpha$. The soil temperatures for the next time step are computed at the end.
- SRFI. Solution of the ice heat budget. Inputs: Ice temperature, longwave radiative flux, tile evaporation, sensible heat flux and shortwave radiative flux. Output: Ice temperature at the next time step. First the modified heat diffusivity, the ice energy per unit area and the right-hand sice of the system of equations are computed. The generalized surface tridiagonal solver, SRFWDIF, is called to solve for the semi-implicit variable, $\hat{T}_I/\alpha$. The ice temperatures for the next time step are computed at the end.
- SRFWL. Solution of the interception layer water budget. Inputs: Interception layer contents, low and high vegetation water cover, maximum capacity of the interception layer, convective and large scale rainfall, snow evaporation of shaded snow tile, and tile evaporation. Outputs: Interception layer at next time step, convective and large scale throughfall and tile evaporation collected (or depleting) the interception layer.
- SRFWEXC. First part of the computation of the soil water budget, ie, computation of the coefficients of the tridiagonal system of equations for $\hat{\theta}$. This includes the partitioning of transpiration into root extraction at the different layers and soil hydraulic coefficients including the effect of frozen water. Inputs: Soil moisture and temperature, convective and large-scale throughfall, snowmelt, tile evaporation, tile evaporation collected (or depleting) the interception layer, and snow evaporation of the shaded snow tile. Outputs: Modified diffusivity for water, right-hand side of the tridiagonal system, and layer depths.
- SRFWDIF. Generalized surface tridiagonal solver. Inputs: Values of ψ at the current time step, generalized modified diffusivities, soil energy (or water) per unit area, and right-hand side of equations. Output: $\hat{\psi}/\alpha$. The routine computes the coefficients on the left-hand side of the equations and solves the equations using and LU-decomposition and back substitution in one downward scan and one upward scan.
- SRFWINC. Computation of next time step soil water. Inputs: $\hat{\theta}/\alpha$ and current time step soil water. Output: next time step soil water.
- SRFWNG. Bounded-value operator for intercepted water (limited to non-negative values and values below or equal the maximum contents of the interception layer) and soil water (limitted to non-negative values and values below or equal saturation). The "soil column" is scanned from top to bottom and the amount of water needed to satisfy physical limits in each layer are borrowed from the layer below. The water exchanged in this way is accounted for as runoff. Inputs: next time step intercepted water and soil water. Output: Bounded values of the same quantities.

Relevant routines from the vertical diffusion code, discussed in full detail in Chapter 3, include:

- SUVEG. Assignment of vegetation related constants.

- VDFBC. Definition of tile fractions and related characteristics.
- VDFSURF. Definition of bare soil resistance, low and high canopy resistances.
- VDFEXCS. Computation of aerodynamical part of exchange coefficients for heat and moisture, including stability computations.
- VDFEVAP. Computation of evapotranspiration for each tile.
- VDFSFLX. Surface fluxes for each tile, defined at time t.
- VDFTSK. Computation of the tile skin temperatures, as a the solution of the tile energy balance.
- VDFTFLX. Computation of the tile fluxes at time $t + 1$.

Part IV: PHYSICAL PROCESSES

CHAPTER 8 Methane oxidation

Table of contents

8.1 INTRODUCTION

A study of stratospheric humidity in analyses and multi-year simulations has shown that the ECMWF system prior to 1999 was capable of producing a broadly realistic distribution of water vapour at, and immediately above, the tropopause, and that the slow upward transfer of water vapour in the tropical stratosphere could be captured quite reasonably given sufficiently fine vertical resolution in the model (*Simmons et al*. 1999). However, values of water vapour in the tropical upper stratosphere, and throughout much of the extratropical stratosphere, were too low. This deficiency has now been remedied by the introduction of a simple parametrization of the upper-stratospheric moisture source due to methane oxidation. A sink representing photolysis in the mesosphere is also included. The scheme was derived as a simplification of an approach adopted by Peter Stott and Anne Pardaens at the Department of Meteorology, University of Edinburgh, notes on which and helpful references were supplied by Bob Harwood.

8.2 METHANE OXIDATION

Methane is produced by natural and anthropogenic sources at the earth's surface, and is well-mixed in the troposphere. Its volume mixing ratio is currently around 1.7 ppmv. It is carried upwards in the tropical stratosphere and decreases in relative density (due to oxidation) to values of around 0.2–0.4 ppmv around the stratopause. Mean stratospheric descent at higher latitudes results in relatively low values of methane at these latitudes in the middle and lower stratosphere.

Brasseur and Solomon (1984) provide an account of the chemistry of carbon compounds in the stratosphere and mesosphere. The long chain of reactions starting from methane (CH_4) ends with the production of water vapour (H_2O) and molecular hydrogen (H_2) in the stratosphere and mesosphere. This occurs such that the sum

$$2[CH_4] + [H_2O] + [H_2]$$

is approximately uniformly distributed in the absence of precipitation, where [ ] denotes a volume mixing ratio. *Le Texier et al.* (1988) provide calculations of the relative amounts of H_2O and H_2, showing that the predominant production is that of water vapour in the vicinity of the stratopause. They indicate, however, that H_2 production in the mesosphere, and relatively strong descent in winter and early spring at high latitudes, may result in the upper

stratosphere being relatively dry in these seasons and latitudes.

There is, nevertheless, good observational evidence that over much of the stratosphere the quantity

$$2[CH_4] + [H_2O]$$

is quite uniformly distributed with a value somewhat over 6 ppmv. *Jones et al.* (1986) provide evidence for this from the LIMS and SAMS instruments on the Nimbus 7 satellite launched in 1978, and a particularly clear demonstration is given by *Bithell et al.* (1994) based on HALOE data from the UARS satellite. In a pressure–latitude section at about the austral spring equinox, *Bithell et al.* show the result to fail significantly only below 10 hPa in the high-latitude southern hemisphere due, presumably, to condensation at the very cold temperatures in the Antarctic polar vortex.

Prior to cycle 25r1 of the IFS, the parametrization used the value 6 ppmv for the sum $2[CH_4] + [H_2O]$. This version was used in production of the ERA-40 reanalyses, which have been found to be generally drier in the stratosphere than the climatology derived by Randel *et al.* (1998) from UARS measurements. From cycle 25r1 onwards, the parametrization uses the value 6.8 ppmv, based on Randel *et al.*'s data as presented in Fig. 8.1 .

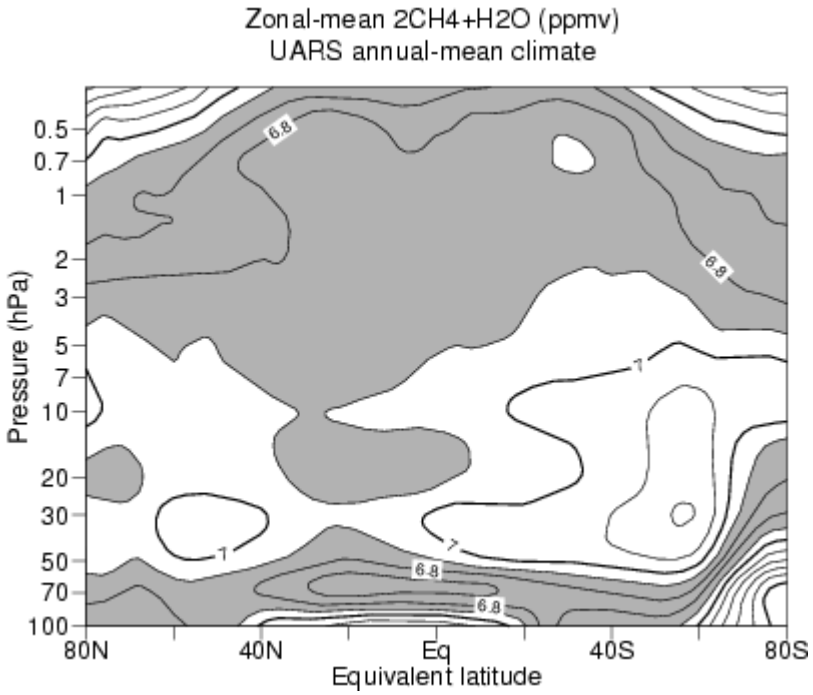

Figure 8.1 Annual-mean distribution of the sum of twice the volume mixing ratio of methane and of the mixing ratio of water vapour (ppmv) as a function of pressure and potential vorticity (expressed as equivalent latitude), derived from UARS (HALOE, supplemented by CLAES and MLS) data analysed by Randel *et al.* (1998). The contour interval is 0.1 ppmv, and shading denotes the range 6.6-6.9 ppmv.

8.3 THE PARAMETRIZATION

8.3.1 Methane oxidation

We assume that the volume mixing ratio of water vapour $[H_2O]$ increases at a rate

$$2k_1[CH_4] \tag{8.1}$$

We further assume that

$$2[CH_4] \;=\; 6.8 \text{ ppmv} - [H_2O] \tag{8.2}$$

The rate of increase of volume mixing ratio of water vapour (in ppmv) is thus

$$k_1(6.8 - [H_2O]) \tag{8.3}$$

In terms of specific humidity, q, the source is

$$k_1(Q - q) \tag{8.4}$$

where (having divided by 1.6×10^6 to convert from volume mixing ratio in ppmv to specific humidity) the parameter Q has the value 4.25×10^{-6}, or 4.25 mg/kg.

The rate k_1 could be determined, for example, from a 2-D model with comprehensive chemistry, as in the scheme developed at Edinburgh University. However, in this first scheme for use at ECMWF we prescribe a simple analytical form for k_1 which varies only with pressure.

The photochemical life time of water vapour is of the order of 100 days near the stratopause, 2000 days at 10 hPa, and effectively infinite at the tropopause (*Brasseur and Solomon* 1984). A prescription of k_1 that gives a reasonable profile up to the stratopause is provided by

$$k_1 \;=\; \frac{1}{86400\tau_1} \tag{8.5}$$

where k_1 is given in s^{-1} and the timescale, τ_1, in days, is given in terms of pressure, p, in Pa, by:

$$\tau_1 \;=\; \begin{cases} 100 & p \le 50 \\ 100\left[1 + \alpha_1 \dfrac{\{\ln(p/50)\}^4}{\ln(10000/p)}\right] & 50 < p < 10000 \\ \infty & p \ge 10000 \end{cases} \tag{8.6}$$

where we define

$$\alpha_1 \;=\; \frac{19\ln 10}{(\ln 20)^4} \tag{8.7}$$

to give a time-scale of 2000 days at the 10 hPa level.

This parametrization moistens rising air in the tropical stratosphere. This air will earlier have been freeze-dried near the tropopause, where specific humidities can locally fall well below 1 mg/kg. Specific humidities approaching the value Q will be reached near the stratopause. Descent near the poles will bring down air with specific humidity close to Q. Expression (8.4) will then yield a source term that is weaker in polar than in tropical latitudes, so reasonable results may be obtained without imposing a latitudinal variation of k_1. (Strictly, k_1 should vanish in the polar night, where photodissociation does not produce the excited oxygen O(^{1}D), which in turn produces the OH radical, these two species being intimately involved in the production of water vapour from methane).

8.3.2 Photolysis in the mesosphere

For model versions with an uppermost level at 0.1 hPa, or lower, there is no strong need to include the sink of water vapour that occurs in the mesosphere and above due to photolysis. However, for completeness we include a simple representation of this effect, modifying the source term (8.4) by adding a decay term $-k_2 q$ above a height of about 60 km. The full source/sink term becomes

$$k_1(Q-q)-k_2 q \tag{8.8}$$

As for k_1 we take k_2 independent of latitude with parameters chosen to match the vertical profile of photochemical lifetime presented by *Brasseur and Solomon* (1984). Specifically,

$$k_2 = \frac{1}{86400\tau_2} \tag{8.9}$$

with

$$\tau_2 = \begin{cases} 3 & p \le 0.1 \\ \left[\exp\left\{\alpha_2 - 0.5(\ln 100 + \alpha_2)\left(1+\cos\frac{\pi \ln(p/20)}{\ln 0.005}\right)\right\} - 0.01\right]^{-1} & 0.1 < p < 20 \\ \infty & p \ge 20 \end{cases} \tag{8.10}$$

and

$$\alpha_2 = \ln\left(\frac{1}{3}+0.01\right) \tag{8.11}$$

The vertical profile of the photochemical lifetime of the combined scheme, $(k_1+k_2)^{-1}$, is shown below in Fig. 8.2, in which we have converted to height as a vertical coordinate assuming an isothermal atmosphere with a temperature of 240 K. Comparison of this profile with that for H_2O shown in Fig. 5.21 of *Brasseur and Solomon* (1984) indicates reasonable agreement.

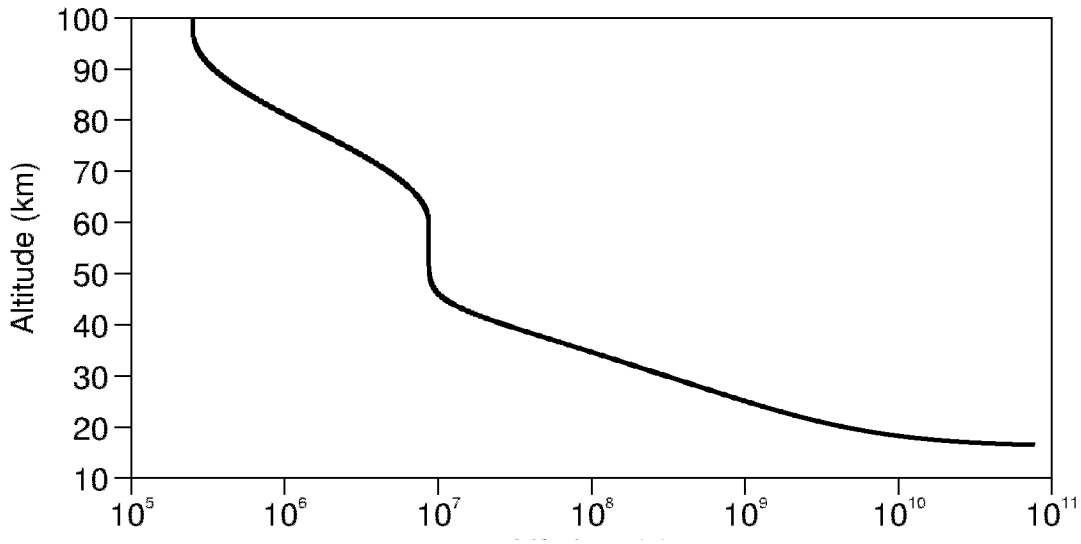

Figure 8.2 Combined photochemical lifetime, $(k_1 + k_2)^{-1}$, as a function of altitude for the analytical specification given by equations (8.5) to (8.7) and (8.9) to (8.11).

8.4 CODE

The calculations for methane oxidation and photolysis of water vapour are performed in subroutine METHOX.

This routine calculates the tendency of water vapour due to methane oxidation and due to photolysis following (8.8). The order of the calculations is as follows:

- find time-scale for methane oxidation following (8.6)
- solve first part of (8.8)
- find time-scale for water vapour photolysis following (8.10)
- solve second part of (8.8)

The setup of the constants used in METHOX is performed in SUMETHOX which is called from SUPHEC. The constants are kept in module YOEMETH. The controlling switch for the methane oxidation is LEMETHOX which is part of namelist NAEPHY.

Part IV: PHYSICAL PROCESSES

CHAPTER 9 Ozone chemistry parametrization

Table of contents

9.1 INTRODUCTION

Ozone is fully integrated into the ECMWF forecast model and analysis system as anadditional three-dimensional model and analysis variable similar to humidity. The forecast model includes a prognostic equation for the ozone mass mixing ratio (kg/kg)

$$\frac{\mathrm{d}O_3}{\mathrm{d}t} = R_{O_3} \tag{9.1}$$

where R_{O_3} is a parameterization of sources and sinks of ozone. Without such a source/sink parameterization the ozone distribution would drift to unrealistic values in integrations longer than a few weeks. The source/sink parameterization must maintain a realistic ozone distribution over several years of integration, without reducing the dynamic variability of ozone. In addition, we would like the parameterization to be able to create an Antarctic ozone hole when the conditions are right.

9.2 THE ECMWF OZONE PARAMETERIZATION

The parameterization used in the ECMWF model is an updated version of Cariolle and Déqué (1986), which has been used in the ARPEGE climate model at Météo-France. This parameterization assumes that chemical changes in ozone can be described by a linear relaxation towards a photochemical equilibrium. It is mainly a stratospheric parameterization. The relaxation rates and the equilibrium values have been determined from a photochemical model, including a representation of the heterogeneous ozone hole chemistry. The updated version of the parameterization (with coefficients provided by Pascal Simon, Météo-France) is

$$R_{O_3} = c_0 + c_1(O_3 - \overline{O_3}) + c_2(T - \overline{T}) + c_3\left(O_3^{\uparrow} - \overline{O_3^{\uparrow}}\right) + c_4(Cl_{EQ})^2 O_3 \tag{9.2}$$

where

$$O_3^{\uparrow}(p) = -\int_{p^0} \frac{O_3(p')}{g}\mathrm{d}p' \tag{9.3}$$

Here c_i are the relaxation rates and T, $\overline{O_3}$, and $\overline{O_3^{\uparrow}}$ are photochemical equilibrium values, all functions of latitude, pressure, and month. Cl_{EQ} is the equivalent chlorine content of the stratosphere for the actual year, and is the

only parameter that varies from year to year (see Fig. 9.1). For the ECMWF model it was necessary to replace the photochemical equilibrium values for ozone with an ozone climatology (Fortuin and Langematz, 1995) derived from observations. The heterogeneous part is only turned on below a threshold temperature of 195 K.

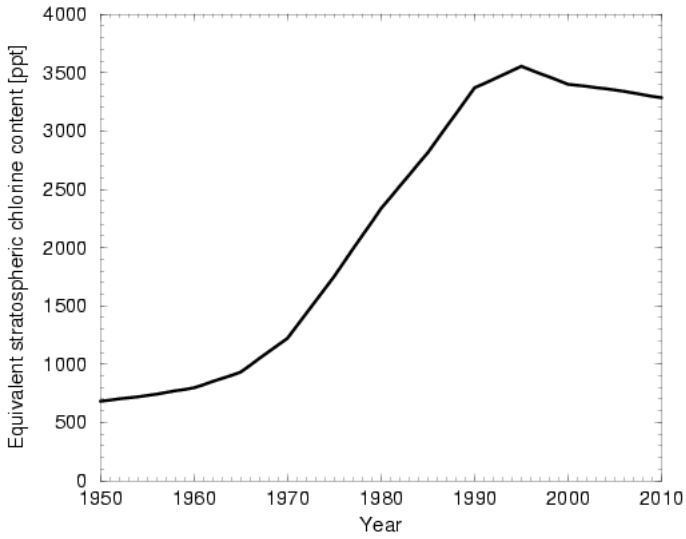

Figure 9.1 Equivalent chlorine content of the stratosphere in ppt for the heterogeneous chemistry part of the ozone source/sink parameterization (provided by Pascal Simon, Météo-France).

Part IV: PHYSICAL PROCESSES

CHAPTER 10 Climatological data

Table of contents

10.1 INTRODUCTION

The ECMWF model uses a series of climate fields of different origin which have different resolution and different projections. *Brankovic and Van Maanen* (1985) describe a set of programs (known as PREPCLIM software) to interpolate the different fields to the requested target resolution. The software handles all the target resolutions that are in use at ECMWF and either full or reduced Gaussian grids. Grid areas at the model resolution are referred to as ECMWF or model grid squares. This appendix describes the different climate fields and the procedures to derive the fields that are needed by the model.

10.2 TOPOGRAPHIC DATA

The model orography and land use fields are based on the terrain elevation data set GTOPO30 at 30” resolution (Gesch and Larson, 1998), the terrain elevation data for Greenland KMS DEM also at 30” resolution (Ekholm, 1996) and the Global Land Cover Characteristics (GLCC) data set at 1 km resolution.

The GTOPO30 data set, as used in the IFS, was completed in 1996 through a collaborative effort led by the US Geological Survey’s Data Centre (EDC, see http://edcwww.cr.usgs.gov/landdaac/gtopo30/gtopo30.html) and was derived from a variety of information sources. It contains terrain elevation above mean sea level at a resolution of 30 arc seconds with -9999 code for sea points. A lake mask is not included.

Greenland KMS DEM replaces GTOPO30 for the Greenland area, because of the better accuracy of the Greenland data.

The Global Land Cover Characteristics (GLCC) data set has been derived from 1 year of Advanced Very High Resolution Radiometer (AVHRR) data, digital elevation models, ecoregions and map data. The nominal resolution is 1 km, and the data comes on a Goode Homolosine global projection. The data base provides for each pixel a biome classification based on several of the popular classifications, including BATS, SiB and SiB2. The BATS

classification has been adopted for the IFS because it contains inland water as one of its classes.

Due to their high resolution and global coverage, these data sets are rather big and therefore difficult to handle by the standard PREPCLIM software. Therefore the original data has been converted to an intermediate resolution of 2'30" which is much easier to handle by the standard PREPCLIM software. The derived 2'30" data set contains the following fields:

- Mean elevation above mean sea level
- Land fraction
- Lake fraction
- Fractional cover for all 20 BATS biome classes (see Table 10.1

TABLE 10.1 LAND USE CLASSIFICATION ACCORDING TO BATTS

Index	Vegetation type	H/L veg
1	Crops, Mixed Farming	L
2	Short Grass	L
3	Evergreen Needleleaf Trees	H
4	Deciduous Needleleaf Trees	H
5	Deciduous Broadleaf Trees	H
6	Evergreen Broadleaf Trees	H
7	Tall Grass	L
8	Desert	-
9	Tundra	L
10	Irrigated Crops	L
11	Semidesert	L
12	Ice Caps and Glaciers	-
13	Bogs and Marshes	L
14	Inland Water	-
15	Ocean	-
16	Evergreen Shrubs	L
17	Deciduous Shrubs	L
18	Mixed Forest/woodland	H
19	Interrupted Forest	H
20	Water and Land Mixtures	L

Finally, also the original US-Navy 10' data is still used for the subgrid orography contribution to the roughness length. It contains the average terrain height of each grid element, as well as maximum and minimum height, number and orientation of significant ridges, and percentages of water and urban areas. In future the roughness length computation will be upgraded to make optimal use of the high resolution GTOPO30 data.

10.3 MEAN OROGRAPHY

Orography, or geopotential height, is derived from the 2'30" data by averaging. Source and target grid are overlaid, and weighted averages are computed by considering the fractions of source grid areas that cover the target grid square.

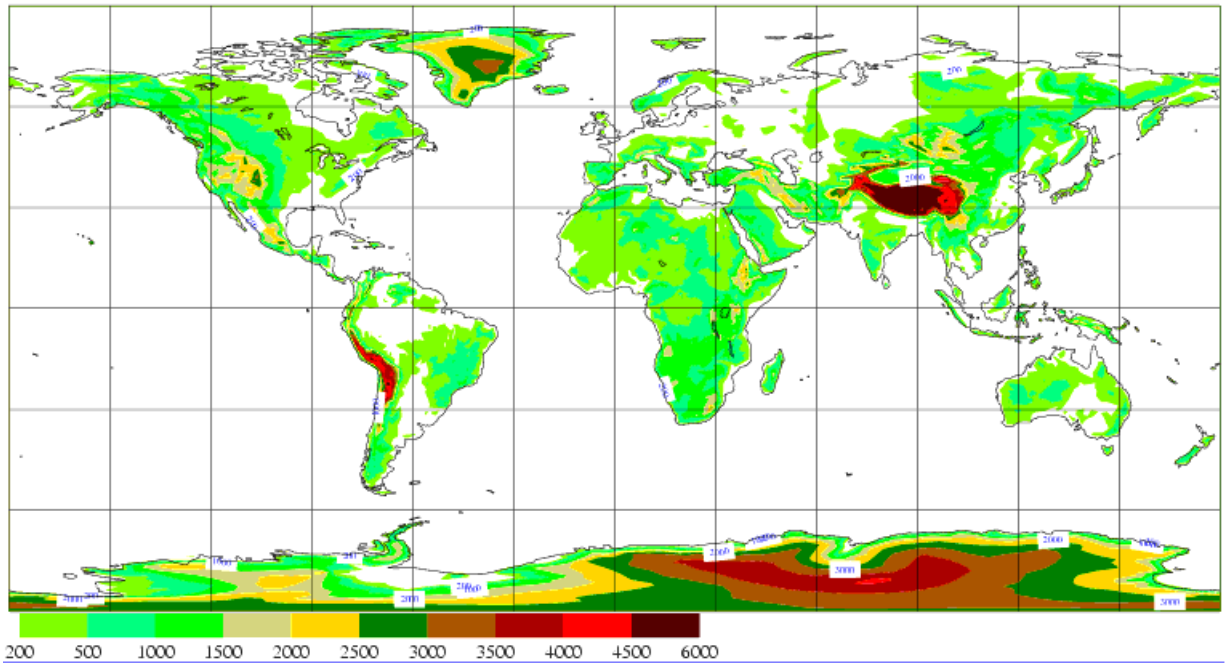

Figure 10.1 Orography at T511 resolution.

The orography is spectrally fitted to ensure consistency in spectral space between the orography and the model resolution. Smoothing is applied in spectral space with a ∇^4 operator, where damping by a factor 5 is applied to the smallest scales. This applies to all operational resolutions (T_L95, T_L159, T_L255, T_L319 and T_L511). Orographic ripples appear as a consequence of the spectral fitting. Fig. 10.1 shows the orography at T511 resolution.

10.4 LAND SEA MASK

Each grid point of the model is provided with a land fraction parameter, derived from the 2'30" data. The model converts this parameter into a mask where grid points that have more than 50% land are considered as land points.

10.5 ROUGHNESS LENGTHS

The model uses 'effective' roughness lengths for momentum (z_{0m}) and heat/moisture (z_{0h}) in the surface boundary conditions for wind and temperature/moisture respectively. These parameters represent the effect on turbulent transport of small-scale surface elements ranging from vegetation and small-scale obstacles to subgrid orography. The roughness lengths area a blend of three contributions: vegetation, urbanization and subgrid orography (see Figs. 10.2 and 10.3). The following procedure is applied:

(a) The vegetation roughness length is taken from a $5° \times 5°$ grid from Munich University (*Baumgartner et al.*, 1977) and interpolated to the requested model grid. Symbols z_{0mVeg} and z_{0hVeg} will be used for the pure vegetation roughness lengths.

(b) The fraction of urbanisation F_{Urb} is computed for every model grid square from the US-Navy data.

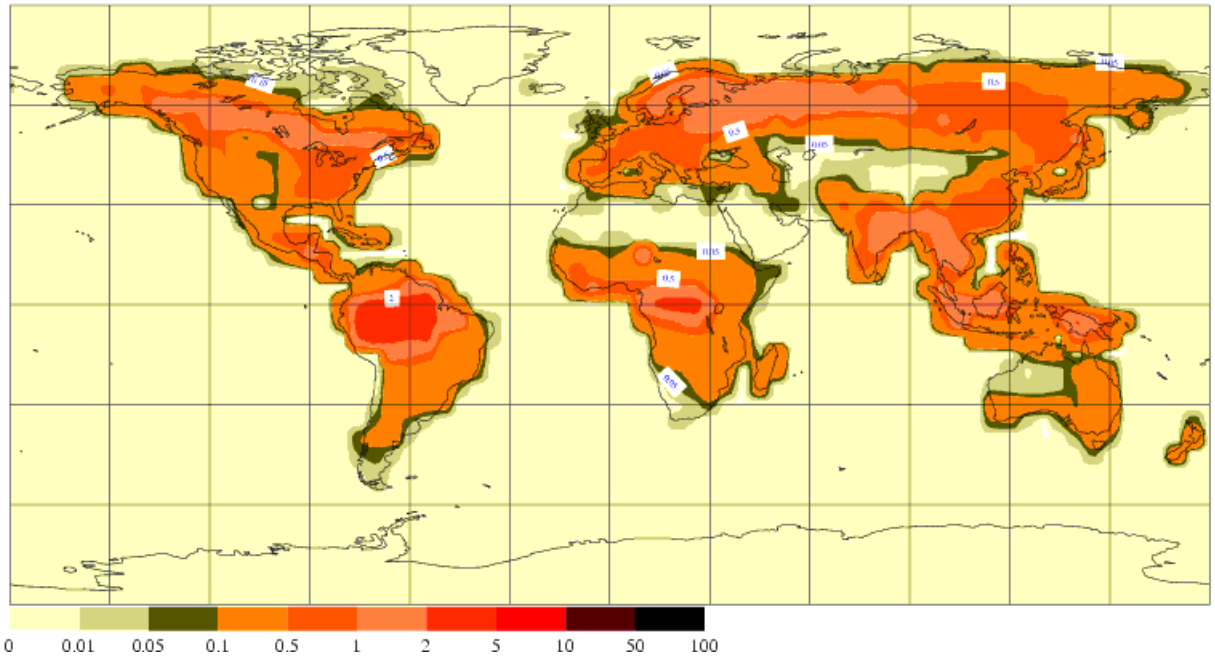

Figure 10.2 (a) Roughness length for vegetation $z_{0\mathrm{mVeg}}$ as provided by Baumgartner et al. (1977) on a $5° \times 5°$ grid.

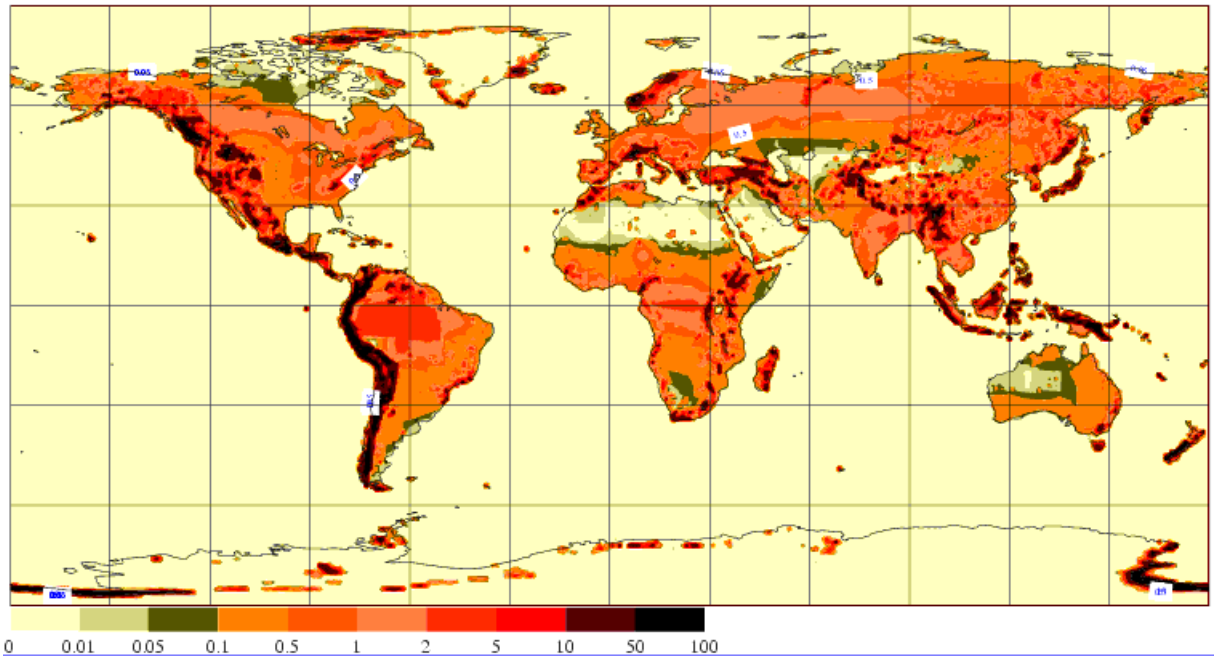

Figure 10.2 (b) The roughness length field including orographic effects (as used by the model) $z_{0\mathrm{m}}$ at T511 resolution plotted on a $1° \times 1°$ grid.

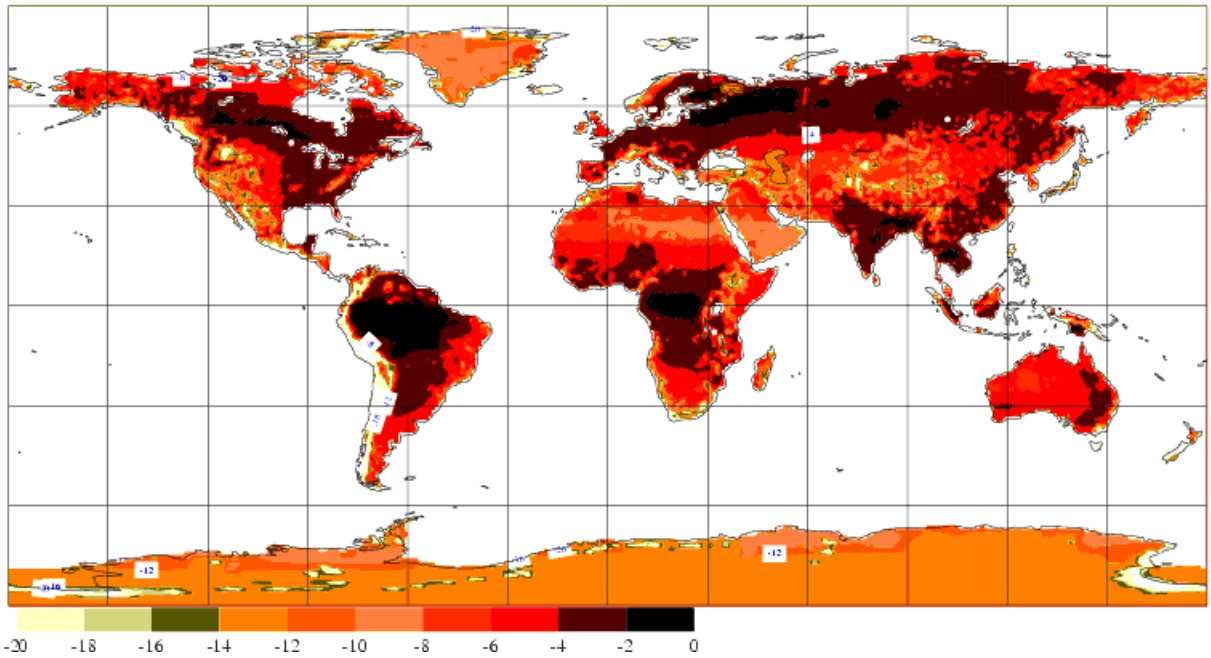

Figure 10.3 Logarithm of the effective roughness length for heat/moisture z_{0h} at T511 resolution.

(a) The vegetation roughness length for momentum z_{0mVeg} is blended with the urbanization roughness length (z_{0mUrb}) using a blending height h_U. The blending-height concept is based on the idea that internal boundary layers merge at a certain height which depends on the horizontal scale of the inhomogeneities (*Claussen* 1990). Below the blending height the different areas have their own logarithmic profile and the resulting stresses are averaged proportional to the area covered by the different roughness lengths. An effective roughness is defined such that over a homogeneous surface it would provide the same drag as the average over the two different surfaces. The effective roughness length z_{0mVeg1} due to fraction F_{Urb} with roughness length z_{0mUrb} and fraction $(1-F_{Urb})$ with roughness length z_{0mVeg} can be found by solving:

$$\frac{1}{\left[\ln\left(\frac{h_U}{z_{0mVeg1}}+1\right)\right]^2} = \frac{F_{Urb}}{\left[\ln\left(\frac{h_U}{z_{0mUrb}}+1\right)\right]^2} + \frac{1-F_{Urb}}{\left[\ln\left(\frac{h_U}{z_{0mVeg}}+1\right)\right]^2}$$

The blended roughness length for heat z_{0hVeg1} is computed from

$$\ln\left(\frac{h_U}{z_{0hVeg1}}+1\right) = \ln\left(\frac{h_U}{z_{0hVeg}}+1\right)\frac{\ln\left(\frac{h_U}{z_{0mVeg}}+1\right)}{\ln\left(\frac{h_U}{z_{0mVeg1}}+1\right)},$$

where $h_U = 100$ m, $z_{0hVeg} = z_{0mVeg}/10$ and $z_{0mUrb} = 2.5$ m.

(b) To compute the orographic contribution to the roughness lengths, a slope parameter (S_l) is needed and a characteristic height (h) of the subgrid orography. From these the typical horizontal scale of

the subgrid orography can be derived (λ). Because the horizontal scales up to 10 km are the most important ones for the roughness lengths, we use also US-Navy information about maximum height, minimum height and number of significant ridges inside the $30' \times 30'$ squares. Two contributions to the subgrid standard deviation are computed (i.e. subgrid to the ECMWF model): the standard deviation σ_r resolved by the $30' \times 30'$ data and the standard deviation σ_s subgrid to the $30' \times 30'$ data

$$\sigma_r^2 = \sum_i p_i h_i^2 - \left(\sum_i p_i h_i\right)^2$$
$$\sigma_s^2 = \sum_i p_i \frac{1}{4}(h_i - h_i^{\min})(h_i^{\max} - h_i)$$
$$\sigma^2 = \sigma_r^2 + \sigma_s^2$$

where:

N	=	Number of relative h_i maxima in the ECMWF grid square,
F	=	Surface area of the ECMWF grid square,
n_i	=	Number of significant ridges in the *i*th $10'$ grid square,
h_i	=	Mean height in the *i*th $10'$ grid square,
$h_i^{\max}$	=	Maximum height in the *i*th $10'$ grid square,
$h_i^{\min}$	=	Minimum height in the *i*th $10'$ grid square,
f_i	=	Surface area of the *i*th $10'$ grid square6
p_i	=	Proportion of the ECMWF grid square occupied by the *i*th $10'$ grid square.

Mason (1991) uses slope parameter $S_l = \sum A/F$, where the summation is over all obstacles in area F (an ECMWF grid square) and A is the frontal, or wind-swept area, of the obstacles. The swept area of the resolved part is estimated from σ_r and the number of relative maxima in the ECMWF grid square N. We assume that the height difference between valleys and hill tops is about $4\sigma_r$. So the resolved part of $\sum A/F$ is (assuming that the individual hills have a vertical dimension of $4\sigma_r$ and a horizontal dimension of $\sqrt{F/N}$ and that there are N hills in a grid square):

$$\left(\frac{\sum A}{F}\right)_r = \frac{4\sigma_r\sqrt{F/N}N}{F}$$
$$= 4\sigma_r\sqrt{N/F}$$

Similarly for the unresolved part:

$$\left(\frac{\sum A}{F}\right)_s = \frac{\sum_i 4\sigma_i \sqrt{f_i/n_i}\, n_i}{F}$$
$$= \sum_i 4\sigma_i \sqrt{\frac{n_i}{f_i}}\frac{f_i}{F}$$
$$= \sum_i 4\sigma_i \sqrt{\frac{n_i}{f_i}}\, p_i$$

where

$$p_i = \frac{f_i}{F}$$
$$\sigma_i^2 = \frac{1}{4}(\overline{h}_i - h_i^{\min})(h_i^{\max} - \overline{h}_i)$$

The total $\sum A/F$ is:

$$S_l = \frac{\sum A}{F} = \left(\frac{\sum A}{F}\right)_r + \left(\frac{\sum A}{F}\right)_s .$$

(c) For the computation of the effective roughness lengths, two different formulations are used in principle: the gentle orography approximation (*Taylor* 1987) and the steep orography formulation (*Mason* 1991). For the gentle orography approximation we need the horizontal wavelength λ of the subgrid terrain which we estimate as:

$$\lambda = \frac{h}{S_l}, \text{ where } h = 4\sigma .$$

The effective roughness lengths z_{0m} and z_{0h} for gentle slopes is determined by:

$$\ln\left(\frac{\lambda}{2\pi z_{0m}} + 1\right) = \left[\ln\left(\frac{\lambda}{2\pi z_{0mVeg1}} + 1\right)\right]\left[1 + C_e\left(\frac{S_l}{\pi}\right)^2\right]^{-\frac{1}{2}}$$
$$\ln\left(\frac{\lambda}{2\pi z_{0h}} + 1\right) = \ln\left(\frac{\lambda}{2\pi z_{0hVeg1}} + 1\right)\frac{\ln\left(\frac{\lambda}{2\pi z_{0mVeg1}} + 1\right)}{\ln\left(\frac{\lambda}{2\pi z_{0m}} + 1\right)}$$

with $C_e = 5$. For steep slopes the effective roughness lengths z_{0m} and z_{0h} are computed from:

$$\ln\left(\frac{h}{2z_{0\mathrm{m}}}+1\right)=\left(\frac{k^2}{\frac{1}{2}C_{\mathrm{d}}S_l+\left(\frac{k}{\ln(h/2z_{0\mathrm{mVeg1}}+1)}\right)^2}\right)^{\frac{1}{2}}$$

$$\ln\left(\frac{h}{2z_{0\mathrm{h}}}+1\right)=\ln\left(\frac{h}{2z_{0\mathrm{hVeg1}}}+1\right)\frac{\ln\left(\frac{h}{2z_{0\mathrm{mVeg1}}}+1\right)}{\ln\left(\frac{h}{2z_{0\mathrm{m}}}+1\right)}$$

where $C_{\mathrm{d}}=0.4$, $k=0.4$ and the transition from gentle to steep formulation should be at about $S_l=0.2/\pi$. In practise the quality of the US-Navy data is not sufficient to resolve the gentle slopes, so the treshold is set to 0 which implies that the steep formulation is always used. Another disadvantage of the transition from the gentle to steep slope formulation is that it is discontinuous, which reflects the sudden transition from attached to separated flow.

Orographic corrections are not applied for $h<10$ m and for $S_l<0.01$. $z_{0\mathrm{m}}$ is not allowed to become larger than $h/10$ and is clipped at 100 m; $z_{0\mathrm{h}}$ has an imposed lower bound of e^{-20}.

(d) A Gaussian filter (the same as for the mean orography) is applied to $\ln(z_{0\mathrm{m}})$ and $\ln(z_{0\mathrm{h}})$, the sea points are reset to $z_{0\mathrm{m}}=0.001$ and $z_{0\mathrm{h}}=0.0001$. Because of the wide dynamical range of parameter $z_{0\mathrm{h}}$, $\ln(z_{0\mathrm{h}})$ is GRIB-coded and provided as input to the model.

10.6 PARAMETERS FOR GRAVITY-WAVE AND OROGRAPHIC DRAG SCHEMES

The following subgrid parameters are needed: standard deviation μ_{GW}, anisotropy γ_{GW}, orientation θ_{GW}, and slope σ_{GW}. They are computed as follows (see *Lott and Miller* 1997; *Baines and Palmer* 1990):

(a) For every point (index i) of the 2'30" data, $(\partial h/\partial x)_i$ and $(\partial h/\partial y)_i$ are computed by central differencing with help of the points to the north, south, east and west. These derivatives are computed after subtracting the mean orography at target resolution to avoid contributions from the slope of the resolved orography. The central differences in the North South direction use adjacent points; derivatives in the East West direction use adjacent points in the tropics but use equidistant points rather than equi-longitude points when approaching the polar regions (to maintain a uniform resolution over the globe). Then parameters K, L, and M are computed by summation, taking into account the weights p_i of every $10'\times 10'$ area in the ECMWF grid:

$$K=\frac{1}{2}\sum_i p_i\left\{\left(\frac{\partial h}{\partial x}\right)_i^2+\left(\frac{\partial h}{\partial y}\right)_i^2\right\}$$

$$L=\frac{1}{2}\sum_i p_i\left\{\left(\frac{\partial h}{\partial x}\right)_i^2-\left(\frac{\partial h}{\partial y}\right)_i^2\right\}$$

$$M=\sum_i p_i\left\{\left(\frac{\partial h}{\partial x}\right)_i\left(\frac{\partial h}{\partial y}\right)_i\right\}$$

(b) Anisotropy γ_{GW}, orientation θ_{GW}, and slope σ_{GW} are computed from K, M and L:

$$\gamma_{GW}^2 = \frac{K - (L^2 + M^2)^{1/2}}{K + (L^2 + M^2)^{1/2}}$$

$$\theta_{GW} = \frac{1}{2}\text{atan}\frac{M}{L}$$

$$\sigma_{GW}^2 = K + \sqrt{L^2 + M^2}$$

and the standard deviation μ_{GW}:

$$\mu_{GW} = \sum_i p_i h_i^2 - \left(\sum_i p_i h_i\right)^2 .$$

No further filtering is applied to the fields. Results are shown in Figs. 10.4 , 10.5 , 10.6 , and 10.7 .

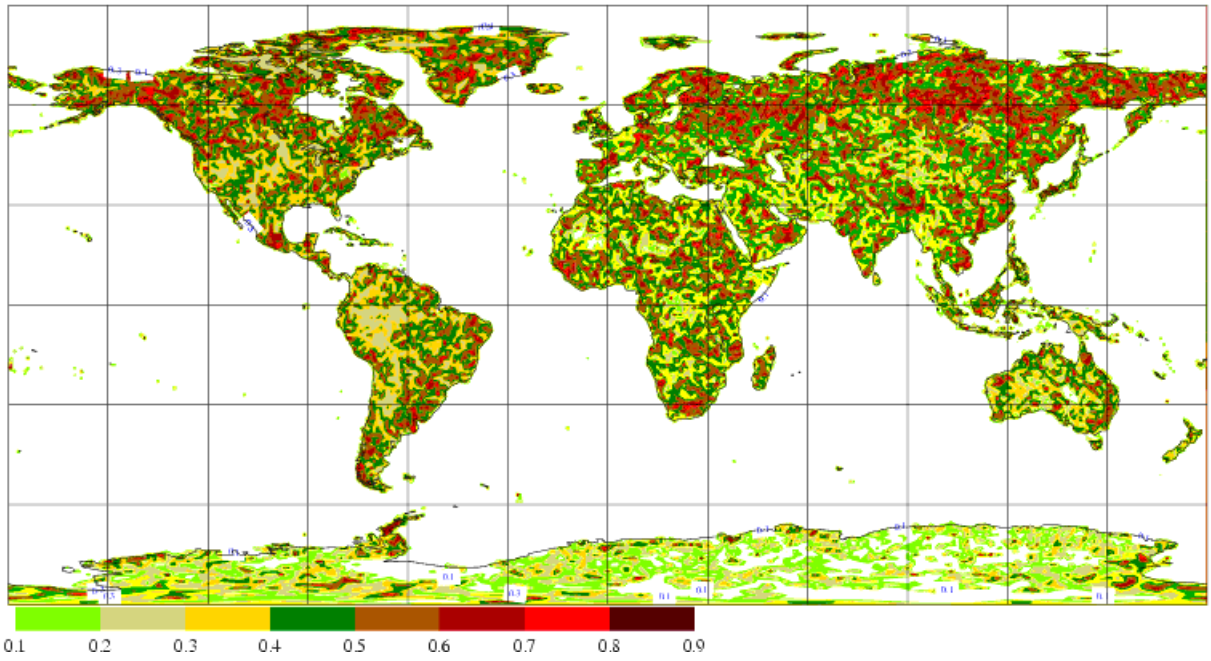

Figure 10.4 Anisotropy γ_{GW} of subgrid orography (1 indicates isotropic, 0 means maximum anisotropy)

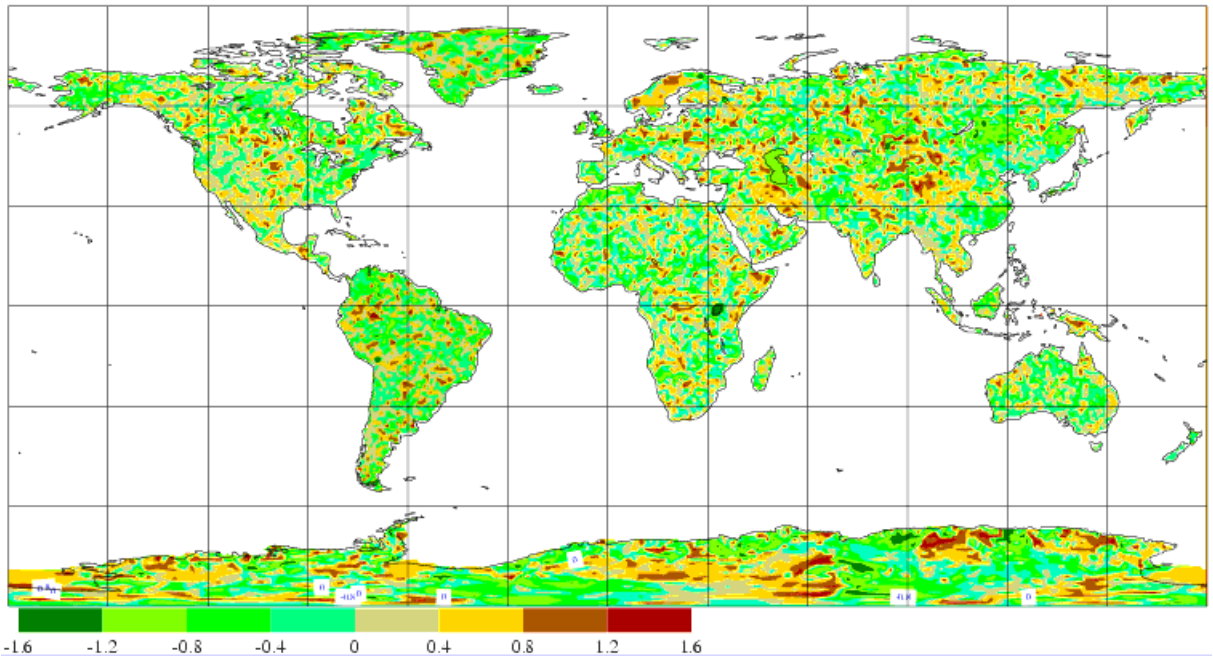

Figure 10.5 Orientation θ_{GW} of subgrid orography.

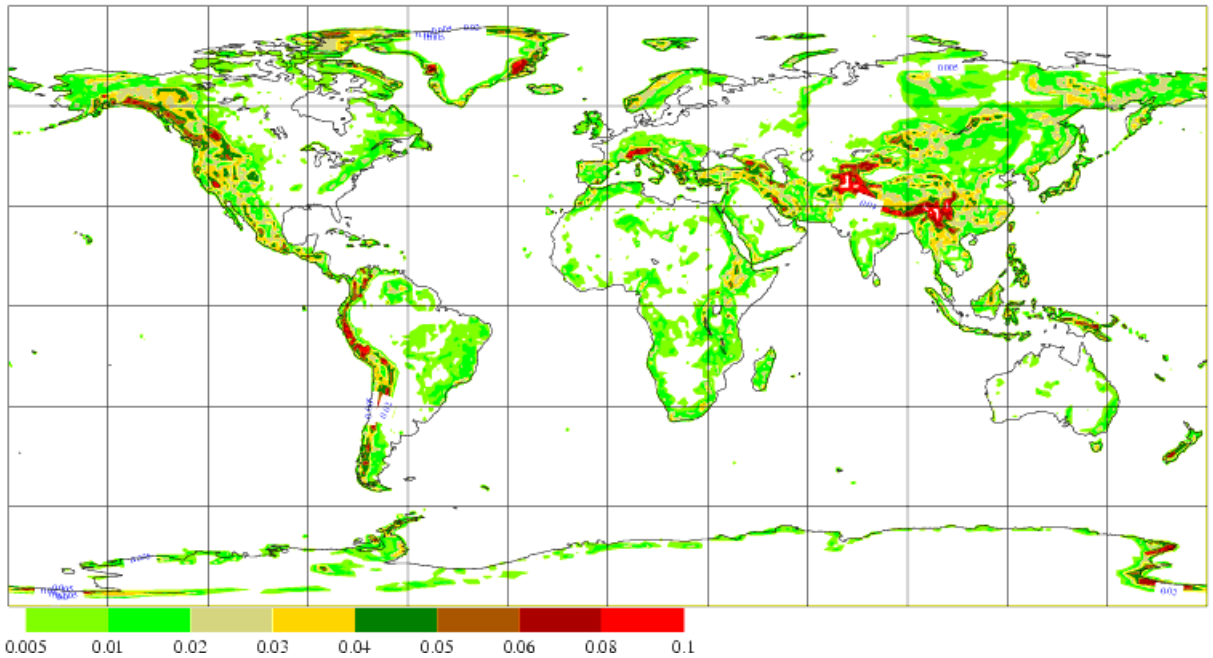

Figure 10.6 Slope σ_{GW} of subgrid orography.

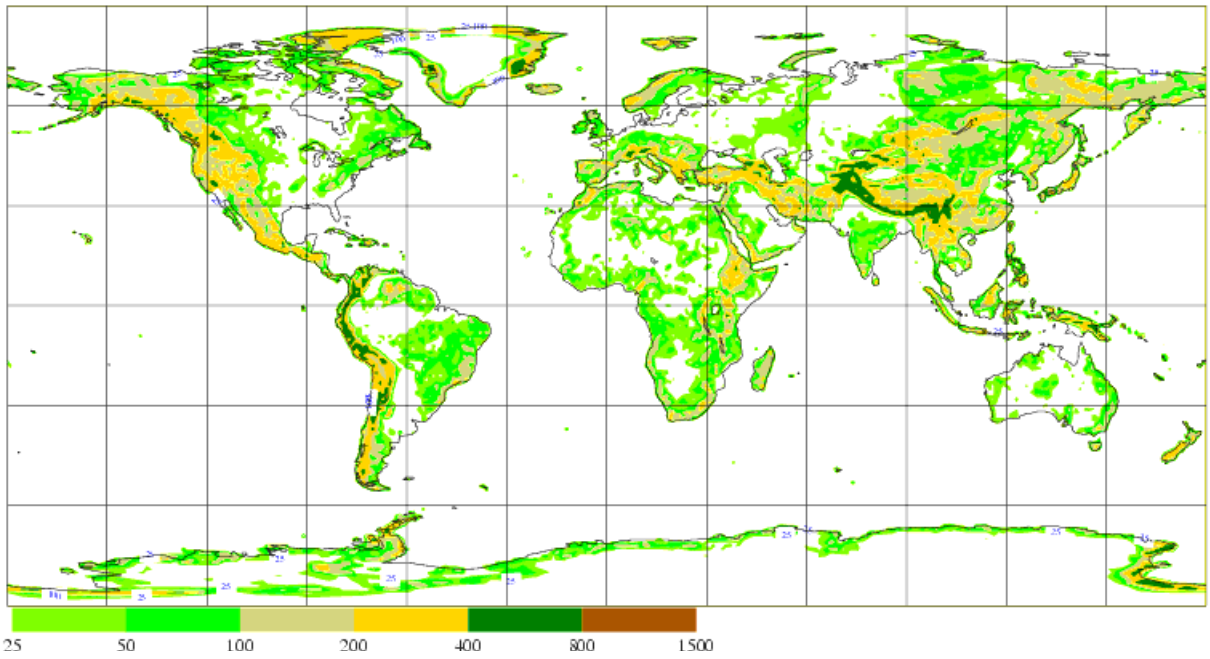

Figure 10.7 Standard deviation μ_{GW} of subgrid orography.

10.7 VEGETATION PARAMETERS

Vegetation is represented by 4 climatological parameters: vegetation cover of low vegetation, vegetation cover of high vegetation, low vegetation type and high vegetation type. These parameters are derived from the 2'30" GLCC data by averaging over the target grid squares. The fractional covers for low and high vegetation are obtained by combining the fractions from all the low and high vegetation types of Table 10.1. The index of the dominant low and high vegetation types are also coded as climatological fields for use by the land surface scheme. The latter two fields can not be interpolated by standard procedures to another resolution. The resulting fields are shown in Fig. 10.8 , Fig. 10.9 , Fig. 10.10 and Fig. 10.11 . Table and Table 10.3 contain statistical information on the number of points in each vegetation class.

TABLE 10.2 PERCENTAGE OF LAND POINTS AT T511 FOR EACH LOW VEGETATION TYPE

Index	Vegetation type	Percentage of land points
1	Crops, Mixed Farming	22.1
2	Short Grass	10.0
7	Tall Grass	13.0
9	Tundra	8.9
10	Irrigated Crops	4.7
11	Semidesert	13.5
13	Bogs and Marshes	2.0
16	Evergreen Shrubs	1.5

TABLE 10.2 PERCENTAGE OF LAND POINTS AT T511 FOR EACH LOW VEGETATION TYPE

Index	Vegetation type	Percentage of land points
17	Deciduous Shrubs	4.6
20	Water and Land Mixtures	0
-	Remaining land points without low vegetation	19.7

TABLE 10.3 PERCENTAGE OF LAND POINTS AT T511 FOR EACH HIGH VEGETATION TYPE

Index	Vegetation type	Percentage of land points
3	Evergreen Needleleaf Trees	7.1
4	Deciduous Needleleaf Trees	3.3
5	Deciduous Broadleaf Trees	6.3
6	Evergreen Broadleaf Trees	12.8
18	Mixed Forest/woodland	3.9
19	Interrupted Forest	29.6
-	Remaining land points without high vegetation	37.0

)

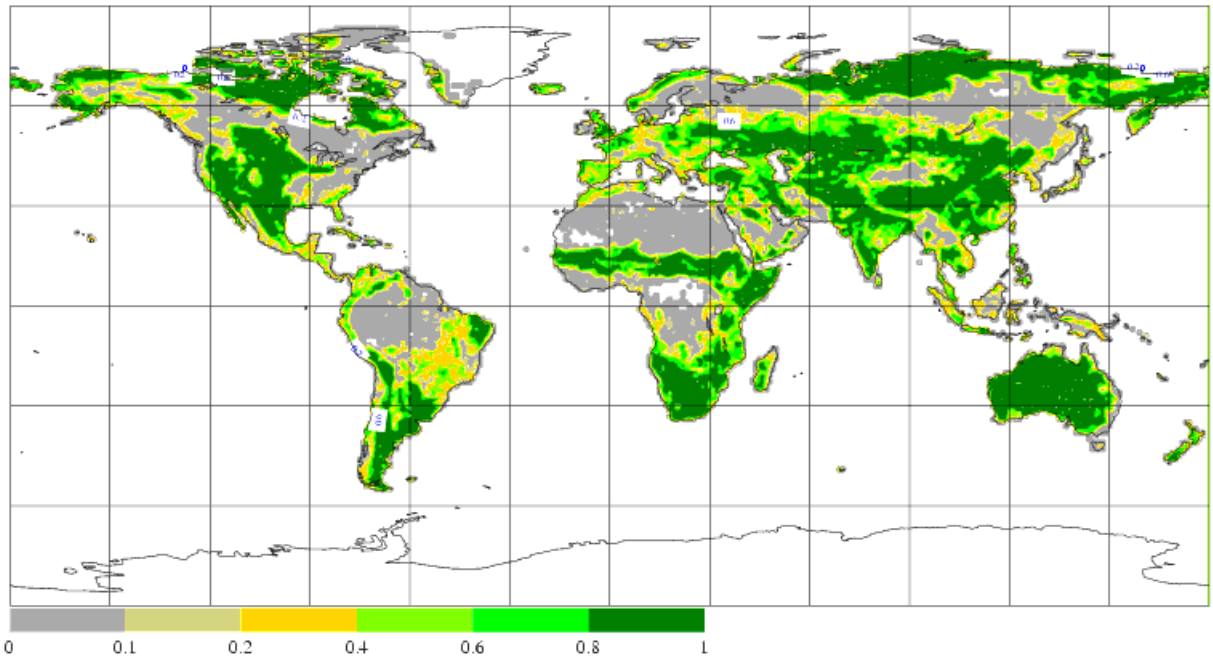

Figure 10.8 Fractional cover of low vegetation.

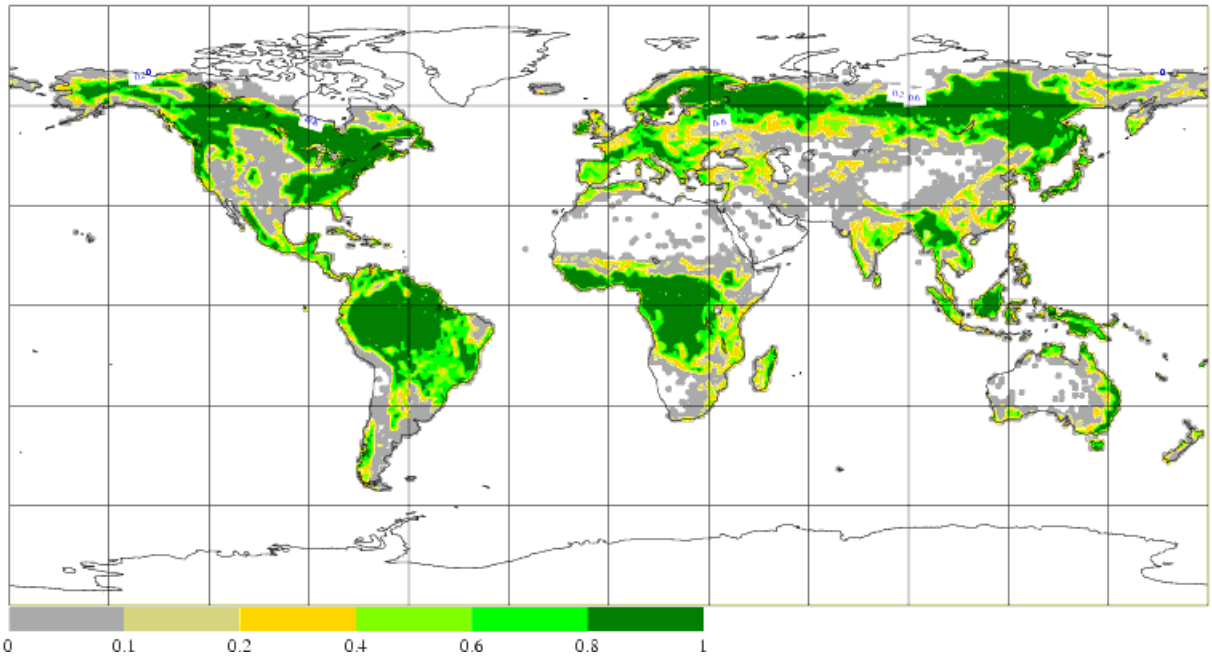

Figure 10.9 Fractional cover of high vegetation.

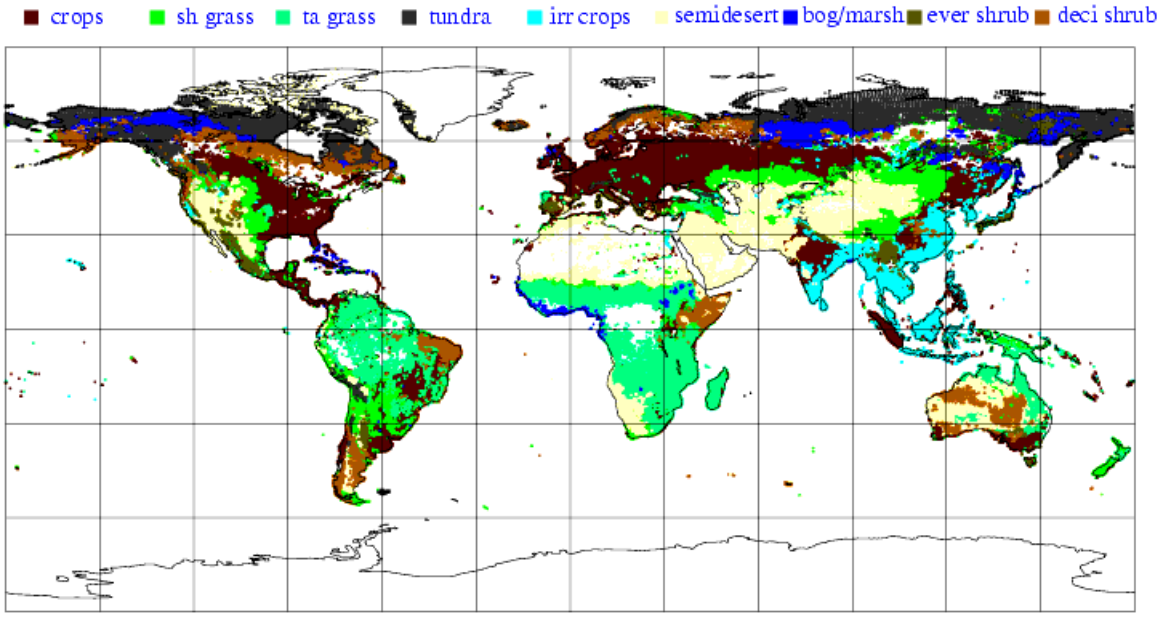

Figure 10.10 Low vegetation type

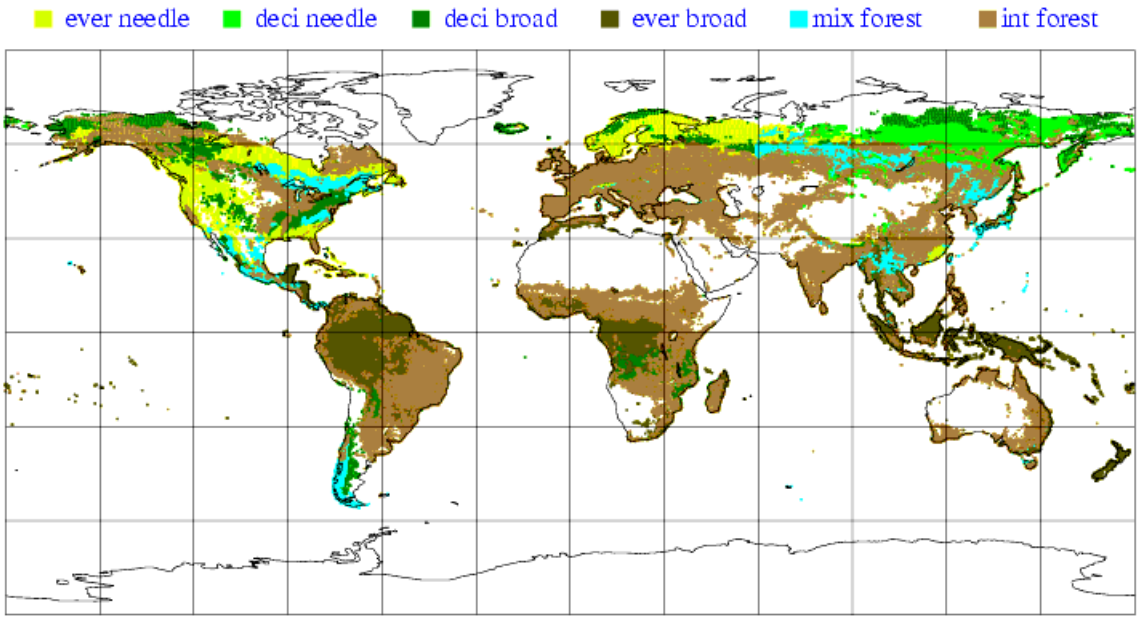

Figure 10.11 High vegetation type

10.8 ALBEDO

The background land albedo is interpolated to the model grid from the monthly mean values of a snow-free albedo produced for the combined 1982-1990 years. The albedo for that dataset was computed using the method of Sellers *et al.* (1996), but with new maps of soil reflectance, new values of vegetation reflectance, and the biophysical parameters described by Los *et al.* (2000).

The fields for January, April, July and October are shown in Fig. 10.12 , Fig. 10.13 , Fig. 10.14 , and Fig. 10.15 . To obtain a smooth evolution in time, the model does a linear interpolation between successive months, assuming that the monthly field applies to the 15th of the month. The model adapts the background albedo over water, ice and snow as documented in the chapter on radiation.

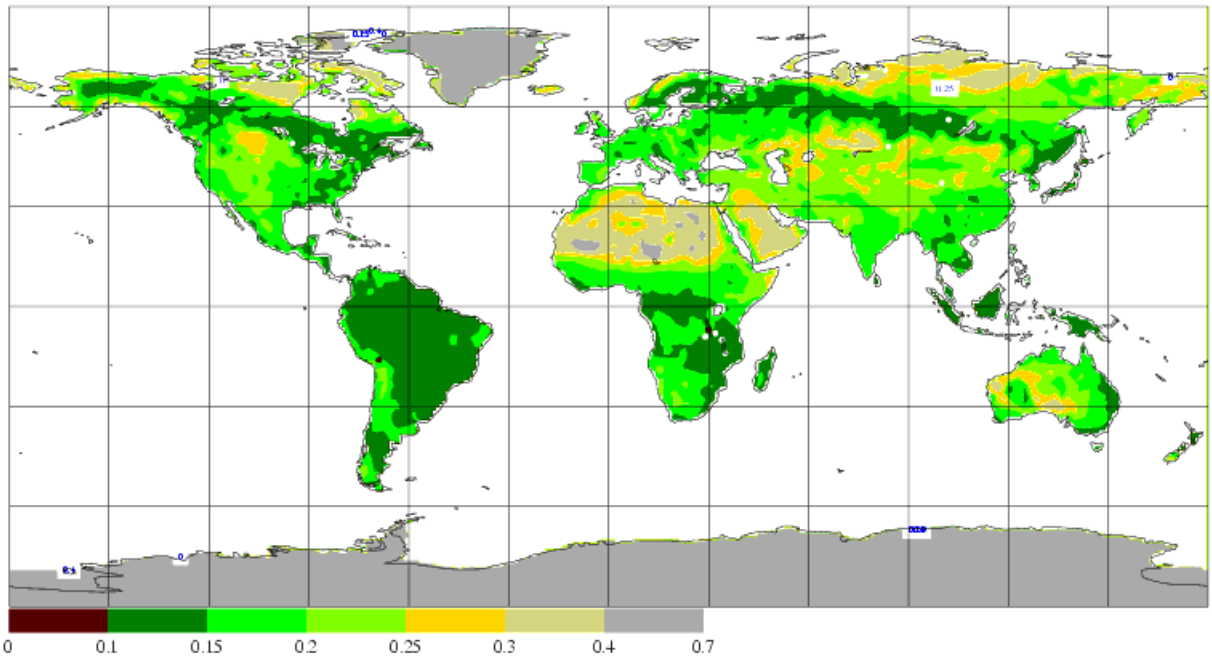

Figure 10.12 Climatological background albedo for January.

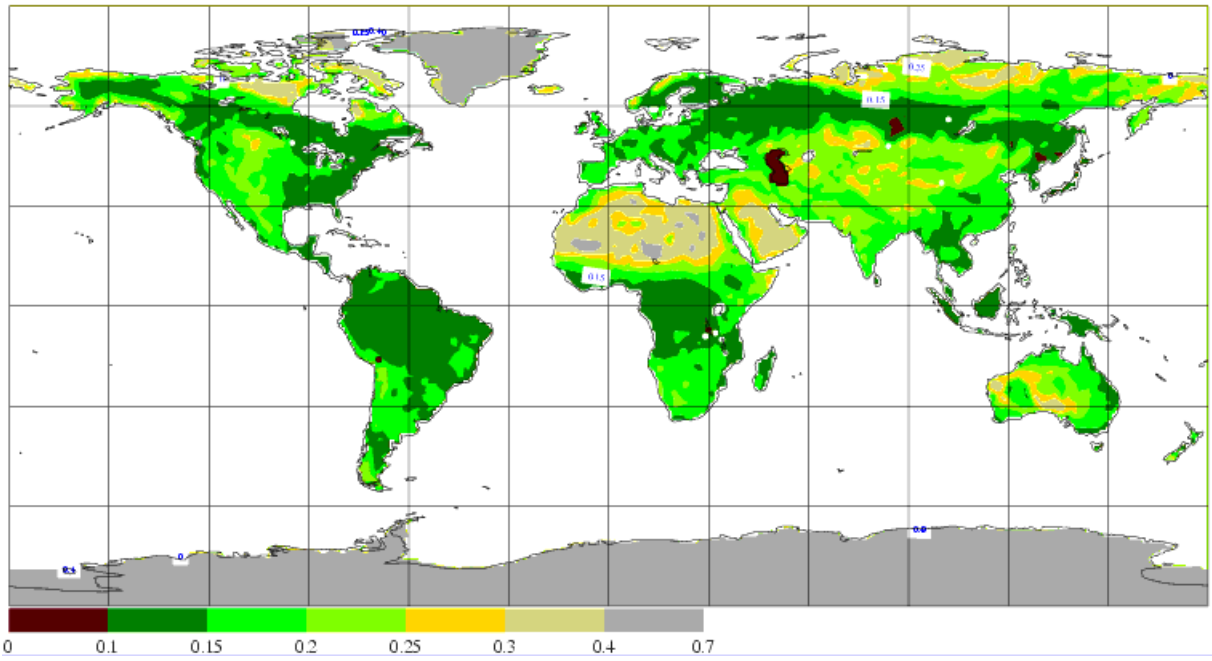

Figure 10.13 Climatological background albedo for April.

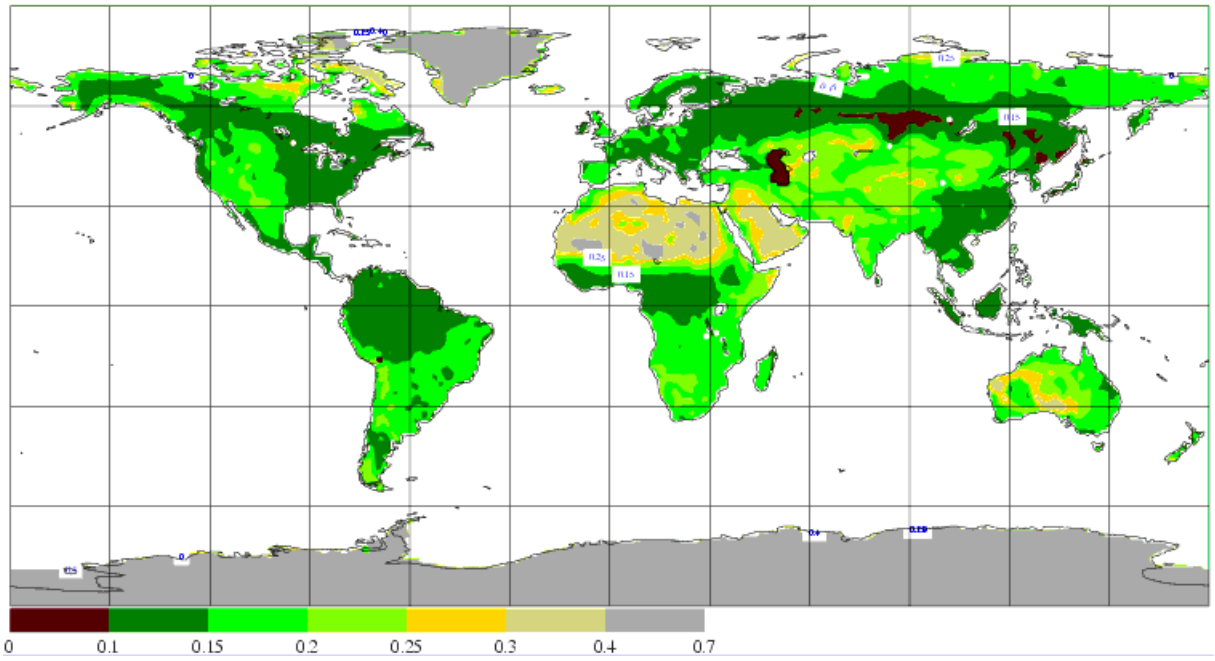

Figure 10.14 Climatological background albedo for July.

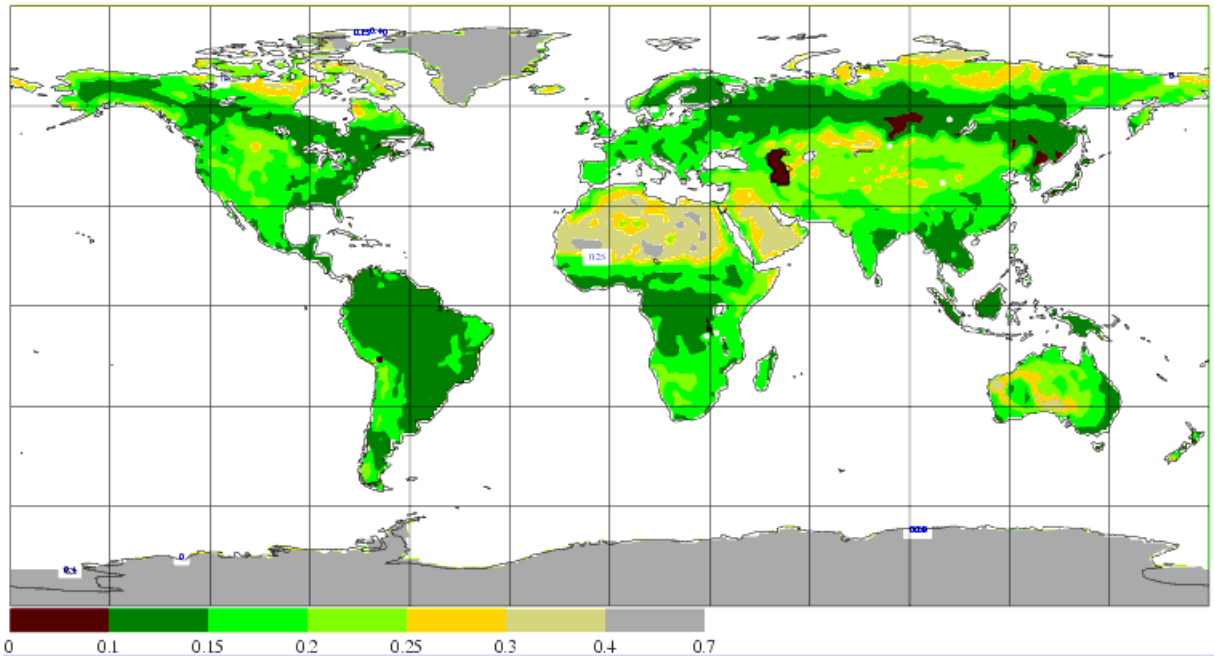

Figure 10.15 Climatological background albedo for October.

10.9 AEROSOLS

Aerosols are considered in the model following *Tanre et al.* (1984). The continental, maritime, urban and desert aerosols are geographically distributed over ice-free land, open sea, industrialized area and desert using a bi-Gaus-

sian horizontal filter of radius 2000 km to get overlapping distributions of each aerosol type, with a maximum optical thickness of 0.2, 0.05, 0.1, and 1.9, respectively (see Figs. 10.16 (a)–(d) for the geographical distributions and Fig. 10.16 (e) for the corresponding profiles). Well-mixed (vertically and horizontally) tropospheric background aerosols with an optical thickness of 0.03 and stratospheric background aerosols with an optical thickness of 0.045 are added to the previous amounts with a rate of change of optical thickness with pressure of 0.037 and 0.233 /atm respectively. The transition from troposphere to stratosphere is obtained by multiplication of the background values with $1 - L_{\text{stratos}}$ and L_{stratos} respectively (see Fig. 10.16 (e)).

(a)

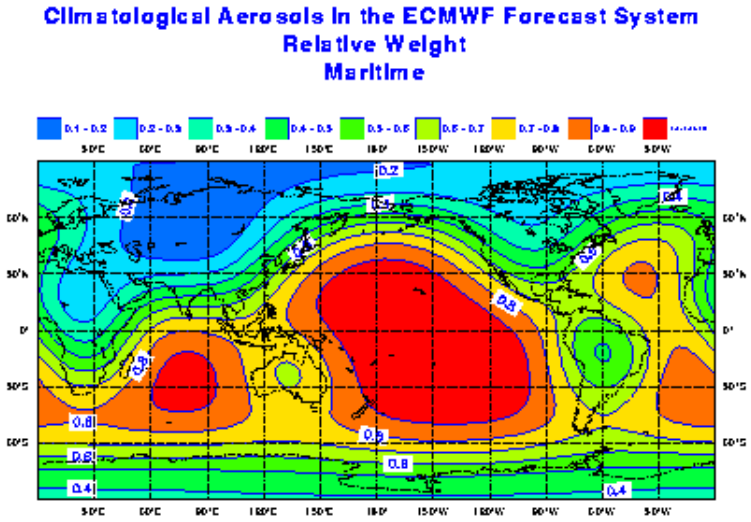

(b)

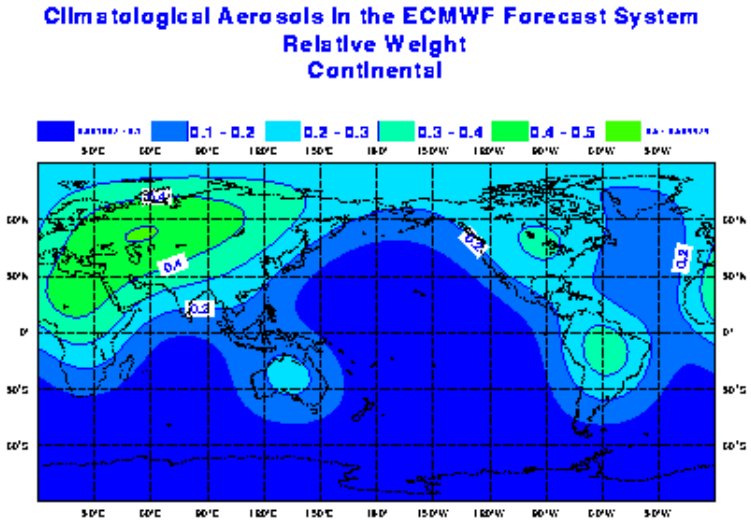

Figure 10.16 Distribution of (a) maritime and (b) continental type aerosols.

(c)

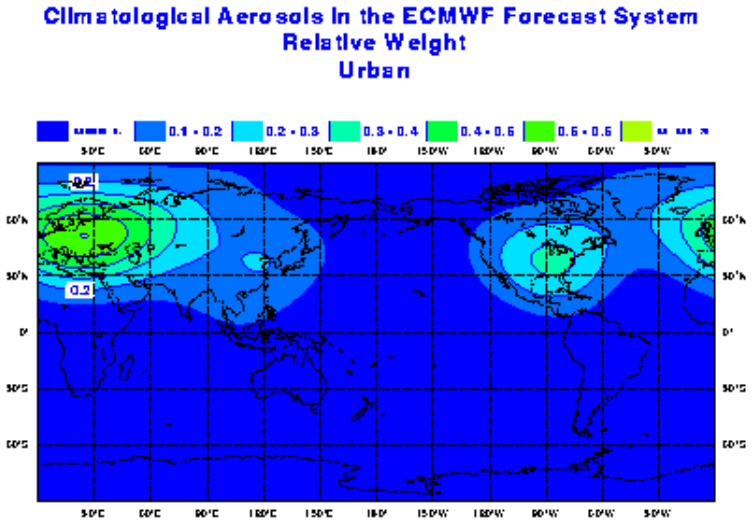

(d)

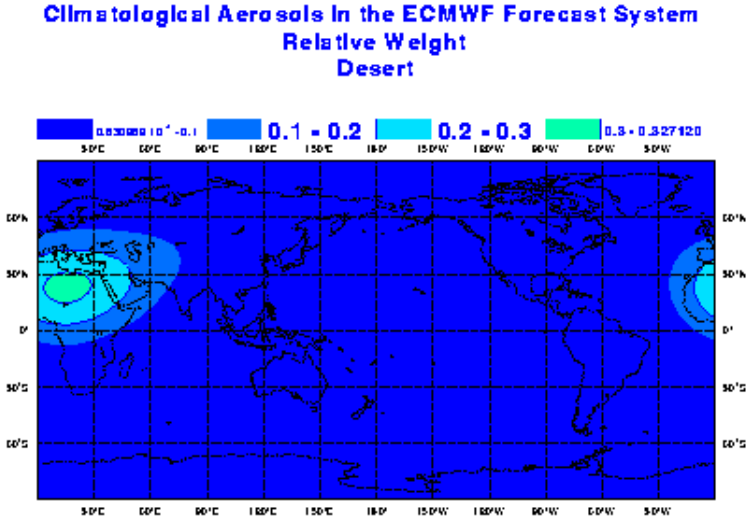

Figure 10.16 Distribution of (c) urban and (d) desert type aerosols.

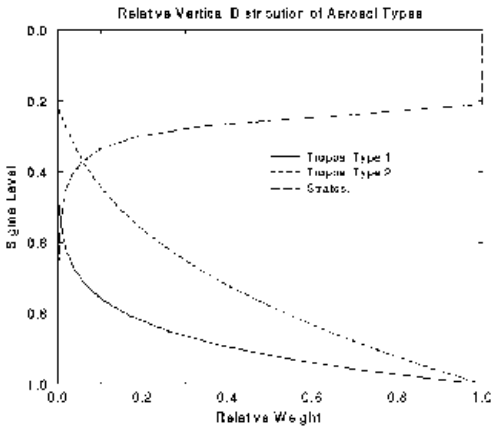

Figure 10.16 (e) Type 1 (full line) profiles apply to maritime, continental and urban type aerosols; type 2 (short dashed line) applies to desert type; the third curve (long dashed line) represents L_{stratos} and is used to determine the transition from tropospheric to stratospheric background aerosols.

10.10 OZONE

The ozone climatology that is operational since August 1997, distributes the ozone mixing ratio as a function of pressure, latitude and month following *Fortuin and Langematz* (1995).

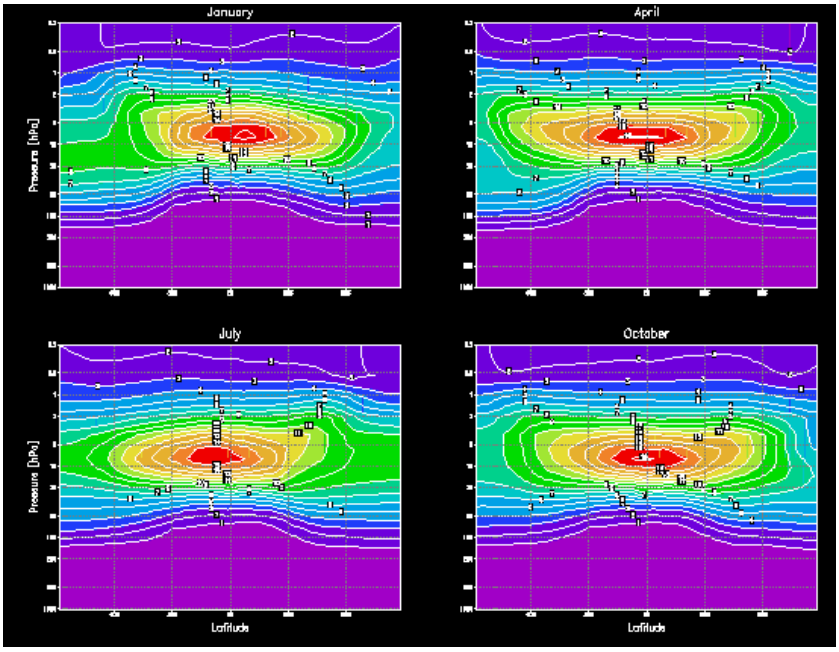

Figure 10.17 Ozone climatology prescribed as a zonal mean according to the climatology by Fortuin and Langematz (1994). Operational in the ECMWF model since August 1997 (mass mixing ratio $\times 10^6$ on 60 levels).

Part IV: PHYSICAL PROCESSES

REFERENCES

Abramopoulos, F., Rosenzweig, C. and Choudury, 1988: Improved ground hydrology calculations for global climate models (GCMs): Soil water movement and evapotranspiration. *J. Climate*, **1**, 921–941

Arakawa, A. and Schubert, W. H., 1974: Interaction of a cumulus cloud ensemble with the large-scale environment. Part I., *J. Atmos. Sci*., **31,** 674–701

Baines, P. G. and Palmer, T. N., 1990: 'Rationale for a new physically based parametrization of subgrid-scale orographic effects'. Technical Memorandum 1699. European Centre for Medium-Range Weather Forecasts.

Baker, D. G., Ruschy, D. L. and Wall, D. B., 1990: The albedo decay of prarie snows. *J. Appl. Meteorol.*, **29**, 179–187

Baumgartner, A., Mayer, H. and Metz, W. , 1977: Weltweite Verteilung des Rauhigkeitparameters *zo* mit Anwendung auf die Energiedissipation an der Erdoberfläche, *Meteorol. Rundsch.*, **30**, 43–48

Bechtold, P., Chaboureau, J.-P., Beljaars, A., Betts, A. K., Koehler, M., Miller, M. and Redelsperger, J.-L., 2004: The simulation of the diurnal cycle of convective precipitation over land in a global model. Q. J. R. Meteorol. Soc., **130**

Beljaars, A.C.M. , 1987: The influence of sampling and filtering on measured wind gusts, J. Atmos. Ocean. Techn., 4, 613-626.

Beljaars, A. C. M., 1991: 'Numerical schemes for parametrization'. Seminar Proceedings on Numerical Methods in Atmospheric Models. Volume 2. ECMWF, Reading, England.

*Beljaars, A. C. M., 199*4: The parametrization of surface fluxes in large-scale models under free convection. *Q. J. R. Meteorol. Soc.*, **121**, 255-270.

Beljaars, A. C. M., 1995: 'The impact of some aspects of the boundary layer scheme in the ECMWF model'. Seminar Proceedings on Parametrization of sub-grid scale physical processes. ECMWF, Reading, England.

Beljaars, A. C. M. and Betts, A. K., 1993: 'Validation of the boundary layer representation in the ECMWF model'. Seminar Proceedings on Validation of Models over Europe. Volume 2. ECMWF, Reading, England.

Beljaars, A. C. M. and Holtslag, A. A. M.,1991: A software library for the calculation of surface fluxes over land and sea. *Environ. Software*, **5,** 60–68

Betjaars, A. C. M. and Viterbo, P., 1994: The sensitivity of winter evaporation to the formulation of aerodynamic resistance in the ECMWF model. *Boundary-Layer Meteorol.*, **71,** 135–149

Beljaars, A.C.M. and Viterbo P., 1999: The role of the boundary layer in a numerical weather prediction model, in: Clear and cloudy boundary layers, A.A.M. Holtslag and P.G. Duynkerke (eds.), North Holland Publishers.

Bennets, D. A. and Hoskins, B. J., 1979: Conditional symmetric instability — a possible explanation for frontal rainbands. *Q. J. R.. Meteorol. Soc.*, **105,** 945–962.

Bennets, D. A. and Sharp, J. C.,1982: The relevance of conditional symmetric instability to the prediction of mesoscale frontal rainbands. *Q. J. R . Meteorol. Soc.*, **108,** 595–602.

Betts, A. K. and Ball, J. H., 1997: Albedo over the boreal forest. *J. Geophys. Res.*, **1028**, 28901–28909

Betts, A. K., Ball, J. H. and Beljaars, A. C. M., 1993: Comparison between the land surface response of the EC-

MWF model and the FIFE-1987 data. *Q. J. R. Meteorol. Soc.*, **119,** 975-1001

Betts, A. K., Viterbo, P. and Wood, E., 1998: Surface energy and water balance for the Arkansas–Red River basin from the ECMWF reanalysis. *J. Climate*, **11**, 19293–19306

Bithell, M., Gray, L. J., Harries, J. E., Rusell, J. M. III and Tuck, A. F., 1994: Synoptic interpretation of measurements from HALOE. *J. Atmos. Sci.*, **51**, 2942-2956

Blackadar, 1962: The vertical distribution of wind and turbulent exchange in a neutral atmosphere. *J. Appl. Meteorol*, **30,** 327-341.

Blondin, C., 1991: 'Parameterization of land-surface processes in numerical weather prediction'. Pp. 31–54 in *Land surface evaporation:Measurement and parameterization.* Eds T. J. Schmugge and J. C. André, Springe

Bonan, G. B., 1994: Comparison of two land surface process models using prescribed forcings. *J. Geophys. Res.*, **99**, 25803–25818

Bonnel, B., Fouquart, Y., Vanhoutte, J.-C. , Fravalo, C. and Rosset, R., 1983: Radiative properties of some African and mid-latitude stratocumulus clouds. *Beitr. Phys. Atmos.*, **56**, 409-428.

Bosveld, F. C., Holtslag, A. A. M. and van den Hurk, B. J. J. M., 1999: Interpretation of crown radiation temperatures of a dense Douglas fir forest with similaty theory. *Boundary-Layer Meteorol.*, **92**, 429–451

Brankovic, C. and Van Maanen, J., 1985: 'The ECMWF climate system'. ECMWF Tech. Memo No. 109

Browning, K.A., Hardman, M. E., Harrold, T. W. and Pardoe, C. W., 1973: The structure of rainbands within a mid-latitude depression. *Q. J. R . Meteorol. Soc.*, **99,** 215–231.

Brasseur, G. and Solomon, S., 1984: *Aeronomy of the middle atmosphere.* D. Reidel Publishing Co. Dordrecht

Brutsaert, W., 1982: *Evaporation in the atmosphere*. D.Reidel

Cariole, D. and Déqué, M., 1986: Soutern hemisphere medium-scale waves and total ozone disturbances in a spectral general circulation model. J. Geophys. Res. 10825–10846.

Carlson, T. N., 1991: Recent advance in modeling the infrared temperature of vegetation canopies. Pp. 349–358 in *Land surface evaporation: Measurement and parametrization*, Eds T. J. Schmugge and J. C. André, Springer

Cheng, L., Yip, T.-C. and Cho, H.-R., 1980: Determination of mean cumulus cloud vorticity from GATE A/B-scale potential vorticity budget. *J. Atmos. Sci.*, **37,** 797–811.

Clapp, R. B. and Hornberger, G. M., 1978: Empirical equations for some soil hydraulic properties. *Water Resources Res.*, **14,** 601–604

Claussen, M., 1990: Area-averaging of surface fluxes in a neutrally stratified, horizontally inhomogeneous atmospheric boundary layer, *Atmos. Environ.*, **24A**, 1349-1360.

Clough, S. A. and M. I. Iacono, 1995: Line-by-line calculation of atmospheric fluxes and cooling rates, 2. Application to carbon dioxide, ozone, methane, nitrous oxide and the halocarbons. *J. Geophys. Res.*, **100D**, 16519-16536

Clough, S.A., F.X. Kneizys, and R.W. Davies, 1989: Line shape and the water vapor continuum. Atmos. Res., 23, 229-241.

Clough, S.A., M.J. Iacono, and J.-L. Moncet, 1992: Line-by-line calculations of atmospheric fluxes and cooling rates: Application to water vapor. J. Geophys. Res., 97D, 15761-15786.

Coakley, J. A. Jr. and Chylek, P., 1975: The two-stream approximation in radiation transfer: Including the angle of the incident radiation. *J. Atmos. Sci.*, **32**, 409-418.

Cosby, B. J., Hornberger, G. M., Clapp, R. B. and Ginn, 1984: A ststistical exploration of the relationships of soil moisture characteristics to the physical properties of soils. *Water Resources Res.,* **20,** 682–690

Deardorff, J. W., 1976: Usefulness of liquid-water potential temperature in a shallow-cloud model. *J. Appl. Meteorol.*, **15**, 98–102

Deardorff, J. W., 1978: Efficient prediction of ground surface temperature and moisture, with inclusion of a layer of vegetation. *J. Geophys. Res.*, **83C**, 1889–1903

Delworth, T. L. and Manabe, S., 1989: The influence of soil wetness on near-surface atmospheric variability. *J. Climate*, **2,** 1447–1462

Deschamps, P.-Y., Herman, M. and Tanre, D., 1983: 'Modelisation du rayonnement solaire reflechi par l'atmosphere et la terre, entre 0.35 et 4 microns'. Rapport ESA 4393/80/F/DC(SC)

De Vries, D. A., 1975: 'Heat transfer in soils'. Pp. 4–28 in *Heat and mass transfer in the biosphere. Part I: Transfer processes in teh plant environment*, Eds. D. A. de Vries and N. H. Afgan, Wiley

Dickinson, R. E., 1984: 'Modeling evapotranspiration for three-dimensional climate models'. Pp. 58–72 in *Climate processes and climate sensitivity. Geophys. Monogr. 29*, American Geophysical Union

Dickinson, R. E., 1988: The force–restore model for surface temperatures and its generalizations. *J. Climate*, **1,** 1086–1097

Dickinson, R. E., Henderson-Sellers, A., Kennedy, P. J. and Wilson, M. F., 1986: 'Boisphere–atmosphere transfer scheme(BATS) for the NCAR community model'. NCAR Technical note, NCAR/TN-275+STR

Dickinson, R. E., Henderson-Sellers, A., Rosenzweig, C. and Sellers, P. J., 1991: Evapotranspiration models with canopy resistance for use in climate models: A review. *Agric. For. Meteorol.*, **54,** 373–388

Dolman, A. J. and Gregory, D., 1992: The parameterization of rainfall interception in GCMs. *Q. J. R. Meteorol. Soc.*, **118,** 445–467

Dorman, J. L. and Sellers, P. J., 1989: A global climatology of albedo, roughness length and stomatal resistance for atmospheric general circluation models as represented by the simple biosphere model (SB). *J. Appl. Meterol.*, **28**, 833-855

Douville, H., Royer, J.-F. and Mahfouf, J.-F., 1995: A new snow parameterization for the Météo-France climate model. \part I: Validation in stand-alone experiments. *Climate Dyn.*, 12, 21–35

Driedonks, A. G. M. and Tennekes, H., 1984: Entrainment effects in the well mixed atmospheric boundary layer. *Boundary-Layer Meteorol.*, **30,** 75-105.

Dubuisson, P., J.-C. Buriez, and Y. Fouquart, 1996: High spectral resolution solar radiative transfer in absorbing and scattering media: Application to the satellite simulation. J. Quant. Spectrosc. Radiat. Transfer, 55, 103-126.

Dyer, A. J., 1974: A review of flux-profile relationships. *Boundary-Layer Meteorol*, **7,** 363-372.

Ebert, E. E. and Curry, J. A., 1992: A parametrization of ice cloud optical properties for climate models. *J. Geophys. Res.*, **97D**, 3831-3836.

Ekholm, S., 1996: A full coverage high-resolution topographic model of Greenland computed from a variety of digital elevation data, J. Geophys. Res., 101 (B10), 21961-21972.

Ebert, E. E. and Curry, J. A., 1993: An intermediate one-dimensional thermodynamic sea ice model for investigating ice-atmosphere interactions. *J. Geophys. Res.*, **98C**, 10,085-10,109.

Elsasser, W. M., 1942: 'Heat transfer by infrared radiation in the atmosphere'. Harvard Meteorological Studies

No.6, 107 pp.

Emanuel, K. A., 1982: Inertial instability and mesoscale convective systems. Part II: Symmetric CISK in a baroclinic flow. *J. Atmos. Sci*., **39,** 1080–1097.

Etling, D., 1989: On atmsopheric vortex streets in the wake of large islands. *Meteor. Atmos Phys*., **41,** 157–164.

Farouki, O. T., 1986: 'Thermal properties of soils'. In *Physics of plant environments*, Ed. W. R. van Wijk, North-Holland Publishing, Amsterdam

Fels, S. B., 1979: Simple strategies for inclusion of Voigt effects in infrared cooling rate calculations. *Appl. Optics*, **18**, 2634-2637.

Flato, G. M. and Hibler III, W. D., 1992: Modeling the ice pack as a caitating fluid. *J. Phys. Oceanog*., **22**, 626–651

Fortuin, J. P. F., and Langematz, U., 1995: An update on the global ozone climatology and on concurrent ozone and temperature trends. Proceedings SPIE, *Atmos. Sensing and Modeling*, **2311**, 207-216.

Foster, D. S., 1958: Thunderstorm gusts compared with computed downdraught speeds. *Mon. Weather Rev*., **86,** 91–94.

Fouquart, Y., 1974: Utilisation des approximants de Pade pour l'etude des largeurs equivalentes de raies formees en atmosphere diffusante. *J. Quant. Spectrosc. Radiat. Transfer*, **14**, 497-508.

Fouquart, Y., 1987: 'Radiative transfer in climate modeling'. NATO Advanced Study Institute on Physically-Based Modeling and Simulation of Climate and Climate Changes, Erice, Sicily, 11-23 May 1986, M.E. Schlesinger, Ed., 223-283.

Fouquart, Y. and Bonnel, B., 1980: Computations of solar heating of the earth's atmosphere: A new parameterization. *Beitr. Phys. Atmos*., 53, 35-62.

Fritsch, J. M., and Chappell, C. G., 1980: Numerical prediction of convectively driven mesoscale pressure systems. Part I: Convective parametrization. *J. Atmos. Sci*., **37,** 1722–1733.

Fu, Q. and K.-N. Liou, 1992: On the correlated k-distribution method for radiative transfer in non-homogeneous atmospheres. J. Atmos. Sci., 49, 2139-2156.

Fu, Q., 1996: An accurate parameterization of the solar radiative properties of cirrus clouds. J. Climate, 9, 2058-2082.

Fu, Q., P. Yang, and W. B. Sun, 1998: An accurate parametrization of the infrared radiative properties of cyrrus clouds of climate models. *J. Climate*, **11**, 2223-2237

Geleyn, J.-F. and Hollingsworth, A., 1979: An economical analytical method for the computation of the interaction between scattering and line absorption of radiation. *Beitr. Phys. Atmos*., 52, 1-16.

Gesch, D.B. and Larson, K.S., 1998: Techniques for development of global 1-kilometer digital elevation models, in: Proceedings, Pecora Thirteenth Symposium, Soiux Falls, South Dakota, August 20-22, 1996 (CD-ROM), Am. Soc. Photogrammetry Remote Sens., Bethesda, Md

Giard, D. and Bazile, E., 2000: Implentation of a new assimilation scheme for soil and surface variables in a global NWP model. *Mon Weather Rev*., **128**, 997–1015

.*Giorgetta, M. A. and Morcrette, J.-J., 1995*: Voigt line approximation in the ECMWF radiation scheme. *Mon. Weather Rev.*,

Godfrey, J. S. and Beljaars, A. C. M., 1991: On the turbulent fluxes of buoyancy, heat and moisture at the air-sea interface at low wind speed. *J. Geophys. Res*., **96,** 22043-22048.

Goutorbe, J.-P., Noilan, J., Valancogne, C. and Cuenca, R. H., 1989: soil moisture variations during HAPEX–MOBILHY., *Ann. Geophys.*, **7**, 415–426

Gregory, D., 1997: Parametrization of convective momentum transports in the ECMWF model: evaluation using cloud resolving models and impact upon model climate., ECMWF Workshop Proceedings on New insights and approaches to convective parametrization, Shinfiled Park, Reading, RG2 9AX, United Kingdom.

Gregory, D., Kershaw, R. and Inness, P. M., 1997: Parametrization of momentum transports by convection. II: Tests in single-column and general circulation models., *Q. .J. R. Meteorol. Soc*., **123,** 1153-1183.

Gurevitch, M. I., 1965: *Theory of jets in ideal fluids*. Academic Press.

HAWKS, 2000: The Hitran Atmospheric WorKStation: http://www.hitran.com

Herzegh, P. H. and Hobbs, P. V., 1980: The mesoscale and microscale structure and organization of clouds and precipitation in mid-latitude cyclones. Part II: Warm frontal clouds. *J. Atmos. Sci*., **37**, 597–611.

Heymsfield, A. J. and Donner, L. J., 1990: A scheme for parametrizing ice-cloud water content in general circluation models. *J. Atmos. Sci.*, **47**, 1865–1877

Hillel, D., 1982: *Introduction to soil physics.* Academic Press

Hogström, U, 1988: Non-dimensional wind and temperature profiles in the atmospheric surface layer: A re-evaluation. *Boundary-Layer Meteorol.*, **42,** 55-78.

Holtslag. A. A. M. and De Bruin, H. A. R., 1988: Applied modelling of the night-time surface energy balance over land. *J. Appl. Meteorol.*, **27**, 689-704.

Houze, R. A., Locatelli, J. D. and Hobbs, P. V., 1976: Dynamics and cloud microphysics of the rainbands in an occluded frontal system. *J. Atmos. Sci*., **35,** 1921–1936.

Jakob, C. and Siebesma, A. P., 2003: A new subcloud model for mass flux convection schemes. Influence on triggering, updraught properties and model climate. *Mon. Weather Rev*., **131**, 2765–2778.

Jacquemin, B. and Noilhan, J., 1990: Sensitivity study and validation of a land-surface parameterization using the HAPEX-MOBILHY data set. *Boundary-Layer Meteorol.*, **52**, 93–134

Janssen, P. A. E. M., Beljaars, A. C. M., Simmons, A. and Viterbo, P., 1992: The determination of the surface stress in an atmospheric model. *Mon. Weather Rev.*, **120,** 2977-2985.

Jarvis, P. J., 1976: The interpretation of the variations in leaf-water potential and stomatal conductance found in canopies in the field. *Phil. Trans. R. Soc. London*, **B723**, 385–610

Johansen, O., 1975: 'Thermal conductivity of soils', PhD thesis, Trondheim, Norway

Johnson, R. H., 1976: The role of convective-scale precipitation downdrafts in cumulus and synoptic scale interactions. *J. Atmos. Sci*., **33**, 1890–1910.

Johnson, R. H., 1980: Diagnosis of convective and mesoscale motions during Phase III of GATE. *J. Atmos. Sci*., **37**, 733–753.

Jones, R. L., Pyle, J. A., Harries, J. E., Zavody, A. M., Russell, J. M. III and Gille, J. C., 1986: The water vapour budget of the stratosphere studied using LIMS and SAMS satellite data. *Q. J. R. Meteorol. Soc*., **112,** 1127-1143

Joseph, J. H., Wiscombe, W. J. and Weinman, J. A., 1976: The Delta-Eddington approximation for radiative flux transfer. *J. Atmos. Sci*., 33, 2452-2459.

Kalnay, E. and Kanamitsu, M., 1988: Time schemes for strongly nonlinear damping equations. *Mon. Weather Rev.*,

116, 1945-1958.

Kessler, E., 1969: On the distribution and continuity of water substance in atmopsheric circulation. *Meteorological Monographs*, 10, Americ.Meteor.Soc., Boston, MA.

Kirchoff, G., 1876: *Vorlesungen über mathematische physik*. Leipzig

Kondo, J., Saigusa, N. and Sato, T., 1990: A parametrization of evaporation from bare soil surfaces. *J Appl. Meteorol.*, **29**, 385–389

Koster, R. D. and Suarez, M. J., 1992: A comparative analysis of two land surface heterogeneity representations. *J. Climate*, **5**, 1379–1390

Kuo, H. L. and Raymond, W. H., 1980: A quasi-one-dimensional cumulus cloud model and parametrization of cumulus heating and mixing effects. *Mon. Weather Rev.*, **108**, 991–1009

Lacis, A.A., and V. Oinas, 1991: A description of the correlated k distribution method for modeling nongray gaseous absorption, thermal emission, and multiple scattering in vertically inhomogeneous atmospheres. J. Geophys. Res., 96D, 9027-9063.

Landweber, L., 1961: *Motion of immersed and floating bodies. Handbook of fluid Dynamics*. 1st ed. McGraw-Hill

Le Mone, M. A. and Pennell, W. T., 1976: The relationship of trade wind cumulus distribution to subcloud layer fluxes and structure. *Mon. Wea. Rev*., **104,** 524–539.

Le Texier, L. Solomon, S. and Garcia, R. R., 1988: The role of molecular hydrogen and methane oxidation in the water vapour budget of the stratosphere. *Q. J. R. Meteorol. Soc.*, **114**, 281-295

Lindzen, R. S., 1981: 'Some remarks on cumulus parametrization'. Rep. on NASA-GISS Workshop: Clouds in Climate: Modelling and Satellite Observational Studies, 42–51.

Liu, J. Y. and Orville, H. D., 1969: Numerical Modeling of precipitation and cloud shadow effects on mountain-induced cumuli. *J. Atmos. Sci.*, 26, 1283–1298

Liu, Q. and Schmetz, J., 1988: On the problem of an analytical solution to the diffusivity factor., *Beitr. Phys. Atmos*., 61, 23-29.

London, J., Bojkov, R. D., Oltmans, S. and Kelley, J. I., 1976: 'Atlas of the global distribution of total ozone, July 1957 - June 1967'. NCAR Technical Note 113+STR.

Los, S.O., G.J. Collatz, P.J. Sellers, C.M. Malmström, N.H. Pollack, R.S. deFries, L. Bounoua, M.T. Parris, C.J. Tucker, and D.A. Dazlich, 2000: A global 9-year biophysical land surface dataset from NOAA AVHRR data. *J. Hydrometeor.*, **1**, 183-199.

Lott, F. and Miller, M. J., 1996: A new subgrid-scale orographic drag parametrization: Its formulation and testing, *Q. J. R. Meteorol. Soc.*, **123**, 101–127.

Louis, J. F., 1979: A parametric model of vertical eddy fluxes in the atmosphere. *Boundary-Layer Meteorol.* **17,** 187–202

Louis, J. F., Tiedtke, M. and Geleyn, J. F., 1982: 'A short history of the operational PBL parametrization at ECMWF'. Workshop on boundary layer parametrization, November 1981, ECMWF, Reading, England.

Loveland, T. R., Reed, B. C., Brown, J. F., Ohlen, D. O., Zhu, Z., Youing, L. and Merchant, J. W., 2000: Development of a global land cover characteristics database and IGB6 DISCover from the 1km AVHRR data. *Int. J. Remote Sensing*, **21**, 1303–1330

Lundin, L.-C. 1989: 'Water and heat fluxes in frozen soils: Basic theory and operational modelling'. Acta Univ.

Uppsala, 'Summary of ssertations from the faculty of Science', 186, Uppsala University

McCumber, M. and Pielke, R. A., 1981: Simulation of the effects of surface fluxes of heat and moisture in a mesoscale numerical model. Part I: Soil layer. *J Geophys. Res.*, **86C,** 9929–9938

McFarquhar, G.M., and A.J. Heymsfield, 1997: Parameterization of Tropical cirrus ice crystal size distribution and implications for radiative transfer: Results from CEPEX. *J.Atmos.Sci*., 54, 2187-2200

Mahfouf, J. F. and Jacquemin, B., 1989: A study of rainfall interception using a land surface paramterization for mesoscale meteorological models. *J. Appl. Meteorol.*, **28**, 1282–1302

Mahfouf, J. F. and Noilhan, J., 1991: Comparative study of various formulations from bare soil using in situ data. *J. Appl. Meteorol*., 30, 1345–1365

Mahfouf, J. F., Manzi, A., Noilhan, J., Giordani, H. and Dequé, M., 1995: The land surface scheme ISBA within the Météo-France climate model ARPEGE. *J. Climate*, **8**, 2039–2057

Mahrt, L. and Pan, H.-L., 1984: A two-layer model of soil hydrology. *Boundary-Layer Meteorol.*, **29,** 1-20.

Manabe, S., 1969: Climate and the ocean circulation. PartI: The atmospheric circulation and the hydrology of the earth's surface. *Mon. Weather Rev*, **97,** 739–774

Manzi, A.O. and Planton, S., 1994: Implementation of the ISBA parameterization scheme for land surface processes in a GCM: An annual-cycle experiment. *J. Hydrol*., **155**, 355–389

Martin, G.M., Johnson, D.W. and Spice, A., 1994: The measurement and parameterization of effective radius of droplets in warm stratocumulus. J. Atmos. Sci., 51, 1823-1842.

Mason, B. J., 1971: The physics of clouds. Clarendon Prress, Oxford

Mason. P. J. , 1985: 'On the parameterization of orographic drag'. MET. O. 14, T.D.N. No. 177, Meteorological Office, Bracknell, UK.

Mason, P.J. , 1991: 'Boundary layer parametrization in heterogeneous terrain'. In: ECMWF workshop proceedings on Fine-scale modelling and the development of parametrization schemes.

Miles, J. W. and Huppert, H. E., 1969: Lee waves in a stratified flow. Part 4: Perturbation approximations. *J. Fluid Mech*., **35,** 495–525.

Miller, M. J., Palmer, T. N. and Swinbank, R., 1989: Parametrization and influence of subgrid-scale orography in general circulation and numerical weather prediction models. *Meteorol. Atmos. Phys.*, **40,** 84–109.

Miller, M., Beljaars, A. C. M. and Palmer, T. N., 1992: The sensitivity of the ECMWF model to the parametrization of evaporation from the tropical oceans. *J. Climate*, **5,** 418-434

Milly, P. C. D., 1982: Moisture and heat transport of hyseretic, inhomogeneous porous media: A matric head-based formulation and a numerical model. *Water Resources Res.*, **18,** 489–498

Milly, P. C. D. and Dunne, K. A., 1994: Sensitivity of the global water cycle to the water-holding capacity of land. *J. Climate*, **7**, 506–526

Mlawer, E.J., S.J. Taubman, P.D. Brown, M.J. Iacono, and S.A. CLough, 1997: Radiative transfer for inhomogeneous atmospheres: RRTM, a validated correlated-k model for the longwave. J. Geophys. Res., 102D, 16663-16682.

Morcrette, J.-J., 1991: Radiation and cloud radiative properties in the ECMWF operational weather forecast model. *J. Geophys. Res.*, **96D**, 9121-9132.

Morcrette, J.-J. and Fouquart, Y., 1985: On systematic errors in parametrized calculations of longwave radiation transfer. *Q. J. R. Meteorol. Soc.*, **111**, 691-708.

Morcrette, J.-J. and Fouquart, Y., 1986: The overlapping of cloud layers in shortwave radiation parameterizations. *J. Atmos. Sci.*, **43**, 321-328.

Morcrette, J.-J., Smith, L. and Fouquart, Y., 1986: Pressure and temperature dependence of the absorption in longwave radiation parametrizations. *Beitr. Phys. Atmos.*, **59**, 455-469.

Nieuwstadt, F. T. M, 1984: The turbulent structure of the stable, nocturnal boundary layer. *J. Atmos. Sci.*, **41,** 2202-2216.

Nitta, T., 1975: Observational determination of cloud mass flux distributions. *J. Atmos. Sc*i., **32,** 73–91

Noilhan, J. and Planton, S., 1989: A simple parameterization of land surface processes for meteorological models. *Mon. Weather Rev.*, **117,** 536–549

Nordeng, T.-E., 1994: Extended versions of the convection parametrization scheme at ECMWF and their impact upon the mean climate and transient activity of the model in the tropics., Research Dept Technical Memorandum No. 206, ECMWF, Shinfield Park, Reading RG2 9AX, United Kingdom.

Ou, S.C. and Liou, K.-N., 1995: Ice microphysics and climatic temperature feedback. Atmos. Res., 35, 127-138.

Panofsky, H. A., Tennekes, H., Lenschow, D. H. and Wyngaard, J. C., 1977: The characteristics of turbulent velocity components in the surface layer under convective conditions. *Boundary-Layer Meteorol.*, **11**, 355-361

Patterson, K. A., 1990: 'Global distribution of total and total-available soil water-holding capacities'. M.S. Thesis,Department of Geography, University of Delaware

Paulson, C.A., 1970: The mathematical representation of wind speed and temperature profiles in the unstable atmospheric surface layer. *J. Appl. Meteorol.*, **9,** 857-861.

Penner, E., 1970: Thermal conductivity of frozen soils. *Canadian J. Earth Sci.*, **7**, 982–987

Peters-Lidard, C. D., Blackburn, E., Liang, X. and Wood, E. F., 1998: The effect of soil conductivity parametrization on surface energy fluxes and temperature. *J. Atmos. Sci.*, **55(7)**, 1209–1224

Philip, J. R., 1957: Evaporation and moisture and heat fields in the soil. *J. Meteorol.*, **14,** 354–366

Phillips, S. P., 1984: Analytical surface pressure and drag for linear hydrostatic flow over three-dimensional elliptical mountains. *J. Atmos. Sci.*, **41**, 1073–1084.

Pitman, A. J., Yang, Z.-L., Cogley, J. G. and Henderson-Sellers, A., 1991: 'Description of bare essentials of surface transfer for the Bureau of Meteoroloy Research Centre AGCM'. Meteorolical Research Report 32

Press, W. H., Teukolsky, S. A., Vetterling, W. T. and Flannery, B. P., 1992: *Numerical recipes in Fortran*. Cambridge University Press.

Richards, L. A., 1931: Capillary conduction of liquids through porous mediums. *Physics*, **1,** 318–333

Richtmyer, R. D. and Morton, K. W., 1967: Difference methods for initial value problems. Interscience

Rodgers, C. D., 1967: 'The radiative heat budget of the troposphere and lower stratosphere'. Report A2, Planetary Circulation Project, Dept. of Meteorology, M.I.T., Cambridge, Mass., 99 pp.

Rodgers, C. D. and Walshaw, C. D., 1966: The computation of the infrared cooling rate in planetary atmospheres. *Q. J. R. Meteorol. Soc.*, **92**, 67-92.

Rothman, L.S., et al., 1986: The HITRAN database, 1986 edition. Appl. Optics, 26, 4058-409.

Rothman, L.S., et al., 1992: The HITRAN database: Editions of 1991 and 1992. J. Quant. Spectros. Radiat. Transfer, 48, 469-507.

Rouse, W. R., 1984: Microclimate of the Arctic tree line. 2: Soil microclimate of tundra and forest. *Water Resources Res.*, **20(1)**, 67–73

Rutter, A. J., Kershaw, K. A., Robins, P. C. and Morton, A. J., 1972: A predictive model of rainfall interception in forests. Part I: Derivation of teh model from observations in a plantation of Corsican pine. *Agric. Meteorol.*, **9**, 367–384

Rutter, A. J., Morton, A. J. and Robins, P. C., 1975: A predictive model of rainfall interception in forests. Part II: Generalization of the model and comparison with observations in some coniferous and hardwood stands. *J Appl. Ecol.*, **12**, 367–380

Sellers, P. J., 1985: Canopy reflectance, photosynthesis and transpiration. *Int. J. Remote Sensing*, **6,** 1335-1372.

Savijarvi, H. and P. Raisanen, 1997: Long-wave optical properties of water clouds and rain. *Tellus*, **50A**, 1-11

Sellers, P.J., S.O. Los, C.J. Tucker, C.O. Justice, D.A. Dazlich, G.J. Collatz, and D.A. Randall, 1996: A revised land surface parameterization (SiB2) fro GCMs. Part II: The generation of global fields of terrestrial biophysical parameters from satellite data. *J. Climate*, **9**, 706-737.

Sellers, P. J., Mints, Y., Sud, Y. C. and Dalcher, A., 1986: A simple biosphere model (SiB) for use within general circluation models. *J Atmos. Sci.*, **43,** 505–531

Sellers, P. J., Meeson, B. W., Hall, F. G., Asrar, G., Murphy, R. E., Schiffer, R. A., Bretherton, F. P., Dickinson, R. E., Ellingson, R. G., Field, C. B., Huemmrich, K. F., Justice, C. O., Melack, J. M., Roulet, N. T., Schimel, D. S. and Try, P. D., 1995: Remote sensing of the land surface for studies of global change: Models - Algorithms - Experiments. *Remote Sens. Environ.*, **51**, 3-26.

Shettle, E. P. and Weinman, J. A., 1970: The transfer of solar irradiance through inhomogeneous turbid atmospheres evaluated by Eddington's approximation. *J. Atmos. Sci.*, **27**, 1048-1055.

Shuttleworth, W. J., 1988: Evaporation from Amazonian rainforest. *Proc. R Soc. London*, **B233**, 321–346

Shuttleworth, W. J. and co-authors, 1984a: Eddy correlation measurements of energy partition for Amazonian forest. *Q. J. R. Meteorol. Soc.*, **110,** 1143–1162

Shuttleworth. W. J. and co-authors, 1984b: Observations of radiation exchange above and below Amazonian forest. *Q. J. R. Meteorol. Soc.* **110**, 1163–1169

Simmons, A. J., Untch, A., Jacob, C., Kallberg,P. and Under, P., 1999: Stratospheric water vapour and tropical tropopause temperatures in ECMWF analyses and muli-year simularions. *Q. J. R. Meteorol. Soc.*, **125**, 353-

Simpson, J., 1971: On cumulus entrainment and one-dimensional models. *J. Atmos. Sci.*, **28,** 449–455.

Simpson, J. and Wiggert, V., 1969: Models of precipitating cumulus towers. *Mon. Weather Rev.*, **97,** 471–489.

Slingo, A., 1989: A GCM parameterization for the shortwave radiative properties of water clouds. J. Atmos. Sci., 46, 1419-1427.

Smith, S. D., 1989: Water vapour flux at the sea interface. *Boundary-Layer Meteorol.*, **47,** 277-293.

Smith, E. A. and Lei, S., 1992: Surface forcing of the infrared cooling profile over the Tibetan plateau. Part I: Influence of relative longwave radiative heating at high altitude. *J. Atmos. Sci.*, **49**, 805-822.

Stephens, G. L., 1978: Radiative properties of extended water clouds. Parts I and II. *J. Atmos. Sci.*, **35**, 2111-2122, 2123-2132.

Stephens, G. L., 1979: 'Optical properties of eight water cloud types'. C.S.I.R.O., Div. Atmos. Phys., Tech. Paper No.36, 1-36.

Sundqvist, H., 1978: A parameterization scheme for non-convective condensation including prediction of cloud water content. *Q. J. R. Meteorol. Soc.* 104, 677–690

Tanre, D., Geleyn, J.-F. and Slingo, J. M., 1984: 'First results of the introduction of an advanced aerosol-radiation interaction in the ECMWF low resolution global model'. In *Aerosols and Their Climatic Effects*. H.E. Gerber and A. Deepak, Eds., A. Deepak Publ., Hampton, Va., 133-177.

Taylor, P.A. , 1987: Comments and further analysis on the effective roughness lengths for use in numerical three-dimensional models, *Boundary-Layer Meteorol.*, **39**, 403–418.

Taylor, J. P., Edwards, J. M. Glew, M. D., Hignett, P. and Slingo, A. , 1996: Studies with a flexible new radiation code. II: Comparisons with aircraft short-wave observations. *Q. J. R. Meteorol. Soc.*, **122**, 839–862.

Tibaldi, S. and Geleyn, J.-F. , 1981': The production of a new orography, land-sea mask and associated climatological surface fields for operational purposes'. ECMWF Tech. Memo No. 40

Tiedtke, M., 1989: A comprehensive mass flux scheme for cumulus parameterization in large-scale models. *Mon. Weather Rev*., **117,** 1779–1800.

Tiedtke, M., 1993: Representation of clouds in large-scale models. *Mon. Weather Rev*.**,** 121, 3040–3061

Tiedtke, M., Heckley, W. A. and Slingo, J. , 1988: Tropical forecasting at ECMWF: On the influence of physical parametrization on the mean structure of forecasts and analyses. *Q. J. R. Meteorol. Soc*., **114**, 639–664.

Troen, I and Mahrt, L., 1986: A simple model of the atmospheric boundary layer; sensitivity to surface evaporation. *Boundary-Layer Meteorol*., **37,** 129-148.

Van den Hurk, B. J. J. M., Viterbo, P., Beljaars, A. C. M. and Betts, A. K., 2000: 'Offline validation of the ERA40 surface scheme'. ECMWF Tech. Mem. 295

Verseghy, D. L., 1991: Class-A Canadian land surface scheme for GCMs. I: Soil model. *Int. J. Cimatol*. **11**, 111–133

Viterbo, P. and Beljaars, A. C. M., 1995: 'An improved land surface parametrization scheme in the ECMWF model and its validation'. Technical Report 75, Research Department, ECMWF.

Viterbo, P., Beljaars, A. C. M., Mahouf, J.-F. and Teixeira, J., 1999: The representation of soil moisture freezing and its impact on the stable boundary layer. *Q. J. R. Meteorol. Soc.*, **125**, 2401-2426

Viterbo, P. and Betts, A. K., 1999: Impact on ECMWF forecasts of changes to the albedo of the boreal forests in the presence of snow. *J. Geophys. Res*., **104**, 27803–27810

Wallace, J. M., Tibaldi, S. and Simmons, A., 1983: Reduction of systematic forecast errors in the ECMWF model through the introduction of an envelope orography. *Q. J. R. Meteorol. Soc.*, **109**, 683–717.

Warrilow, D. A., and Buckley, E. , 1989: The impact of land surface processes on the moisture budget of a climate model. *Ann. Geophys.*, **7**, 439-450.

Warrilow, D. L., Sangster, A. B. and Slingo, A., 1986: 'Modelling of land-surface processes and their influence on European climate'. UK Met Office Report, Met O 20, Tech Note 38, 92 pp.

Washington, W. M. and. Williamson, D. L, 1977: 'A description of the NCAR GCMs'. In *GCMs of the Atmosphere*. *Methods in computational physics*, Vol. 17, J. Chang, Ed., Academic Press, 111-172.

Wexler, R. and Atlas, D., 1959: Precipitation generating cells. *J. Meteorol*., 16, 327-332. Yanai, M., S. Esbensen

and J.-H. Chu, 1973: Determination of bulk properties of tropical cloud clusters from large-scale heat and moisture budgets. *J. Atmos. Sci.*, **30,** 611–627.

Wilcox, R. W. and Belmont, A. D., 1977: ‘Ozone concentration by latitude, altitude and month, near 80 W’. Report, Control Data Corporation, Contract No. DOT-FA77WA-3999.

Wilson, M. F. and Henderson-Sellers, A., 1985: A global archive of land cover and soils data for use in general circulation models. *J. Climatol.*, **5,** 119-143

Wilson, M. F., Henderson-Sellers, A. Dickinson, R. E. and Kennedy, P. J., 1987: Sensitivity of the biosphere–atmosphere transfer scheme (BATS) to the inclusion of variable soil characteristics. *J. Climate Appl. Meteorol.* **26**, 341–362

Xue, Y., Sellers, P. J., Kinter, J. L. and Shukla, J., 1991: A simplified biosphere model for global climate studies. *J. Climate*, **4,** 345–364

Zeng, N., Neelin, J. D. and Chou, C., 1998: The first quasi-equilibrium tropical circulation model: Implementation and simulation. *J. Atmos. Sci*.